# Ultra-Widefield Optical Coherence Tomography of the Human Retina


**Anthony Terence Corcoran**

**BSc (Hons), MSc**

School of Physics and Astronomy

University of Glasgow

*This Thesis is submitted in fulfilment of the degree of*

*Doctor of Engineering*

August 2015

I would like to dedicate this thesis to my loving wife Charli without whom I would not have had the belief to complete my doctorate. Furthermore, I would like to thank her for all the great milestones we have shared over the course of my research; such as getting married, buying a house, getting our puppy (Thorin) and for kindly waiting until I had submitted my thesis before bring our first child into the world (Hamish).

# Declaration

I declare that, except where explicit reference is made to the contribution of others below, that this dissertation is the result of my own work and has not been submitted for any other degree at the University of Glasgow or any other institution.

**Stephen Pemberton**: Senior Mechanical Design Engineer at Optos, produced the mechanical files (parts, assemblies and drawings) for a wide-field phantom eye housing and the 3D-printed targets reported in Chapter 6. Stephen also provided significant technical advice on possible fabrication methods and tolerance analysis for my initial designs, improvements and verification.

**Optos Research and NPD**: For the development of the software and electronic control used in the demonstrators and *Lotte OCT* prototype, for access and training on the *Optos OCT/SLO, 200Tx* and *Daytona*, the manufacture of the USAF-Target and finally the acquisition of images from the *Spectralis*, *iVue*, *Cirrus* and *FF4* from clinical sites for me to analyse in Chapter 7 and 8.

**Dr Lengyl Imre**: For the design of the experiment on the Mounted-Retinal Target, in Section 6.5; including the supply of fluorescing materials and RPE tissue.

Anthony Terence Corcoran
BSc (Hons), MSc
August 2015

# Acknowledgements

I wish to thank each of my supervisors for their considerable time and patience spent reviewing my work. Firstly, my academic supervisor **Professor Andy Harvey** for both giving me the opportunity to study for my doctorate and his continued support. Secondly my industrial supervisor **Dr Gonzalo Muyo**, who has always been a source of honest advice and has repeatedly placed my success and development above other priorities. Thirdly, my industrial supervisor **Dr Jano van Hemert**, for both helping and encouraging me to be a better researcher, writer and planner. Finally, I would like to thank **Optos** and the members of the Research Department who have made both time and space for me within their group.

I also wish to acknowledge the support of friends and family who have allowed me to get to this this point in my life. The best man at my wedding **Dr Blair Johnston**, who was the first person to believe that I could be accepted to study and awarded a degree in Physics from The University of St Andrews. Secondly, my father **James Corcoran**, who has always provided the support and financial backing over both my further education and life. **Dr Bruce Sinclair** for accepting me for the Bobby Jones Fellowship where I gained the belief that I could succeed at post graduate education.

# Abstract

Optical coherence tomography (OCT) has become a standard of care in ophthalmology since it was first demonstrated over 20 years ago. Images acquired using commercial OCT systems have been reported to have a maximum imaging length of only 9 mm, which is equivalent to an internal-field of view of 45°. This narrow-field limitation has been acceptable because of the high level of clinical data available in the macular region and the relative simplicity of imaging this area of the retina. Commercially-available scanning laser ophthalmoloscope (SLO) systems such as the *Optos 200Tx* are capable of providing a fundus image with an internal-field of view of 200°. These systems have shown that significant early disease markers can be found earlier by investigating the retinal periphery. It is therefore clinically desirable to merge the 3D measurement of OCT with the ultra-widefield capability of the *Optos* SLO to allow clinicians to investigate the underlying morphology and progression of disease in the retinal periphery.

To meet this clinical need, an ultra-widefield SD:OCT prototype system has been developed using the *Optos* ellipsoidal-mirror architecture. Modifications were made to the standard SD:OCT system to compensate for off-axis defocus, varying optical path difference, the changing corneal birefringence and the limitations inherent for the *Optos* ellipsoidal mirrors. The optical performance of the ultra-widefield SD:OCT system was verified using a novel wide-field phantom eye (WPE). The WPE was designed to measure; the transverse and axial point-spread function, field of view, imaging range, sensitivity roll-off, dispersion and measurement accuracy of the ultra-widefield SD:OCT system in both the posterior and peripheral segments of the retina.

From these modifications, commercially-viable, ultra-widefield, SD:OCT has been demonstrated and verified using the WPE. In addition, we report the use of the WPE to compare both the imaging performance and measurement accuracy of the following ophthalmic instruments: the *Optos 200Tx*, *Heidelberg Spectralis*, *Zeiss FF4*, *Optovue iVue*, *Zeiss Cirrus* and *Optos OCT/SLO*. The WPE was successful in extracting image performance metrics for imaging feature sizes above 20 μm; however, targets fabricated using 3D-printing will require either a further advancement of the technology or hybridising with higher-precision structures to measure axial and transverse resolution.

# Publications

[Conference Proceedings] (Chapter 6) A. T. Corcoran, G. Muyo, J. I. van Hemert, and A. R. Harvey. Development of a widefield phantom eye for retinal optical coherence tomography. *SPIE BiOS*, pages 89450F–89450F. International Society for Optics and Photonics, 2014. doi:10.1117/12.2037767

[Peer Reviewed] (Chapter 6 & 7 & 8) A. T. Corcoran, G. Muyo, J. I. van Hemert, A. Gorman, and A. R. Harvey. Application of a wide-field phantom eye for optical coherence tomography and reflectance imaging. *Journal of Modern Optics*, June 2015, doi:10.1080/09500340.2015.1045309

[Patent] (Chapter 6) "Improvements in or Relating to Scanning Laser Ophthalmoscopes" Brown, W. and Williams, M. and Corcoran, A. and Swan, D. *WO Patent App. PCT/GB2013/052,556* (2014) https://www.google.co.uk/patents/WO2014053824A1?cl=en

# Table of contents

# List of figures

# List of tables

# Nomenclature

**Product Glossary**

| | |
|---|---|
| 200Tx: | Final ophthalmic platform using COE architecture, inc. SLO, FA/AF |
| **opto**map | Brand name for Optos UWF Red/Green SLO image |
| ART: | Automatic Real Time Montaging from Heidelberg |
| Cirrus: | Mid-range OCT device from Carl Zeiss |
| COE: | Architecture for products: P200, 200MA, 200Dx & 200Tx |
| Daytona: | Latest Optos optometry product using compact architecture, inc. SLO |
| iVue: | Mid-range OCT device from Optovue |
| P200: | Original panoramic product from Optos aimed at the Optometry Market |
| Spectralis: | WF ophthalmic platform from Heidelberg, inc. OCT, SLO, FA/AF and ICG |
| Zeiss FFA: | Conventional fundus camera from Carl Zeiss |
| Zemax: | Commonly used optical design and modelling program |

**Acronyms / Abbreviations**

| | |
|---|---|
| A-Scan: | 1D-Scan, column in the Z-Axis |
| AF: | Autofluorescence |
| AL-Target | Axial Layers Target |
| AMD: | Age-Related Macular Degeneration |
| B-Scan: | 2D-Scan, cross-sectional image in OCT |
| BE-Target | Bullseye Target |
| BK7 | Borosilicate - common crown glass |
| C-Scan: | 3D-Volume in OCT |
| CaF2 | Calcium Fluoride - fragile mid-IR glass |
| COE: | Confocal Optical Engine - Architecture for Optos products: P200 and 200Tx |
| DC-Term: | Direct current term describing the 0 Hz signals |
| EF-Target | Embedded Feature Target |
| ELM | External-Limiting Membrane |
| FA: | Fluorescein Angiography |
| FD:OCT | Fourier-Domain OCT |

| | |
|---|---|
| $FOV_{int}$: | Field of View - Angle from the optical axis internal to the eye |
| FSi | Fused Silica - high purity glass |
| full-$FOV_{ext}$: | Field of View- Twice the angle from the optical axis external to the eye |
| FWHM: | Full-Width Half-Maximum |
| HAP: | Hydroxyapatite |
| ICG: | Indo-Cyan Green |
| MEMS | Micro-Electro-Mechanical |
| MTF: | Modulation Transfer Function |
| NA: | Numerical Aperture |
| OCT: | Optical Coherence Tomography |
| OPD: | Optical Path-Difference |
| OPL: | Optical Path-length |
| PMMA | PMMA - Polymethyl Methacrylate - common optical plastic |
| PSF | Point-Spread Function |
| RMS | Root-Mean Square |
| RPE: | Retinal Pigment Epithelium |
| SD:OCT | Spectral-Domain OCT |
| SLD | Superluminescent Diode |
| SLO: | Scanning Laser Ophthalmoscope |
| TD:OCT | Time-Domain OCT |
| USAF: | United State Air-Force (Target) |
| UWF: | Ultra-widefield |
| WPE: | Wide-field Phantom Eye |

# Chapter 1

# Introduction

## 1.1 Summary of the Thesis

*The human retina can be imaged using optical coherence tomography across an external-field angle of* $\pm 70^{\circ}$*, with an imaging performance equivalent to that demonstrated on-axis.*

The purpose of this thesis is to demonstrate this statement and to present my contribution to both the development and characterisation of the technology necessary for achieving wide-field imaging of the retina with optical coherence tomography (OCT). This introductory chapter includes both a brief summary of thesis chapters and also contains a review of the current state of the art for ultra-widefield OCT.

Chapter 2, *Development of OCT in Ophthalmology*, has been provided to introduce three aspects of OCT. Firstly, the history significance and general challenges in ophthalmology; secondly, the underlying mathematics of interferometric imaging and finally, the primary factors influencing image performance, processing and enhancement in OCT.

Chapter 3, *Development of Ultra Wide-Field OCT*, has been provided to explain the challenges of integrating an OCT module into an ultra-widefield (UWF) ophthalmoscope. The first section of the chapter has been used to familiarise the reader with the scanning laser ophthalmoscope (SLO) architecture from Optos known as the COE and includes an analysis of the optical performance of this device. The next section contains the development and integration of an OCT module into the UWF-SLO from bench top to demonstrator. In particular, this chapter reports the outcomes of the collaborative work with the OCT system developers *Wasatch Photonics*. Finally, this chapter demonstrates the successful integration of the *Opko* OCT device, rebranded as the Optos OCT/SLO, into the Daytona SLO system.

Chapter 4, *The Challenges of Wide-Field OCT Introduced by the Eye*, has been provided to report the findings of an investigation into the principle optical challenges of increasing

the field-of-view of an OCT device. The five primary technical risks have been identified and are described in detail. A method to empirically demonstrate these challenges has been explored in Chapter 5, *Performance Assessment in a Wide-field Ophthalmic Device*. This chapter showed both the need for device grading and the associated metrics which should be measured using a wide-field phantom eye.

Chapter 6, *A wide-field phantom eye for OCT and reflectance imaging*, expands upon work first presented at the BiOS conference proceedings [1] and is published in the Journal of Modern Optics [2]. This chapter is used to describe how to build a wide-field phantom eye (WPE) for the characterisation of multi-modal wide-field ophthalmic imaging. This chapter also demonstrates the use of 3D-printing to create three distinct calibration targets for OCT and SLO and discusses the effectiveness and limitations of this technology for retinal layer simulation. In addition, we use the WPE and targets as a mount for *in-vitro* imaging of retinal tissue to validate a new ophthalmic biomarker.

Chapter 7, *Performance Comparison in Widefield Reflectance Systems*, has been provided to report the extent that the FOV, warping and image quality impact the measurement capability of the *Optos* reflectance devices, *200Tx* and *Daytona*, in comparison with competitor systems: *Heidelberg Spectralis* and *Carl Zeiss FFA* fundus camera. This chapter also reviews the intra-device variability in *Optos* devices and demonstrates the improvements from recent developments in the technology. Measurements are provided on the distortion, field of view and measurement capabilities of the devices.

Chapter 8, *Performance Comparison in Commercial & Widefield OCT Systems*, is used to report a comparison between the performance of *Optos OCT/SLO*, *Heidelberg Spectralis*, *Carl Zeiss Cirrus* and *Optovue iVue* and to investigate how image quality impacts on the measurement performance of these commercial OCT devices. A summary of the key performance metrics from the devices has been compiled at the end of the first section. In addition, navigated images across $\pm 40^{\circ}$ were acquired on each of the commercial devices to investigate if the predicted artefacts stated in Chapter 4 would manifest in off-axis images. In addition, these images were used to investigate what further requirements are needed to design and calibrate a wide-field OCT system to provide consistent measurement between on and off-axis. Images were acquired from the *Optos* prototype device which show that high-performance imaging is possible across a wide-field using an ellipsoidal scan system.

Chapter 9, *Conclusions*, includes my analysis of the claims that support the outcomes of the thesis statement, *The human retina can be imaged using optical coherence tomography across an external-field angle of* $\pm 70^{\circ}$*, with an imaging performance equivalent to that demonstrated on-axis.*, based on the evidence presented in this thesis. In addition, it includes critical analysis of the limitations of my research and intended avenues for further work.

## 1.2 Current State of the Art in Ultra-Widefield OCT

*As of December 2014*

The jargon term 'ultra-widefield' is typically associated with the imaging modality SLO. This term was coined to differentiate the first *Optos* ophthalmoscope, the *Panoramic 200*, from the current fundus cameras available when this device was released in 1999 [3]. All SLOs from *Optos* have an internal-FOV ($FOV_{int}$) of approximately 200° (equivalent to an external-field angle of ±70°), which is much greater than the closest $FOV_{int}$ from a non-contact, 'wide-field' device of approximately 74° [4]. The motivation for wide-field imaging has been provided in Section 2.5 with a complete explanation of the terminology used to define $FOV_{int}$ / $FOV_{ext}$ in Section 5.3.2.

My research into UWF-OCT began for *Optos* in early 2011, at this time the leading OCT manufacturers did not view a wide FOV a clinically valuable. Instead, manufactures competed on the performance only in the regions of the retina where the macula or optic disc were visible. This narrow-field use of OCT only required an $FOV_{int}$ of 30° and increasing the FOV above 30° reduced the pixel density across the anatomy. Success of the *Panoramic 200* device (P200) and developments in acquisition speed has lead academic groups to develop research devices that can image an $FOV_{int}$ of 94° [5, 6]. These developments encouraged manufacturers to develop wide-field OCT devices such as: the *Topcon DRI OCT* (released 2013) that claims an $FOV_{int}$ of 57°; the *Optovue Avanti* (released 2013) that claims a $FOV_{int}$ of 62° and an update to the *Heidelberg Spectralis* (released 2014) that claims an $FOV_{int}$ of 74° [7–9].

Fig. 1.1 A recent edition of the *Optos P200* first released in 2011, branded as the *Optos 200Tx*. This device was designed to image a $FOV_{int}$ of 200° of the retina in 320 ms. [10]

# Chapter 2

# Development of OCT in Ophthalmology

## Chapter Summary

This chapter is used to introduce three aspects of Optical Coherence Tomography (OCT). Firstly, an introduction to ophthalmology is provided that has been broken down into: the anatomy of the eye, the technological development of ophthalmology and the pathologies of the eye that require diagnosis and classification. Second, the underlying mathematics of interferometric imaging is presented to provide a theoretical description of OCT. Finally, the primary factors influencing image performance are discussed alongside some of the practical aspects of image processing and image enhancement in OCT.

## 2.1 The Anatomy of the Human Eye

The human eye, as seen in Figure 2.1, is one of the most complex and interesting organs in the body. The eye has been the subject of many extensive investigations and the optical and biological properties of this organ are catalogued in many books [11, 12]. Light entering the eye passes through the transparent membrane in the opaque sclera known as the cornea. The cornea provides around 70% of the focal power of the eye. The fluid filled bulge inside the cornea, known as the anterior chamber, is filled with a clear gel known as an aqueous humour. The primary purpose of the aqueous humour is to provide nourishment to the anterior chamber and causes little refraction of the light. The light traversing the aqueous humour then passes through the ocular aperture that is known as the iris, creating the pupil of the eye. The key function of the iris is to control the amount of light reaching the back of the eye and defines the numerical aperture of the eye. The iris can vary its diameter from around 8 mm in darkness to 2 mm in bright light.

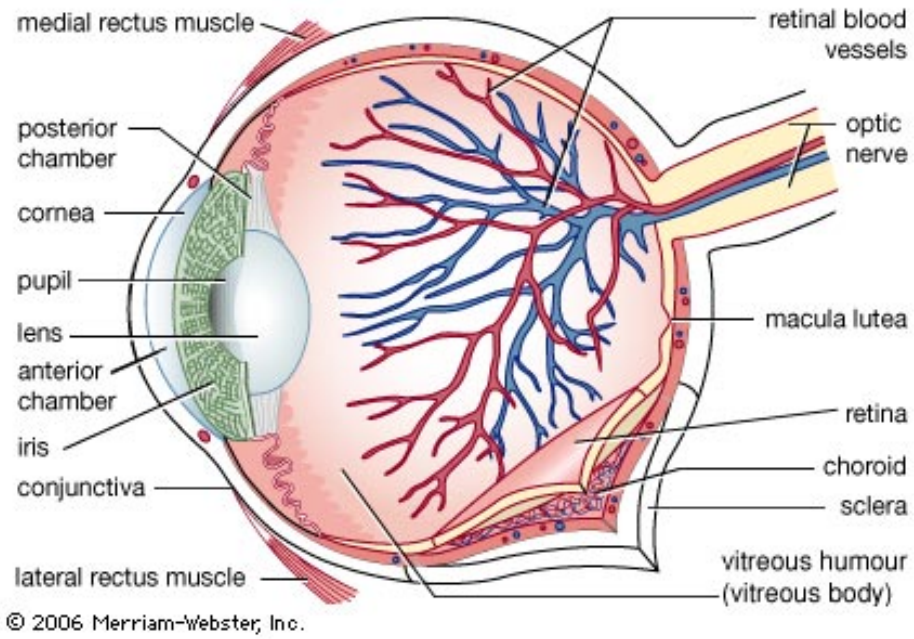


Fig. 2.1 An illustrative cross section of the human eye [13].

The second, focusing element is the crystalline lens. This lens is made up of a fibrous bundle of cells encased inside an elastic membrane. The crystalline lens has a variable curvature to provide accommodation; however, both its refractive index [14], shape and flexibility decay with age, reducing this capability [15]. Rays originating from distant objects require the lens has a low curvature to focus the near parallel-rays. This infinite conjugate is accommodated by a tightening of the suspensory ligaments holding the lens and thus stretches the lens flat. Rays originating from any near objects have a high divergence and therefore require a large curvature to be brought into focus at the retina. This focal length is accommodated by a relaxing of the ciliary muscle.

The common condition of over-focusing distant objects by the lens is called myopia (near-sightedness) and the inability to focus close objects is called hyperopia (far-sightedness). The two principle causes of myopia are firstly, pathological myopia, where the axial elongation of the eye exceeds the focal length of the lens or secondly, non-pathological myopia, where a dysfunction in one the ocular systems such as a weakening of the muscles that control the lens reduces the refractive properties of the lens [16]. Hyperopia is very common in ageing eyes (Presbyopia) and is typically caused by a denaturing of the lens proteins, which makes the crystalline lens and cilirary muscles less flexible. The water-like gel posterior to the lens is known as the vitreous humour, which provides support to the eye and creates the optical depth required to focus light onto the back of the eye [17].

The detection component of the eye is the thin layer, between 0.1 mm and 0.4 mm thick, which coats the inner wall of the eye and is known as the retina. The retina contains an array of photoreceptor cells called rods and cones that have a diameter between 2-6 μm that when a photon is absorbed, trigger a structural change in the cell pigment through a process called phototransduction [18]. The rod cells provide scotopic vision and have a higher light sensitivity than the cone cells; however, have no colour definition. A concentration of cone photoreceptor cells is found in the central area of the retina, known as the fovea; this area has a diameter of around 1.25 mm and is depressed relative to the rest of the retina. At the centre of the fovea is the foveola. This 350μm wide region contains only cone cells at a density of 50 per 100μm. The foveola is responsible for the sharp focus at the optical-axis of vision. An array of nerves is required to communicate the electrical impulses generated by the photoreceptor cells. These nerves intersect at the optical disk, which connects the retina to the brain. A dense layer of blood vessels, known as the choroid, lies between the sclera and the retina. The purpose of this layer is to supply the photoreceptor cells with nutrients and oxygen and remove waste material [17].

## 2.2 Schematic Model Eyes

Schematic-eye models are an empirically-determined set of parameters that describe the optical properties of a healthy human eye for use in computational analysis [19]. In most cases, schematic eyes are used to model the practical performance of emmetropic eyes so that aberrations can be corrected in applications such as surgery, optometry and ophthalmology. One of the first and most well known schematic eyes is the near-paraxial Gullstrand Eye, 1909 [20]. This early schematic model does not include either the aspheric surfaces and a GRIN crystalline lens found in real eyes. Aspheric surfaces were included in the Navarro schematic eye [21] which is shown in Table 2.1 to account for the off-axis aberrations within the eye. Although this model is considered a simplified eye, as it lacks a GRIN lens and retains spherical symmetry, it is still accepted as a good model for off-axis performance in the eye [19, 22]. The Liou-Brennan schematic eye seen in Table 2.2 includes both a GRIN lens and aspheric surfaces making it an ideal model for predicting on-axis imaging performance of the eye [23]. More recently, Goncharov and Dainty published the complex schematic, which is in Table 2.3. This eye model was designed to retain both the wide-field accuracy of the eye while including the effect of ageing and other demographics on the eye [22].

There is little variation in the schematic eyes outside the treatment of the crystalline lens. The Liou-Brennan model is considered to be one of the best representations of on-axis aberrations. However, choice of which model ultimately is determined by the application

| Surface | Radius | Thickness | Ref. Index | Conic |
|---|---|---|---|---|
| Cornea Front | 7.72 | 0.55 | 1.38 | -0.26 |
| Cornea Back | 6.5 | 3.05 | 1.34 | 0 |
| Lens Front | 10.2 | 4 | 1.42 | 3.316 |
| Lens Back | -6 | 16.3203 | 1.34 | -1 |
| Retina | -12 | - | - | 0 |

Table 2.1 1985 Navarro Wide-field Schematic Eye [21].

| Surface | Radius | Thickness | Ref. Index | Conic |
|---|---|---|---|---|
| Cornea Front | 7.77 | 0.5 | 1.376 | -0.18 |
| Cornea Back | 6.4 | 3.16 | 1.336 | -0.6 |
| Lens Front | 12.4 | 1.59 | Grad Ant | -0.94 |
| Lens Middle | Infinite | 2.43 | Grad Post | - |
| Lens Back | -8.1 | 16.27 | 1.336 | 0.96 |
| Retina | -12 | - | - | 0 |

Table 2.2 1997 H.L Liou and N. A. Brennan Schematic Eye. Gradient Described by coefficients [$n_{00}$, $n_{01}$, $n_{02}$, $n_{10}$]: Gradient Anterior [1.386, 0.049057, -0.15427, -0.001978] and Gradient Posterior [1.407, 0, -0.006605, -0.001978] [23].

| Surface | Radius | Thickness | Ref. Index | Conic |
|---|---|---|---|---|
| Cornea Front | 7.76 | 0.55 | 1.376 | -0.10 |
| Cornea Back | 6.52 | 3.06 | 1.336 | -0.30 |
| Lens Front | 11.51 | 3.69 | Gradient | 0 |
| Lens Back | -7.67 | 16.60 | 1.3347 | 0 |
| Retina | -12 | - | - | 0 |

Table 2.3 2007 A. V. Goncharov and C. Dainty simplified schematic eye (for a 30 year old. Gradient described by coefficients [$n_1$, $n_2$, $n_3$, $n_4$, $n_5$, $n_6$] = [-0.002149, -0.0000106, 0.049467, -0.51958, 0.0001715, 0.000141] [22]

and should be treated only as an approximation as there is a substantial variability across non-emmetropic eyes [22].

## 2.3 The History of Ophthalmology

You can observe many of the difficulties involved in viewing the retina simply by looking at your reflection in another's eye. The pupil appears black and the reflection occurs at the cornea; a feature known as the corneal reflex whose influence in retinal imaging is in most cases, severely unwanted. The intrinsic purpose of the eye requires that it is an efficient absorber of light and thus a poor reflector in the visible region. The small amount of light that is reflected by the retina is wavelength dependent; with wavelengths in the near-infrared levelling at around out at 5% reflectance [24], as seen in Figure 2.2 (a). The transmission of light through the eye increases towards the near-infrared as the blue-green part of the spectrum is strongly absorbed by both the blood and melanin pigment, which protect the eye from UV radiation. This absorption creates a natural axial-segmentation that can be exploited through the use of different wavelength channels. In addition to the low reflectance of the retina, the optics of the eye impede external examination; for example, all the refractive interfaces between the retina and the observer provide their own reflection, refraction, birefringence and dispersion that will interfere with clear image formation.

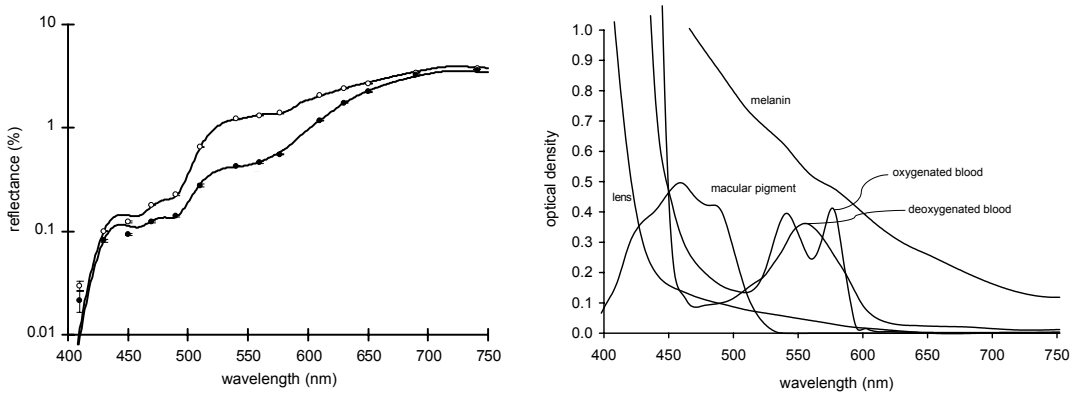


(a) (b)

Fig. 2.2 (a) Reflectance of the fundus for dark and light adapted retina; represented by open and closed circles, respectively. (b) Absorption spectra resulting from the molecular composition of the retina [25]. This figure shows that for wavelengths above 600 nm the primary absorber in the eye is melanin resulting in higher reflectivity for this wavelength region

The living retina was first viewed by Johannes Prukinje in 1823 while the first working ophthalmoscope was constructed by Charles Babbage in 1887; although, his instrument obscured the view of the observer during illumination [24]. These developments lead to Hermann von Helmholtz being credited with the first practical ophthalmoscope in 1850. [26]. These ophthalmoscopes were a considerable achievement as they were constructed before the invention of critical technologies that modern engineers now take for granted; such as the light bulb, from Edison in 1880 and the photographic film, from Eastman in 1891. These technologies were used to develop the first fundus camera from Gullstrand in 1910, an invention that is still conceptually similar to current fundus camera designs and for which he received a Nobel Prize [20]. Further Nobel-Prize winning technologies that are crucial to modern ophthalmoscopes include, the invention of the laser in 1960, by Gordon Gauld *et al.* [27] and the first charge-coupled device (CCD) in 1969, from George Smith and Willard Boyle [28]. With the invention of coherent sources, snapshot and real-time imaging the required tools were finally available to overcome the challenges of today's ophthalmoscopes.

## 2.4 Ophthalmic Pathologies

### 2.4.1 Common Pathologies

It is crucial that engineers understand the relevance of their designs, particularly in a medical-technology industry where there is a greater need for efficient screening of diseases. Viewing the retina is a necessity of medical practitioners as most retinal pathologies eventually lead to blindness. Furthermore, the retina being composed of brain tissue allows non-invasive early diagnosis diseases such as Alzheimer's disease and multiple-sclerosis due to the deteriorating thickness of the retinal-nerve fibre layer (RNFL) [29–33]. There are a greater number of pathologies that can be seen in the retina, some of the more common are listed below.

*Diabetes mellitus* is associated with hyperglycaemia, an excess of blood sugar that causes the degradation of the blood vessels and nerve cells in the body. When this pathology manifests itself within the retina, it is referred to as diabetic retinopathy and will result in either of two unfavourable responses from the eye. The first, ischemia, is the formation of overly weak veins that haemorrhage into the vitreous humour. The second, macular oedema, results in a breakdown of the blood-retina barrier, which causes a build up of blood inside the retina and leads to retinal bulging.

Diabetes is considered a pandemic, with the increase in the global number of adults with the disease expected to rise from 285 to 439 million in 2030. A rise in the prevalence from 6.4% to 7.7% is expected with in addition to a tripling of the costs per patient [34, 35].

Type-2 diabetes is predominantly caused by life-style and the possible savings from early intervention make the screening for this disease likely to become routine practice in the future. The impact of diabetes on global blindness is still relatively low with only 4.3% of recorded cases of blindness being attributed [36]; however, diabetes is considered of primary importance to ophthalmology due to the relative ease that disease classification and diagnosis can be achieved by imaging the retina.

*Age-Related Macular Degeneration* (AMD) is the leading cause of visual impairment for the developed world (excluding the USA) [37]. AMD comes in two forms: dry and wet. Dry is typically less severe and is characterised by a gradual loss of vision resulting from a break down of the retinal pigment epithelium. This form of the disease typically presents with the development of many small drusen across the retina. Wet AMD is highly threatening to vision and causes veins to grow inwards around the macula. This abnormal growth results in an increased permeability of blood in the veins and causes fluid to build in the retina. The number of people with AMD is expected to soar as life expectancy increases [38]. Though 40% of the blind registered in the UK suffer AMD, its global influence is only 7.9%.

*Cataracts* is the leading cause of blindness worldwide and is estimated to cause 47.9% of all blindness in the world [36]. Cataracts results from a denaturing of the proteins in the crystalline lens leading to an increased opacity of the crystalline lens. This general increase in ocular scattering is easily mistaken by the patient for the natural effects of ageing and therefore requires diagnosis as is easily left untreated which will lead to blindness [39]. Cataracts is commonly remedied by the surgical removal of the lens, thus it is less prevalent in developed countries. The development of cataracts is thought to be due to either an excess of UV light, a genetic defect, or as a side effect of another disease.

*Glaucoma* refers to the damage of the optical nerve fibre and retinal ganglion cells (RGC) located near the surface of the retina. Glaucoma is primarily caused by an increased pressure in the aqueous humour. The increase occurs after the trabecular meshwork becomes blocked and fails to regulate fluid pressure [40]. Diagnosis of glaucoma is most readily seen from the three dimensional shape of the optic nerve head and is characterised by the cupping ratio of the optic nerve fibre head. Glaucoma is more prevalent in non-white demographics and afflicts 12.3% of blind people globally.

*Cardiovascular Disease* can be detected in the retina during ophthalmic examinations. A change in the ratio of artery to vein diameter, known as the A/V ratio, caused by hypertension in the eye has been linked to both stroke and myocardial infarctions [41].

*Cone-Rod Distrophy (CRD)* is a genetic degenerative disease that causes the loss of the retinal photosensitive cells. CRD is can be identified by lesions on the retina [42].

*Retinoblastoma* is a form of cancer that attacks the developing retina in children. This disease has one of the highest cure rates for cancer thanks mainly to early detection through screening as standard [43].

*Choroidal Melanoma and Metastases* refers to the presence of a tumour in the retinal choroid. When cancer undergoes metastasises then a local breakdown in the cancer cells results in a section of the tumour breaking off allowing it to spread to other organs making treatment much more difficult. The occurrence of tumours originating within the choroid is rare, meaning detection of choroidal melanoma is typically indicative of cancer that has already under went metastases and is in the blood stream. The lack of symptoms and the severity of the disease if left untreated highlight the key role of ophthalmic screening.

*Retinal Detachment* is the process in which the retina detaches from the choroid. This detachment eventually results in a loss of vision [44]. This pathology is of particular importance to *Optos* as the undiagnosed occurrence of a retinal detachment in the founder's son was the motivation for the development of an easy-to-image, wide-field ophthalmoscope [3].

There are three significant trends related to blindness that engineers investigating solutions must take note of. Firstly, 82% of people afflicted with blindness are over 50; secondly, 87% of the blind are from developing countries, and lastly 85% of global blindness is avoidable [36]. These statistics suggest that there is a tremendous opportunity to reduce the prevalence of worldwide blindness and that the demographic is increasingly elderly who are typically difficult to image and unlikely to have emmetropic eyes. The greatest impact to reduce global blindness for an manufacturer would be through developing devices that are accessible to all i.e. require inexpensive equipment for screening, rather than push the limits of the current technology.

### 2.4.2 Peripheral Pathologies

Imaging the retinal periphery is sometimes seen by ophthalmologists as less important than imaging the fundus. The fundus is typically defined as the 30° solid angle measured externally along the optical axis. The fundus of the eye provides the central vision; therefore, if both the fundus and anterior of the patient is healthy then the sight of the patient will also be healthy. Although retinal pathologies can be treated or at least slowed, retinal damage can rarely be reversed. Many of the above listed pathologies, such as AMD and diabetic retinopathy may be present in the peripheral retina before appearing in the fundus [45]. Thus, imaging of the retinal periphery is typically used as a crucial early detection system [46] for pre-symptomatic treatment. In addition to the pathologies listed above, an ophthalmologist will likely be looking for the pathologies listed below.

*Rhegmatogenous* refers to an area of the retina that has suffered degeneration, such as lattice degeneration, which makes it more likely to develop holes and tears that will lead to a retinal detachment. These damaged areas typically present out of the central view of the fundus cameras [47]. Any indication of probable subsequent retinal detachment is crucial as around half of the patients with retinal detachment are unable to discern their own symptoms in the early to mid-stage of the condition. Retinal detachments that are non-rhegmatogenous typically indicate serious forms of cancer from other parts of the body that have migrated in the blood. Thus, tracking the route of retinal detachment has crucial connotations [48].

*Retinoschisis* is a degeneration of the nerve tissue in the retina, resulting in lesions, holes and a splitting of the nerve fibre layer. Diagnosis of this pathology can be seen earlier in the periphery. Peripheral imaging also helps to differentiate retinoschisis from retinal detachment; the latter of which requires potentially harmful invasive surgery, unlike retinoschisis, which can only be treated with dietary supplements [49].

*Vitreoretinal Adhesion* is an unusual formation of the retinal tissue which has resulted in a firm attachment to the vitreous membrane. As the vitreous humour naturally shrinks with age, the retina can be torn off. Either small amounts can be torn, leaving the likelihood of retinal detachment to be small; or in serious cases, retinal detachment can become inevitable [50]. Viteroretinal adhesion is equally probable across the entire retina thus the maximum retinal periphery must be monitored.

## 2.5 Wide-Field Imaging of the Retina

Ophthalmic instruments typically image only a small portion at the centre of the retina as a consequence of the vignetting by the iris, plus the inadequate acquisition times imposed by patient motion. This constraint is acceptable to those ophthalmologists who are investigating only the central fundus of the eye. As discussed above, there are many reasons to look at the entire retinal surface. Wide-field imaging pertains to expanding the field of view (FOV) of ophthalmic images. In some wide-field ophthalmoscopes such as wide-field OCT [8], this expansion has managed only to increase the field by a few degrees, where as in other imaging modalities such as the SLO provided by *Optos*, [10] 80-95% of the retina can be viewed (depending on whether single frame or montaged capture is used) as seen in Fig. 2.3 (a). Wide-field imaging benefits both the ophthalmologist and the patient. Wide-field imaging provides the ophthalmologist with more information for disease classification and aids the navigation of the retina thanks to more landmarks and reduces the chance of missing pathology. For the patient, wide-field imaging decreases the number of scans required to view the whole retina and reduces the chance of pathology being missed during that navigation.

Two main methods exist for providing wide-field imaging. The first, seen in Fig. 2.3 (c-d) is through the use of a wide-angle lens attachment, such as the Staurenghi lens used with the *Heidelberg Spectralis* [4, 51] or the *RetCam3* which are predominantly used for surgical and premature retinopathy diagnosis respectively [52]. The contact lens is a lower cost method ( $3000) than the *Optos* approach with the contact minimising the dioptors of the cornea; however, it does not accommodate for patient comfort or allow imaging of the entire retina as it cannot be steered. A recent advance in this technique has improved the patient comfort of lens attachments by allowing non-contact acquisition placed a few millimetres from the cornea; however, this attachment is much more expensive as it requires more optical elements ( $20,000). Both of these lens have been developed for non-reflectance imaging modalities due to the difficulty in removing Purkinje and systematic reflexes.

The second method of wide-field, used by *Optos* uses an elliptical mirror to relay scanning laser beams onto the pupil of the patient. This method is more comfortable and provides a wider field of view than lens-based ophthalmoscopes. A free-form elliptical mirror is typically cheaper to manufacture than a complex lens system; however, the lack of flexibility as whether ultra-widefield in a device is provided can make it these systems seem more expensive than a lens based approach, where you buy a conventional ophthalmoscope and upgrade it for wide-field imaging option if desired. This form of wide-field imaging will be covered in detail in Chapter 3 as the base platform for the ultra-widefield OCT investigated in this thesis. A comparison of the two methods of wide-field acquisition has been provided in Chapter 7.

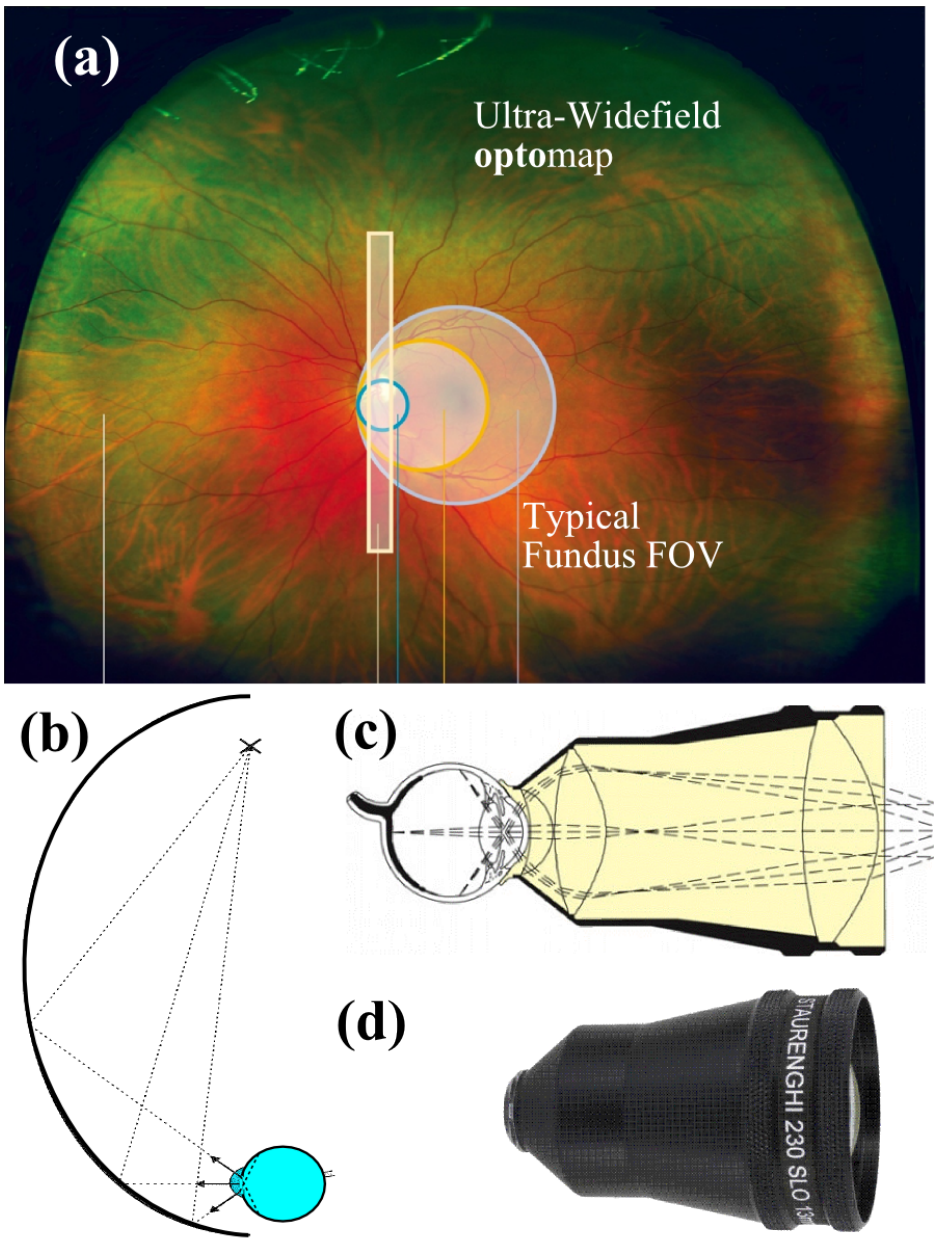


Fig. 2.3 (a) Image Demonstrating the value of ultra-widefield Imaging showing the difference in FOV between a conventional an UWF-ophthalmoscope. White: Slit Lamp, D. Blue: Direct Ophthalmoscope, Yellow: In-Direct Microscope, L. Blue: Fundus Camera. (b) Elliptical mirror schematic diagram showing two scan vertex. (c-d) Staurenghi contact lens used to achieve ultra-widefield imaging.

## 2.6 History of Optical Coherence Tomography

Ophthalmologists have a large variety of equipment at their disposal to diagnose an even larger variety of pathologies. Frequently used ophthalmic equipment like the indirect microscope and the confocal scanning laser microscope (c-SLO) provide high resolution 2D images both quickly and relatively easily. Unfortunately, many indicators of ocular pathologies do not present on the retinal surface; for example, retinal oedema occurs when poorly formed vasculature results in blood leaking into the subsurface layers of the retina. c-SLO can be used to produce 3D images of tissue by scanning the confocal gate that attenuates light out-with the image plane. This method is ideal for in-vitro imaging where a large numerical aperture allows tight axial-gating; however, the low NA possible in ophthalmology of under 0.1 makes axial-resolution below 100 μm unachievable. Furthermore, this technology cannot achieve sufficient signal intensity without exposing the eye to unsafe levels of light [53].

Optical coherence tomography (OCT) enables three-dimensional structural imaging of biological tissue in real-time. This modality is used to produce consistant images of tissue substructure as an alternative to the excision required in microscopy. The quantitative images produced allow the regular tracking of disease progression and the sharing of that information to databases for the automated disease diagnosis. Ophthalmic OCT images have an axial resolution as high as 3 μm [54] and transverse resolutions which are typically limited by the aberrations of the eye to around 20 μm. OCT can be used to measure functional features such as blood flow, molecular densities and micro-structural changes as imaging does not perturb the sample. Current-commerical systems can image small 3D segments, typically about $(4\ \text{mm})^3$, in the order of a few seconds. However, recent advances in the device acquisition speed have allowed companies such as *Optovue* to image volumes as large as 12 x 9 x 2 mm. These volumes permit *en-face* OCT imaging to fulfil the function of fundus cameras and provide access to many other disease indicators in a signal scan [8, 55].

In 1991 Huang *et al.* demonstrated the first OCT images of the retina during his PhD at MIT [56]. The idea of using coherence gating in ophthalmology was developed previously by Fercher *et al.* in 1988 when he used low-coherence interferometry (LCI) to measure the axial length of the eye [57]. LCI had originally been developed as a 1D range finder within fibre optics [58]; however, when it was developed into a fast 3D-imaging technique it became known as OCT. Unlike well known 3D-scanning technologies such as X-Ray computer-assisted tomography (CT) and positron emission tomography (PET) that are used to characterise the absorption and emission properties of a material, OCT measures the reflective and back-scattering properties of a material through the discontinuities in refractive indices. This limits OCT to imaging low-scattering organs such as the eye, skin and arterial walls (using rotating endoscopes).

In 2006, the ophthalmic OCT market became heavily competitive as the ending of the OCT-related patents held by *Carl Zeiss* allowed many new entrants to the market. After this period, a split developed in the progress of the technology between industry and research. The commercial manufacturers of devices released after 2006 focused on improving the interface, features and repeatability of their devices while maintaining the overall technology and cost [59]. The research community focused on the core technology and the advancement of capabilities of the technology at the expense of cost and simplicity. A comparison of the specifications of a high-end commercial ophthalmic system and an ophthalmic research system can be seen in Table 2.6.

| Predominant Method | Commercial | Research* |
|---|---|---|
| | Spectral Domain | Swept Source |
| Axial Resolution | 3$\mu m$ | 1$\mu m$ |
| Lateral Resolution | 20$\mu m$ | 5$\mu m$ |
| A-Scan Rate | 70 kHz | 20 MHz |
| Imaging Range | 2 mm | Whole Eye |
| B-Scan Length | 12 mm | 25 mm |
| Sensitivity | -80 dB | -98 dB |
| Depth | 1.5 mm | > 8 mm |

* Individually Optimised

Table 2.4 Comparison between of commercial and research ophthalmic OCT devices in 2014. The industrial specifications are from the *Optovue Avanti* system. The research specifications are from separate publications focusing on individual metrics [60–62]. A description of each of these metrics are provided in Section. 2.9

The main performance bottleneck of commerical devices is the A-Scan speed. As the sensitivity and speed of the spectrometers naturally progresses, so will the performance of commerical devices increase. However, key opinion leaders such as Wolfgang Drexler [62] have stated that cost and consumer confidence are the two primary barriers between different techniques used in the commercial and research ophthalmic systems. These barriers will likely be overcome by the increased demand for swept-wavelength sources in non-ophthalmic uses such as endoscopic OCT and the potential success of the *Topcon's* recent swept-source OCT device (SS:OCT), which has currently stalled due to failing to achieve FDA clearance. [63].

## 2.7 Theoretical Description of Optical Coherence Tomography

At the heart of OCT is the common optical configuration known as the Michelson interferometer, shown in Fig 2.4 and described in detail in any good physics textbook [17]. This system splits light into two beams which are subsequently recombined after reflecting off a mirror or sample. The recombination of the coherent light adds constructively when the phase of the oscillating electric field is equal between the two beams. The number of cycles of constructive and destructive interference caused by the relative translation of one of the paths provides a very precise method to measure the relative optical-path-difference (OPD) translated between the two reflectors.

To perform OCT, a polychromatic source is employed as it has a short coherence length. This characteristic means interference is only produced close to the point where the difference between the two paths is approximately zero. When a sample reflector has an OPD within the coherence length from the reference mirror, a coherent amplification of the light can be detected which is proportional to the reflectivity of the sample. To produce a column of pixels in an OCT image, known as an A-scan, scanning can be provided by sweeping the signal in one of two domains. The first domain, known as time-domain employs a moving reference arm with a fixed periodicity to allow the pixels to be linearly sampled in time. Synthetic data from this domain is shown in Fig. 2.4 (b). The second domain, known as spectral-domain, uses the capability of the Michelson interferometer to act like a periodic frequency-filter. In this domain the intensity at the detector depends on the phase difference for the detected frequency between the reference and sample beam. When all of the frequencies of polychromatic source are sampled, the periodic variation in intensity caused by the chromatic filtering is observed across the source spectrum. This signal is known as a channel spectrum and has been shown on the bottom left of Fig. 2.4.

Many reviews have provided a mathematical description of the interference pattern in OCT [64–67], each with variations in notation and emphasis. The Frecher *et al.* review in 2003 is possibly the most complete theoretical review of OCT as it maintains the vector notation which allows for scattering in the analysis [68]. The Izatt and Choma chapter from the Drexler and Fujimoto OCT book on OCT [69] presents a simple model that provides a more practical description of the interference signal in OCT across both domains. I will maintain the same notation in this thesis and present the key points from the text.

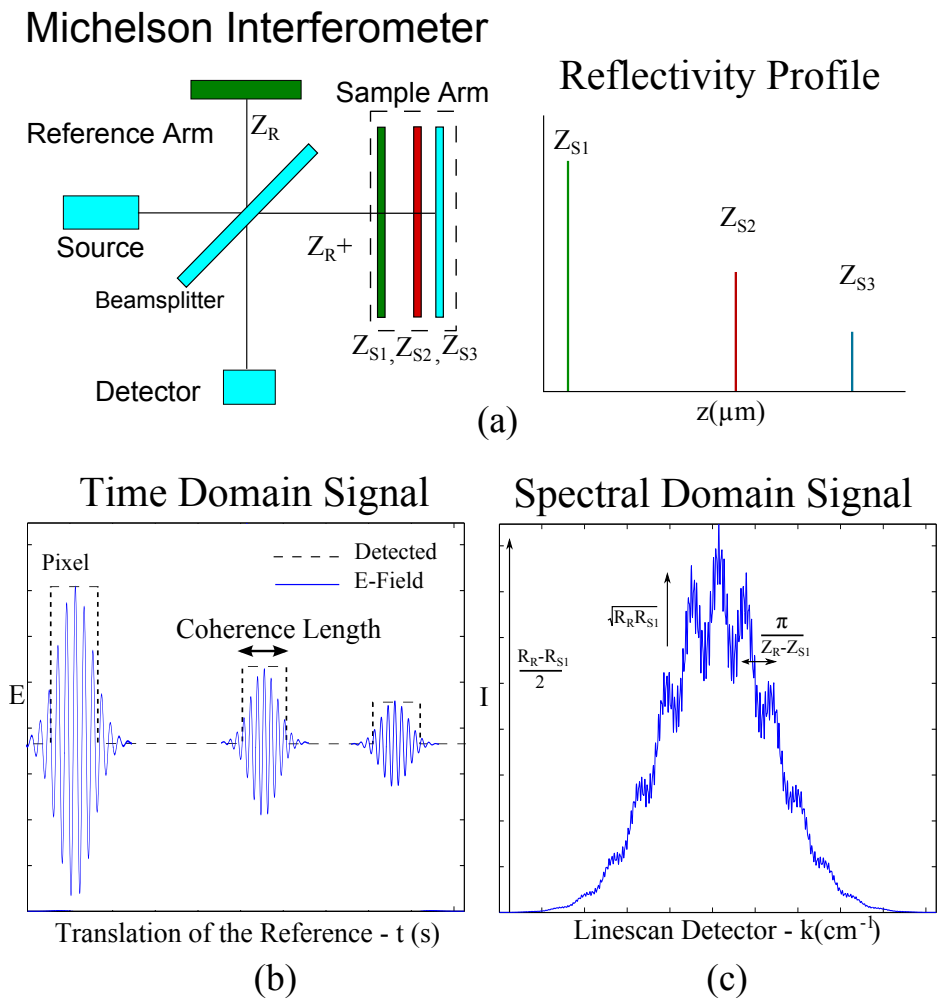


Fig. 2.4 (a) Example of OCT signal from a Michelson interferometer OCT set up. (b) The time-domain signal produces A-scans after each sweep of the reference arm. The coherence length has been exaggerated to show the interference fringes which are below the sampling rate of the detector. (c) The spectral domain signal shows three periodicities which increase with distance from the DC location.

### 2.7.1 Michelson Interferometer

The OCT input signal is split into the reference arm and the sample arm signal. A description of each of each these signals is provided by:

$$E_i = S(k)e^{i(kz-\omega t)} \tag{2.1}$$

"*Input Signal*"

$$E_R = \frac{E_i}{2} r_R e^{i(2kz_R)} \tag{2.2}$$

"*Reference Arm Signal*"

$$E_S = \frac{E_i}{2} \sum_{n=1}^{N} r_{Sn} e^{i(2kz_{Sn})}. \tag{2.3}$$

"*Sample Arm Signal*"

The equation for the input signal is simply the common description for a light wave, where S(k) is the spectral power density from the broadband light source, typically described using a Gaussian distribution and proportional to the propagation constant $k = 2\pi n(\lambda)/\lambda$. The propagation constant is dependant upon $n(\lambda)$ and will introduce chromatic dispersion.

The amplitude of the electric field of the reference arm signal is composed of the input signal $E_i$ divided by a factor of $\sqrt{2}$ for each transmission through a double pass of a 50:50 beam splitter. This amplitude is multiplied by the electrical field reflectivity of the reference mirror $r_R$, which can be converted to the power reflectivity via $R_R = |r_R|^2$. The phase shift imposed by the return trip optical path length of $z_R$ is described by the phasor $e^{i\phi}$ where $\phi = (2kz_R)$.

The amplitude of the sample arm signal also depends on $\frac{E_i}{2}$; however, the reflected signal originates from the discontinuities in the refractive index within the media. This signal is approximated to a series of N discrete reflectance sites localised at $z = z_{Sn}$, and described by $r_s(z_s) = \sum_{n=1}^{N} r_{Sn}\delta(z - z_{Sn})$. When this sum is multiplied by the phasor for each discontinuity in the refractive index, the sample arm signal can be described by the discrete convolution used in Eq. 2.3 The aim of OCT imaging is to map the function $\sqrt{R_s(z_s)}$.

The reference arm and sample arm interfere at the detector, which generates a current $i_D$,

$$i_D = \rho \left\langle |E_R + E_S|^2 \right\rangle, \tag{2.4}$$

where $\rho$ is the responsivity of the detector (Amperes/Watt). Combining Eq. 2.2, 2.3 & 2.4 creates,

$$i_D = \rho \left\langle |\frac{S(k,\omega)}{2} r_R e^{i(2kz_R - \omega t)} + \frac{S(k,\omega)}{2} r_{Sn} e^{i(2kz_{Sn} - \omega t)}|^2 \right\rangle. \tag{2.5}$$

Using Euler's equations to simplify the Eq. 2.5 gives Eq. 2.7 below. The imaged A-scan profile $I_D(z)$ is then generated via the Fourier transform pair ($\frac{1}{2}[\delta(z+z_o) + \delta(z-z_o)] \rightarrow cos(kz_o)$) producing a images around the centre of the A-scan, referred to as the real and mirror image.

$$\begin{gathered} i_D(k) = \frac{\rho}{4}[S(k)(R_R + R_{S1} + R_{S2} + ...)] + ... \\ \text{"}DC\ Component\text{"} \\ \frac{\rho}{2}[S(k) \sum_{n=1}^{N} \sqrt{R_R R_{Sn}}(\cos[2k(z_R - z_{Sn})]) + ... \\ \text{"}Cross - Correlation\ Component\text{"} \\ \frac{\rho}{4}[S(k) \sum_{n \neq m=1}^{N} \sqrt{R_{Sn} R_{Sm}}(\cos[2k(z_{Sn} - z_{Sm})]), \\ \text{"}Auto - Correlation\ Component\text{"} \end{gathered} \tag{2.6}$$

This general model of the detected OCT intensity splits the signal into three components. The first; referred to as the DC component, is a sum of all pathlength-independent signals. The amplitude of this component is dominated by the reference signal $R_R S(k)$. The second part; the cross-correlation component, consists of the pathlength-dependent components used to generate the reflectivity profile in OCT. The sum of these terms are typically much smaller than the DC component, reduced by the weight of the $\sqrt{R_{Sn}}$ factor. The last term, referred to as the autocorrelation term, occurs from interference between two reflectivity sites inside the sampled. This is typically much weaker than the previous two terms because there is no amplification from the reference arm; however, lens surfaces and air-gaps in the fibre system can contribute to this fixed-pattern noise.

### 2.7.2 Time-Domain OCT

The early method of sampling the reflectivity via coherence gating with the distance from a scanning reference arm is known as time-domain OCT (TD:OCT). Fig.2.5 shows the generic layout of a TD:OCT system. TD:OCT is limited by the rate at which one can capture a depth scan (A-scan). The speed of the A-scan is determined by the speed of the scanning reference

mirror. The mechanical requirements to increase TD:OCT above 2 kHz began to reduce both its cost effectiveness and any increase in the axial sampling resulted in an unacceptable reduction in SNR below 100 dB [70].

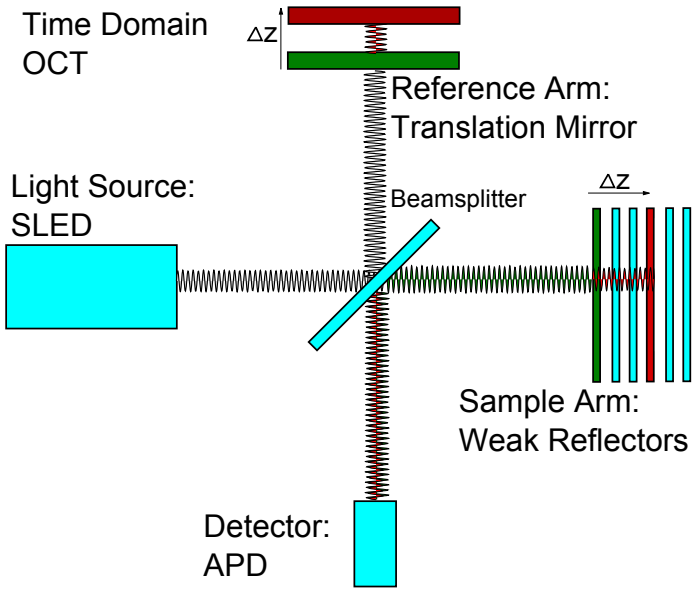


Fig. 2.5 shows the generic layout of a time domain OCT system. The moving reference arm shifts the coherence gate axially to detect different weak reflectors

### 2.7.3 Spectral Domain OCT

Extracting a depth profile from the spectral response of the sample was first proposed by Fercher *et al.* in 1995 [71], over a decade before the technique over took TD:OCT as the most commonly used OCT domain. This frequency domain imaging was first employed successfully to image the retina in 2002 by Wojtkovski *et al.* [72] which inspired further interest in this method. The principle motivation behind this development was to remove the need for the rapid mechanical elements in TD:OCT [73].

Similar to TD:OCT, a broadband light source is used to illuminate the sample; however, the reference mirror is fixed. Each frequency from the broadband source has a different phase across the optical path difference (OPD) to the reference mirror. This phase difference modulates with frequency producing a sinusoidal pattern in the detected spectrum. The period of this spectrum is proportional to the inverse of the OPD $(Z_R - Z_{Sn})$ shown in Fig. 2.4 (c) and therefore for larger differences the periodicity is smaller. This channel spectrum is encoded in wavelength onto a line scan camera using a diffraction element. The amplitude

as a function of depth is then recovered by performing a Fourier transform on the spectrum encoded in the frequency. This method is known as Spectral Domain OCT (SD:OCT) and a diagram of SD:OCT can be seen in Figure 2.6.

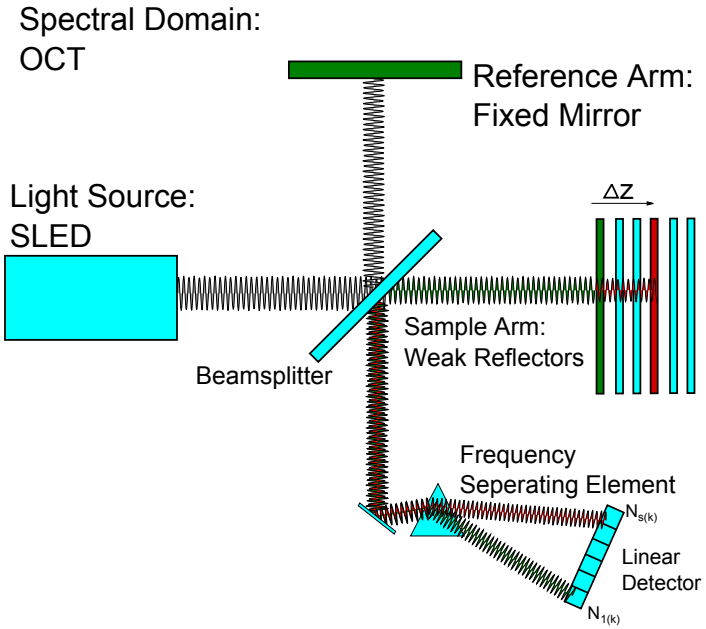


Fig. 2.6 shows the generic layout of a SD:OCT system. The reference arm is stationary and the light is collected into frequency components. Each frequency has a periodic difference in interference visibility resulting from the different phase for the round trip.

A year after its successful demonstration by Wojtkovski *et al.*, three independent publications were able to show that the theoretical relationship between the SNR between spectral and time domain was:

$$SNR_{SDOCT} = SNR_{TDOCT}\frac{N_s}{2}, \tag{2.7}$$

where $N_s$ are the number of pixels in the spectrometer or the number of samples across the frequency chirp in swept-source OCT [67, 74, 75]. This improvement results because there is no correlation between the noise in each of the detectors/samples when detecting in the Fourier domain [76]. The coherent signal is additive for each sample where as the noise-floor remains constant. The factor of $\frac{1}{2}$ is introduced by the removal of the complex signal required during the transformation from the Fourier domain (k) to spatial domain (z). For a typical OCT detector $N_s$ is 2048, making the $10^3$ improvement (practically closer to 100) directly transferable to increasing the imaging speed. As the power at the eye is limited to 0.75 mW, imposing a 'photon budget' then improvements in the SNR are the only opportunity to increase imaging speed. This metric is described in more detail in Section 2.9.3. In addition,

recording the spectral signal in SD:OCT simplifies the image processing used for dispersion compensation or the application of functional OCT compared to TD:OCT.

### 2.7.4 Swept Source OCT

Four main limitations remained for the OCT despite the improvements yielded by spectral domain imaging. Firstly, the use of a line-scan detector results in a considerable increase in the cost of OCT devices; secondly, aliasing of the signal by the line-scan detector reduces the practical range of the devices, thirdly, the use of silicon detectors in typical spectrometers constrained the OCT to a central wavelength to around 800 nm and more recently there has been a lack of advancement in the acquisition speed of the spectrometers [70]. Advances in MEMS technology, in-particularly Fabry-Pérot resonators provided the opportunity for a previously demonstrated spectral OCT technique [57] known as swept-source OCT (SS:OCT) to offer acquisition speeds nearly two orders higher than those of conventional SD:OCT [77, 78] with similar noise performances.

SS:OCT, as depicted in Figure 2.7, is a mix between time-domain and spectral-domain OCT, owing to a similar layout and detector configuration as that of TD:OCT but having a similar signal processing to that of FD:OCT. This style of OCT replaces the expensive spectrometer with a simple single pixel detector, such as an avalanche photo-diode. The super luminescent diode is replaced by a broadband laser, which is rapidly tuned to emit a changing narrow wavelength beam or pulse. Tuning is typically performed by an external-cavity Fabry-Pérot resonator. This filter allows the transmission of a narrow line-width beam only when the distance between the two mirrors is an integer multiple of the transmitted frequency. The tuning of the external cavity through a range of frequencies creates a wavelength chirped signal incident on the sample. As the beam reflects off the sample, each refractive interface inside the sample will produce beams that have a slightly different OPD. Each reflected beam interferes with the reference beam with a different frequency offset, creating depth dependent beating frequencies that will arrive on the detector at different intervals, determined by the sweep rate. As with the TD:OCT, SS:OCT measures the amplitude verses time; however, it is the frequency-dependent beating amplitude that encodes the depth dependence. A Fourier transform is then used to extract the amplitude verses distance which provides the A-scan [61].

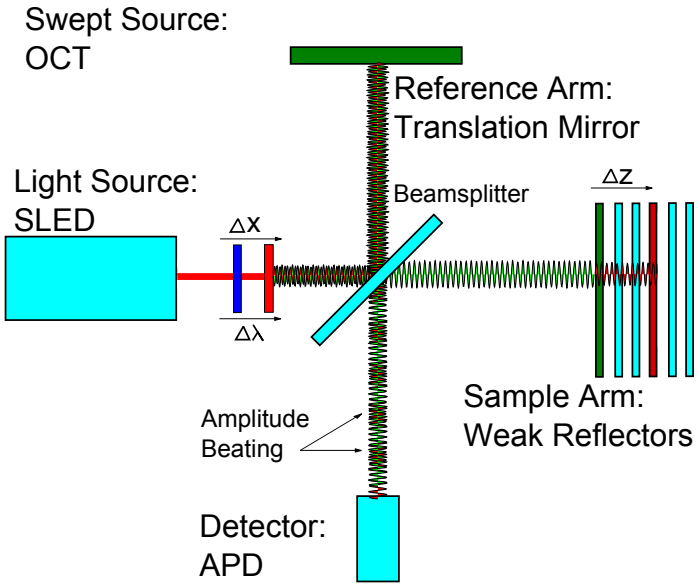


Fig. 2.7 depicts the generic layout of a swept source OCT system. A Fabry-Pérot resonator isolates a single frequency from a broadband laser. When the resonators sends out a burst of frequencies known as a chirped pulse, instantaneous wavelength of the reference single and mixes with a different frequency from the sample at the detector and displays a oscillatory beating the is related to the optical path difference to the weak reflector

## 2.8 Functional OCT

OCT is a non destructive, label-free imaging modality; and therefore, it can be used to image more than structural features. The imaging of processes of rapid change via OCT are referred to as functional OCT and it holds a key role in the diagnosis of disease before any damage has become apparent. Measurements available in functional OCT such as blood perfusion, hemodynamics, oxygen saturation, micro-structural changes and retinal birefringence provide diagnosis of pathologies such as cancer, haemorrhaging, blockages, retinal activity and burn depth. [79–82] The most common form of functional OCT is Doppler OCT, sometimes referred to as optical doppler tomography (ODT), combines the velocity measurement of laser velocimetry with the structural capability of OCT to create a velocity map. ODT has ophthalmic importance in the tracking and measurement of the vascular etiology of diabetic retinopathy, low-tension glaucoma, anterior ischemia and macular oedema [83, 84].

This brief description of functional OCT has been included to provide the reader with an understanding of the terminology when used later in the thesis; however, as functional OCT does not have a significant impact on the thesis, if the reader wishes to learn further about

this field then these references have been useful to the author when investigating the field [85–87].

## 2.9 Key Parameters in an OCT System

### 2.9.1 A-scan Rate

The key parameter for OCT imaging is the duration that is required to acquire an axial scan. The biggest jump in the development of A-scan rate was the transition from TD:OCT to SD:OCT. Practical factors such as read-out time, analogue to digital conversion and sensitivity limits the aquasition speed of the detector in SD:OCT.

In SD:OCT, the limiting factor is the read-out rate of the detector in the spectrometer. In 2003, Wojtkovski *et al.* used a CCD detector array to develop the first ophthalmic SD:OCT device with an 15 kHz A-scan rate [88]. The image was scanned along only one row of the array and the rest of the detector was used as an internal memory device for increasing speeds. The development of detectors within SD:OCT transitioned towards high-speed line-scan cameras, from companies like *Basler*, *Goodrich* and *Horiba*, which have market leading duty cycles and can cater for both 800 nm and 1300 nm. Line-scan cameras are typically used in present commercial systems, achieving scan rates up to 40 kHz [89]. Acquisition speeds were further advanced following the industry's switch to using advanced CMOS cameras. In 2008, Postaid *et al.* developed 70-312 kHz OCT images using a CMOS detector [61]. CMOS detectors are ideal for OCT because they allow the user to define the number of pixels actively detecting. This variation allows a trade off between imaging time and spectral resolution which is critical to the imaging depth. For retinal imaging where image depth needs only to be 1-2 mm this advance was effective [90].

Acquisition speed was the primary limit to the commercial application of SS:OCT; however, improvements in Fabry-Pérot resonators and development of mode-locking laser techniques, imaging speed is now the primary advantage of SS:OCT. Novel commercially designed devices such as the integrated OCT engine from *Axsun* [91], have produced commercially viable SS:OCT devices [92] with an A-Scan rate of 400 kHz. Swept-sources from other companies such as *Insight* are able provide greater than 400 kHz scan rates without the need for a mechanical filter without buffering or duel spot techniques. *Insight* use the natural refractive index increase of a semiconductor diode with input current, to increase the cavity length and use a semiconductor optical amplifier to normalise the pulse height. In a research-appropriate systems sweep rates as high as 5 MHz were achieved using piezo-electric actuator Fabry-Pérot filter. This technique was combined with buffered output

delay line, to increase duty cycle and parallel beam output to sweep at 20 MHz by Weiser *et al.* [60, 77]. This A-scan rate is high enough to achieve wide-field images with comparable pixel numbers and FOV comparable to that of fundus cameras, without incurring imaging artefacts from imaging durations of less than 3 Hz [5], the threshold used by *Optos* as the speed that images must be captured to mitigate motion artefacts.

### 2.9.2 Resolution

Interest was first generated in OCT as an alternative to tissue biopsy to negate the need for excision [93]. Tissue biopsy using a confocal microscope can image with a sub-micron resolution for cellular definition and through the use of florescence or Raman scattering to provide chemical contrast in sub-cellular features [94]. OCT lags behind the biopsy technique as the aberrations from the human eye dominate any beam with a numerical aperture above 2 mm diameter. This entrance pupil results in an numerical apeture of approximately 0.06 and a beam waists at the retina of around 20 μm, with respoct to oil immersion microscope objectives with an NA of 1.4 and a comparable resolution of 0.25 μm. The development of OCT systems with resolutions that are increased by an order of magnitude, comparable to that of confocal microscopy, are known as ultra-high resolution [95–99].

In OCT the transverse and axial resolutions are decoupled. The theoretical axial resolution is determined by the coherence length of the light source [57],

$$\delta z = \frac{2ln(2)}{\pi}\frac{\lambda_o^2}{\Delta\lambda}. \tag{2.8}$$

This relationship provides two options for increasing the axial resolution; first, decrease the imaging wavelength; second, increase the bandwidth. Typically the wavelength is chosen to suit the imaging needs, such as patient safety, imaging depth or resolution required. For example the difference between the resolution of the two extremes of medical OCT systems, 1310 nm and 780 nm, is nearly threefold if all other parameters are constant. The other option for improving the axial resolution is increasing the source bandwidth $\Delta\lambda$. This common method is achieved using broad-bandwidth lasers, SLDs, and femtosecond lasers [100]; however, this approach increases both the impact of chromatic dispersion from the eye and compromises the birefringent response of the system, which without compensation will degrade the resolution.

In OCT devices, resolution is the most common parameter to be misrepresented. Manufacturers and researchers routinely imply that their system has an axial resolution that is equal to the theoretical full-width at half-maximum (FWHM). The theoretical axial-resolution limit is imposed by the ratio of the bandwidth and central wavelength of the source, provided

previously in Eq. 2.8. In standard devices, this calculation of axial resolution is not likely to be close to the practical day-to-day value. Firstly, Eq. 2.8 assumes a Gaussian-spectral distribution, which is not necessarily the case, especially with the recent move to multiple-peak sources which have a wider spectral bandwidth. Secondly, this description of resolution does not account for chromatic dispersion from the eye or inherent to the system [101, 102]. Thirdly, smaller effects like polarisation mismatch, chromatic and wave-front aberration in the device optics, mechanical imperfections and approximations in the signal processing are unaccounted for in this description [103].

The theoretical transverse resolution is reported in many forms, all based in principle on the Rayleigh criterion on resolution. The criterion states that the minimum resolvable distance $\delta x$ between two point sources occurs when the spatial distance between the Gaussian intensity profiles $\delta l$ is equal to the distance between the peak intensity and first intensity minimum $\omega_o$ the airy radius. Therefore the theoretical transverse resolution can be represented by the equation for the first airy-radius Eq. 2.9,

$$\delta x = 1.22 f \frac{n\lambda}{2D}, \tag{2.9}$$

where $f$ is the focal length of the eye and $D$ is the diameter of the beam at the pupil. The variables in Eq. 2.9 are of greater consequence for design considerations than the exact value of $\delta x$ as complex variables such as pathology, scan density and scattering and noise will increase the empirical value of $\delta x$ considerably. The lack of precision in transverse resolution leads manufacturers of many devices to not even provide an estimate of transverse resolution nor the resulting diffraction-limited depth of field, related to the axial resolution by,

$$b = \frac{4\delta x^2}{2\lambda} \tag{2.10}$$

where an improvement in transverse resolution results in a reduction in the depth of focus in the image.

### 2.9.3 Sensitivity, Dynamic Range and Noise

For OCT, sensitivity refers to the weakest detectable reflectivity in the sample arm $R_{S,min}$. This metric can be measured by the attenuation required to image a perfect reflector with a SNR of one as shown by Eq. 2.11,

$$S(dB) = -20\log \frac{1}{R_{S,\min}}\bigg|_{SNR=1}. \tag{2.11}$$

Sensitivity is defined in OCT using a 20 dB scale to account for the voltage to current relationship in the detector. The motivation for quoting sensitivity is that it quantifies both the noise floor of the system and any systematic attenuation of the signal.

The other metric commonly quoted for a system is the dynamic range. This property defines the maximum possible variation in detectable signal inside a single A-scan from $R_{S,min}$ to $R_{S,max}$. The dynamic range is proportional to the number of electrons within the detector, referred to as well-capacity, which has led to a rise in the number of 'tall-pixel' line-scan detectors, where the pixels are an order of magnitude larger in the dimension perpendicular to the detector-row. The quoted sensitivity of an OCT system is typically around 100 dB where as OCT images have a dynamic range of around 40-60 dB [104]. The intensities of $R_s(z_s)$ are on the order of $10^{-4}$ to $10^{-5}$ below the intensity of $R_R$ which accounts for the difference between the dynamic range and sensitivity.

The SNR of an imaging system is described by ratio of the square of the mean signal intensity and the standard deviation of the detected noise,

$$SNR = \frac{\langle i_D \rangle^2}{\sigma^2}. \tag{2.12}$$

As provided in the second term of Eq. 2.7.1 the detected intensity on the detector line array can be represented as,

$$\langle i_D(k) \rangle^2 = \frac{\rho^2 S(k)^2}{2}[R_R R_s]. \tag{2.13}$$

There are four primary sources of noise in the detector. First, the read-out noise which accounts for all the noise sources in the signal processing, such as amplification, quantisation, analogue-digital conversion and electronic interference. Second, is the dark noise which accounts for the imperfections in the semiconductor material which allow a small variable background current to flow in the absence of photons. Both these parameters are typically characterised by the manufacturer and OCT literatures together as the noise term $\sigma_{r+d}$ [105]. Thirdly, the shot noise accounts for the quantisation of the source being detected by the fixed

bandwidth of the detector. Finally, the relative-intensity noise accounts for the stability of the power source. These terms can be represented as [104],

$$\sigma^2_{noise} = \sigma^2_{r+d} + \frac{e\rho\tau_i S(k) R_R}{E_v} + \left(\frac{\rho S(k) R_R}{E_v}\right)^2 \tau_i \tau_c, \tag{2.14}$$

where $e$ is the electron charge, $E_v$ is the photon energy (h$v$) and $\tau_i$ is the integration time and and $\tau_c$ represents the coherence time divided by the speed of light. This description neglects $R_S$ as it is much smaller than $R_R$. The ideal situation in OCT imaging is to be shot-noise limited, where the other sources of noise are below the practical limit imposed by the quantum effect of shot-noise. This situation is described by the idealities $\frac{\sigma_{shot}}{\sigma_{r+d}} > 1$ and $\frac{\sigma_{shot}}{\sigma_{RIN}} > 1$. Fulfilling of these idealities occurs by choosing a reference arm power that is substantially below the detector saturation [106].

The justification of the noise advantage in spectral domain over time domain arises from the discrete inverse Fourier transform of $i_D(k)$,

$$\begin{aligned} i_D(z_n) &= \sum_{n=1}^{N_s} i_D(k_n) e^{\frac{ik_m z_m}{N_s}} \\ &= \frac{\rho}{2}\sqrt{R_R R_s} \sum_{n=1}^{N_s} S(k_n) \\ &\approx i_D(z_n) N_s. \end{aligned} \tag{2.15}$$

where $N_s$ is the number of samples across the spectrum. This approximation describes a flat-topped spectrum which in practice is typically a Gaussian distributional. The shot-noise properties within the spectrometer equate as,

$$\begin{aligned} \sigma^2[z_n] &= \sum_{n=1}^{N_s} \sigma^2[k_n] \\ &= \frac{e\rho\tau_i S(k_n) R_R}{E_v} Ns. \end{aligned} \tag{2.16}$$

applying this description of the noise in a spectral domain system to the SNR equation then,

$$SNR_{FD} = \frac{\langle i_D \rangle^2}{\sigma^2} = \frac{\rho E_v S(k_n) R_s}{4e\tau_i} N_s. \tag{2.17}$$

This description of the SNR in Spectral/Fourier Domain is a factor of $N_s/2$ larger than the equivalent expression used to describe time domain [69].

### 2.9.4 Imaging Depth

There are two main components of axial depth within SD:OCT. The first, the spectral resolution of the Fourier transform varies in definition between SD:OCT and SS:OCT. In SD:OCT the imaging range is given by,

$$\Delta z = \frac{\lambda_o^2}{4n\delta\lambda} = \frac{\lambda_o^2 N_S}{4n\Delta\lambda}, \tag{2.18}$$

where $\delta\lambda$ is the wavelength resolution, and $N_S$ equals the number of pixels being used along the spectrometer [103]. For SS:OCT $\delta\lambda$ represents the linewidth of the diode source. Second, attenuation of the light via scattering, absorption and reflection, reaching and returning from the lower layers of tissue from the increased probability of multiple scatter sites is governed by Beers law,

$$I(z) = I_o e^{-\mu_t(\lambda)z}, \tag{2.19}$$

where $\mu_t(\lambda)$ is the extinction coefficient of light. The attenuation of light through the eye was shown previously in Figure 2.2 with the transmission for the IR shown in 2.8. As can be seen in both these figures, light has the least attenuation in the near infra-red spectrum; however, exhibits high absorption in the 'water bands' of 980 nm and 1200 nm [107].

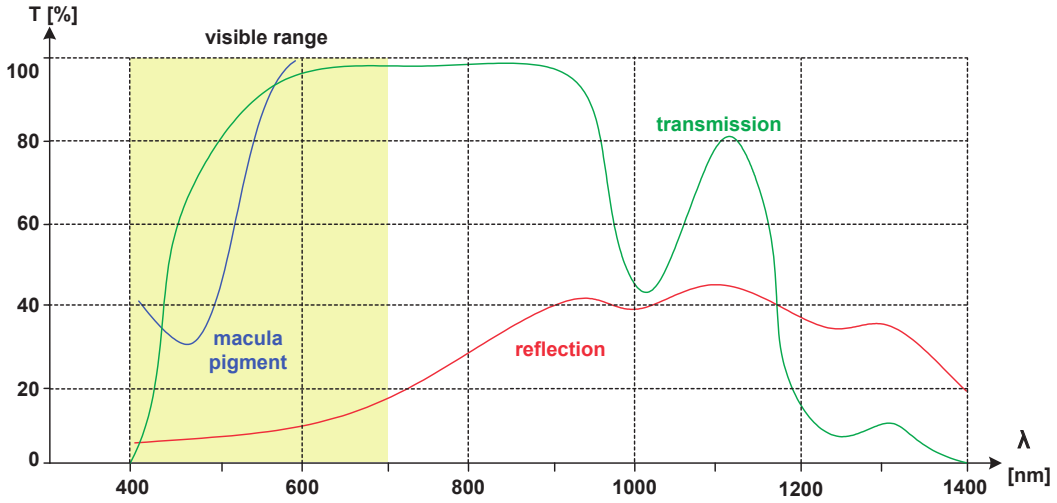


Fig. 2.8 The impact of each anatomical element to the transmission of light, reproduced from the Handbook of Optical Systems [108] with the data originally by Boettner et. al in 1962 [107].

SD:OCT exhibits a reduction in sensitivity with depth known as spectral roll-off. This reduced performance is caused by both the under sampling of a continuous spectra of

wavelengths and the imperfect focusing of the light onto a finite number of pixels. Ideally the pixel size of the detector would be infinity small to preserve the Nyquist sampling of all the wavelengths or infinity large to ensure maximal collection of the focused light; however, the choice of the pixel spacing $\delta\lambda$ is a trade off between imaging depth with axial resolution. If $\Delta\lambda$ is too small as a result of a very small $\delta\lambda$, then the full spectrum will be truncated and the diffraction limited spot will exceed the size of the pixels. To ensure the axial resolution is preserved then $\delta\lambda \approx \frac{\pi\Delta\lambda}{2ln2N_s}$ [72]. The spectral line-width recorded by the detector in-effect defines the path-difference over which coherent interference can occur between the reference and sample beam and is equivalent to the line-width of the laser in SS:OCT. A typical SD:OCT system will suffer a reduction in the sensitivity by $\approx$ 20 dB or less across a 2 mm image as a result of spectral roll-off and attenuation [60].

The optimal sensitivity roll-off is given by the convolution of the Gaussian profile of the spot focused onto the detector and the square CCD pixels [70] given by,

$$I(z) = \frac{sin^2\left(\frac{\pi z}{2\Delta z}\right)}{\left(\frac{\pi z}{2\Delta z}\right)^2} \exp\left[-\frac{\pi^2\alpha^2}{8ln(2)}\left(\frac{z}{\Delta z}\right)^2\right] \tag{2.20}$$

where z denotes reflection depth. This decay is similar to an MTF plot and provides an excellent ideality value '$p$', for the spectral sampling. $\omega$ is defined as the ratio of the grating resolution ($\delta\lambda$) and spectrometer pixel resolution ($(\lambda_{max} - \lambda_{min})/N_{Pixels}$) [74]. $\alpha_{measured}$ will differ from $\alpha_{theory}$ as a result of aberrations in the spectrometer and non-perfect mapping of high-frequency fringes. A comparison of the discrepancy using curve fitting can yield how far the device is operating from ideal. This characterisation was performed on the first OCT demonstrator reported in 3.3. This parameter can also be used to predict how the axial resolution will decay with depth because the interpolation from $\lambda$-space to k-space is sensitive to discontinuities in the sampling of the high-frequency fringes [109].

## 2.10 Acquisition and Processing

### 2.10.1 Acquiring the Spectrum

The method of processing an OCT data set is as crucial as how the data set was acquired. Much of the emphasis on commercial device performance is placed on the ability to average successive images [110] which in turn is dependent on the complexity of the distortion and alignment of the images acquired. A block diagram is provided in Fig 2.9 that explains the work flow of the OCT processing algorithms that were developed by myself for the research in this thesis. Not all steps are required in each experiment such as dispersion

compensation and averaging; however, this is the complete description of the code provided in Appendix B.1.

The first step in processing spectral data from SD:OCT is to remove the DC term in the signal (along with fixed pattern noise). Three methods can be used to remove the DC term. The first method is to block the sample arm and acquired a 'dark image'. This dark image can then be subtracted from all subsequent images. This method is useful as it also removes any cross correlation terms not associated with the sample. The downside is that the process must be repeated after any thermal drift in the device. Second, the spectrum can be averaged across subsequent scans and filtered to remove the high-frequency terms, this image is then subtracted from subsequent images. This method has been used in the OCT processing in Fig 2.9. The latter two methods are effective as they are done before the Fourier Transform and thus reduce the relative weight of the signal. A third method to remove the DC signal is to clip the image in the spatial domain to remove any pixels saturated by the DC term. This filtering method is useful as it very computationally efficient.

The interference fringes are recorded by the line-scan array within the spectrometer (or photodiode for swept source). The dispersion of the frequency components within the spectrometer is provided by a holographic diffraction grating and is in most cases is distributed linearly in wavelength across the pixels; therefore, the sampling of the spectrum is linear in wavelength. This property is not ideal as the Fourier transform maps period (t) to frequency ($\nu$) or as we are interested in distance ($d = \frac{c}{n}t$) to wavenumber ($k = \frac{2\pi n\nu}{c}$). The sampled intensities must be interpolated to find the corresponding value that would have been recorded linearly in k. There are many methods to interpolate which balance processing expense a review of which can be found from Dorrer *et al.* [111]. In my own analysis the interpolation accuracy was considered more important than speed and therefore I used the robust cubic B-spline interpolation.

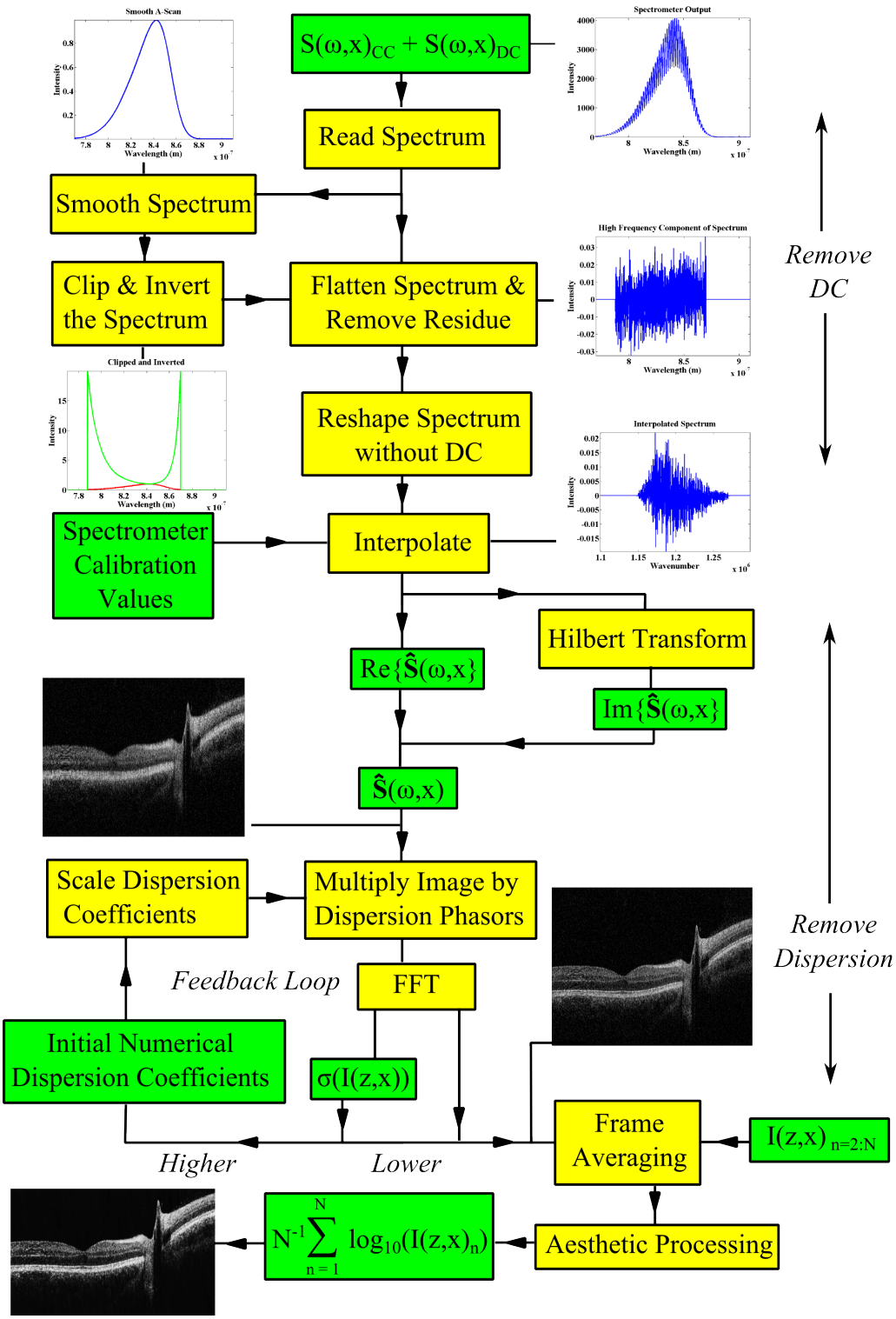


Fig. 2.9 A block diagram of the work-flow for the OCT processing used in the research reported in this Thesis, source code in Appendix B.1. Dispersion compensation is not significant in narrow-bandwidth sources used in the *Optos* OCT/SLO and Prototype.

### 2.10.2 Speckle Reduction

In OCT, speckle is the name given for the grainy effect seen in unprocessed OCT images. Schmitt et al [112] has published an extensive review of speckle, in which it they discuss the main components of speckle and include the main processes involved in its reduction. Speckle is a common effect in laser sources with long coherence lengths. Coherent interference between localised wavelets, each of which has an random phase as shown in Figure 2.10. Speckle impacts OCT as long as the path differences are within the coherence length of the backscattering particle being imaged. Despite the use of a low-coherence source, coherence noise is still a substantial problem in OCT because matched OPD ensures that the reference and sample light are effectively coherent on the detector.

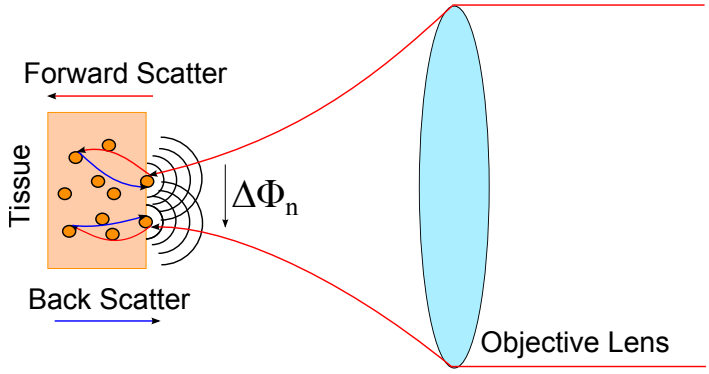


Fig. 2.10 Diagram showing multiple scatter sites in OCT which give off interfering wavelets and varying the phase relationship per scatterer across the numerical aperture of the objective lens. Furthermore the influence of forward scattering events as the photons permeate the tissue from it can cause further unpredictable change in phase.

The primary method of speckle reduction used in commercial ophthalmology is image averaging [113]. Averaging relies on the local differences in the source-to-detector perspective between successive images to generate a new speckle pattern in final images [112]. Averaging reduces the variance in the pixel-to-pixel intensity. The risk posed by this easy solution is that averaging may reduce the contrast of small features in an image. OCT manufacturers apply registration protocols to stitch successive frames correctly to minimise the blurring of patient motion. Registration allows over 100 frames to be averaged; however, the diminishing SNR improvement of averaging is often exaggerated [114]. Varying the polarization, frequency from the source [115] and focus compounding with either multiple images or multiple beams [116, 117] can be used to trade resolution for reduced speckle contrast. Also heterodyne detection using four detectors with signal mixing can produce reduce speckle contrast by up to a half. Image processing techniques such as spatial array detection and wavelet filters have also been successful [118].

### 2.10.3 Dispersion Compensation

Light propagates through a material a group velocity that is inversely-proportional to the refractive index. The refractive index $n(\omega)$ is dependent on frequency; therefore, each wavelength travels at a unique speed throughout a media. This frequency depended phase shift $\Omega(\omega)$ is referred to as chromatic dispersion where $\omega$ is the angular frequency. This smearing of the phase relative to the reference beam results in a decreased sensitivity and a dispersion of the channel spectrum in OCT systems. A system with mean wavelength $\lambda_o$ of 800nm and a bandwidth $(\Delta\lambda)$ greater than 14nm is limited to an axial resolution of 20µm unless there is dispersion compensation for the eye [119].

The propagation constant $\beta(\omega) = n(\omega)\omega/c$ can be expanded as a Taylor series around the central frequency $\omega_o = 2\pi\nu$ via:

$$\beta(\omega) = \beta(\omega_o) + \left.\frac{d\beta}{d\omega}\right|_{\omega_o}(\omega-\omega_o) + \frac{1}{2}\left.\frac{d^2\beta}{d\omega^2}\right|_{\omega_o}(\omega-\omega_o)^2 + \frac{1}{6}\left.\frac{d^3\beta}{d\omega^3}\right|_{\omega_o}(\omega-\omega_o)^3 + \ldots \tag{2.21}$$

$\beta(\omega_o)$ is the propagation constant for the central wavelength and the first order derivative is the inverse-group-velocity term. The combination of these two terms gives rise to the improved axial resolution in the higher refractive index medium than in for free-space. The second and third order derivatives correspond to the group velocity dispersion (GVD) and the variation in group velocity (VGV), respectively. GVD results in broadening of the interferogram and thus a reduction in the axial resolution. VGV describes the asymmetry or chirping in the dispersion. Higher-order terms occur with diminishing significance.

All OCT systems minimise dispersion by at least ensuring that there is a similar dispersion in both the sample and reference paths. This means that not only are the optical paths equal (around the axial range of the image processing) but also that the light propagates through equal lengths of high index (fibre) and low index (free-space) regions. To include the eye as part of the optical system in the sample arm and compensate for its dispersion using either bulk glass, a water cell or the variable shifting prisms is typically called physical dispersion compensation.

Physical dispersion compensation has the simplicity that once implemented it generally does not require further effort. This compensation has three drawbacks, first the inter-patient variability requires either a generalised solution or a mechanically varied solution. Second it is not depth dependent; therefore, not appropriate for optimising regions of the eye. Finally, it has a lower precision of matching as approximations of water/glass are used to represent the dispersion of cornea/lens/humour/tissue. These limitations lead to numerical dispersion compensation being developed for ultra-high resolution OCT [95, 102, 120–122].

Numerical dispersion is now commonly found in commercial OCT devices as it can balance out not only the variation in sample characteristics but also the variations within the optical device such as thermal drift in the fibres. A common approach developed by Wojkovski *et al.* is to create an optimisation routine that maximises sharpness in an image by varying GVD and VGV [101]. Image sharpness can be quantified by measuring the intensity variance in an image.

The measured A-scan is composed of the real part of the complex analytical signal $\hat{S}(\omega)$. This signal can be described using the phasor description of 2.7.1 to include the change in phase between signals as

$$S(\omega) = \text{DC} + \text{Noise} + A.\text{Re}\{\sum_n \sqrt{R_R(\omega)R_Sn(\omega)}\exp[i(\omega\tau_n + \Phi(\omega,\tau_n))]\}, \tag{2.22}$$

where $\Phi(\omega,\tau_n)$ is the phase of the signal, $\tau_n$ optical delay and $A$ is a constant. Processing to remove the DC, noise and interpolating the sample in (k) space leaves only the real part of the signal. The imaginary part of $\hat{S}(\omega)$ can be generated by taking the Hilbert transform of the processed real signal and adding it to the original data.

$$\hat{S}(\omega) = \text{Re}\{\hat{S}(\omega)\} + iH\left[\text{Re}\{\hat{S}(\omega)\}\right] \tag{2.23}$$

As $\hat{S}(\omega)$ can be written in polar coordinates $\hat{S}(\omega) = |S(\omega)|\exp(i\Phi\omega)$ which allows a complex exponential variable to be created which can alter the magnitude of the phase of the signal.

$$\hat{S}(\omega)_{dc} = \hat{S}(\omega)\exp(-ia_1(\omega-\omega_o)^2 - ia_2(\omega-\omega_o)^3), \tag{2.24}$$

where $a_1$ and $a_2$ are constants. The value of these constants are generated using an auto-focus routine which maximises sharpness. In images reported through this thesis a combination of both procedures has been implemented, with physical compensation providing the majority of the correction and numerical compensation used for fine tuning [101].

## 2.11 Conclusion

Ophthalmology and the understanding of the human visual system have matured considerably over the past two hundred years. There remains a need to improve the efficiency and costs of ophthalmic technologies to increase patient access to retinal screening as most diseases present with no early symptoms. In most diseases, patient outcomes can be improved by the

early diagnosis provided by technologies such as wide-field imaging. Wide-field imaging is still limited to the ophthalmic modalities scanning laser reflectance and fluorescence imaging.

The ophthalmic modality, optical coherence tomography has been developed to a considerable maturity for imaging the retina in three dimensions and its uptake for the quantitative monitoring of disease progression in ophthalmology has accelerated following the commercial availability of spectral-domain OCT devices with their superior imaging performance over time-domain. OCT offers both structural information along with functional information such as Doppler OCT. OCT in the retinal periphery would allow quantitative assessment disease progression already demonstrated on-axis; however, the technical challenges of providing interferometry on-axis are likely to be exacerbated in the periphery.

This chapter forms the basic understanding of OCT required to develop and characterise the wide-field OCT systems discussed in the next chapter. Furthermore it provides context to both the methods used to characterise the these systems and features provided in the state of the art competitors systems compared in Chapter 3 and 8.

# Chapter 3

# Development of Wide-field OCT

## Chapter Summary

The aim of this chapter is to introduce the challenges of integrating an OCT module into an ultra wide-field ophthalmoscope. The first section has been provided to familiarise the reader with the ultra wide-field ophthalmoscope from *Optos* known as the Confocal Optic Engine (COE). The chapter begins with a system diagram for the COE which is annotated to help the reader navigate the subsequent chapter sections. Section 3.1.1 contains a review of the modalities offered by the COE. Section 3.1.2 includes an introduction to both the properties of an ellipsoidal mirror and the image capture procedure of the COE. Finally, in Section 3.1.5 an analysis of the optical performance of the COE has been presented with predictions on how that performance is expected to impact OCT.

The development and integration of the OCT module from bench top to the third OCT demonstrator is reviewed in Section 3.2 to 3.5. In particular, these sections describe the outcomes of the collaborative work with the OCT system developers *Wasatch Photonics*. In Section 3.4.3 the considerations and verification of the technique used to couple the OCT beam into the input path has been provided. In Section 3.4.4, the dynamic optical system used to mitigate the impact of the varied power across the ellipsoidal mirrors is analysed. Finally in Section 3.5, the successful integration between the *Opko OCT* device into the *Daytona* SLO system is described.

## 3.1 The Optos Wide-field SLO

The scanning laser ophthalmoscopes (SLO) sold by *Optos* share a similar overall optical design, centred around an architecture known as the confocal optical engine (COE). The COE consists of a pair of ellipsoidal mirrors configured to allow the scanning at one foci to be replicated at a 'virtual point' at the other foci. The approach to wide-field OCT described

in this thesis predominantly revolves about the COE, which is shown in figure 3.1. Any pertinent differences in other optical systems will be detailed where they impact the thesis.

### 3.1.1 The Modalities of the COE

The latest COE product is sold under the commercial name *200Tx*. This device offers green (532 nm), red (632 nm) and blue (488 nm) reflectance imaging. In addition to these modalities, the device is capable of recording fluorescein angiography (FA), an imaging modality that has an absorption peak in the blue (494 nm) and an emission peak in green (521 nm in water). This process begins with blue light incident on the retina being used to excite an intravenous contrast dye. The excited dye emits green light which is detected by the device after high-pass filtering the blue reflectance image. A similar imaging modality known as auto-florescence (AF), uses the natural-florescence of lipofuscin to detect the pathological function within the retina. Regions of the retina containing high concentrations of lipofuscin are indicative of abnormal activity that typically surround damaged retina and will appear hyperfluorescent; however, when RPE cells die or are absent, the lipofuscin is not present leading to dark areas of hypofluorescence. Finally, in recent devices indo-cyan green fluorescence imaging (ICG) has been integrated which requires a forth near-infrared (802 nm) source. Images from this modality are recorded on a third detector configuration across a band centred at a higher wavelength (835 nm). ICG is used predominantly for choroidal diagnostics as the longer wavelengths allow a greater transmission through the high concentration of melanin found in the retinal pigment epithelium (RPE), which separates the retina and choroid.

### 3.1.2 The Ellipsoidal Scan System of the COE

The properties of an ellipsoid are exploited in the COE to achieve wide-field imaging. An ellipsoid is the three-dimensional analogue of the ellipse for which any point on the surface can be described by the equation,

$$\frac{x^2}{a^2}+\frac{y^2}{b^2}+\frac{z^2}{c^2}, \tag{3.1}$$

where, (x,y,z) are the Cartesian coordinates and (a,b,c) are radius of the semi-principal axes. The unique case where a=b=c can be used to described the points within a sphere. An ellipse contains two focal points that lie along the longest axis at an equal distance to the edge of the shorter axis. Any 2D-cross section of the ellipsoid that includes the ellipsoid centre can be

considered an ellipse. This simplification is useful in optical modelling through ray-tracing software such as *Zemax*.

Two key aspects of an ellipsoid that make this shape useful for optical design are: firstly, the shortest distance from one focal point to the other that includes the surface of an ellipsoid, is constant regardless of the path taken. This aspect allows the introduction of optical elements at one focal point which change the beam properties equally at both focal points. Secondly, the curvature changes along any axis of the plane formed by the unequal semi-principal axes. Although this property generally introduces severe aberrations along this axis, the merits of high-FOV imaging, free of chromatic aberration, justifies the compromise in imaging performance with field angle.

The ellipsoid used by *Optos* is a degenerate ellipsoid meaning that it can be described by

$$\frac{x^2+y^2}{a^2}+\frac{z^2}{b^2}. \tag{3.2}$$

This surface can be modelled in *Zemax* using a toroidal surface with the polynomial aspheric coefficients

$$z=\frac{cy^2}{1+\sqrt{1-(1+k)\,c^2y^2}}, \tag{3.3}$$

where the curvature $c$ and conic constant $k$ are used to describe the vertical axis and the variable radius of rotation used to describe the horizontal axis. The conic constant is related to the eccentricity of the ellipse by, $k=-e^2$.

### 3.1.3 The Input Optics of the COE

A simplified schematic diagram of the COE is provided in Fig. 3.1, which includes three ray paths with different horizontal and vertical field angles. The optical coupling of the input light to the eye is achieved by the linking of a foci between two ellipsoids. These foci can be seen in Fig. 3.1 at Scan 1, Scan 2 and at the Eye. The source of the input beam is a laser module that emits circularly-polarised and collimated light into the COE through a fenestrated mirror. Lasers are used for illumination as they are the most energy efficient method of producing a collimated beam with a narrow-bandwidth, both of which are necessary for a long spatial coherence. The input beam passes through a singlet input-lens that provides the required beam divergence to produce a collimated beam that is positioned on-axis after one pass of the optical system.

The beams reflects off the first, fast-scanning sub-system, which is a rotating polygon. The polygon is a highly polished 16-sided mirror that spins at a rate of 38363 rev/min. The beam first strikes the polygon when the facet is orientated with a deflection of -10.1° relative

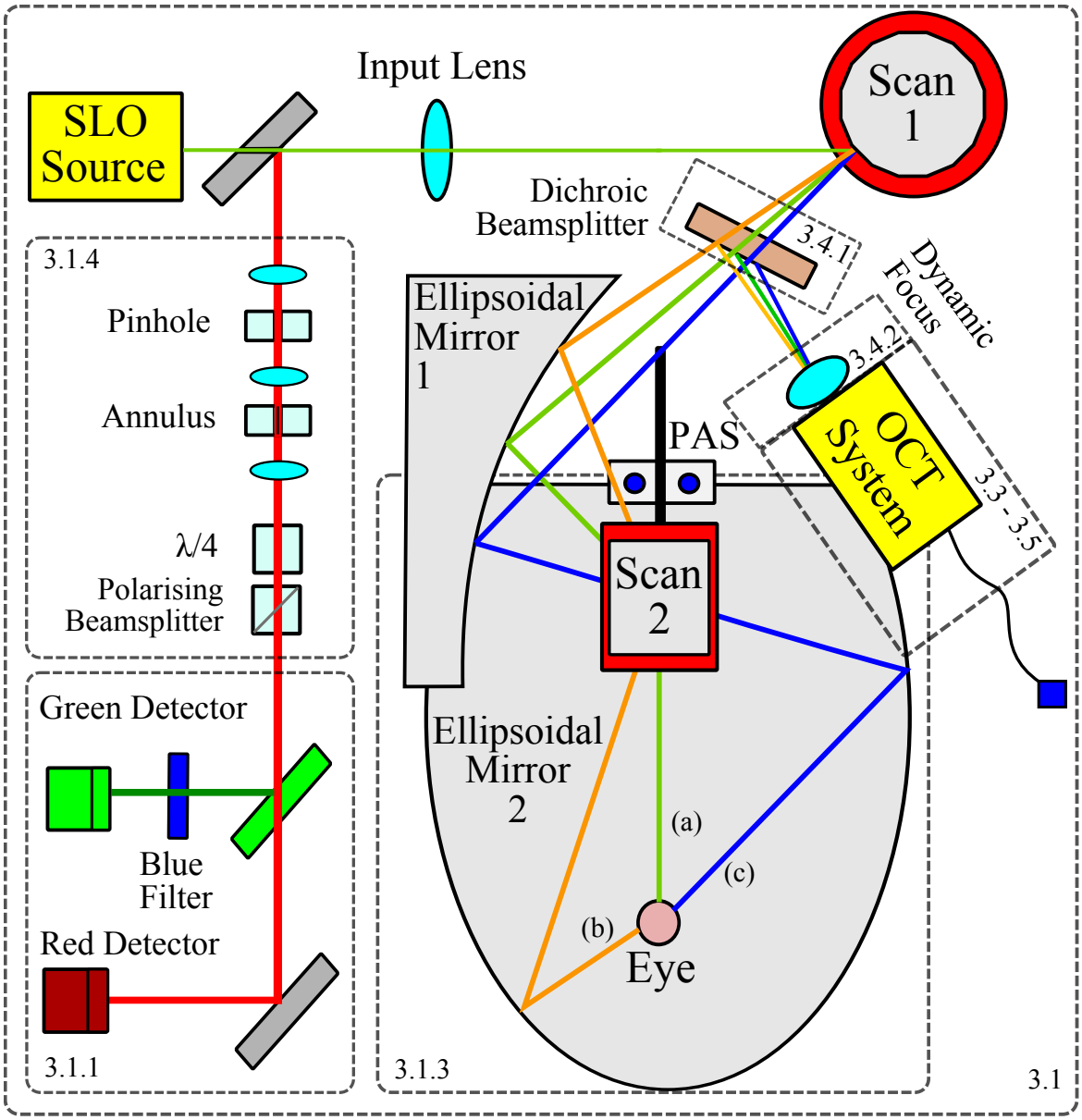


Fig. 3.1 This figure is used to show how the subsystems fit into the wide-field scanner. The dashed boxes denote the section that these subsystems will be covered in greater detail. The green line (a) segmenting most of the elements is the central pole input beam. The orange beam (b) strikes the retina in the superior-temporal region (for a right eye) and the blue beam (c) strikes the retina at the nasal-inferior region. The red line denotes the return path

to the folded optical path. As the polygon is rotated the facet changes its angle relative to the beam by 21.35°, which imparts an optical deflection of 42.7°. This pre-magnified vertical field-of-view (FOV) was measured by modelling the greatest angular extent without the vignetting in the *Zemax* model. The actual image height recorded may be increased slightly by including vignetted beams or decreased by a variation in the line start location. The period of each facet is calculated by dividing the revolution rate by the number of polygon facets, forming the line-scan from the polygon, which lasts 98 µs. As the vertical scan is sampled 3072 times and scans approximately 150°, then the dwell time per pixel is 31.6 ns with an average pixel pitch of 10 µm measured at the retina.

After scanning by the polygon, the ray fan is incident on the first ellipsoid mirror for which the incidence point of the polygon facet is positioned at one foci of the ellipsoid. The rays reflect off the first ellipsoidal mirror and converge towards the second foci where a second slower-scanning motorized mirror scans at a rate of 0.32 seconds; providing approximately 3 frames per second. The rays spread from the scanning mirror across a second ellipsoidal mirror which acts as the final relay before the eye. The third foci, is centred on the pupil of the eye and is referred to the virtual-scan point. The beam entering the eye at the virtual-scan point and has been subject to a 2.77 demagnification in the beam diameter whilst gaining an equal increase in scanning field (from 42.7 to 118.3) due to the combined optical power of the ellipsoidal mirrors. As the horizontal scan is sampled 3900 times across approximately 180° of the eye then this corresponds to a line scan period of 82 µs and a pixel pitch of 10 µm across the horizontal axis. The impact of the ellipsoidal mirrors on imaging performance of the COE will be covered in more detail in Section 3.1.2.

### 3.1.4 The Return Optics of the COE

The return optics in the COE can be modelled independently from the input optics by approximating the source of the return beam to be a point-source illumination from a lambertian scatterer. This approximation is limited else the coherence properties such as phase and polarisation would be lost in tissue imaging. The value of this approximation is that it assumes that the pupil is fully illuminated from the point source on the retina and therefore emits a collimated beam on-axis; with some divergence off-axis from the aberrations in the eye. Unfortunately, the symmetrical defocus for light originating at the retinal periphery is not repeated by either of the ellipsoid mirrors as the beams from the positive and negative field angles of the eye are incident on different curvatures of the ellipsoid. As discussed above, the beam diameter of 4 mm returning through the system has its width magnified by 2.77 by the optical system curvatures while the angular extent of the scan is equally reduced. This magnification results in a substantially larger beam in the return path than in the input

path. The change in beam-width by 2.77 is an approximation that is independent of the beam divergence. The true scaling factor of the beam width through the system may in fact be larger as a result of the divergence of the beam exiting the cornea.

The divergence of the return beam is collimated by the input lens. Next, the collimated beam is then folded into the detector arm by exceeding the aperture of the fenestrated mirror, a mirror with a small hole in the centre used to split different sized beams. The fenestrated mirror folds the beam down towards three optical filters that are designed to remove unwanted reflections. The first filter uses a singlet lens to focus light through a 1.5 mm pinhole, which has been positioned at the conjugate plate for the retina. This configuration ensures that light originating from the retina are preferentially transmitted. This technique of axial gating, known as confocality, is used to increase the contrast of an image that has originated from the object plane. The second filter is configured to focus light from the conjugate plane of the cornea onto an annulus, this ensures that Purkinje reflections from the cornea and crystalline lens are preferentially attenuated.

The final mechanism used for corneal extinction is provided by polarisation filtering. A quarter-wave plate is used to change the circularly-polarised light into linearly-polarised light that is transmitted through a polarising beamsplitter. This element extinguishes any secularly-reflected light with the same polarisation state as the input beam. This filtering is the reason why it the input beam is polarised, as specular reflection contains only the properties of the illuminating source and therefore adds to the noise in the image, commonly saturating the image. The choice of circularly polarised light in the input path demonstrated by *Optos* is to reduce the sensitivity of the return optics to birefringence in the eye. This technique reduces the variation in polarisation transmission as circularly polarised light can be considered as light two equal beams of linearly polarised light, oriented with 90° difference in phase. Although this results in rejection of half the signal, the reduced variability in return intensity allows for a more effective use of the dynamic range in the image. Further spatial filtering is provided by various blockers throughout the optical and scanning elements. In particular, the aperture of the polygon has been designed to maximise throughput of retinal reflection while minimising the coupling of unwanted scattered light.

The final filtering of the return path is the chromatic segmentation of the beam into the detectors using dichroic filters. The green and blue light is reflected onto the first detector channel and the red light is transmitted to a mirror which folds the beam onto the red detector. The polarisation filtering can be performed after this chromatic filtering as polarising beamsplitters cost less if they have a narrow wavelength tolerance. This low cost configuration has been adopted in the replacement optical platform known as the *Daytona*. Further filters can be mechanically added to the path to tune for the narrow separation in

excitation and emission wavelengths in ICG or to switch between blue and green detection for better visibility of pathology. The electronic control of the COE is described in the Appendix A.1 of the thesis.

### 3.1.5 The Optical Performance of the COE

The major axis runs along the vertical plane in both the ellipsoidal mirrors of the COE. This property results in both the optical power and magnification of the system varying with scan height. The COE has been configured so that the focus is best for imaging the centre of the eye as shown in Table 3.1 and Fig. 3.1 to maximise the resolution of the macula and optic disc. Table 3.1 was generated by tracing a uniform density of rays in *Zemax* through an optical model of the COE and measuring the radii where the number of rays is below the root mean square (RMS) of the total number of rays . The table shows that the spot size of the system increases by over ten times in the extreme periphery and shows that the focal properties of the device are symmetrical about the horizontal axis.

| Scan Location | Angle of Scan | Tangential (μm) | Sagittal (μm) |
|---|---|---|---|
| 1 | $(\theta, \phi)$ | 38.6 | 38.6 |
| 2 | $(\theta, \phi + 10.5°)$ | 88 | 320 |
| 3 | $(\theta, \phi - 10.5°)$ | 200 | 413 |
| 4 | $(\theta + 20°, \phi + 5°)$ | 156 | 90 |
| 5 | $(\theta - 20°, \phi + 5°)$ | 156 | 90 |
| 6 | $(\theta + 20°, \phi - 5°)$ | 75 | 52 |
| 7 | $(\theta - 20°, \phi - 5°)$ | 75 | 52 |

Table 3.1 In this table the RMS spot radii show a change in size with various positions on the ellipsoidal mirror. $\phi$ represents the vertical scan angle of the system Scan 1, annoted in Fig 3.1 for on-axis imaging. $\theta$ represents the horizontal scan angle for the system Scan 2, for on axis imaging.

Ray tracing is effective at modelling optical systems such as the COE as the wave-properties of light (diffraction, interference and polarisation) do not impact either the refraction or optical path length (OPL) of the light in this system. At interfaces where this is not the case, such as the diffraction-limited spot size or the transmission through a polarisation filter, then analysis of the physical optics propagation can be considered for that local system. For comparison the x-y cross section of six-PSF plots at on-axis and off-axis points along the vertical plane have been given in Fig. 3.2. The impact of field angle on image contrast can be determined as the cross sections display the normalised intensity spread for the off-axis locations, as seen in Fig. 3.2. The ellipsoidal mirror has a vertically-asymmetric impact on

contrast with the superior field being more diminished due to defocus than the inferior field. The PSFs for nasal region of the retina have not been included as they show the same oblique astigmatism as the temporal side of the eye.

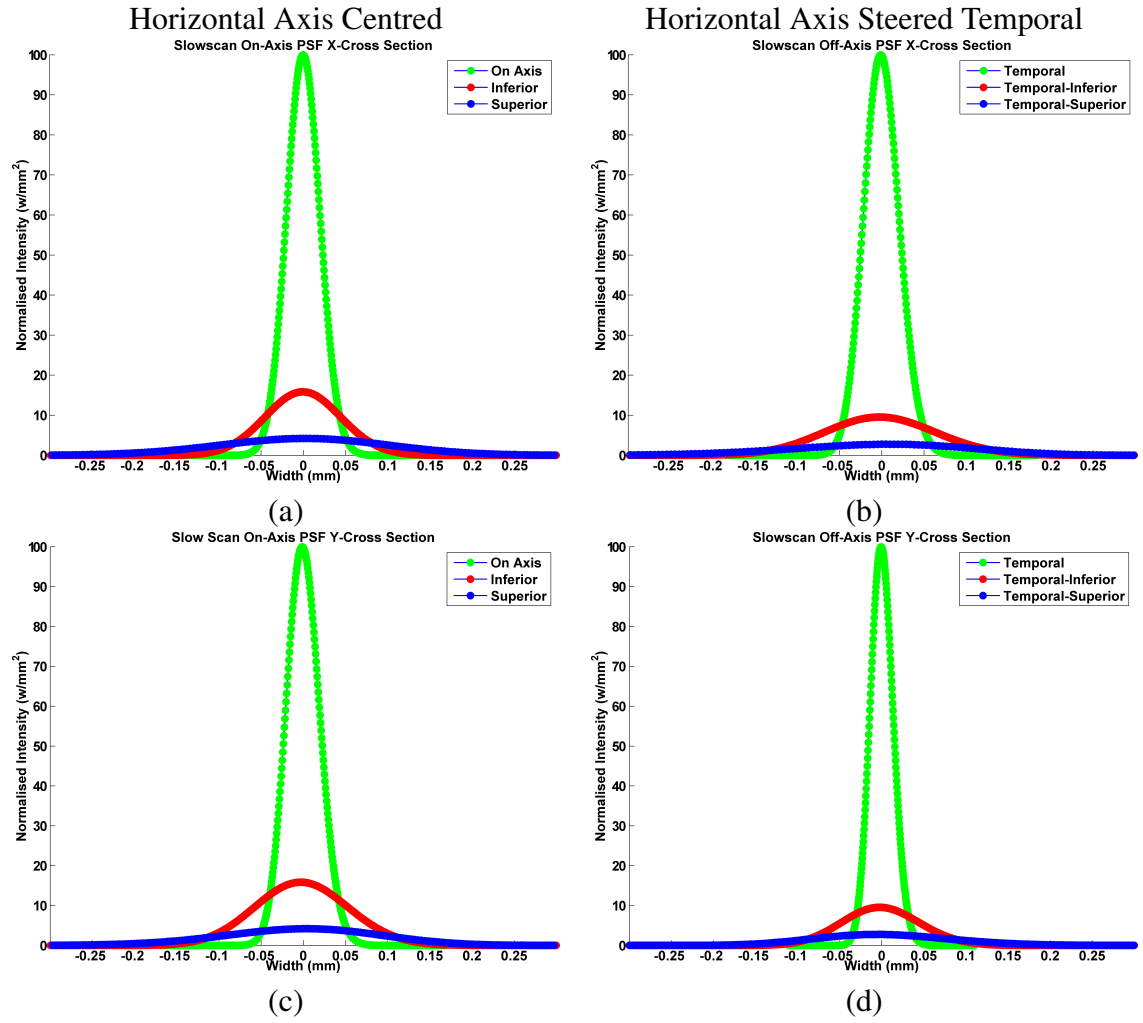


Fig. 3.2 Cross sectional view of physical optics propagation plots from *Zemax* from four locations in the eye. The PSF plots from these positions have been provided in Appendix A.2. Translation in the horizontal axis has little difference to the image quality, where as translations in the vertical axis critically diminish performance. The worst region being the superior field which has >5% peak intensity compared to on axis peak intensity.

The plots provided in Fig. 3.2 were generated from modelling the COE using a beam width of 0.32 mm at the cornea. This beam width is relatively narrow and under fills the pupil of the eye, which ideally illuminated by a beam width of 2 mm to maintain diffraction limited while imaging the eye. The system was designed this way is to ensure an acceptable PSF across all fields, as larger beam waists would be more sensitive to aberrations in the

ellipsoidal mirrors. This design compromise will not be acceptable for OCT or true confocal imaging where the beam must be focused into an aperture of around 5 μm. Despite this compromise, images from the COE feature a degradation in light collection and a degradation in contrast in the superior and ingerior portions of images as this energy is spread across a wider area, which is not ideal for the spatial filters within the COE.

## 3.2 Bench-Top Spectral Domain Interferometer

The first step toward designing an ophthalmic-OCT device is to understand the practical challenges involved in building a bench-top SD:OCT system. The objective of the experiment described in this section was devised to use a basic lab kit to detect the channel spectrum from a single glass-slide cover in the sample arm of the interferometer. The aim of this experiment was to provide an insight into both the theoretical and practical considerations that must be addressed when building a SD:OCT system. In addition, this experiment provided the first opportunity to acquire real data to begin the development of the signal processing in an ophthalmic system.

The experimental diagram can be seen in Figure 3.3. The source, a *Superlum* superluminescent diode (SLD), had a central wavelength of 802.5 nm and a FWHM-bandwidth of 17 nm as measured using a broad-bandwidth *Ocean Optics* spectrometer. The theoretical in-air axial resolution of the system was determined as 16.72μm using Equation 2.8. The spectrometer was configured to record from 340-1030 nm across 2048 pixels, which corresponds to a spectral resolution of 0.366 nm. The generic spectrometer used in this experiment is not ideal for this application as the wide bandwidth of detection, (low pixel density across the spectrum) resulted in a one-way axial range of 0.317 mm, which was calculated using Equation 2.18. This short range made locating the fringes extremely challenging.

Light was collimated from the SLD onto the beam splitter using a singlet lens, with another free-standing lens used to couple light into the fibre. The sample was provided by a glass slide measured using callipers to be $140 \pm 0.5$μm thick. The location of zero path difference was found by placing a mirror in the sample arm; in addition, this configuration allowed intensity from both the sample and reference arms to be balanced. The channel spectrum from the double-mirror configuration can be seen in Figure 3.4 (a). The balanced intensity from both arms should have allowed for high visibility interference; however, the actual fringe visibility recorded was approximately 50%. The most likely reason for the diminished fringe visibility is the larger acceptance angle and various pathlengths through the multi-mode fibre used to couple into the spectrometer. The 400 μm core fibre would allow the coupling of waves with shifts in the transverse wave-front from tilt and de-centre,

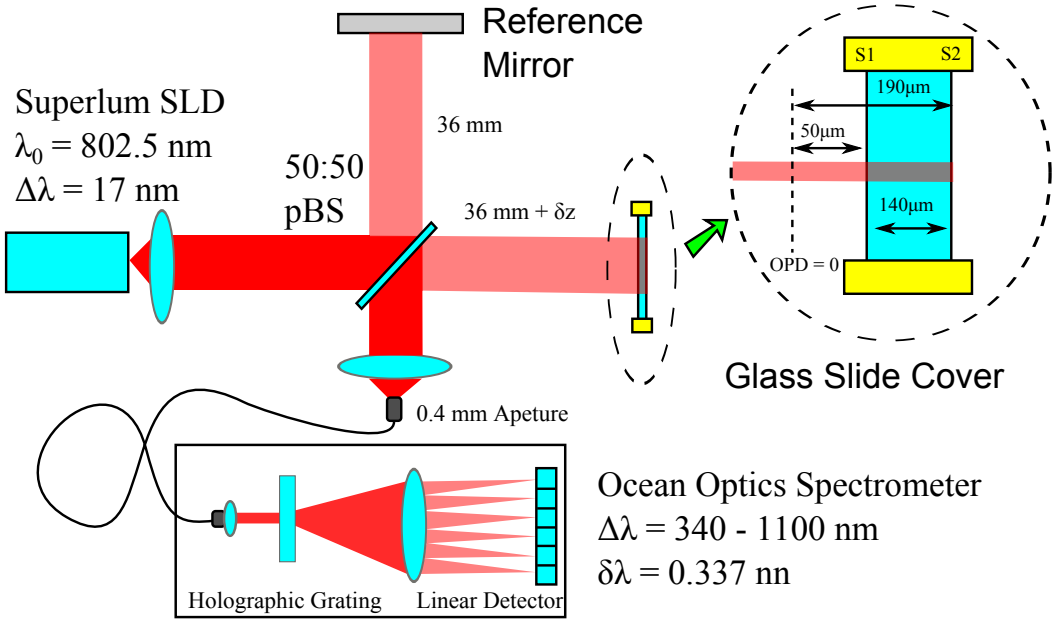


Fig. 3.3 Set up of the 1D SD:OCT experiment. The light from the SLD is split equally towards a thin glass slide cover and reference mirror. Light reflects and transmits off the air to glass interface (S1). The transmitted light reflects and transmits off the glass to air interface (S2). The reflections from each of the sample locations recombine with the reference light through the beam splitter and are focused onto the spectrometer fibre head. Within the spectrometer, the light is dispersed linearly in wavelength and sampled on a linear CCD detector

which would increase the total light collected and lead to an increase in shot noise in the detector. However, this increase in noise wont prevent fringes being detected as the acceptance of multiple transverse modes would degrade only axial resolution [123]. This limited degradation from the use of multi-mode fibre is still effective as an introduction to OCT as it is easier to achieve coupling. More conventional reasons for loss of coherence such as polarisation, dispersion and scattering are less significant in this configuration as the arms are effectively symmetrical.

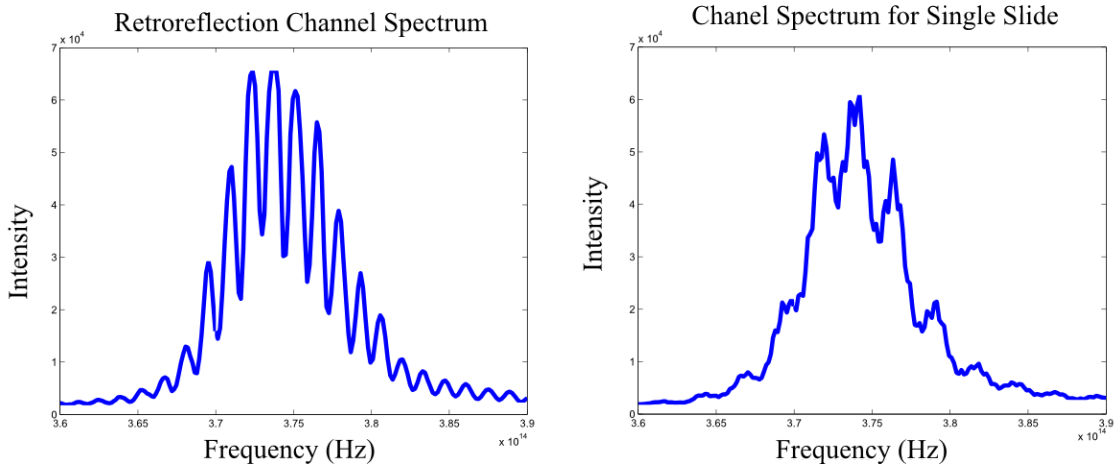


Fig. 3.4 **(a)** Channel spectrum for a mirror positioned in the sample arm with optical path difference of near zero from the reference mirror **(b)** The channel spectrum of a single glass slide. Two dominant periodicities are clearly present in the spectrum that are of different amplitude to each other, which correspond to the front and back interface of the slide.

The mirror in the sample arm was replaced by single glass cover. The channel spectrum recorded for this set up can be seen in Figure 3.4 (b) and the Fourier transform of this spectrum and another sample with an approximate 70 µm displacement of the glass from the first, in Fig. 3.5 (a) and (b). Assuming that the reference reflection $R_R$=0.5 from the Fresnel Equation,

$$R = \frac{n_{glass} - n_{air}}{n_{glass} + n_{air}}, \tag{3.4}$$

with $n_{air} = 1$ and $n_{glass} = 1.51$ then the reflection from the first interface is 20% and the second is 16%. Using the intensity weighting $\sqrt{R_R R_{Sn}}$ from Eq. 2.7.1 the fringe contrast from the first and second surface can be estimated to be approximately 0.22 and 0.2, respectively.

Three peaks are consistent for both Fig. 3.5 (a) and (b); positioned in Fig. 3.5 (a) at 40 µm 140 µm and at 180 µm. The first and last peaks have shifted to 110 µm and 250 µm

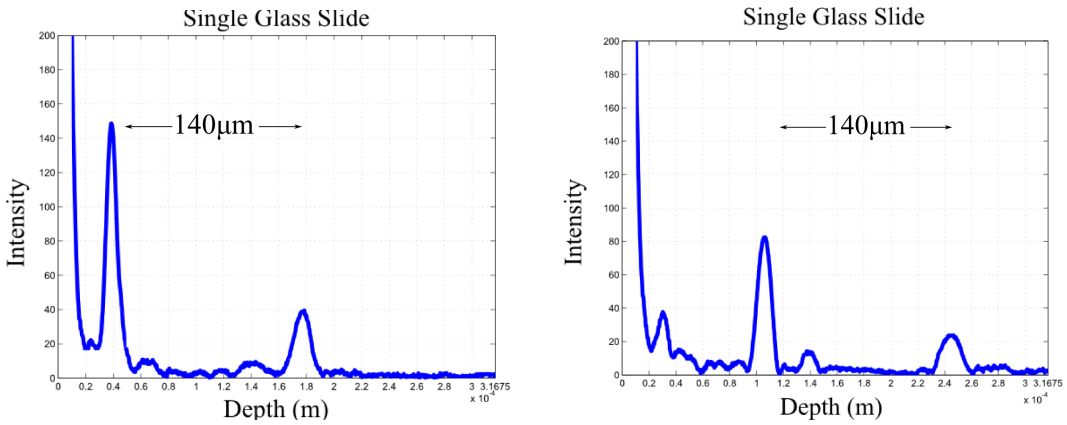


Fig. 3.5 **(a)** Depth scan attained from FFT of the channel spectrum in Fig. 3.4 plotted with a linear intensity. **(b)** Depth scan attained from FFT of a channel spectrum after an axial translation.

in Fig. 3.5 (b) and the SNR of the peaks has reduced. The static peak at 140 µm is most likely the autocorrelation between the two interfaces as its the only OPD in the configuration to match the peak location. As can be seen from both the channel spectrum and the FFT plots the intensity of the second interface is approximately four times less than the first. However, the constant ratio between the two peak intensities (approximately 4:1) in both plots indicates that this deviation in expected intensity is most likely to be caused by the spectral roll-off across the spectrometer, explained in Section 2.9.4.

## 3.3 Wasatch/Optos OCT Demonstrator One

The integration of OCT into a wide-field imaging platform was first investigated at *Optos* in early 2011. The context of this development was that swept-source OCT remained confined to the research community and despite trends within the literature supporting SS:OCT suitability over SD:OCT for wide-field imaging, this technology was viewed as having a greater technical risk and cost as described previously in Table 2.4. Initially, the engineering resources required to develop and integrate an OCT engine into the COE were not available at *Optos* because of the high commitment to an ongoing development within the company. This commitment required *Optos* to use an external collaborator to provide solutions for both the development of the OCT module and some of the integration challenges involved the development. The external collaborator chosen was a holographic gratings company known as *Wasatch* which had recently created a systems-development department

for customised spectral detection. *Wasatch* were chosen because they were willing to develop the engine openly with *Optos* and allow *Optos* to retain IP on the device design. My role in this collaboration was to inform Wasatch of the primary technical challenges unique to the development of wide-field OCT via the COE and to verify the performance of the final system.

The integration of OCT development was broken into two phases, the objective of the first phase was to produce a wide-field OCT demonstrator to answer the primary integration questions of the development and the objective of the second phase was to produce an integrated wide-field OCT SLO demonstrator that was capable of providing clinical feedback on the efficacy of wide-field OCT. Three aims were established for the first phase of the development:

1. Measure the impact of aberrations across the COE for OCT image quality.
2. Generate a B-scan which has signal-to-noise characteristics that are commercially competitive.
3. To validate proposed methods for the correction of systematic defocus in the COE at large elevation angles.

The second aim is particularly challenging across a wide-field as the field-variant aberrations reduce the efficiency of coupling into the single-mode fibre without higher-order adaptive optics. The first demonstrator required commercially-competitive specifications for both the source and detection, these specifications are given in Table 3.2 and a schematic diagram of the demonstrator can be found in Figure 3.6. The SLD used to illuminate the eye was verified as having a 48.5 nm bandwidth using an *Ocean Optics* spectrometer as used in Section 3.2. The source was split in-fibre equally across the input arm and the reference arm. The reference arm was composed of a free-space collimating lens and a folded pair of mirrors. The final mirror and collimating lens were both mounted on manual translation stages to control the reference arm pathlength and power. The polarisation between the sample and reference arm was balanced using stress-induced birefringence in the fibre. This control was induced by loops of fibre across two paddles; the first paddle controlled the ellipticity of the polarisation, by mimicking a quarter-wave plate and the second the overall orientation of the polarisation, by mimicking a half-wave plate. The paddles were optimised manually by attempting to achieve maximum fringe visibility of an attenuated mirror in the detected channel spectrum.

The beam delivery to the eye was performed on a COE skeleton chassis containing only the two ellipsoidal mirrors and a mirror capable of rotating along a single axis to address

| Specification | Limiting Device | Promised | Observed |
|---|---|---|---|
| Axial Scan Rate | Basler spL2048-70km | 47 kHz | 20 kHz |
| Transverse Scan Rate | XY Thorlabs Galvos | 1 khz | 1 kHz |
| Transverse Scan Field | XY Thorlabs Galvos | $\pm$ 15° | $\pm$ 12.5° |
| Source Wavelength | Exalos SLD | 840 nm | 833 nm |
| Source Bandwidth | Exalos SLD | 40 nm | 48.5 nm |
| Source Power | Exalos SLD | 5mW | 4mW |
| Axial Resolution | Exalos SLD & NDC | 2.7 µm | 12 µm |
| Transverse Resolution | Varioptic Liquid Lens | 20-40 µm | 50-100 µm |
| Polarisation | Exalos SLD | 90% | 88% |
| Spectrometer Pixels | Basler spL2048-70km | 2048 | 2048 |
| Axial Range | Basler spL2048-70km | 2.8 mm | 2.8 mm |
| Sensitivity | Basler spL2048-70km | 97.5 (dB) | N/A |
| Roll-off | Basler spL2048-70km | 20 (dB) | 22 (dB) |
| OL Scan Head | Mirror Coatings | 3.3 (dB) | 5.1 (dB) |
| OL OCT Engine | Fibre Insertion Loss | 3.2 (dB) | 9.67 (dB) |

Table 3.2 This table shows the specifications of the Wasatch/Optos demonstrator one. The term limiting device refers to the device reducing the promised specification that which was measured. NDC refers to numerical dispersion compensation and OL refers to optical loss

over 180° at the cornea. A pair of galvanometer scanners centred at the scan foci for the polygon scanner were mounted on a rotation stage to provide navigation about the vertical field. Initially, a motorised telescope was proposed to compensate for vertical defocus in the system across a narrow field. This system was replaced by the use of a liquid lens after recent advances in the technology indicated the possible advantages in using the *Varioptic Artic 316* liquid lens. The clear aperture of this liquid lens was 2.5 mm meaning that the beam diameter at the cornea was at most 900 µm. The verification and merits of the liquid lens are covered in greater detail in Section 3.4.4. Light was coupled from the scan head to the engine via a single-mode fibre as shown in Fig. 3.7. This sample and reference signals were dispersed in wavelength using a holographic grating 1200 lines/mm and recorded on the Basler spL2048-70km CMOS camera. The 7 µm camera pixels size were illuminated by a lens focusing with a theoretical FWHM spot size of 5.5 µm. The bandwidth measured was 80 nm dispersed across the 2048 pixels providing 0.04 nm/pixel spectral resolution.

### 3.3.1 Results from Wasatch/Optos OCT Demonstrator One

Early evaluations of the prototype system in October 2011 showed that the system was not operating as expected. The device had excessive sensitivity roll-off with depth, poor

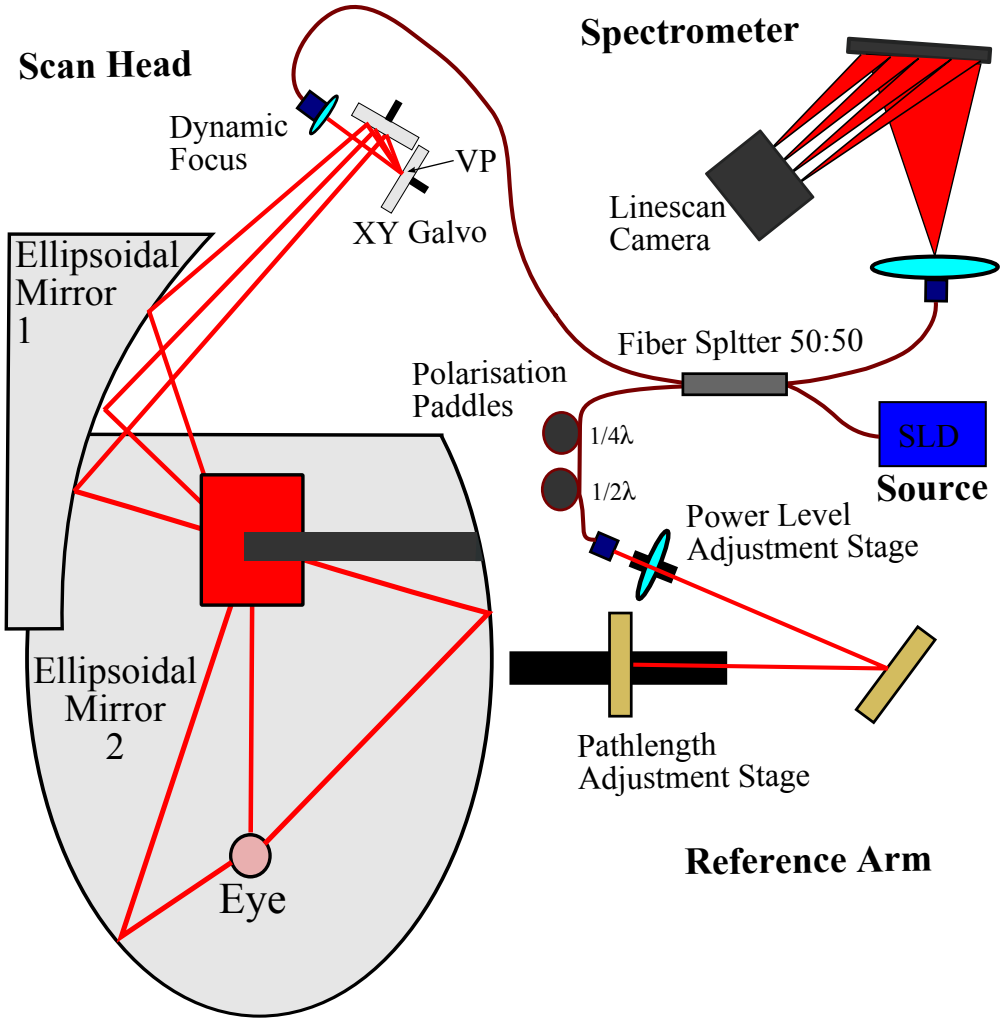


Fig. 3.6 Schematic Diagram of the *Wasatch/Optos* OCT first demonstrator. Key features of this device are the galvanometer scan pair replacing the polygon scanner in the COE and manual optimisation of reference arm, polarisation and focal control.

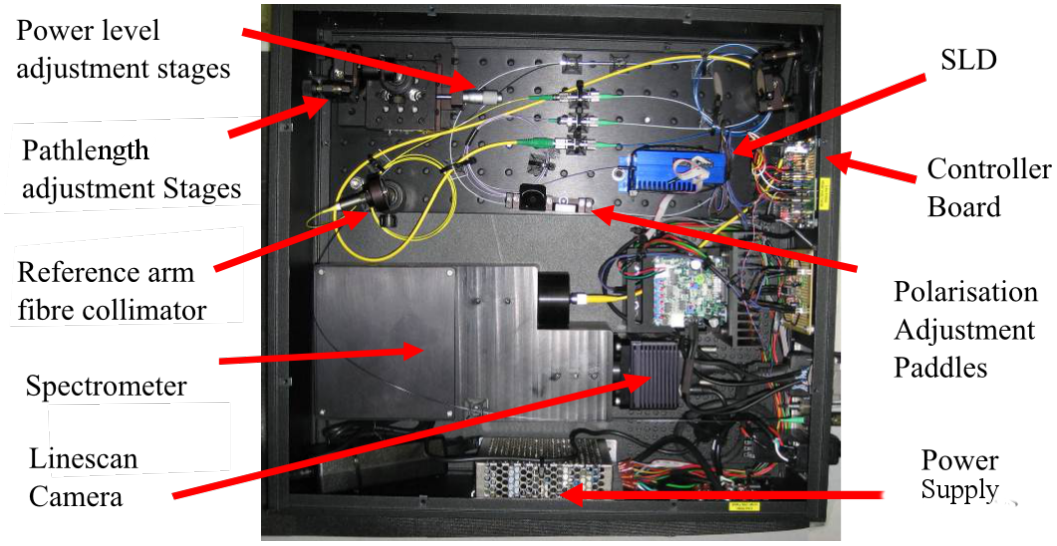


(a)

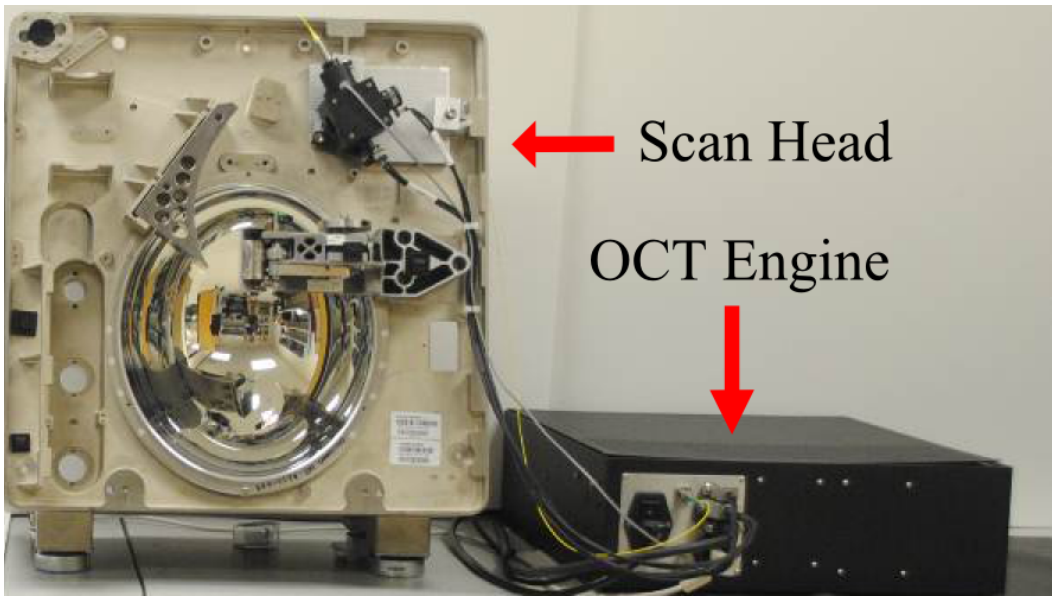


(b)

Fig. 3.7 **(a)** Labelled photograph of the OCT engine from the first Wasatch/Optos OCT Demonstrator One **(b)** Photograph showing the stripped Optical scan head connected to the OCT engine.

sensitivity and the off-axis resolution was below what I had demonstrated during a visit to the laboratory of *Wasatch Photonics*. The optical power levels within the system were measured to be as expected and therefore, it was determined that the lens within the spectrometer had moved in transit. The spectrometer was realigned to maximise the intensity on the detectors and recalibrated using the spectral lines from a mercury-argon calibration light source. Images from the first demonstrator were used to assess the optical efficiency of the device and impact of field angle; images from this device can be seen in Fig. 3.8. From these images we can see that the SNR is substantially below that of commerical OCT device. A reference 'commercial-quality' image can be found in Fig. 5.1. Averaging is unlikely to restore the definition of external-limiting membrane (ELM) or choroidal vasculature, which is unresolvable in these images despite the post processing available to commercial systems.

The first demonstrator was capable of capturing only ultra-wide field vertical scans as the aperture of the first ellipsoidal mirror was 30 mm. This aperture permitted a horizontal FOV of approximately 6 mm at the retina. The COE chassis was rotated by 90° so that both the macula and optical nerve head could be imaged. This orientation was advantageous because it allowed the FOV to be approximated from anatomy. The arclength for which signal was collected was estimated at around 20 mm, by estimating the distance between the macula and fovea to be 4 mm and assuming that the number of A-scans per-mm is constant in Fig. 3.8 (a). The collected signal appears to vary greatly across this scan and the vitreoretinal interface is only visible for approximately 12 mm; however, this limitation was expected given the varying optical power along the vertical axis of the ellipsoidal mirrors. It was planned that this degradation would eventually be mitigated by ramping the voltage applied to the liquid lens to correspond to vertical field angle.

The repeatability of the first demonstrator was challenging to maintain because the device lacked a direct fixation target, a chin rest or any form of automated reference arm. To reduce the variability, the performance assessment of the device was conducted using two phantom eyes, designed previously for the calibration of reflectance imaging in the COE. The first phantom was a water filled two-lens system that contained a flat white surface, sputtered with black chrome at the image plane to form a USAF resolution chart. The second phantom comprised of a silicone ball of radius 12 mm with a polished aperture at the cornea to allow focusing of parallel rays onto the etched surface. The silicone phantom had vasculature etched at the image plane as seen in Fig 3.9. The USAF phantom was used to calibrate the focus, polarisation and dispersion compensation of the device; although, fine tuning was always required to generate optimal images of real eyes. The silicone phantom was used to verify the performance of the system as the phantom mimicked the geometry of the eye. The

(a)

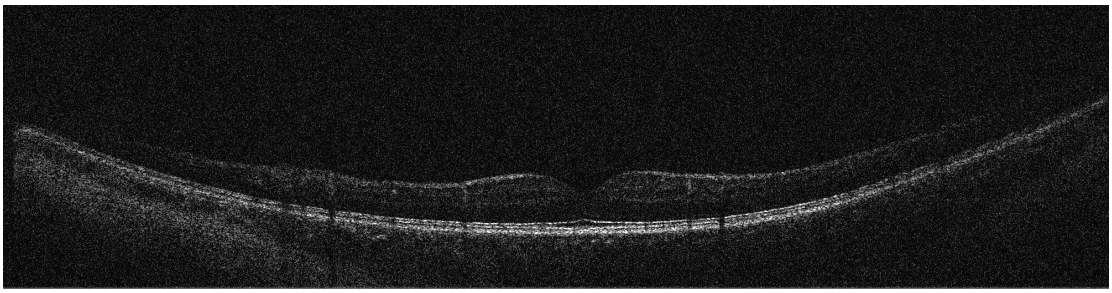

(b)

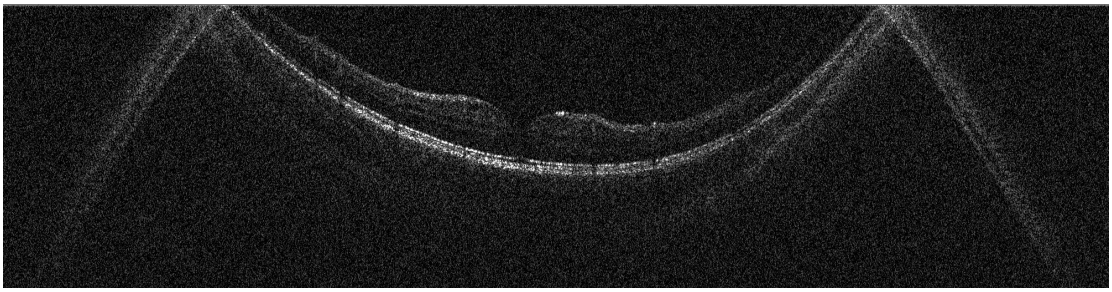

(c)

Fig. 3.8 The three best images of a colleagues retina acquired by myself using the first demonstrator with a power at the eye measured to be 0.73 mW. The images have been cropped along the z-axis from 1024 to 512 pixels. **(a)** Image acquired during my visit at Wasatch Photonics in North Carolina in September 2011. **(b)** Image acquired after the device was shipped to *Optos* and recalibrated in November **(c)** Complex-side image acquired in December.

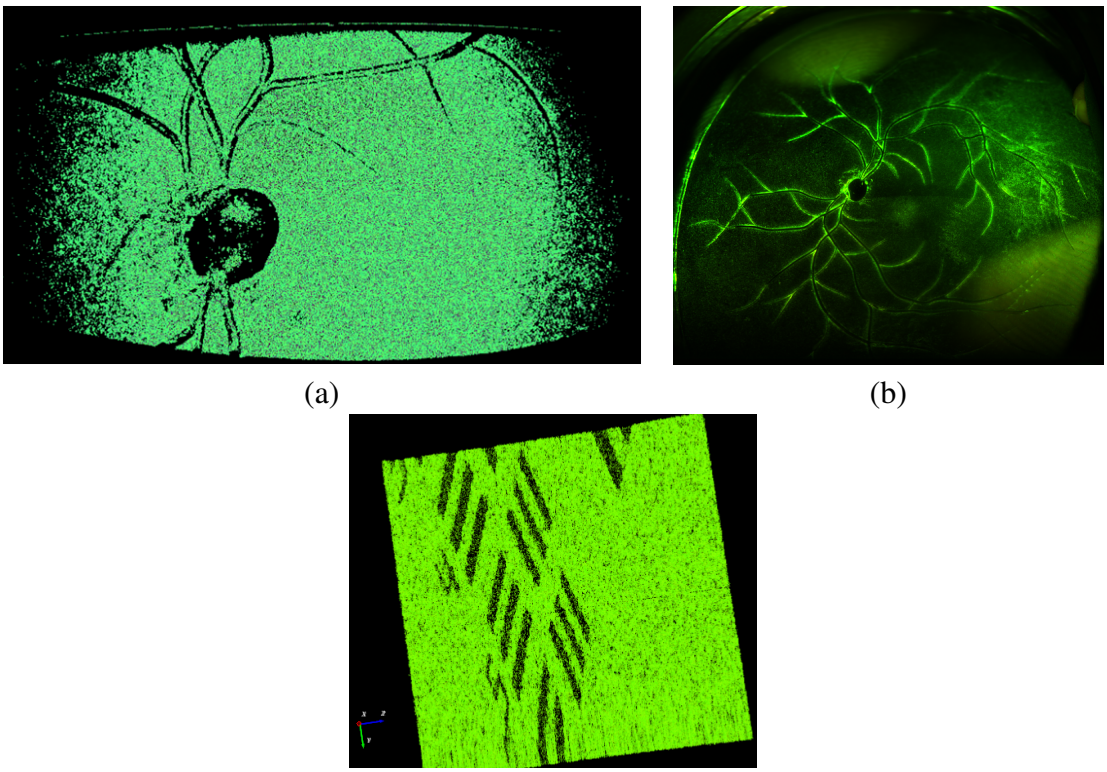

(a) (b)

(c)

Fig. 3.9 **(a)** En-face view of a C-scan of Silicon Eye rotated by 90°. The FOV of the first demonstrator, as limited horizontally by the width of the first ellipsoidal mirror and vertically by the systematic defocus. The FOV in (a) is estimated as 6 mm x 14 mm or 21 x 50° external field. **(b)** SLO Image of Rube Eye used to compare the FOV in (a) with that of an optomap. **(c)** En-face C-scan of resolution target, used to estimate warping within the image. . The changing FOV and thus reducing pixel dwell time shows a low change in SNR at the macula; however, the reduced SNR and and appeared thinning in the periphery means the increased useful FOV is minimal.

on-axis axial resolution was determined to be 12 µm in the silicone phantom. This value was determined from the number of pixels a single interface created in the image.

### 3.3.2 Discussion on the Wasatch/Optos OCT Demonstrator One

Valuable lessons were learned from the first phase of the wide-field OCT project, despite the signal to noise in the first demonstrator being insufficient for performance comparison with commercial systems. Firstly, we learned that aperture of the input lens is critical to the SNR in OCT images as light which exceeds the entrance pupil of the input beam, which was limited to 2.5 mm by the liquid lens, will not be coupled into the detector. The magnification of the optical relay results in a demagnification of the beam diameter by 2.77, producing a

spot on the cornea of 0.9 mm. However, the return beam that is initially limited by the 4 mm (non-dilated) iris, is magnified by the 2.77 factor producing a spot diameter of 11 mm at the input lens. Compounding the issue is that the input/return beam will be subject to high-order aberrations as it passes through the COE that cannot be mitigated entirely by narrow-field focal control. Although this requirement poses a significant technical risk of integrating OCT into the COE architecture, the response of the system to the dynamic focal control of the liquid lens shown in Fig. 3.10 indicated that this challenge can be overcome with further development.

The second valuable lesson from this device was that there did not appear to be any correlation between field angle and a need to optimise the birefringence in the reference arm. This property was assessed qualitatively by adjusting the polarisation response during live imaging of an attenuated mirror and observing the change in contrast across a wide-field image. The concern with birefringence arose as the main ellipsoidal mirror uses an oxidised dielectric coating ($AlO_2$) of around 100 nm thickness to protect it against damage. However; the range of angles incident on this mirror is in fact relatively low and therefore a change in birefringence with field angle was not observed. The largest range of angles can be found in the horizontal scan mirror (Scan 2 in Fig. 3.1) which is composed of pure aluminium. Aluminium naturally corrodes to have a 4 nm oxide layer at the surface which is likely to contribuate to some change in birefringence with field angle.

Further sources of polarisation variation in the system include the variation in birefringence due to thermal changes near the internal fibre networks, stress on the fibre umbilical cord and loops of fibre within the OCT engine, which explain the need for optimising the polarisation of the reference arm before each image acquisition in the first demonstrator. Measurement of systematic birefringence does not included a varied birefringence provided by the eye; however, this will be investigated in the next chapter.

The optical efficiency of the scan head was measured at each interface using a power metre and are shown in Table 3.3. The principle source of loss in the scan head was shown to be the main ellipsoidal mirror and horizontal scan mirror. Replacing both aluminium mirrors with silver would increase the detected signal by up to 1.96 dB or 20% improvement in return signal as shown in Fig. 3.11; however, this would likely be costly for the second ellipsoid as a result of its size and increased durability requirements.

### 3.3.3 Conclusions form the Wasatch/Optos OCT Demonstrator One

The first demonstrator was key in assessing the changes to the imaging plane of wide-field OCT. Firstly, the radius of curvature of the image of the retina is altered by the axial position of the patient relative to the COE virtual point. The curvature of the eye required re-optimising

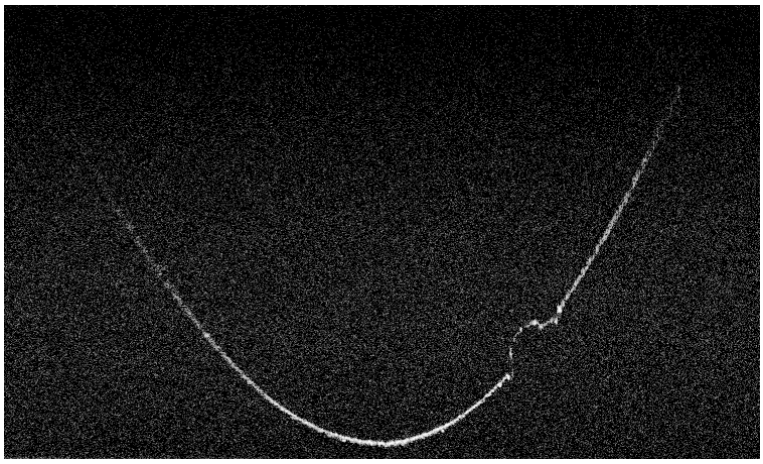

(a)

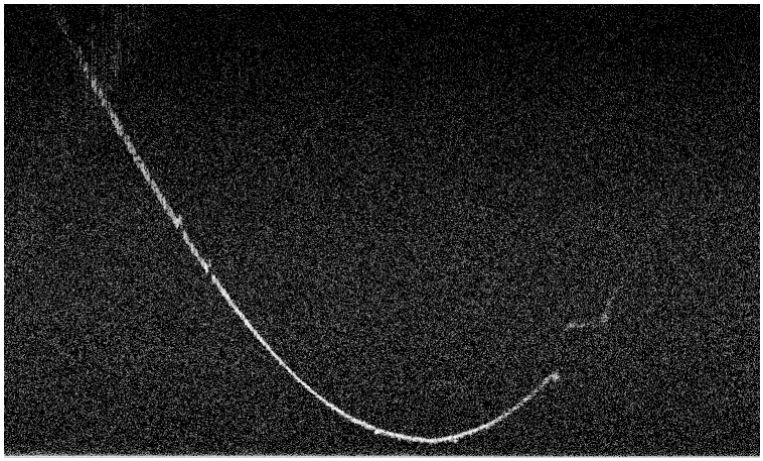

(b)

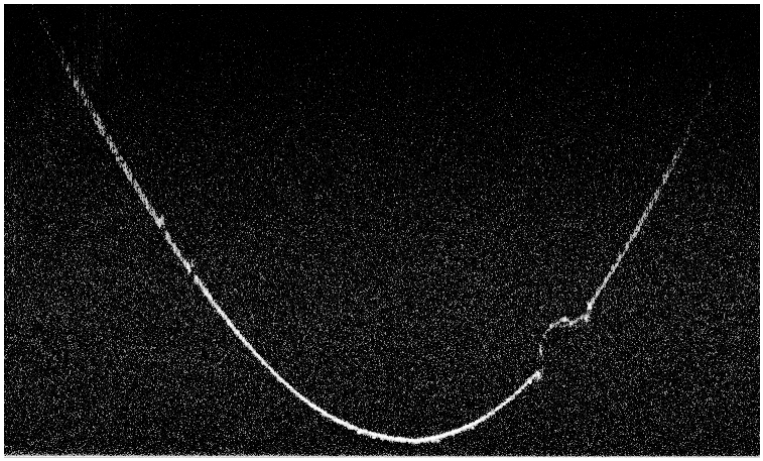

(c)

Fig. 3.10 **(a)** Image of the silicone eye recorded using the liquid lens driven with a current of 156 mA **(b)** Image of the silicon eye driven 171 mA **(c)** Averaged image of **(a)** and **(b)**, showing that the field and SNR in an image can be increased by montaging navigated images

| Part | Power (mW) | Loss (dB) | Primary Material |
|---|---|---|---|
| OCT Engine | 1.313 | | Glass |
| Collimator & Galvo | 1.127 | 1.33 | Silver & Glass |
| Liquid Lens | 1.051 | 0.61 | Water |
| Ellipsoid 1 | 1.003 | 0.40 | Silver |
| Horz. Scan | 0.867 | 1.27 | Aluminium |
| Ellipsoid 2 | 0.730 | 1.49 | Aluminium Oxide |
| **Total** | **0.583** | **5.10** | |

Table 3.3 Efficiency of the optical surfaces in the first demonstrator, the sensitivity and loss in an OCT system is measured on a $\mathbf{20log_{10}}$ scale.

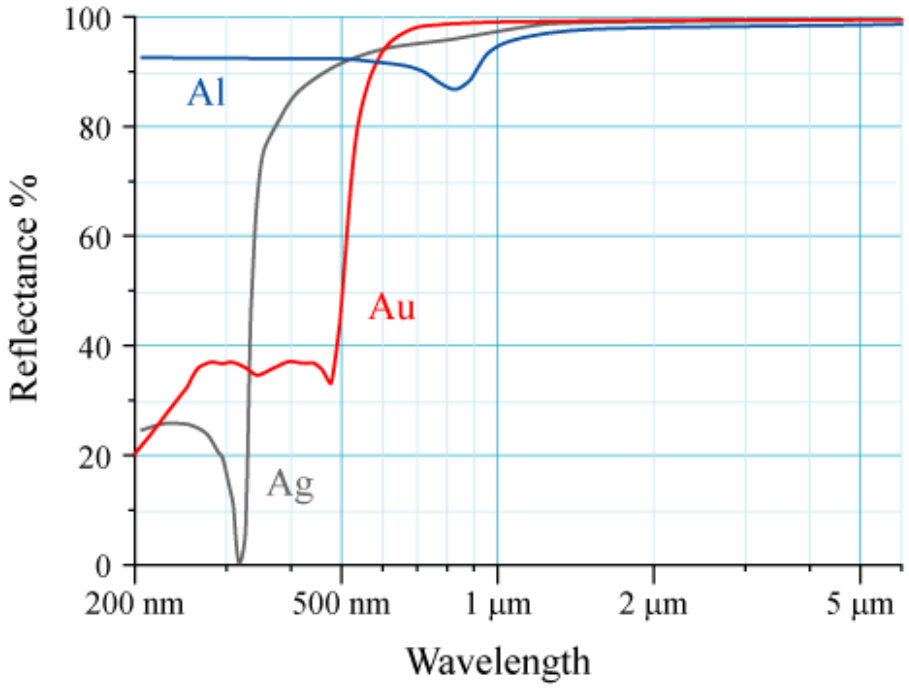


Fig. 3.11 Reflectivity of common optical surfaces [124]

the focus, optical pathlength and dispersion compensation with field angle. Although it is technically achievable to optimise these parameters via closed-loop optimisation during live imaging, it will be computationally efficient to achieve this without calibrated look up tables, or close starting positions for the parameters.

The COE lacks the methods to achieve a steady patient interface that have become standard in modern OCT devices such as a guided fixation target, retinal tracking and use of a chin rest. This omission results from the fact that it is challenging to focus fixation-light onto the macula without compromising other imaging modalities. For the first demonstrator, two LEDS were installed on either side of the first ellipsoidal mirror to improve patient fixation and comfort by asking those imaged to maintain the position of their eye between these spots. This was sufficient for research purposes but not a clinical demonstrator.

The first demonstrator failed to achieve all three of the desired aims of the initial phase of the project listed at the start of this section. The positive outcomes of this development were the device succeeded in informing future designs as to the key challenges of wide-field OCT and possible tools such as the liquid lens for developing the technology. Unfortunately, the demonstrator failed to allay the primary technical risk of the project as the whether a commercial competitive image quality can be acquired through the COE either on-axis or off-axis. Furthermore, the software and hardware control was so unstable that repeated measurements and comparative studies were not possible.

## 3.4 Wasatch/Optos OCT Demonstrator Two

The aims of the second wide-field OCT demonstrator were based on the premise that the first demonstrator succeeded in providing positive answers to the outlined technical concerns. The primary aim of this development was to create a device that could support clinical studies to identify the efficacy of a wide-field OCT device, integrated into a COE platform. Two secondary aims were also defined; firstly, to assess the technical risks of using a MEMS scanning module provided by *Mirrorcle Technology* for OCT and to measure if there was any impact on the existing modalities of using a dichroic mirror to couple OCT into the beam. Secondly, to investigate if the current techniques used by *Optos* to position and steady the patient, both the patient-alignment module (PAM) and front covers, were effective for OCT devices.

The additional requirements for this second demonstrator were stricter than those of the first as the new demonstrator needed to be multi-modal for clinical trials. The requirements were:

- The device must capture SLO and OCT imaging within the same patient session i.e not require the powering down of the system, removal of covers or swapping of parts.
- The OCT must not diminish the performance of the SLO device.
- The device must be able navigate to the same field of view as addressed during an optomap acquisition. All the retinal layers, excluding the ELM, must remain visible ($\delta z = 12\mu$m) with an off-axis transverse resolution that does not hide small retinal features such as drusen and vasculature ($\delta x = 50\mu$m).
- The device must be operable by a clinician without training in engineering.

The principal changes between the first and second demonstrator were the use of a dichroic window to combine the SLO with the OCT and the change in liquid lens supplier from *Varioptic* to *Optotune*. The performance of the dichroic and liquid lens are reviewed in Sections 3.4.3 and 3.4.4 respectively. Furthermore, the line-scan camera was shifted to the *Cobra* spectrometer from *Wasatch Photonics*. This camera utilised tall pixels (7µm x 500µm) to provide a well depth of 80K$e^-$ for increased light collection, a larger dynamic range and a reduced sensitivity to misalignment in the spectrometer . Other specifications such as line-speed and noise remained the same as the *Baslar Sprint* camera (pixel size of 10µm x 10µm) used in the first demonstrator.

### 3.4.1 Results from the Wasatch/Optos OCT Demonstrator Two

The images captured on the second demonstrator, two of which are shown in Figure 3.12, show that the device had insufficient SNR and system stability for clinical studies. The use of an automated liquid lens was shown to be effective at maintaining an optimal SNR and transverse resolution capable by the device at a low computational time and expense. The dichroic mirror did not appear to deteriorate the SLO and recorded only a negligible loss in the transmission of the OCT light. A detailed comparison of the SLO performance with and without the dichroic mirror was not possible as the electronic control of the SLO in this demonstrator failed early in the trials. In addition, the automated numerical-dispersion compensation proved effective at maintaining on-axis resolution, but appeared to require unique optimisation of the dispersion coefficients for different field angles. This apparent change in dispersion is contradicted in the modelling of chromatic dispersion with field angle in Section 4.6 and therefore the change in parameters are thought to be caused by the variation in sampling density with axial distance.

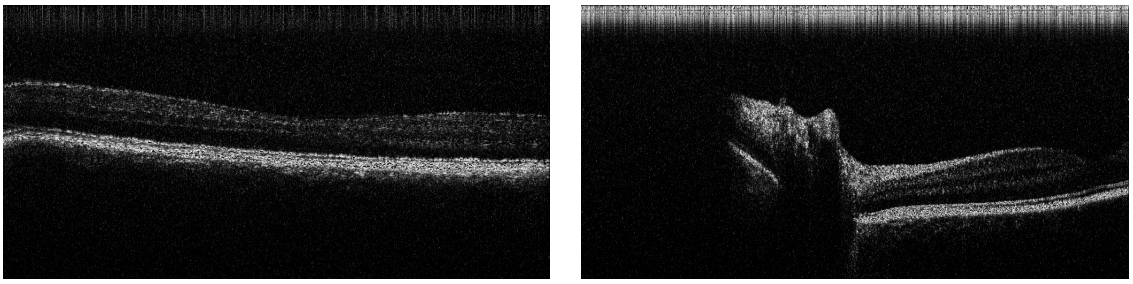

(a) (b)

Fig. 3.12 **(a)** B-scan of the macula averaged over five scans. **(b)** B-scan through the optic disc showing vignetting at the second ellipsoidal mirror averaged over five scans.

### 3.4.2 Discussion on the Wasatch/Optos OCT Demonstrator Two

The fundamental limitation of the second demonstrator was that the SNR and the transverse resolution of the system was compromised by the 1 mm diameter of the 2D MEMS scanner. The use of small MEMS mirrors have been shown recently to be fast, compact and inexpensive in hand-held OCT devices [125]. In addition, the ability to scan in both horizontal and vertical from a single surface allows the scan vertex axis to be precisely reproduced at the virtual point maximises the scan linearity. Hand-held devices using MEMS scanners are successful because the distance between the scanner and the eye is small and therefore does not need to accommodate for any beam expansion through the optical system; such as exists in the COE. To integrate OCT effectively in the COE then the minimum diameter of a mirror that is positioned at the first scanning location is 5.5 mm. This value is simply 2 mm multiplied by the magnification of 2.77. Although an undilated pupil is typically 4 mm in diameter, accommodating for this entire aperture is ineffective as the aberrations within the eye begin to dominate after 2 mm [126]. These aberrations prevent efficient coupling into a single-mode fibre without adaptive optics.

The loss associated with vignetting by the MEMS diameter in the second demonstrator was calculated using the ratio of the intensity flux for a 1 mm and 5.5 mm aperture. This ratio shows that a 1 mm mirror reduces the sensitivity of the system by 29.6 dB. This scale of signal attenuation would limit the performance of the second demonstrator to similar to the first SD:OCT system published by Wojtkowski et. al in 2012; assuming that there are no other losses in the demonstrator [72]. In addition, the scan linearity of the second demonstrator was compromised by both the MEMS and the Scan 2 mirror, which was used to provide a wider field of view than the MEMS mirror. These artefacts can be seen in Fig. 3.14 and Fig. 3.13.

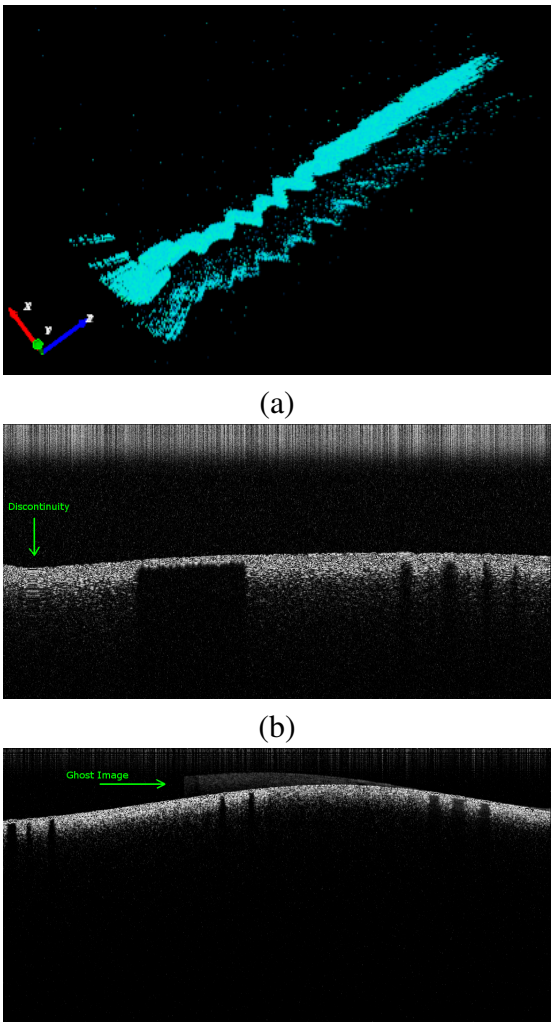


(a)

(b)

(c)

Fig. 3.13 **(a)** Cross-sectional view of a C-scan of a flat phantom, showing a mechanical vibration from the driving of MEMS mirror **(b)** B-scan showing failing synchronising of MEMS mirrors and capture, shown by the discontinuity in the curvature on the left side. This artefact is typical of a mirror stopping to change scan direction **(c)** Ghosting artefact from poor registration of B-scans during average.

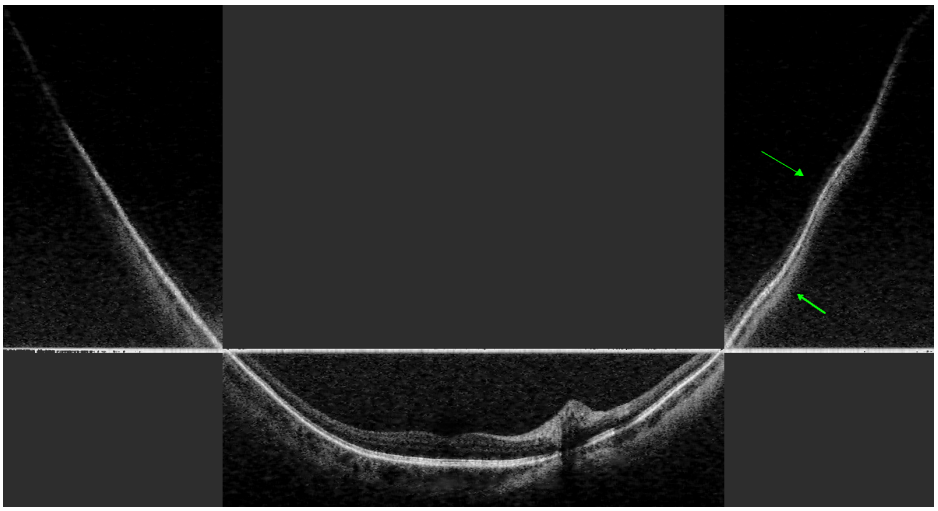

(a)

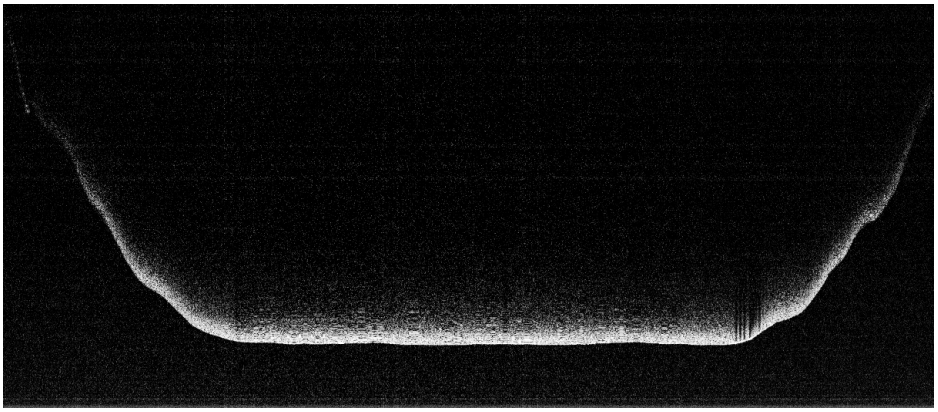

(b)

Fig. 3.14 Horizontal scan from the second demonstrator. **(a)** Ultra wide-field B-scan from the second demonstrator whilst operating normally. The mirror artefact from the image has been inverted. The estimated arclength where signal is collected including the mirror artefact is 30 mm. In the right quadrant ripples are visible caused by the vibration in the SLO scanning arm, which was used to achieve this field of view **(b)** Ultra wide-field B-scan of resolution target, the flattening of the image shows that there is a non-linear scanning rate caused by problems in the hardware control

### 3.4.3 Method for Coupling OCT to SLO

Injecting the OCT beam into the SLO beam path in the COE is nottrivial. When integrating a new modality there are common problems to all ophthalmic devices such as the power budget on the retina, the linearity of scan and interfering with the existing modalities.

The requirements for OCT SLO coupling method were:

- The addition of the OCT imaging modality must not contribute to the total power exposure on the retina. This requirement is explained further below.
- The scan must maintain the same linearity in angle as the SLO, as variations in the linearity within the device will require post processing to remove distortion for co-registering images between OCT and SLO or to extract measurements from the images.
- The method used to insert the OCT beam must not interfere with the original optics; for example, by vignetting or alter the optical properties of the SLO beam. This requirement is significant for the acquisition of ICG as this modality shares a similar emission wavelength as that of OCT. The inclusion of ICG is not a requirement for this device and therefore can be neglected for now.
- The scanning element must share one of the two elliptical foci of the COE. Deviation from this requirement by as little as 1 mm would cause the fan of the scanning beams to be vignetted at the pupil.
- The beam injection system must be integrated into the limited space envelope within the COE and given consideration to the *Daytona* platform which is even more compact than the COE.

Multiple integration solutions were proposed; however, the only clear option was to position a dichoric mirror in the beam path which would provide a virtual image of the polygon where a 2D MEMS device could scan. The primary advantage of this method is that it retained the magnification of the system. The specified mechanical tilt available by the MEMS was $\pm$ 8 $^{\circ}$, which given the magnification at the polygon corresponded to an external FOV of 44$^{\circ}$ at the eye. The disadvantages of the dichroic solution were that it would not transmit the wavelengths of ICG and therefore would need to be removed for that modality. In addition, the dichroic mirror must be placed close to the polygon to reduce the range of angles incident on the mirror as the incidence could vary the transmission. Furthermore, although use of a dichroic mirror to couple imaging modalities in OCT is common [127], the

full impact on polarisation and coherence has not been verified. The implementation of the dichroic mirror can be seen in Fig 3.15

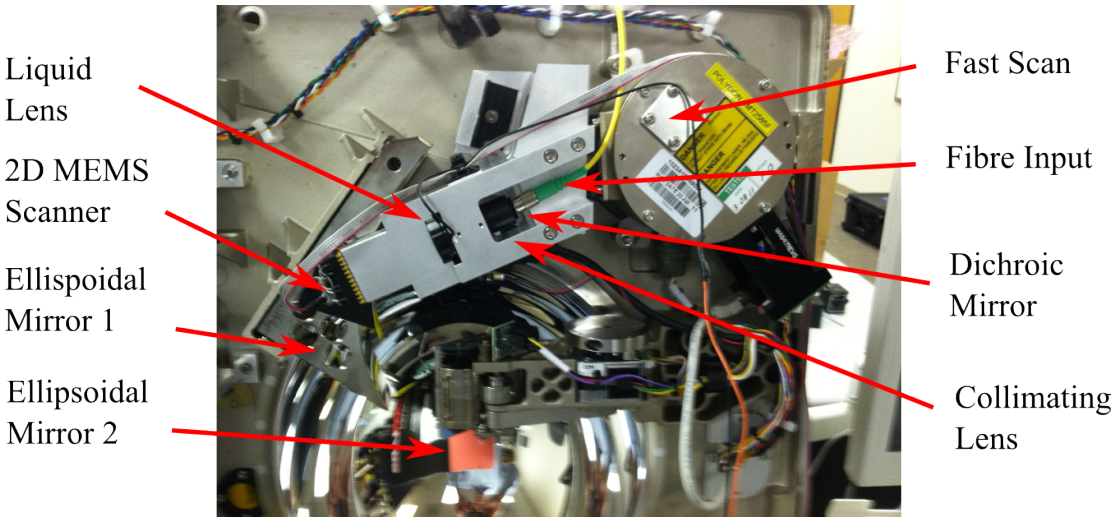


Fig. 3.15 Picture of the beam injection system used in the second demonstrator.

### Laser Safety of Simultaneous SLO/OCT

OCT devices provide live SLO imaging for a more intuitive navigation of the B-scan cross sections. This acquisition can be performed by recording a small amount of the full spectra on an APD or by generating *en-face* images with fast volume acquisition. The unique advantages of ultra-widefield SLO make it desirable to perform the narrow-field OCT acquisition simultaneously while providing wide-field SLO images as this would facilitate accurate registration between the two modalities. Simultaneous use of OCT with visible ultra-widefield SLO has not been preformed previously and new calculations are required to quantify how the two exposures will combine safely. The accessible emission limit (AEL) or 'power budget' can be obtained from the most recent laser safety standards found in IEC60825-13, using the following equation for static exposure (between 10 s and 30,000 s in duration).

$$AEL = 3.9E^{-4}C_4C_7P_{SLD}(W), \tag{3.5}$$

where $C_4 = 10^{0.002(\lambda-700)}$ and $C_7 = 1$ and $\lambda = 830$ nm. This relationship produces a static AEL of 0.71 mW. This value is equivalent to the commonly quoted safe exposure of 0.75 mW. The SLO exposure can be considered as a pulsed laser of period below 625 µs, which is true for both the pixel dwell time and line-scan period, with a scan extent of less than $\alpha$=5 mrad

in the horizontal axis. This extent allows the use of the relationship:

$$AEL = 7x10^{-4}C_6T_2^{-0.25}(\mathrm{W}), \tag{3.6}$$

where the constant $C_6$ can be assumed to be 1 and the period required for tissue to recover to thermal equilibrium $T_2$ to be 100 s. These are conservatives estimates that can be found in laser safety document IEC60825-13. This produces an AEL of 0.221 mW, with the equivalent power across this scan extent of $P_{SLO}(\alpha) = \frac{5}{2000}.2.5$ mW = 6.25 µW, assuming the scan extent is approximately 2 rad. To safely combine these two exposures requires the fulfilment of the following condition,

$$AEL_{total} = \frac{P_{SLD}}{AEL_{SLD}} + \frac{P_{SLO}}{AEL_{SLO}} < 1. \tag{3.7}$$

This condition can be rearranged to show that as long as $P_{SLD} < 0.69$mW then the device is safe for simultaneous imaging. This calculation is a brief example of the considerations required to demonstrate class one operation. The safety document that will be submitted to the regulatory body should also include tolerances for both laser and scanning variability and calculations for each possible assumption, to ensure the most conservative AEL is adhered to.

### Verification of the Dichroic Mirror Transmission Spectrum

The dichroic mirror used for the beam injection was custom built from *Archer OpTx* (MIR-FLTER-802) and was characterised to ensure that it met the specifications provided. The minimum transmission of the dichroic mirror from 532 nm to 802 nm was 80 % and the minimum reflectance from 812 nm to 900 nm was above 95% at an angle of incidence of 9°. Initially, the transmission and reflectance of two wavelengths bands were measured using a power meter and are shown in Table 3.4. The 9° incidence angle was attained by overlapping the retro-reflected spot to find 0° and rotating on a translation stage by 9°.

Table 3.4 The transmission and reflectance of the dichroic window.

| λ (nm) | $P_{In}$ (mW) | $P_T$ (mW) | $P_R$ (mW) | Transmission (%) | Reflection (%) |
|---|---|---|---|---|---|
| 635 | 0.356 | 0.349 | Negligible | 98.0 | < 2.0 |
| 830 | 1.116 | Negligible | 1.09 | < 0.8 | 97.7 |

These measurements show that the dichroic will have a negligible impact on the optical efficiency of the system and are considerably better than the performance expected. The

transition point of the dichroic mirror was characterised with a tungsten halogen source and an *Ocean Optics* spectrometer. The transmission spectrum, shown in Fig. 3.16, was averaged ten times and divided by the reference spectrum in *Matlab*.

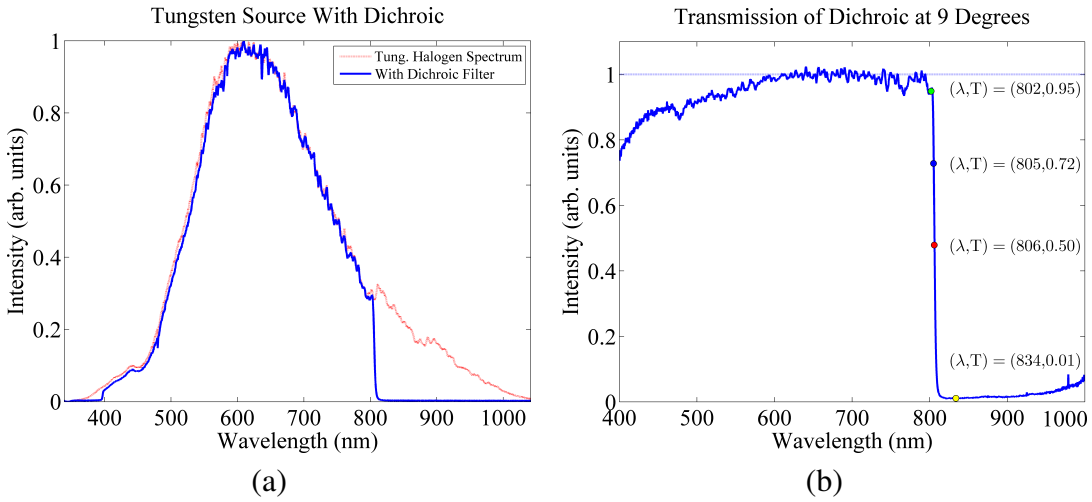


Fig. 3.16 (a) Tungsten halogen source transmitted through the dichroic mirror, shown in blue. (b) Normalised transmission spectra of the mirror. The slight rise in transmission after 900 nm is result of normalising the transmission with spectral intensities near zero.

The green dot in Fig. 3.16 corresponds to the emission wavelength of the nIR laser used for ICG. Although this shows that the transmission is sufficient at 95% for 802 nm, it is crucial that the rotation of the mirror, relative to the optical axis, does not exceed 9° as this will shift the transition point to lower wavelengths. The blue dot shows the transmission at the edge of the OCT sampling spectrum is 72%. The yellow dot shows transmission at the peak emission of the SLD is 1% across the 24 nm FWHM bandwidth. Further verification is required to ensure that the dichroic mirror does not impact either imaging modalities by inducing spectral dispersion, increase scattering in the return path or cause a deviation in the virtual point at the iris.

### 3.4.4 The Dynamic Focus System for OCT

To focus on the retina across a wide-field while compensating for the variable power in the ellipsoidal mirrors requires a change in liquid lens focal length of 86 mm to 36 mm which is equivalent to a change of 16.1 dioptres. In addition, patients with non-emmetropic eyes provide an additional need for $\pm$ 6 dioptres focal correction [108]. This variation means a device designed to image the entirety of the eye should provide up to 22.1 dioptres change in optical power across a wide-field image. In a typical OCT device, this focal variation is

achieved by moving a free-space lens system on a mechanical stage, which is a cost effective solution when the lens is stationary during a scan. To image the entirety of the eye in a single scan would require a shift of 5.6 diopters to account for field curvature and at a rate of 3 Hz to minimise movement artefacts. The tight tolerance required to efficiently couple into a fibre rules out mechanical focal-correction which would suffer severe vibrations at that speed.

Recent development into low-cost, first-order adaptive optics using liquid lenses demonstrate speeds of up to 1 kHz [128] with focal shifts of up to 18 dioptres. Although, this technique has not yet been reported for OCT, the simplicity, low cost and high speeds have made it particularly attractive to wide-field OCT. Investment into the liquid lens technology has generally been toward the mobile phones industry where the principle requirement was to minimise the dimensions of the camera optics. This market requirement for liquid lenses does not benefit large aperture needs of the COE; as such, only two companies *Varioptic* and *Optotune* offer liquid-lens modules with apertures greater than 2 mm at the time of the development. The *Arctic 316* from *Varioptic* was initially chosen for the first two demonstrators because it was more readily available. Subsequent designs have all used the *Optotune* EL-10-30 because they offered an increased aperture. Recently *Holochip* has announced a lens similar to the *Optotune* lens; however, a demonstrator sample would be required to compare its performance with that of *Optotune*.

| Manufacturer | Varioptic | Optotune |
|---|---|---|
| Model | Artic 316 | EL-10-30 |
| Focal Range | 18 Diopters | 14 Diopters |
| Clear Aperture | 2.5 mm | 10 mm |
| Response Time | 33 ms | 2.5 ms |
| Technique | Electrowetting | Membrane |

Table 3.5 Specifications for the two types of liquid lens used in the wide-field OCT demonstrators.

The electro-wetting technique from *Varioptic* uses the interface between two immiscible fluids of different refractive indexes to create a variable curved surface shown in Fig. 3.17 (a). An electrolyte solution and non-conducting oil are sealed together between a pair of hydrophobic windows. When no voltage is applied between the oil and the hydrophobic window then the oil forms a bead that is repelled by the hydrophobic window. By applying an electric field across the fluids the wetting of the oil is increased allowing a greater contact to the hydrophobic window; thus flattening the interface.

The *Optotune* liquid lens uses dielectric elastomer membrane Fig. 3.17 (b). Applying a voltage across the membrane results in an expansion of the polymer. An aqueous solution

is sealed between the membrane and a window with extra fluid stored in a reservoir. When the membrane expands, water is pulled from the reservoir filling the curved chamber and providing an increased optical power. This method is both faster and requires a lower voltage; however, gravitation pull induces a minor sag along the vertical axis of the lens.

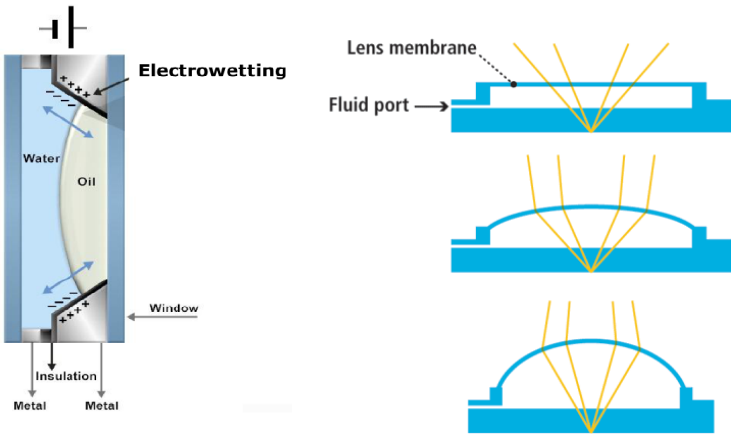


(a) (b)

Fig. 3.17 Liquid lens concept diagrams **(a)** Varioptic Liquid Lens **(b)** Optotune Liquid Lens [129]

### Response time of the Optotune Liquid Lens

The principle technological risk of the liquid lens was considered to be the response time to changes in drive current. Investigating the response of the liquid lens to a step/continuous current is important for two implementations of the lens. Firstly, vertical scans require a continuous change in the current is maintain optimum focus while synchronised to the vertical field angle. No data was provided on how the liquid lens responded to a continuous signal; however the quoted response time of the liquid lens of 2.5 ms is smaller than the expected 50 ms B-scan acquisition time. Secondly, it is important to verify that the response time conforms to the 2.5 ms quoted as image acquisition would need to wait until the lens has refocused.

An experiment was devised as shown in Fig.3.18, to measure the response time of the liquid lens (model EL-10-30-NIR-LD SN:B716). A collimated beam was focused through an aperture onto a detector using the liquid lens. The varying focus of the lens resulted in a variable loss by the optical system as the light being truncated at the aperture. The liquid lens was driven by a signal generator and the output from both the generator and detector

were recorded on an oscilloscope. The entire experiment was orientated perpendicular to the optical bench to mitigate the impact of gravity of the liquid lens.

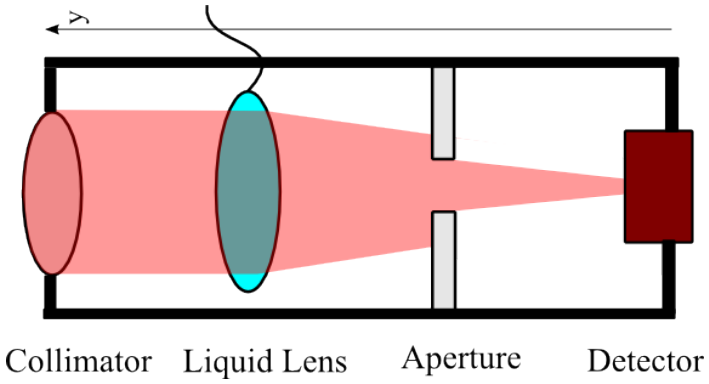


Fig. 3.18 Experimental set up from the liquid lens investigation, as the current to the liquid lens increases the transmission through the aperture increases. This equipment was oriented 90° clockwise from what is shown to mitigate gravity induced lens sag.

The first stage of the experiment investigated the impact of applying a continuous sinusoidal signal to see if various drive frequencies changed either the focal shift or the response time with a constant change in drive current. The frequency range investigated was 0.2 Hz to 80 Hz based on the maximum reasonable drive frequency of 80 Hz for a 80 kHz spectrometer needed to produce B-scans consisting of 1000 A-scans. The raw data from this measurement is provided in Appendix A.3 as these figures may assist the reader in understanding the results of the experiment. Across 0.2 Hz to 80 Hz the response time or 'lag' induced by the liquid lens is reduced from 144.7 ms to 4.3 ms with a relative increase in phase from 10.4° to 123.1°. Furthermore, at 80 Hz the amplitude of the focal shift is reduced to 22% of the initial range induced from 0-5 Hz. These values are plotted in Fig. 3.19 (a) and (b). This means that to increase the variation in response B-Scan rate requires a varying delay to synchronise the correct optical power with vertical field angle. In addition, the optical power changed appears to have reduced for higher modulations.

The second stage of the experiment investigated the relationship between the magnitude of focal shift with the modulation frequency. The focal shift was altered by changing the current from 20mA to 160 mA as shown in Fig. 3.19 (c-d). With the exception of 20mA, the change in did not impart a substantial variation in response time. Ray-tracing in *Zemax* showed that a focal length shift from 50 to 62 mm, equivalent to 3.9 dioptres, would be required to maintain focus across ± 3 mm arclength, required to provide a vertical cross section of the optic disc. Each lens comes with a current-to-lens focal length reference table, for this liquid lens, the required focal shift was induced by a change in current $\Delta I$ of

approximately 60 mA. For this $\Delta I$ the frequency was increased from 1 Hz to 100 Hz and $\Delta I$ was increased to maintain the same peak-voltage on the oscilloscope. The reduced amplitude of light detected with frequency, plotted in Fig. 3.19 can be off-set by an increase in the drive current. The drive current required to maintain a constant focal shift of 50 mm to 62 mm has been provided in Fig 3.19 (f).

The impulse response of a 50µs impulse, was measured to provide the frequency response that is shown in Fig. 3.20 (a-c). The modulation transfer function of the impulse response plotted in Fig. 3.20 (d) did not appear as a typical DC response. Firstly, there appears to be a zero-amplitude frequency centred at 0 Hz, where the response should be strongest. Secondly, the response is dwarfed by a resonant frequency centred at 320 Hz. This value is corroborated by a recent amendment to the characterisation report by *Optotune* as to this resonance; however, the null-frequency is likely to be an artefact from sampling.

From this investigation it was determined that the settling time of the liquid lens was 16 ms which is in agreement with subsequent investigation from *Optotune* stating a settling time of 15 ms. The maximum drive frequency that the liquid lens can be driven without scaling the current with frequency was determined from Fig. **(e)** to be approximately 5 Hz; however, increasing the current range of the liquid lens has been shown to allow up to 100 Hz. This investigation was not able to observe if this technique had any impact on the beam profile or if the calibration was unique to each lens.

Investigation into the polarisation response of the liquid lens relative to input current should also be performed on the *Optotune* lens, as plastics can exhibit increased birefringence when subjected to strain [130]. The supporting documentation for this system states that there is not an increase in the birefringence with current; however, exploratory investigation on the *Varioptic* liquid lens recorded a 12% reduction in linearly polarised light for a small focal shift of 5.2 dioptres, when measured through a polarisation analyser. The *Optotune* system also claims to be polarisation insensitive. In addition, there should be further investigation into the variation in optical characteristics across different liquid lenses.

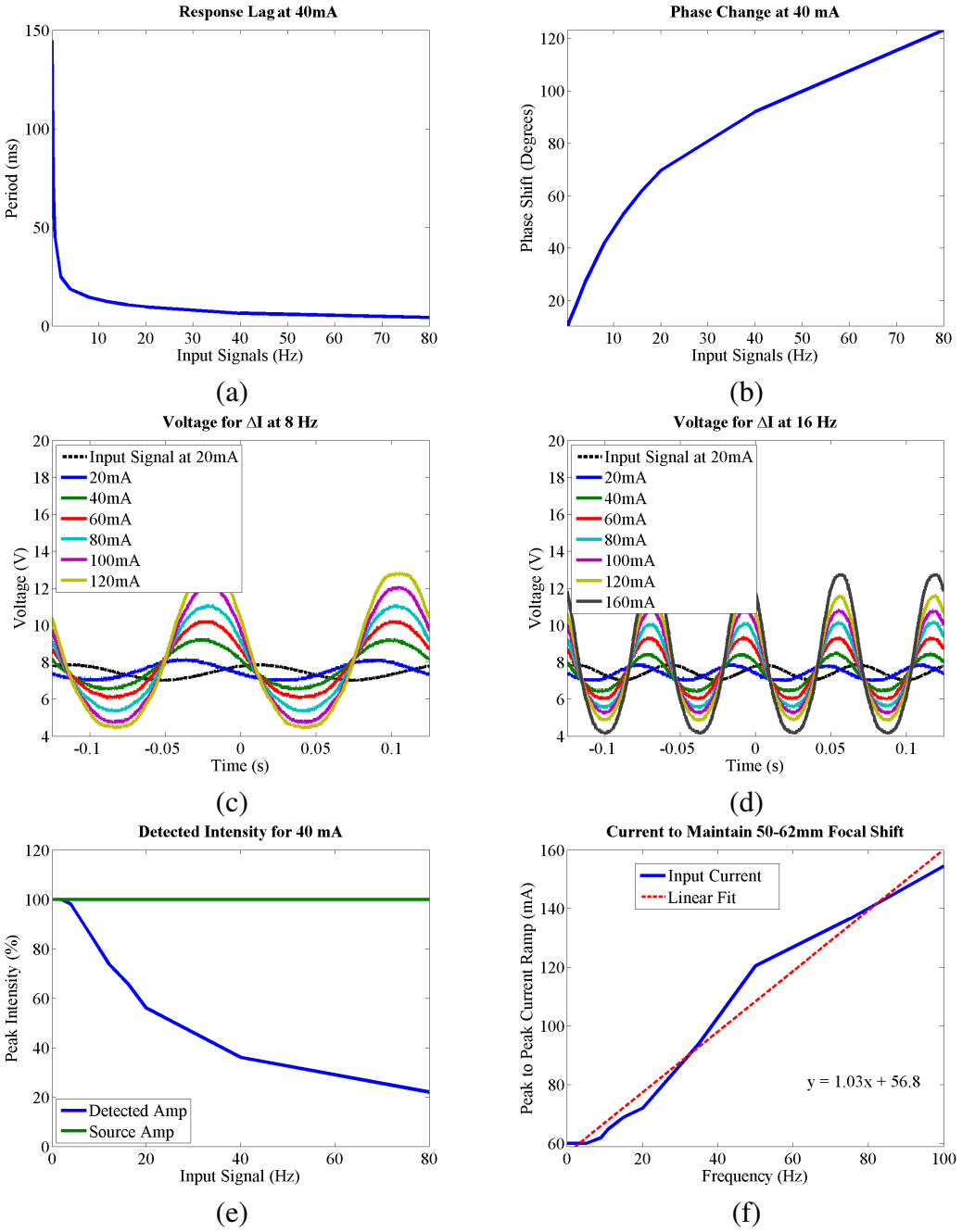


Fig. 3.19 **(a)** and **(b)** are plots showing phase lag from the measurements in Appendix A.3. The changes in phase with frequency means that for a continuous scan the power of the liquid lens will be increasingly wrong with field angle. **(c)** and **(d)** show the impact of altering the current applied to the liquid lens, this shows that the phase depends only on the drive frequency above 40 mA. Fig. **(e)** shows the percentage of the low frequency response is detected as the frequency increases. **(f)** Plots the required current ramp to maintain a fixed focal shift.

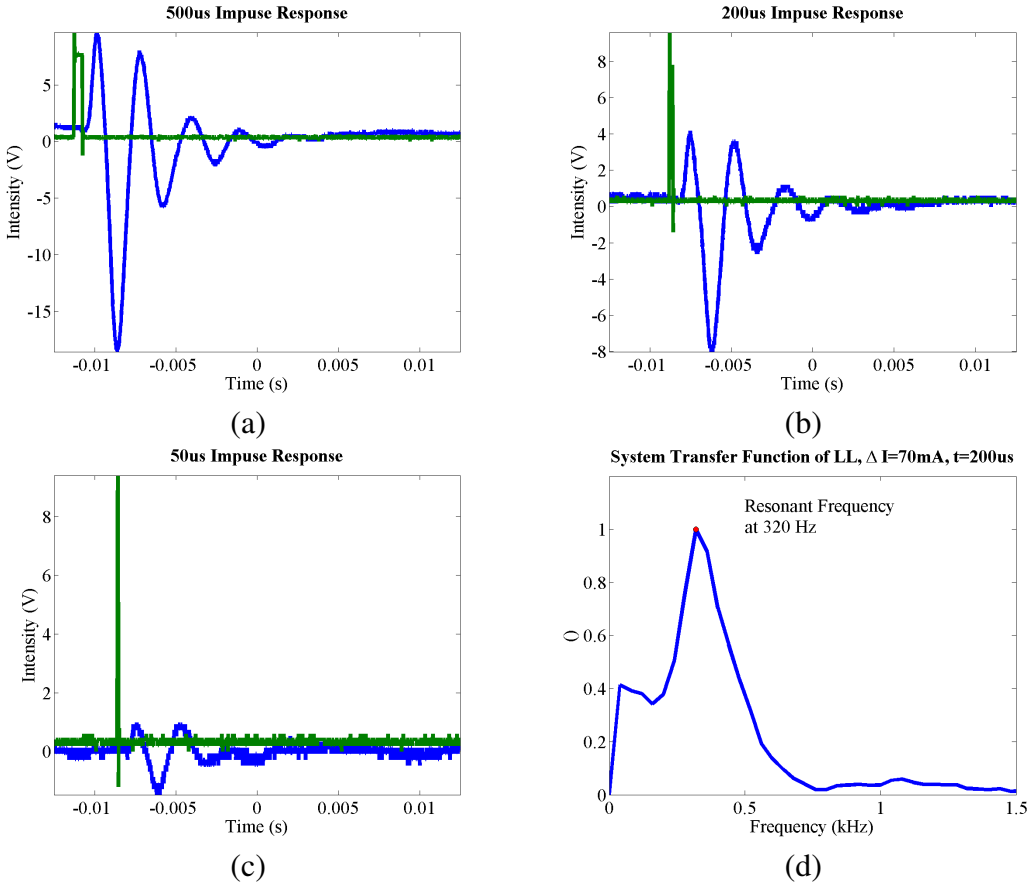


Fig. 3.20 The impulse response of liquid lens is shown **(a-c)** along with the system transfer function **(d)**. The impulse resonances was measured as (a) 16 ms (b) 16 ms (c) 10 ms, although the low amplitude of the response indicates that the 50 µm pulse period is too narrow to be fully detected by the liquid lens.

## 3.5 Optos OCT Demonstrator Three

*Optos* purchased the OCT-ophthalmic devices company *Opko* at the end of 2011. The purpose of the acquisition was to gain access to the OCT sales channels of *Opko* and to prepare the company for the regulatory challenges of releasing wide-field OCT. Furthermore, the ongoing development of integrating OCT into the COE platform had demonstrated that the complexity of OCT was not likely to yield a new device within the next financial year and would require further support of engineers with expertise in the field. The collaboration with *Wasatch* was minimised in favour of integrating the established *Opko* platform, known as the *Model E*, into the new *Optos* platform, known as the *Daytona*, as the second demonstrator had began to show that it would not fulfil its initial objectives. The optics system of the Daytona was approximately equivalent to the COE with the only difference, relevant to OCT use, being that the first ellipsoidal mirror was now 20 mm thick, thinner than the 30 mm COE mirror.

The aim of the third demonstrator was to answer the outstanding question, could light be coupled from the eye, through the ellipsoidal mirrors, with an SNR that is comparable to competitor systems. The reasons for focusing on only the second aim listed in Section 3.3, was to allow a simplification to the device. The third demonstrator used the 28 kHz E2V-SM2 spectrometer, used in the *Opko* Model E as this spectrometer was already integrated with the *Opko* research software. The advantage of reusing this software was that it acquired B-scans without excessive processing and software bugs that limits image analysis within the *Wasatch* system. The fibre network and reference arm were recycled from the first demonstrator and all scanning was provided by the horizontal slow scan mirror. The SLD was switched on to a higher power source, from *Superlum*, that had an 18 nm bandwidth. This change was implemented to reduced the need for the compensation of chromatic dispersion and birefringence and the liquid lens was replace by a fibre collimator lens.

### 3.5.1 Results from the Optos OCT Demonstrator Three

A mechanically-adjustable lens with a 10 mm aperture and a 16 mm focal length was found to provide the highest SNR after testing multiple input-lens prescriptions that were available on site. Assuming that the NA of the fibre was 0.14, then this element produced an exit beam diameter of 4.5 mm out of the lens and a 1.6 mm diameter onto the cornea on-axis. As can be seen from the image provided in Fig. 3.21, the SNR of the device has significantly improved. This shows that the most crucial parameter for efficient light collection was the beam diameter from the fibre coupler. This conclusion is based on both the testing of free-spaced lenses available on site and the comparison of the images in Fig. 3.21 with the

images acquired on the first and second demonstrator in Fig. 3.8 and 3.12. The axial rippling in the images from the third demonstrator, in particular Fig. 3.21 (a), result from vibrations in the scanning mirror being amplified by the new cantilever mirror mount used in the Daytona which is longer and lighter than in the COE. Three possible remedial actions to remove this artefact are firstly, adding a counter balance along the mirror scan axis to dampen the cantilever; secondly, to change the PID values used in the mirror acceleration to minimise the variable drive current and finally if the ripples were consistent they could be removed using a software algorithm. The first two solutions were implemented in later versions of the device, with particular haste as the observation of this artefact informed *Optos* of a similar 'beading' of the vasculature in the SLO images.

### 3.5.2 Discussion on the Optos OCT Demonstrator Three

The primary outcome of the third demonstrator was to demonstrate that light could be coupled through the ellipsoidal mirrors to generate a competitive SNR. The images in Fig. 3.21 show neither a defined ELM or choroid; however, this is attributed to the minimised polarisation and dispersion control within the demonstrator. In addition, the demonstrator provided visualisation of the impact that design choices would have on OCT such as the slow scan mirror vibration or the reduced horizontal B-scan width that resulted from the thinning of the first ellipsoidal mirror. Furthermore, these images were used to attribute the mirror wobble to an artefact presenting in the SLO images. The impact of using a narrow bandwidth source on axial resolution could not be determined from comparison between the first and second demonstrator with the third, as the change in SNR between devices is too great. In addition, there was no reason to believe that the increase in SNR could be attributed to the removal of the liquid lens or the dichroic mirror and there these will return in subsequent designs. A further observation in the images was that the retinal thickness appeared to display a significant thinning in the periphery. It is not yet clear whether is anatomical or an imaging artefact further modelling is provided in Chap. 4 to investigate the likely impact of the anatomy on OCT images.

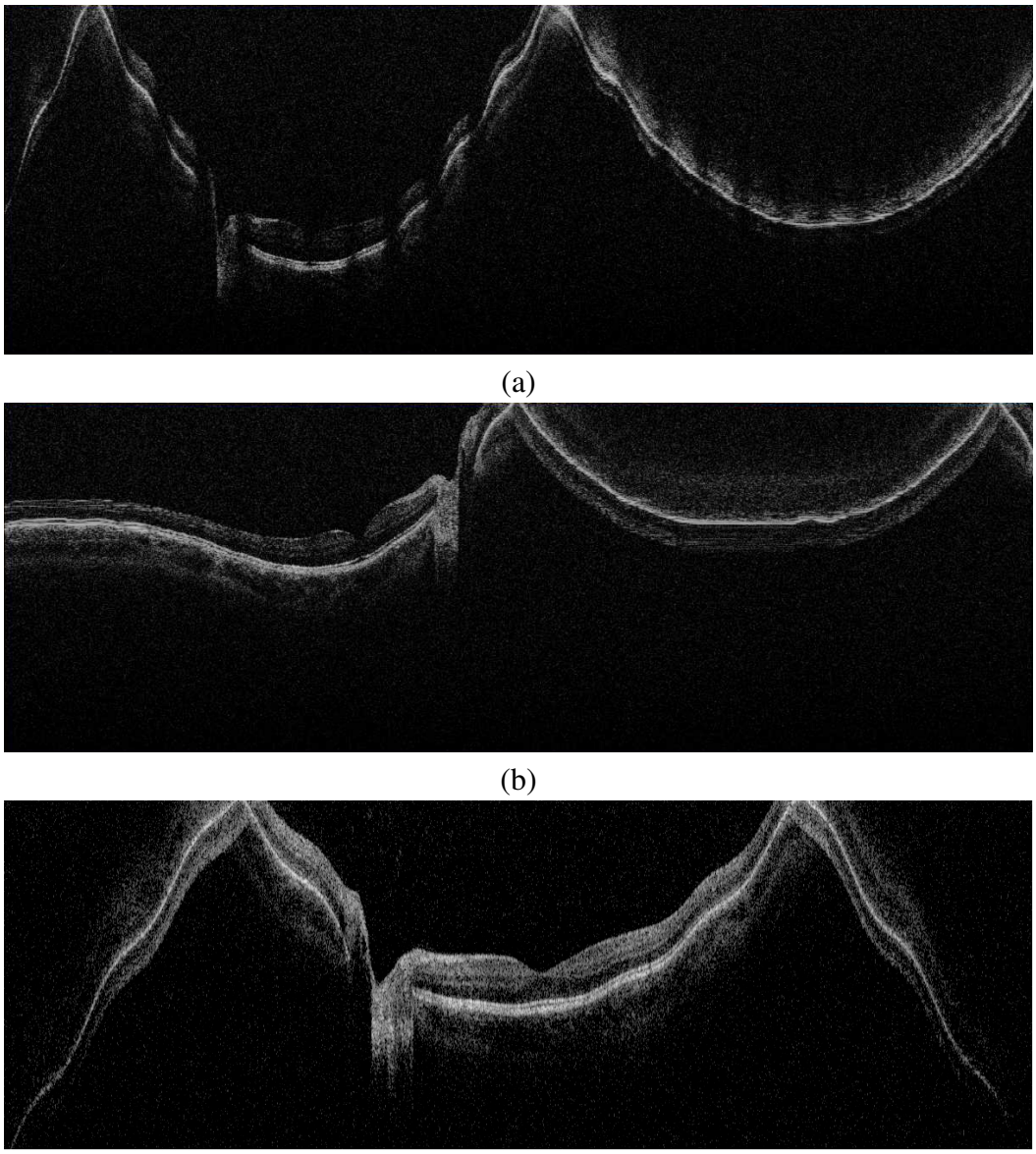

(a)

(b)

(c)

Fig. 3.21 **(a)** The first OCT image acquired through a Daytona, the apparent folding of the curvature is where the OPD of the retinal curvature exceeds the range capable by the device. The banding is caused by vibrations in the motorised mirror. Mirror driven by a triangular waveform **(b)** Image from the demonstrator three where the mirror is driven by a constant current. **(c)** Final image from the third demonstrator showing that sufficient light can be coupled through the system for competitive OCT. The increased signal is attributed to the use a wide aperture input lens. The estimated arclength where the signal is recorded, including the mirror image is 25 mm.

## 3.6 Chapter Conclusions

The use of ellipsoidal mirrors is both crucial to the acquisition of ultra wide-field images as well as the principle source of aberrations with in the device. To scan the retinal periphery, *Optos* devices employ a pair of ellipsoidal mirrors to link scanning foci with the pupil of the eye. The ellipsoidal mirrors provide a 2.77 times magnification to the scan angles from the first polygon scanner; however, this magnification also results in a narrowing of the beam waist at the cornea. A narrow beam waist was determined to balance the resolution on-axis of 38.6 μm with reducing the aberrations off-axis. Despite this compromise, the off-axis spot size is still over ten times larger at the furthest field angles.

The development of an integrated OCT SLO demonstrator was repeatedly limited by a small beam size through the COE. This beam size both reduced the coupling of light into the SM-fibre and the achievable transverse resolution. The small beam size was initially caused by the small aperture of the liquid lens in the first demonstrator and then the MEMS scanner in the second. Images from this demonstrator prove that an OCT device can be integrated into the COE for on-axis OCT imaging. Light collection in the third demonstrator was increased by widening the aperture of input lens and increasing the width of the scanning element. This allowed a larger beam at the cornea to pass through the COE without observable vignetting. These images display aberrations caused by both the geometry and the stability of the scan system. To reduce the instability in the COE the scanning mirror, which was driven with a stepping motor, could be replaced with a large galvanometer as this scanning method was successful in the first demonstrator. The full impact of the ocular geometry on imaging performance will require further investigation, which has been provided in Chap. 4.

Characterisation of the dichroic mirror has shown that this element can be used to couple OCT beam-path efficiently to the eye and back without perturbing the SLO performance. So far there has been no reason to believe that the dichroic mirror reduces fringe visibility, although further investigation will be required to verify that the range of angles incident on the mirror will not reduce the transmission of the longer wavelengths. The investigation can be easily performed on a stable device by comparing the image quality with both a dichroic mirror and a standard mirror. Increasing the frequency of the drive signal to the liquid lens beyond 5 Hz resulted in the lens being unable to achieve the desired focal shift as for slower speeds. However, it was demonstrated that by scaling the input current (by approximately 1 mA per Hz) then the desired focal shift could be achieved up to a 100 Hz drive.

The aim of establishing whether a commercially-competitive, wide-field OCT device is achievable requires further investigation despite the positive results from the third demonstrator. The success of this aim will require both clinical investigation and the conformance to an ever improving benchmark in the technology. The images acquired in each of the

demonstrators show both a reduction in signal off-axis and an apparent thinning of morphology that does not appear to be representative of the retina. In addition, we have still not acquired high-quality vertical images or even horizontal images at a different azimuthal angles. In theory, navigating the eye with horizontal scans should be achievable with a liquid lens acquired with a step function; however, the acquisition of volume scans will require the liquid lens to be driven at fast pace and will require a scaled-increase in drive current.

The testing of the demonstrators showed that OCT requires the patient to be stationary for tens of seconds, to even minutes, substantially longer than the 0.32 s in the SLO. This means that all devices containing OCT will require a head rest, a suitable patient alignment system and a fixation target. In particular, an internal fixation target will be challenging to develop without degrading the scanning of the ellipsoidal mirrors. Although it may be possible to flicker light from an off-axis source with enough phase shift to create an image a fixed position target on the eye.

Finally, the performance assessment of images in this Chapter has been qualitative as it was based on visible SNR levels between images. As the system design converges upon the optimal configurations and the improvements per-iteration become more moderate, then this subjective analysis will not be sufficient to compare the performance of a new system to either a previous design or competitor performance. A method must be developed that can be used to grade these iterative improvements. The narrow-field SLO phantom eyes used in this Chapter have already proved useful for calibrating the system though out the initial design; therefore, I propose the creation of a wide-field OCT phantom eye to assist in the development, calibration and characterisation of wide-field OCT, this work is provided in Chap. 6 with quantitative image analysis methods investigated in Chap. 7 and Chap. 8.

# Chapter 4

# The Impact of Eye Characteristics on Wide-field OCT Design

## Chapter Summary

Within this chapter the principle challenges of wide-field OCT are reviewed that are highlighted in the previous chapter by the OCT demonstrators. Five of these challenges are explored in greater detail and include modelling to predict their impact on image quality. Modelling in this chapter indicates that aberrations and the range of optical path lengths are the principle sources of image quality degradation that are caused by the eye; however, further empirical data is required to understand and mitigate these challenges.

## 4.1 The Technical challenges of Wide-Field OCT

The conclusions reached after developing the first demonstrator have been used to create an exhaustive list of the technical challenges that required further investigation or mitigation before the development of wide-field OCT could proceed. The challenges are segmented into three categories; those introduced by the eye, the system and finally the patient interface. The impact of eye characteristics on wide-field OCT design form the basis of what is theoretically achievable in a wide-field OCT platform and are independent of the chosen method to achieve a wide-FOV. The challenges of the system are integral to estimating the cost and market of the wide-field product.

Five technical risks to the development of wide-field OCT are identified to be caused by the eye. These risks are outlined below:

i. The wider input beam than SLO is likely to be vignetted by a non-dilated iris for higher field angles and transmit non-uniformly across the field upon reflection due to the pupil appearing elliptical to off-axis beams.

ii. The varying OPL of the beam through the cornea and crystalline lens will introduce varying birefringence with field angle as these lenses introduce 80% of the birefringence in the eye [131]. This variation will likely need varying polarisation-compensation with field angle to maintain the SNR performance of on-axis imaging.

iii. The OPL introduced by the curvature of the eye exceeds the imaging range of any commercial OCT device. To compound this challenge, a commercial device will typically have a signal roll-off of approximately 20 dB across the A-scan, which will reduce the useful imaging range of the system, as was discussed in Section 2.9.4. The OPL required to image the curvature of the eye is likely to be achievable in a research-grade swept-source device as the coherence length of these sources exceeds 12 mm [5].

iv. The variation in the OPL with the field angle will result in a variation in the chromatic dispersion that would be challenging to compensate for mechanically.

v. The large surface area of the eye will require the pixel density to be compromised to reduce the scan duration and motion artefacts as a result of the current limitations of detector speeds.

There were four technical challenges outlined for a wide-field OCT device based on ellipsoidal mirrors.

i. The change in optical power with vertical field angle in the ellipsoidal mirrors will substantially reduce the optical efficiency and transverse resolution in images.

ii. The aluminium-oxide on the mirror surface within the scan system will impart both a variable retardance with angle of incidence. In addition, the mirror and reduce the optical efficiency of the system as aluminium has a reflectance dip at 805 nm.

iii. The large variation of angles that are incident on the retina with field angle will lead to an axial distortion (warping and skewing) of a retinal image.

iv. An ultra-widefield volume would be computationally intensive to process and each image would be in the order of tens of gigabytes of data .

The complexity of using a wide-field OCT system exceeds that of a standard device for three reasons.

i. The navigation of the retina is more challenging as there is a reduced density of unique features away from the fovea.

ii. Wide-field OCT images will require image registration to SLO images to assist in the classification of disease progression and targeted treatment.

iii. The large range of imaging angles will require a patient fixation point that is independent of the scan optics of the device and will require a novel approach to fixation and patient alignment in an ellipsoidal scan system.

From the above challenges, the proposed mitigation of the four risks thought to be of greatest concern at the early stages of wide-field OCT development are listed below:

1. The *defocus* due to the ellipsoidal mirrors could be mitigated with an autofocus that is provided by a liquid lens. This compensation could be implemented with a look-up table of optical power with field angle for fast changes or a closed-loop optimisation, in a navigated approach to wide-field OCT. The use of a liquid lens in the wide-field OCT is described earlier in Section 4.2.

2. The *variation in the retardance* with field angle from the eye can be compensated with motorised fibre-compression paddles. This compensation will be investigated further in Section 4.3. The retardance with FOV from the mirrors in the device is not likely to cause a significant deterioration in the phase matching in the OCT as 4 nm oxide layer naturally forming on the mirrors [132] will not significantly change phase of the s and p states. In addition, the inferior optical efficiency of aluminium mirrors for near-IR current used in the COE, will likely lead to these mirrors being replaced by silver mirrors in future anyway.

3. The *insufficient imaging depth* on a SD:OCT device could be mitigated by translating the reference arm during a scan to maintain a fixed path length in the sample and reference arm. This challenge is described further in Section 4.4.

4. Image warping requires retinal segmentation that includes a look-up table for weighted measurement along with an algorithm developed to create a projected volume and is described in Section 4.5.

5. The variable group-velocity dispersion with field angle will likely require a numerical dispersion algorithm that has different dispersion-compensation coefficients relative to the field angle. This challenge is described in Section 4.6.

Each of these technical solutions require some form of prior modelling of the eye either based on computational ray tracing or empirical data. The rest of this chapter covers the computational analysis of these technical risks.

## 4.2 The Impact of Aberrations on Wide-Field OCT

The defocus along the vertical field angle caused by the ellipsoidal mirrors was described in Section 3.1.5. The repeatable nature of this vertical defocus in the COE implies that the integration of static compensation could be sufficient to restore the image quality in the retinal periphery. Once this systematic defocus has been mitigated either by a static phase plate, dynamic focusing or by restricting the scan angles to a narrow-field that is slowly navigated around the eye, then the next step would be to compensate for the defocus introduced by the eye.

The focal correction for the eye was modelled in the ray-tracing software *Zemax* using the Navarro schematic eye parameters provided in (Table 2.1). A pair of paraxial lenses were positioned at 8.8 mm from a 0.12 NA source to produce a 2 mm beam on the cornea for the on-axis configuration (dark blue). The working distance of 14 mm was arbitrarily chosen to match the vertex distance of spectacles. The system was optimised to minimise the RMS spot radius by adjusting the focal length of the final lens. The ideal focal correction to minimise the spot radius on the retina has been plotted in Fig. 4.1.

As can be seen from Fig. 4.1, the 830 nm beam required 0.73 dioptres of focal correction on-axis; however, it should be noted that the first 0-0.2 dioptre correction remained diffraction limited. Despite this optimisation, the off-axis spot remained significantly larger than the on-axis spot radius due to astigmatism and coma. These aberrations result in a reduction in optical efficiency coupling into the fibre. Three losses exist in a wide-field system where light is coupled into a fibre; the impact of these losses is shown in Fig. 4.2. The first loss is that of coupling efficiency (the flux of photons entering the fibre pupil): By approximating the retina as a Lambertian scatterer this loss be described by,

$$I_{out} = \frac{cos(\theta_i)}{d^2} A_o P_o, \tag{4.1}$$

where $\theta_i$ is the angle of incidence, from normal, on the retina, $d$ is the distance between the iris and retina and $A_o$ and $P_o$ correspond to the pupil area and source power, respectively. The

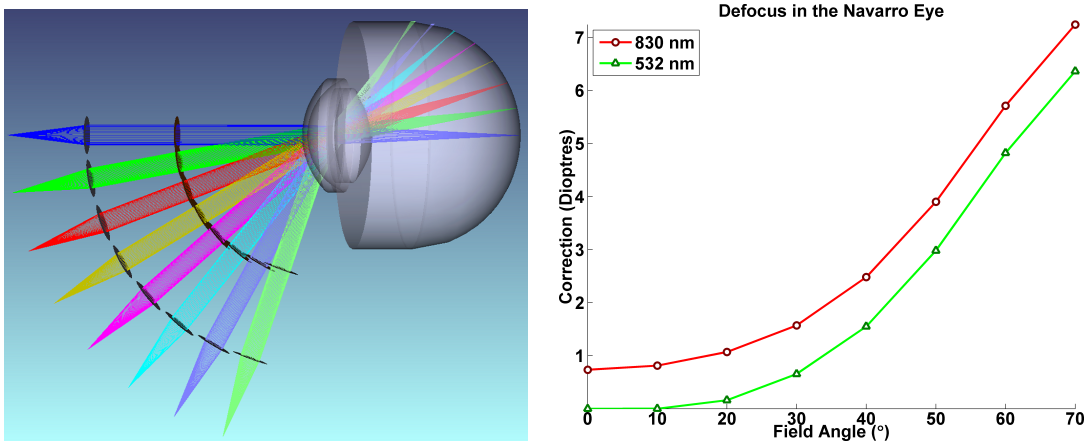


(a) (b)

Fig. 4.1 (a) Layout of the modelling used to determine defocus with external field angle. The field angle in degrees refers the external field angle subtended by the chief ray and the optical axis. (b) Plot of the focal correction in dioptres (inverse of the focal length) required to achieve the minimum spot radius on the retina for 830 nm (red) and 532 nm (green).

relative intensity with field is shown to be relatively flat by the green line in Fig. 4.2 as the impact of the inverse-square proportionality in Eq. 4.1 is offset by the oblique aperture of the iris.

The vignetting and fibre-efficiency plots in Fig. 4.2 (b) are two ways of considering the optical efficiency in the system. The vignetting of the ray trace shows the relative number of rays (assuming a planar distribution) that were not vignetted after passing out of the eye and through a 5 μm aperture; allowing for refocusing by the *Thorlabs* AC080-016-B fibre-collimating lens. This plot shows that as much as 90% of the light is lost. The fibre coupling was also calculated using the *Zemax* physical optics propagation tool. This data indicates that there will be significant losses off-axis that result from higher order aberrations than defocus; however, as the beam exiting the eye is not Gaussian then the quantitative accuracy of this tool is limited.

Further investigation should be conducted to show whether the coupling of light into the fibre across large field angles can be modelled by ray tracing, Gaussian beam propagation or most likely will require further development of the description of the light that entering the fibre.

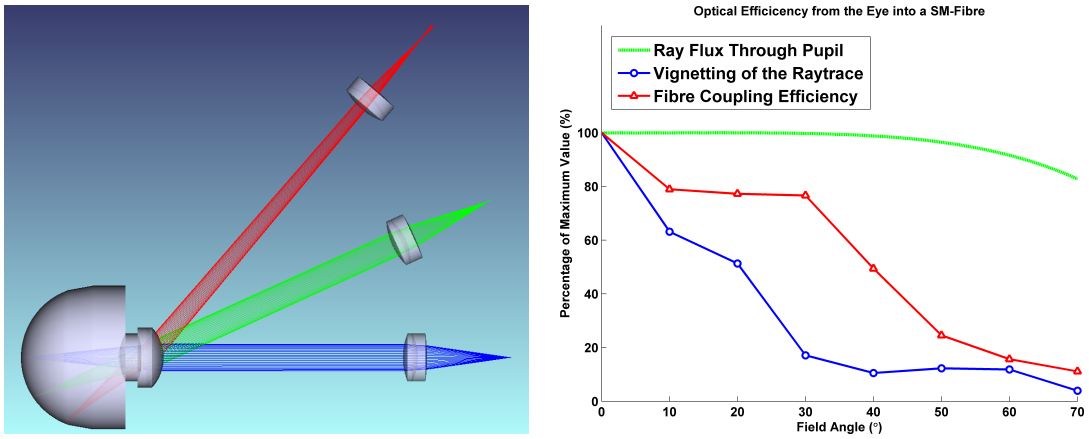


(a) (b)

Fig. 4.2 (a) Layout of model used to determine the fibre coupling efficiency out of the eye for all field angles. (b) Plot of the optical Efficiency exiting the eye based on Zemax Modelling.

## 4.3 The Need for Polarisation Control in Wide-Field OCT

The polarisation control within a commercial OCT device is typically designed to match the birefringence of the reference arm to that of the imaging system, excluding the eye. The birefringence can be achieved by using either a combination of wave-plates in a free-space reference arm or compression elements within a fibre-based reference arm. The optimum reference arm polarisation is found by placing an attenuated reflector at the imaging plane and then manually tuning the reference arm to maximise the interference contrast in the channel spectrum. For a commercial device, the polarisation configuration can then be fixed and subsequently tuned during the periodic servicing of the device. The limitation of this technique is that it both ignores the birefringence of the eye or the variation in birefringence between patients.

A review of ocular birefringence can be found by Bour L. J. ref [133]. The cornea is the first birefringent element within the eye and contributes more retardance to the transmitted light than any other element within the eye. The birefringence within the cornea occurs as a result of both the structural arrangement and the intrinsic birefringence of the collagen fibres in the stroma that provide strength to the cornea. The crystalline lens is the second retarding element within the eye. This lens has been shown to contribute only a minor amount of retardation to transmitted light and therefore it can be neglected when considering the local fluctuations in birefringence across an image [131]. Finally, the retina has birefringent properties that are caused by anatomy such as the RNFL and the Henle fibre layer [134]. With the exception of these regions, the retina is mainly considered to be a weak depolariser [133].

This response is effectively a loss mechanism as depolarised light cannot be re-polarised without a significant loss. As the birefringence of the RNFL is clinically significant and therefore undesirable to correct, the retina will also be neglected from the modelling of retardance for the remainder of this section.

The birefringence through the cornea varies with radius from the optical axis, incidence angle, local orientation of the fibres, patient prescription and wavelength [135]. The lack of radial symmetry along with the variance between patients make a quantitative model of birefringence with field angle beyond the scope of this thesis; however, there is sufficient empirical data in publications to allow qualified predictions on the corneal birefringence with field. For on-axis applications, retinal scanning laser polarimetry devices such as those from *Carl Zeiss* which operate at 780 nm, now compensate for the variation in the corneal birefringence between patients through variable mechanical and numerical compensation [134]. The retardance of the cornea measured by this device ranges from 33 nm to 88 nm with a variation in orientation of the slow axis up to 46°. Further studies using similar polarimeter examinations at 532 nm have found on-axis corneal retardance varied as much as from 0 to 190 nm with a variation in slow-axis orientation of 45° [136]. From these measurements, we conclude that even the imaging performance of narrow-field OCT devices could be improved by a flexible polarisation control that is calibrated using either a real eye or a phantom that contains a comparable retardance to the eye.

The cornea can be approximated as a uni-axial birefringent crystal with an average birefringence $\beta$ of 0.002 for light entering peripheral portions of the retina at wavelengths of 633 nm [137]. In the Navarro eye, the OPL scanning through the cornea varies with field from 0.76 mm on-axis to 1.07 mm at 70°. The retardance based on these values is plotted in Fig.4.3. This change in OPL indicates that the change in retardation $\delta\beta = (\mathrm{OPL}_{\mathrm{offaxis}} - \mathrm{OPL}_{\mathrm{onaxis}})\beta$ could be as high as 628 nm, approximately three-quarter waves. More recently, *in vitro* measurement of corneal transplants found that the change in retardation was approximately 720 nm across a radial distance of 4 mm, when measured parallel optic axis [138]. The data from the Jaronski study has been plotted in Fig. 4.3 along with the fixed retardance with OPL from Bour *et al.* . The change in retardance from both measurement concur on-axis; however, the Jaronski study predicts a greater increase in retardance with field angle.

This methodology for measuring the retardance with field angle is overly simplified to predict the precise retarding with field angle; however, the scale of the retardance for both these models would imply that a B-scan of the full length of the retina would suffer local signal attenuation and include a region that exhibits complete extinction of the signal within the image. Images from recent publications in wide-field OCT do not report this effect, nor do the publications contain any mention of a need for the correction for polarisation with

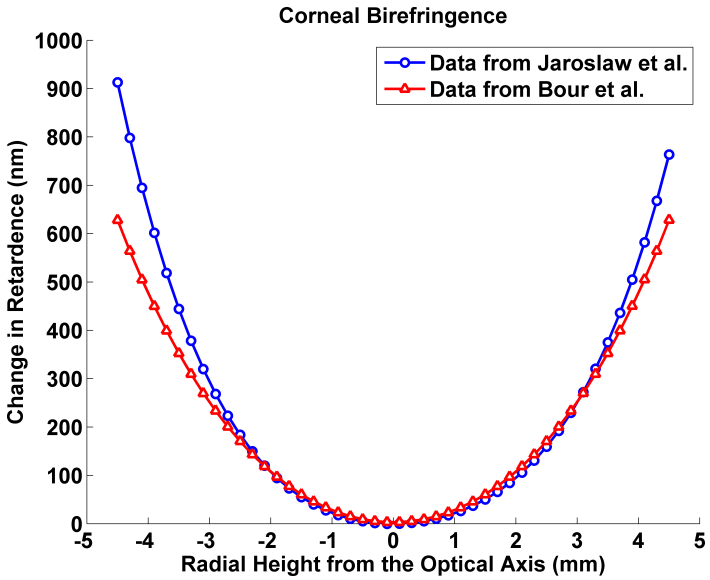


Fig. 4.3 The change in retardance of the cornea assessed by applying the retardance to the coefficient of birefringence measured by Bour et al. [137] and the measured data reproduced from Jaronski *et al.* [138] .

field angle [5] [78]. This could be attributed to the lower radial height on the cornea of around 1.7 mm, estimated from their publication which would produce only a 76 nm change in the retardance, based on the data in Fig. 4.3. Within an image this birefringence would only manifest in a small increase in the roll-off of a well optimised system. A better model of local retardance would need data from live patients as the eye deforms significantly *in/ex vitro*, in addition, the eye is not a homogeneous crystal therefore theoretical approximations would need to account for the varying crystalline properties through the cornea.

The COE is a practical example with an equivalent FOV to the *Zemax* modelling. The reflectance images within the COE suffer from intensity fluctuations across an image that have been attributed by *Optos* engineers to a birefringence induced dichroism of the eye when combined with the polarising filters in the COE return path. To combat this artefact the COE uses circularly polarised light. This configuration is successful at reducing the sensitivity of the COE to the local retardance. The only way to reproduce this solution in OCT would be to measure the orthogonal polarisations and then average both the images; however, this solution would be unrealistic in SD:OCT where the detector is the most expensive element in the system. For this reason, any device that is designed to image with a field that exceeds the retinal arcades should contain a dynamic polarisation control.

## 4.4 Imaging Range of Wide-Field OCT

The shape of eye in many creatures has developed to be approximately spherical to allow them to move their eyes independently of their head. The curvature of the eye and therefore the retina also contributes to maintaining the Petzval image plane and OPL of light passing through the human eye. The optimum retinal curvatures for best focus, or for a fixed OPL in the Navarro schematic eye, are 14.7 mm and 20.32 mm respectively. The OPL that would be seen in an OCT image can be seen in Fig. 4.4. This OPL was modelled by tracing rays from a curved surface, sharing the same radius of curvature as the horizontal axis of the second ellipsoidal mirror, to the retina for multiple field angles. The single-pass, in-air OPL difference is shown in the plot, which is equivalent to the distance a retro-reflecting reference arm mirror would need to move to fixate on that surface. The upper and lower curve are separated by 0.5 mm in the model representing the front of the retina and back of the cornea. The green line shows the image range of a typical OCT device of 1 mm in the eye (1.33 mm in air).

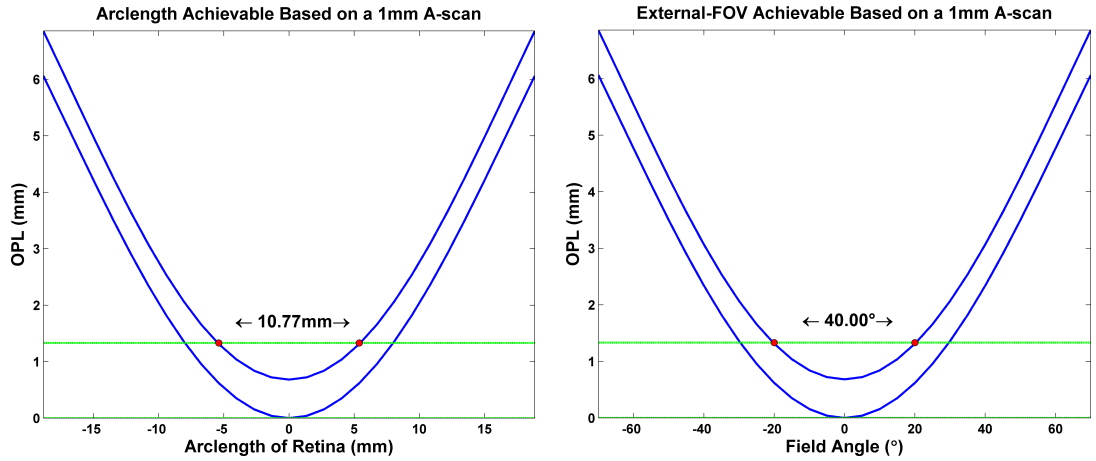


(a) (b)

Fig. 4.4 (a) The arclength that can be imaged by 1 mm scan. External FOV that can be imaged by the 1 mm scan, without showing a mirror artefact.

An obvious solution to the OPL limit is to scan the reference mirror through the OPL of the eye while synchronised to the duration of a single B-scan. A risk of this technique is that if during the detector integration time the reference mirror was moved by half a wavelength or more then the interference signal would be completely washed out. The limit of fringe wash-out can be calculated relatively simply. The displacement of the mirror during an A-scan is,

$$D_A = v_m t_A, \tag{4.2}$$

where $v_m$ is the velocity of the mirror and $t_A$ is the duration of an A-scan. The velocity of the mirror is equal to twice the OPL of the eye (required to image the periphery, then posterior, then periphery of the retina) divided by the duration of a B-scan, $t_B$. To achieve high contrast interference then the distance moved by the mirror must be less than the distance to make the wavelength destructive $\frac{\lambda}{2}$:

$$\lambda_o \geq OPL\frac{4t_A}{t_B} \tag{4.3}$$

As the wavelength is generally relatively constant and the bottleneck is the speed of the line-scan array $t_A$ then,

$$\frac{1}{t_A} = f_A \geq OPL\frac{4}{t_B\lambda_o}. \tag{4.4}$$

For an 830 nm laser, taking an UWF B-scan with a round trip OPL of 12.1 mm with a B-scan duration of a third of a second, then the minimum line-scan detection frequency is 177 kHz. The scan frequency required to achieve an image with only a 10% contrast drop can be calculated by dividing the line-scan frequency by $\frac{\arccos(0.9)}{\pi}$ which is equal to 1.23 MHz. In light of this requirement, the most practical way to image the entire retina is to discretely step the mirror and use image processing to smooth and reconnect the mosaic.

## 4.5 Image Distortion in Wide-Field OCT

The angle of incidence at 70° external field is 32.5°, this angle of incidence will result in two distortions in the image. The first, is that the retinal thickness will appear stretched as the ray passes through the retinal layers at an angle of incidence greater than zero. This distortion is easily modelled in *Zemax* by creating a 500 µm layer across the back of the retina shown in Fig. 4.5 (a) with the OPL plotted in Fig. 4.5 (b). This figure shows that the increase in measured retinal thickness does not exceed 17%. This value is relatively low and can be calibrated to ensure there is no impact on the diagnostic performance of the device

The second distortion is the transverse displacement between the radial coordinate on the retinal surface the back of the choroid, which would appear as a skewing of the image. This distortion has been calculated as the tangent of the angle of incidence from normal to the retina. As can be seen in Fig. 4.5 (b) the transverse displacement introduces a greater error to the image, although it remains to be determined how this will impact the diagnostic performance or the complexity of registration.

The transverse magnification off-axis remains fairly linear as shown in Fig. 4.6 with less than 5% barrel distortion for 50% of the field angle. The distortion in an image increases with the field angle and at 70° the distortion reaches 21%. This distortion would result in the

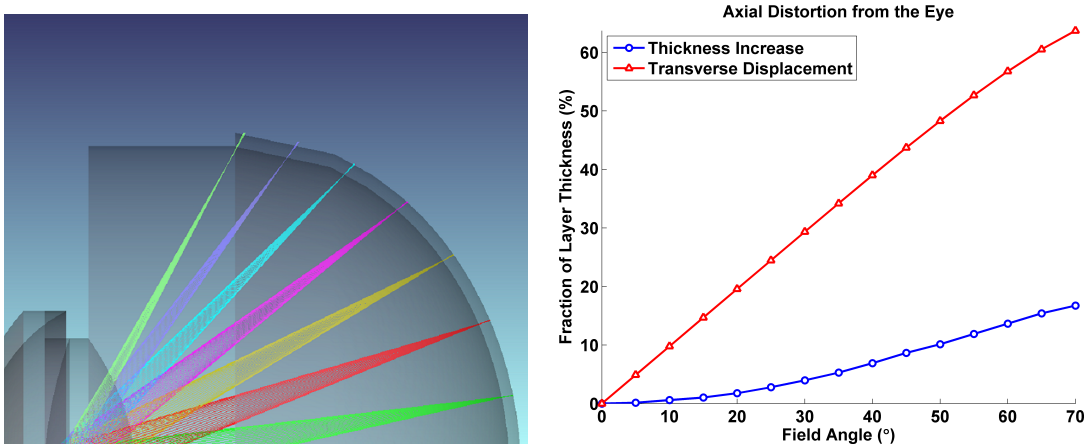


(a) (b)

Fig. 4.5 (a) Model showing the oblique angle passing through the retina. (b) Normalised thickness of that would be measured based on OCT images.

pixel to mm scale off-axis being 21 % less that the on-axis, in addition to any distortions in the scan system.

The outcome of this distortion analysis is that, with calibration, accurate transverse measurement and registration is possible. This calibration needs to include the distortion of the eye as well as that of the system. Unfortunately, these values depend on a fixed schematic eye and the variation in patient eye length will be a significant source of variation in measurements.

## 4.6 The Impact of Axial Dispersion in Wide-Field OCT

As discussed in Section 2.10.3, a numerical dispersion algorithm can be used to compensate for the systematic variations in the chromatic dispersion between scans or as an alternative to mechanical dispersion compensation. Mechanical dispersion compensation is ideal for imaging where there is little change in the OPL between images: however, off-axis imaging has been shown to introduce a substantial change in OPL with field angle. The change in the OPL with field angle has been plotted in Fig. 4.7 for an 830 nm source. The maximum round-trip dispersion that the eye introduces on-axis was found to be 23 μm. The maximum ΔOPL was found to be only 1.3 μm. This shows that although the total dispersion within the eye must be corrected to achieve the commercial axial resolutions of below 10 μm the off-axis dispersion is insufficient to compromise significantly an OCT device with current resolutions. Should ultra-high resolution OCT devices become required for wide-field OCT

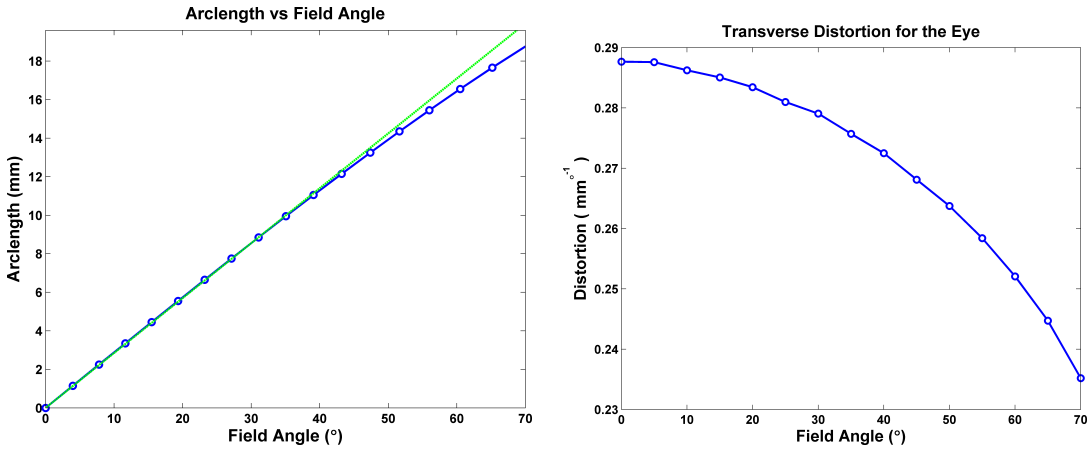


(a) (b)

Fig. 4.6 (a) Shows the arclength from the centre for each field angle, with a line of best fit gradient of 0.285 (b) Shows the distortion in terms of arclength per degree of the Navarro Eye.

then a weighted numerical dispersion algorithm could maintain axial resolution of below 5 μm.

## 4.7 Chapter Conclusion

The four primary challenges to the commercial realisation of wide-field OCT that result from the anatomy of the eye are: a loss in the optical efficiency, variation in birefringence, insufficient imaging range and image distortion. A variation in the axial dispersion was thought to be a concern; however, it is unlikely to cause a significant impact to the variation in the resolution of commercial OCT devices with field angle.

The loss of light through the system will significantly reduce the SNR in images. Modelling shows that vignetting at the iris plays a minor role in optical efficiency variation, however, third-order aberrations reduce coupling into a fibre. This result shows that although focal correction with field angle is key to imaging the retinal periphery, further aberration correction will be required to maintain image quality off-axis. The quantitative impact of this roll-off will require measurement through the use of a phantom.

The birefringence of the eye is non-zero with a variation between patients. The principle source of birefringence is the cornea imparting over $\frac{3}{4}\lambda$ of retardance. This retardance will prevent whole-eye OCT images as local compensation will be required beyond an external field angle of 40°. To confirm this hypothesis navigating a narrow-field OCT device to

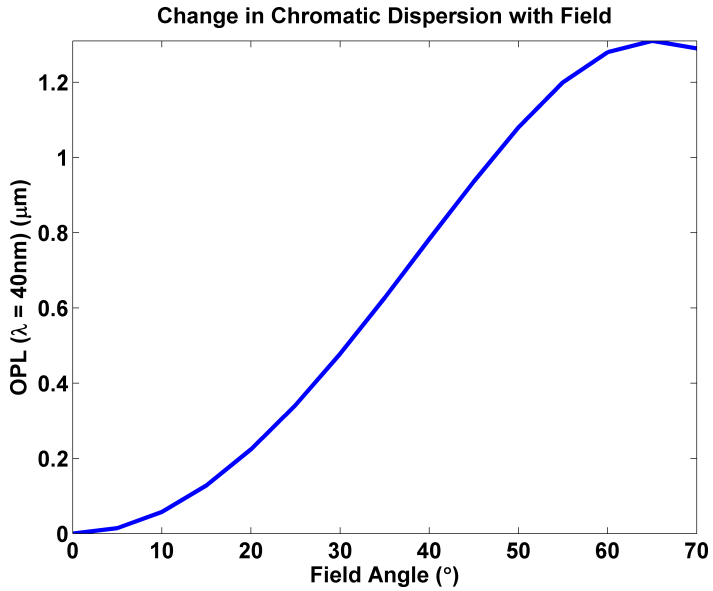


Fig. 4.7 Change in OPL with Field Angle for a 40 nm bandwidth source .

different regions of a patient or phantom eye and monitoring the use of dynamic polarisation control. This capability is only possible if the other challenges of the second demonstrator were over came.

The geometry of the eye means that conventional OCT devices can have a maximum full field angle of 40° before the image is compromised by mirror artefacts. These artefacts are a result of the change in OPL and incidence angle with field angle. Smooth translation of the mirror would result in fringe wash out at the detector and thus a loss in signal unless the A-scan rate was above 1.23 MHz. In addition, the geometry of the eye imposes warping in the layer thickness, transverse position and magnification. A phantom with known feature sizes would be required to calibrate measurement in a wide-field OCT devices and inform the navigation of narrow-field device.

Based on the above results, wide-field OCT with whole eye images or slices is not currently feasible. Should the technical conventional challenges of wide-field imaging be overcome, such as optical efficiency, distortion and data management, then the unique challenges, such as maintaining interference contrast and imaging range, will prove too great barrier for the current state-of-the-art technology. Wide-field OCT will be possible through the use of a well calibrated narrow-field navigated device. For this reason, I have developed a wide-field phantom eye for optical coherence tomography which is presented in Chapter 6.

# Chapter 5

# Performance Assessment in a Wide-field Ophthalmic Device

## Chapter Summary

This chapter highlights the need for performance assessment of ophthalmic devices and outlines associated requirements for this characterisation. The current methodology for device characterisation is separated in two sections; firstly, device validation in Section 5.2 and secondly, device verification in Section 5.3. The methodology behind a new set of metrics for device grading is provided in Section 5.4. These metrics are used as evidence for the development of a wide-field phantom eye, which is reported in Chapter 6 and the application of these metrics is reported in Chapter 7 and Chapter 8.

## 5.1 Methods for Performance Assessment in OCT

The variability in the performance of the *Optos* demonstrators showed that there was a substantial need to compare OCT systems quantitatively. In addition, providing a benchmark to compare the *Optos* demonstrators performance proved challenging as the published commercial performance showed a marked difference between their reported specification and their demonstrated imaging quality. This need for performance assessment of ophthalmic devices motivated the following investigation into the established methods used to assess the performance of a clinical device.

To quantify disease progression in a clinical application requires that three parameters are evaluated about the measurement tool:

1. The systematic error (accuracy) of each measurement, which is required for effective multi-modal and inter-device comparison.

2. The intra-device statistical error (precision/repeatability) in the measurement, which is required for longitudinal tracking of disease progression over time.

3. The sensitivity of the device measurement accuracy to ocular diseases, required for firstly, the classification of disease progression and secondly, the maintenance of imaging performance despite disease pathology.

Device characterisation is typically broken into two phases in the development of a new device: validation and verification.

## 5.2 Validation of OCT devices

Device validation is the process by which the capabilities of a device are confirmed to match the purpose of the device. [139]. Validation assessment of a medical device is crucial for establishment of both high-performance products and the establishment of the gold standard of disease diagnosis [140]. This process is especially important in the development of OCT devices because interferometric imaging is susceptible to subtle fluctuations in imaging, which can be difficult to differentiate from changes in the anatomy. For example, a variance in repeated depth measurements can be introduced *intra*-device from fluctuations in polarisation, focus or a change in the patient position. Variance can be introduce *inter*-device as a result of manufacturers using a different method to calibrate for distortion, anatomical definitions or segmentation methods.

The most common method to validate an OCT device is to compare the images acquired on a device with that of a reference OCT image, such as the b-scan from an *Opko Model E* Fig. 5.1 shown annotated with the key retinal features. Prominent features, such as the visibility of the weak-reflecting retinal layers or the macular shape can provide a simple qualitative assessment of image validation [141]. This method of validation is insufficient to characterise a device for three reasons. Firstly, this method does not quantify the precision or accuracy in measurements and therefore does not assess the principle value of OCT - the ability to quantify pathology. Secondly, retinal morphology can vary considerably in diseased eyes. This variability means that the user has to make assumptions when comparing the image of a diseased eye to an expected image. Thirdly, an image does not account for the experience of the photographer, the motion of the patient or the ease of image interpretation for the grader.

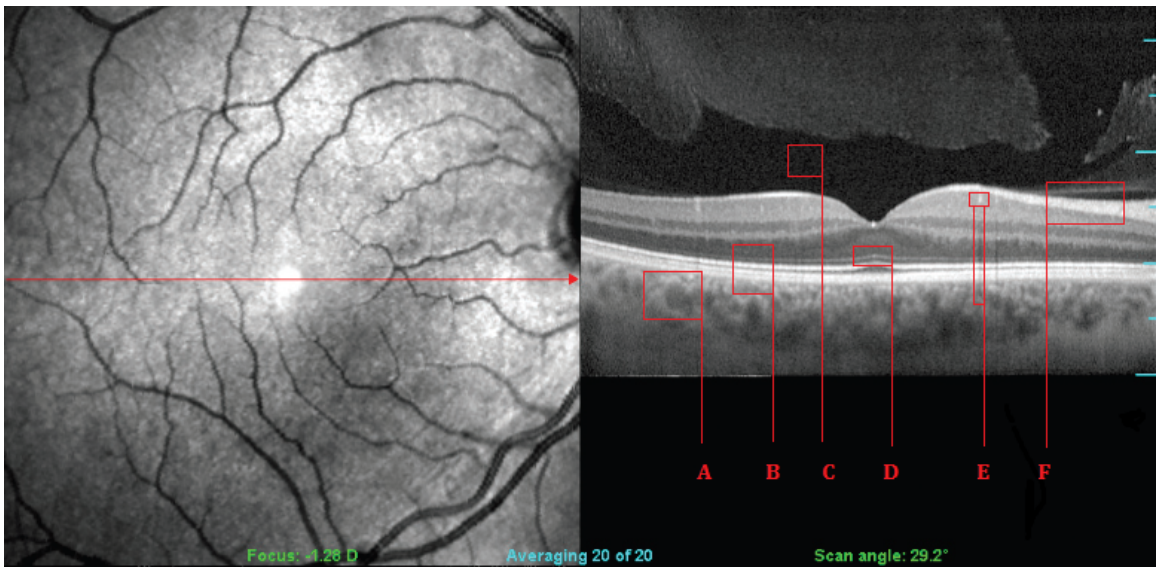


Fig. 5.1 A 20 x time-averaged image from the *Optos OCT/SLO* device of a healthy-fundus [142]. **A**: A cloudy textured choroid demonstrates good sensitivity roll-off and allows the measurement of choroidal thickness where the cloud texture ends [143]. **B**: The ability to distinguish three layers in the RPE indicates good axial resolution as the RPE (the thick posterior layer) is 12 µm. **C**: The vitreous should contain floaters and some noise though this image has extensive time averaging to remove speckle. Absence of these features tends to indicate that averaging is excessive as the ability to see the vitreous is critical in diagnosing disease like vitreomacular traction syndrome **D**: A visible ELM demonstrates the ability to detect the weakest of signals, indicating a good sensitivity, resolution and dynamic range. **E**: Clear vasculature, bright dot with a shadow, indicates a good transverse resolution. **F**: The ability to distinguish key layers such as the RNFL indicates a good SNR and polarisation control.

As mentioned in Section 2.4, thinning of either the macular thickness or RNFL can be linked to many diseases such as type-2 diabetes, glaucoma and neurodegenerative and brain diseases such as multiple sclerosis and Parkinson's disease [144–147]. An image of the RNFL, which has been automatically segmented, has been provided in Fig. 5.2. Recent publications into the validation the OCT devices have focused on quantifying either the inter-device variation or the comparison of the intra-device precision in measurements of health anatomy such as the RNFL. [148–152]. This quantitative method of validating devices is helpful when comparing devices because the variation in device measurement is predominately influenced by the image quality [153]. The limitation of this method is that there is no information provided as to the accuracy of measurements, which would allow for the comparison of measurements from multiple devices from the same or different manufacturers [154], or even results from different types of medical device such as OCT versus *ex vivo* biopsy and surgery [155]. Furthermore, the performance from OCT devices becomes less reproducible in unhealthy eyes, where signal strength and morphology vary substantially, meaning the comparison could be inconsistent [156].

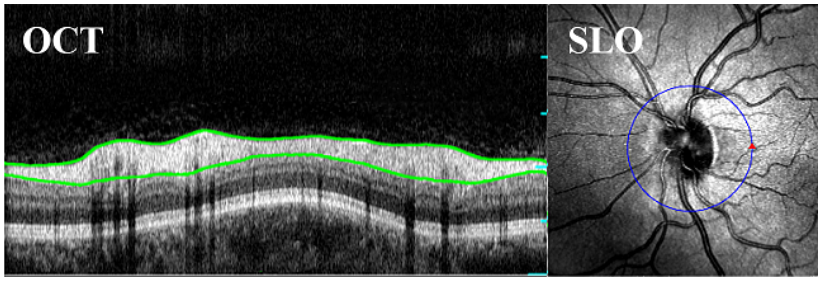


Fig. 5.2 Left: a circular OCT B-Scan of a human retina with the retinal nerve fibre layer (RNFL) segmented in green, acquired on the *Optos OCT/SLO*. On the right is the SLO image corresponding to the B-scan.

Device validation is also commonly performed by analysing the sensitivity and specificity of a device. Sensitivity quantifies the ability to detect the presence of a disease where as specificity quantifies the ability to detect the lack of a disease. The two main benefits of this type of study are firstly, each study is specific to a single disease and therefore the results of the study are linked to the application of the tool. This feature allows the establishment the gold standard for disease diagnosis across all possible methods of detection. Secondly these studies include any pathologically-induced variation in image performance. OCT has been shown to perform well in sensitivity and specificity for morphological diseases such as macular tears, oedema and glaucoma [157]. Unfortunately, ranking commercial systems on disease specificity and sensitivity is challenging as the sample size required to appropriately

study for every disease and device feature is not practical nor do these studies provide any feedback to device designers that could be used to improve the device.

## 5.3 Verification of OCT Devices

Device verification is the process by which the specification of a device are confirmed to match the design of the device [139]. This process allows the assessment of the factors which impact on the performance of the device for both improvement and calibration. In addition, commercial systems require an empirical, easily-measurable and comparable set of performance metrics against which the device can be verified to allow manufacturers to rank their devices amongst competitors. Device ranking would allow users to assess which devices best meets their need, based on evidence rather than on marketing.

Simple metrics such as spatial resolution, frame rate and field of view (FOV) are sufficient for defining system performance if stated together, measured with consistent protocols and linked to clinical outcomes. However, the current specifications provided in commercial literature are in effective as they lack any empirical corroboration or are linked to clinical requirements. For example, axial and transverse resolution, (theoretical description provided in Section 2.9.2) will routinely be specified by manufacturers and researchers as being equal to the theoretical full-width at half-maximum (FWHM) or airy radius. In typical OCT devices, this representation of resolution is not likely to be close to the practical day-to-day value. Firstly, the application of the Eq. 2.8 and 2.9 describing the theoretical airy spot assumes a Gaussian spectral and spatial distribution, which is not necessarily the case, especially with the recent move to multiple-peak sources which have a longer spectral bandwidth. Secondly, this description of resolution does not account for chromatic dispersion in the sample [101, 102]. Thirdly, smaller effects such as polarisation mismatch, chromatic and wave-front aberration in the device optics, mechanical imperfections and approximations in the signal processing and averaging can cause further deterioration from the theoretical limit [103]. As can be seen, simply stating the theoretical resolution is not sufficient for device characterisation.

### 5.3.1 Measuring Spatial Resolution in OCT

The axial-PSF (more precisely the line-spread function) of a device can be verified easily by imaging a reflector that has been positioned in a saline bath at normal incidence to the optical axis. A close approximate would be to image a glass flat in air, and scale for the air-tissue refractive difference and ensuring that the signal does not saturate the detection. The FWHM

of the axial-PSF is a reasonable approximation to the resolving limit of a device as this is the resolving limit stated in the Rayleigh criterion [17] for transverse airy spots. However, this method does not account for the impact of the many sources of noise within OCT imaging. The resolution of the system would therefore be best measured by imaging the minimum spacing for which two objects remain resolvable.

The USAF target is the conventional tool for the measurement of the minimum spacing for which two objects in devices that image the surface of a sample. The use of an USAF target that can be used to measure axial resolution in OCT has still to be developed; however, with appropriate contrast materials this target can be applied to measure the transverse resolution in OCT. A USAF target mounted on a flat surface inside a narrow-field phantom eye has been provided in Fig. 5.3. From this image we can determine that the *Optos OCT/SLO* device has a transverse resolution of between 22.1 μm and 19.7 μm (group number four, element five). The resolution group/element was determined by the smallest element where the bar contrast $(I_{max} - I_{min}/I_{max} + I_{min})$ exceeded the $\sigma$ of the image noise. In the vertical axis, this condition is achieved in Element 5, where as in Element 6 it is not, as can be seen in Fig. 5.4 (a). In the Horizontal axis, Element 4 achieves this condition, shown in Fig. 5.4 (b) where as Element 5 it does not, shown in Fig. 5.4 (c). The theoretical transverse resolution calculated using airy spot size from 2.9 is $\delta x = 5.8\ \mu m$.

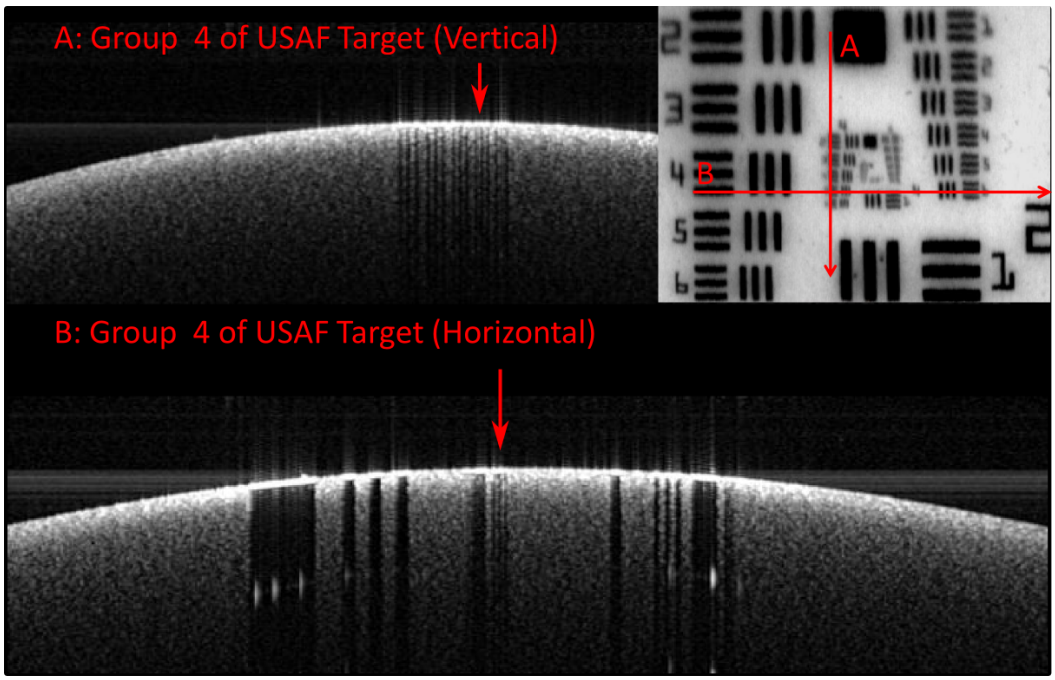


Fig. 5.3 B-Scan of narrow-field phantom eye acquired on the *Optos OCT/SLO*.

The use of this USAF to measure resolution could be improved in three ways. Firstly, using materials with a similar contrast to tissue and vasculature would better account for noise in the image. Secondly, repeating the USAF target across a large field angle would allow the measurement of off-axis resolution. Finally, the phantom eye used here was designed for SLO imaging only and therefore does not match the optical path length, aberrations or geometry within the eye. Modelling the prescription of this phantom indicates that it would produce a smaller spot size then a human eye would.

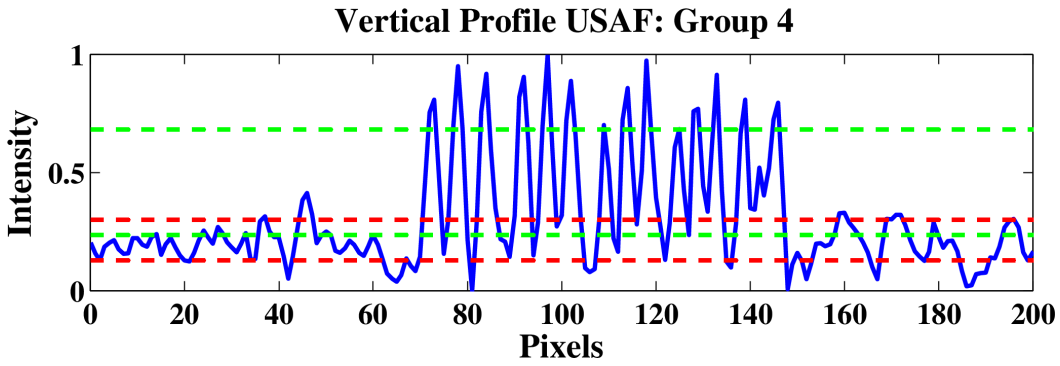


(a) - Element Five Selected in Green

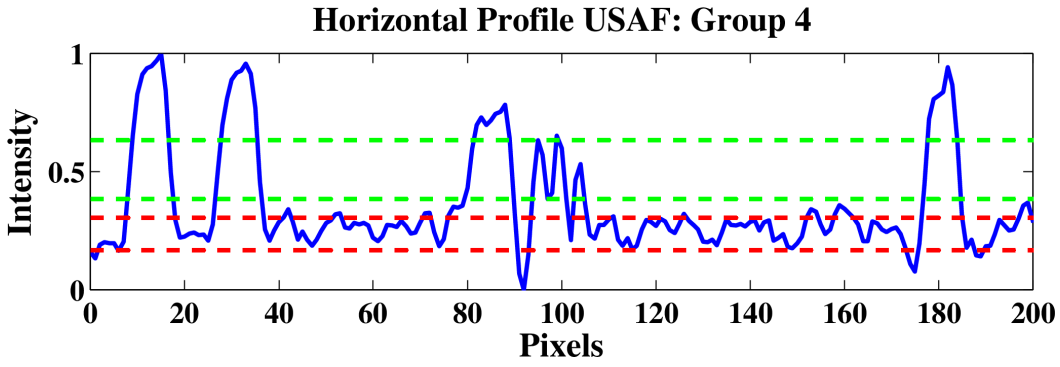


(b) - Element Five Selected

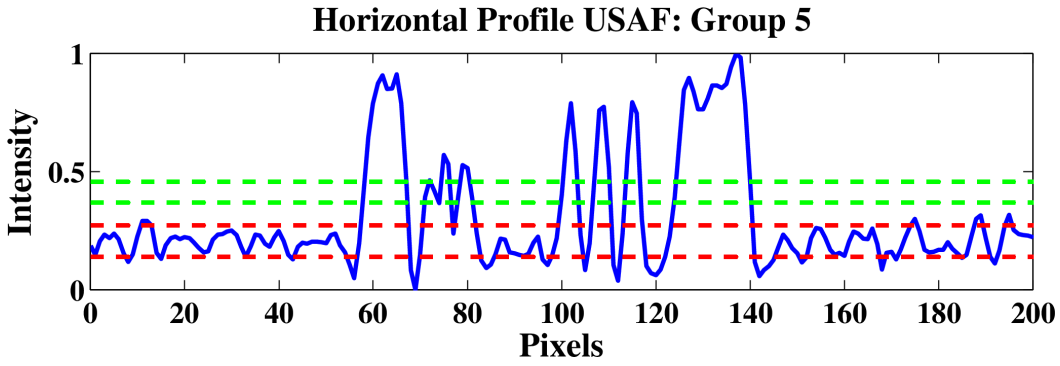


(c) - Element Six Selected in Green

Fig. 5.4 Profile through the B-Scans of the USAF-target shown in Fig. 5.3. Field curvature was removed from the image allowing averaging of 50 pixels along the vertical axis. The green dashed-line highlights the minimum peak-to-tough for the group four features. The contrast for Horizontal E5 = 46%, E6 = 15% and for vertical E5 = 25%, E6 = 9% with a noise level of from the STD pixels out with the groups at 17%

Many groups have recently began to addressing some of the challenges involved in measuring the resolution of commercial system through the use of point-spread function (PSF) targets [158, 159]. These PSF targets can be used to deconvolve PSF and ultimately improve the resolution of the system [160]. This technique can be challenging in practice as the digital resolution of commercial systems typically under-samples the PSF [161]. This problem can be overcome by sampling multiple-scatterers at different lateral positions [162]. In addition layered targeted similar to the USAF target have been developed which show promising results for the measurement of the contrast of different spatial frequencies based on similar patterns to the USAF target [163–165].

### 5.3.2 Measuring Field of View in OCT

The field of view of a device can be represented in a number of ways. The simplest and most common description of FOV is the largest angle accepted by the pupil relative the optical axis [5]. In ophthalmology this angle is measured immediately before refraction by the cornea. In this thesis, this angle is referred to as $\mathbf{FOV}_{\text{ext}}$.The use of $\text{FOV}_{\text{ext}}$ is favoured by optical engineers because it is invariant to the dimensions of the patient's eye, assumes rotational symmetry and complies with optical modelling software. This angle is half the $\text{FOV}_{\text{ext}}$ commonly used in other forms of microscopy to describe the field of the objective lens. This distinction will be made clear by the use of $\pm$ to represent this rotational symmetry.

Although invariance is a favourable characteristic for device characterisation, presenting the FOV from the point of view from the centre of the eye, defined as $\mathbf{FOV}_{\text{int}}$, is more readily relatable to quantifying the pathology imaged. The convention by manufacturers to present $\text{FOV}_{\text{int}}$ as double the angle around the optical axis or full-$\text{FOV}_{\text{int}}$ means we will use the full-$\text{FOV}_{\text{int}}$ when comparing the performance of commercial ophthalmoscopes in Chapter 7 and 8. These descriptions of FOV are shown in Fig. 5.5. The conversion between internal and external angle is given as,

$$FOV_{int} = \overline{m} FOV_{ext} + 2\sin^{-1}\left(\frac{R-x}{R}\sin\left(\frac{\overline{m} FOV_{ext}}{2}\right)\right), \tag{5.1}$$

where $\overline{m}$ is the ocular magnification from the cornea and lens, $R$ is the length of the eye, and $x$ is the distance from the circumference of the retina to the scan point in the iris, as shown in Fig. 5.5. Using the published values of $R$=12 mm, $x = 2R - f$ = 3.68 and the change in ray-angle due to refraction of $\overline{m}$=0.819 [12] then the corresponding values of $\text{FOV}_{\text{ext}}$ and $\text{FOV}_{\text{int}}$ are a close match to those determined from ray tracing as shown in Fig. 5.6.

The convention for measuring the FOV based on angle is best suited to radially symmetric systems. Providing FOV in $\text{mm}^2$ is a more accurate metric for quantifying the FOV in non-

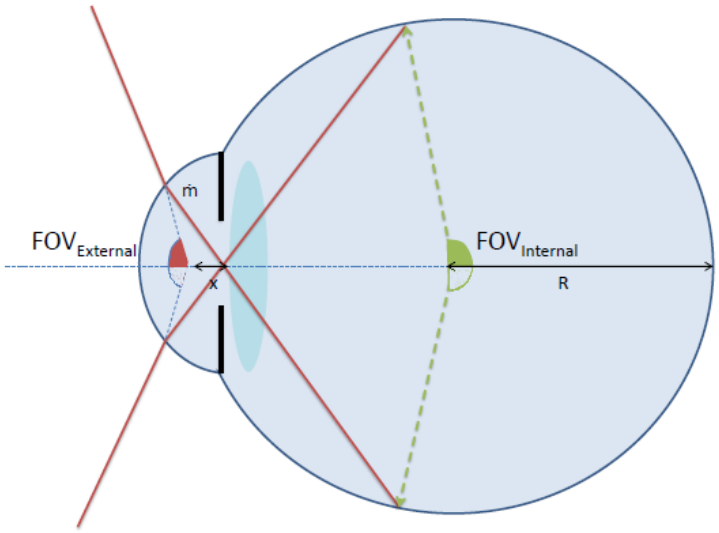


Fig. 5.5 A simple diagram depicting the two different ways to describe (half) FOV, $FOV_{ext}$ and $FOV_{int}$

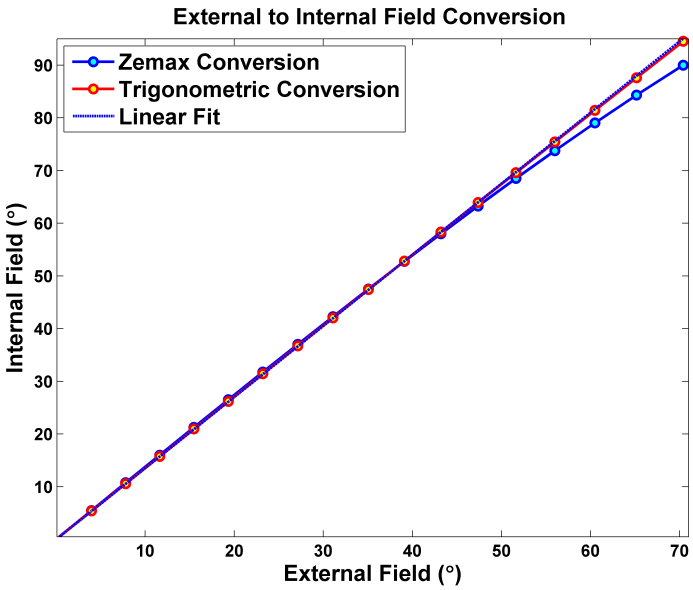


Fig. 5.6 Plot providing a conversion between the FOV notation. An approximate conversion factor of 1.35 can be used to switch between the field definitions for most relevant angles. A factor of two will allow full-field to be converted; although, care must be taken at large field angles to account for the non-linearity correctly

radially symmetric systems, with non-symmetric distortion or non-spherical scan area. The most basic way to perform an area measurement of FOV is to count the number of pixels in an area and apply a known pixel calibration. This method is difficult in wide-field system as it becomes challenging to accurately applying a weight to the pixels that includes distortion. The area viewed by a $\text{FOV}_{int}$ is given by,

$$A = 2\pi R^2 \left(1 - \cos(\frac{FOV_{int}}{2})\right). \tag{5.2}$$

As the retina encompasses a full-$\text{FOV}_{\text{int}}$ equal to 230° or 1300 $\text{mm}^2$, then a C-Scan with an external field of 20° will view only 1.8% of the retina. Measurement of the $\text{FOV}_{\text{ext}}$ for a reflectance image can be achieved by either imaging a known structure such as a ruler or marking fixed angular steps such as on grid paper. Measurement of the $\text{FOV}_{\text{ext}}$ for an OCT device requires imaging an axially-displaced reflector or an object with fixed fluctuations in the scattering density. To empirically measure $\text{FOV}_{\text{int}}$ requires an optical phantom that mimics the optical and geometric properties of the eye. Measurement of FOV must be achieved at integer locations across an image to account for inhomogeneous magnification within the eye. In addition, this provides the calibration required to perform measurement within images.

### 5.3.3 Measuring Acquisition Speed in OCT

The principle metric that OCT manufactures advertise is the A-scan acquisition rate. This parameter indicates; firstly, the number of frames that can be averaged for speckle reduction; secondly the sensitivity of the device to patient motion and finally the field of view addressable during pixel-intensive C-scans. Increasing the A-scan rate is the primary motivation for the development of a swept-source OCT device. However, as there is no proportional increase in the number of photons per second, then increasing this rate must be balanced by a reduced detector noise, a proportionally-increased device scan rate (which introduces mechanical noise) and finally an increase in the complexity of frame averaging. These factors mean that there is a diminishing benefit of increasing the number of averages as eventually speckle is removed without further benefit [114]. For this reason the specified A-scan rate as typically provided from manufacturers is incomplete.

Measurement of A-scan rate must also be confirmed with a measurement of sensitivity because as decreasing the exposure time of a device decreases the number of the photons for each pixel. Measurement of the A-scan speed is provided by recording the exposure duration and dividing that duration by the number of pixels recorded. Sensitivity can be measured by placing a variable ND-filter between a perfect reflector at the output of the system; this

was mentioned previously in Section 2.9.3. The sensitivity of the system is the maximum acceptable loss (dB) where the reflector remains observable. The commonly used qualitative measure of a system's speed is the number of frames per second where the external limiting membrane (ELM) is clearly visible across a fixed FOV within each image. *Although this form of verification is technically a form of device validation.*

## 5.4 Performance Metrics

The use of verified metrics to characterise system performance have two main limitations. Firstly, unless methods used to measure the metrics are agreed upon by the device manufacturers then similar results can have different meaning. This variation leads to the current metrics being insufficient for comparison and leave device manufactures open to increased product scrutiny. However, the use of metrics which are both relevant to clinical outcomes and agreed upon across industry leaders would allow for more effective requirements generation in prototype-device design. The second problem with the use of metrics, in particular the numerical metrics investigated by various groups [166–168], is that they typically have little connection to information relevant to a physician, who does not necessarily have a technical background required to relate the metrics to their application. Therefore, any metrics used in marketing literature will have to be easily convertible to clinically relevant data.

Based on the arguments provided, the primary requirements for our performance metrics used for device comparison are that the metric must be:

1. obtained using reproducible measurements
2. applicable to all ophthalmic OCT devices
3. relatable to clinical outcomes

In addition, metrics ideally will:

1. accommodate root-cause analysis of the limits to performance
2. be compatible to what is currently published by manufacturers
3. be measurable by device users without a fundamental knowledge of the device design, or access to device feature not normally available

Table 5.1 outlines six proposed metrics that all commercial devices should be verified to provide. Also the table includes a brief description of how these metrics should be measured and provides the implication of the metric on image quality. The metrics have been chosen so that the device is tested in its operational state with the aim to probe all the primary sources

of poor image quality. None of the metric measurements produce ideal values but all have ideal equivalents. This choice was made to allow the metrics to show how close the device is running to theoretical limits.

| Metric | Measurement | Effect on Image if Substandard |
|---|---|---|
| Axial Resolution | Target containing sub-resolution layers of different contrast ($\sim$1$\mu$m) of radially-increasing thickness | Retinal layers are unresolvable causing low precision in segmentation |
| Transverse Resolution | Target containing sub-resolution columns such as USAF target or spoke target ($\sim$0.1-10$\mu$m depending on the user) | Vasculature and pathology such as dursen are unresolvable |
| SNR | Intensity ratio of a weak reflector and water at a fixed OPD and include A-scan rate | Weak reflectors and changes in intensity due to pathology are undetectable |
| Range | The change in OPD that reduces the SNR by a factor of two | Imaging will require a sub-mm patient-position tolerance |
| $FOV_i$ | Image a target with a fixed geometry that can be related to retinal arclength | Device will only image a small fraction of the retina |
| $\Delta M_i$ | Comparing $FOV_i$ with expected $FOV_i$ from on-axis pixel scale | Measurements precision will be poor and images will be distorted |

Table 5.1 Proposed performance metrics that all commercial devices should be tested against. $\Delta M_i$ is radial distortion given by Eq. 7.2.

## 5.5 Conclusion

The large variation in the methods used to define and measure the performance of ophthalmic devices has led to a degradation in the value of the currently provided specifications. A new set of metrics have been proposed here which incorporate the considerations outlined in this chapter; in particular, the metrics should be obtained using agreed and reproducible measurements, the metrics should be applicable to all ophthalmic OCT devices and relatable to clinical outcomes.

The development of an ocular phantom specifically for OCT is the most obvious solution to measure the performance metrics in Table 5.1 whilst achieving the requirements listed above. A phantom can be designed to contain all of the required reflectors to measure the performance metrics in a single image and contain enough morphology to be linked to clinical outcomes. The next Chapter will discuss the development of a wide-field phantom eye with the closest published capability of measuring these metrics across the entire retina.

# Chapter 6

# A wide-field phantom eye for OCT and reflectance imaging

## Chapter Summary

This chapter expands upon the publication in the Journal of Modern Optics [2] and the proceeding presented at BiOS [1] which reports both the application and design of a wide-field phantom eye (WPE) for the characterisation of multi-modal, wide-field ophthalmic imaging.

In Section 6.1, we introduce the requirements of a wide-field phantom. In Section 6.2, we present both the optical specifications and design considerations of the WPE and report on the lens verification. In Section 6.3, we outline the design and verification of the housing and interchangeable retinal targets. In Sections 6.4.1, 6.4.2 and 6.4.3, we demonstrate the use of 3D-printing to create three distinct calibration targets for OCT and SLO and discuss the effectiveness and limitations of this technology for retinal layer simulation. In Section 6.4.4, we present the methods used to verify the target properties. Finally in Section 6.5, we use the WPE and targets as a mount for in-vitro imaging of retinal tissue to validate a new ophthalmic biomarker.

## 6.1 Phantom Eyes for OCT

Eye phantoms are commonly used in the development and assessment of new retinal imaging modalities ranging from adaptive optics [169] and oximetry [170] to established reflectance imaging techniques such as traditional fundus photography, scanning laser ophthalmoscopy (SLO) and recently optical coherence tomography (OCT) [90, 171]. We report a wide-field phantom eye (WPE) that provides a closer approximation to the optical properties of a human eye for wide-field imaging than do the planer-geometry phantom eyes that have been previously published for narrow-field ophthalmology [159, 172, 173].

The primary use of OCT, to image the fovea and optic disc, requires that a device can image a relatively modest 30° full-FOV$_{int}$. An example OCT B-scan around the optic disc was shown in Fig. 5.2, including segmentation of the retinal nerve-fibre layer (RNFL). The growing appreciation of peripheral pathologies has fuelled a trend towards increasing the field of view (FOV) of ophthalmic cameras and more recently OCT devices; achieving 200° and 94° respectively [5, 8, 46]. Current wide-field reflectance and fluorescence imaging modalities have been successfully used to monitor disease indicators in the retinal periphery such as non-perfusion and haemorrhaging in diabetic retinopathy and an increase in lipofuscin, which is associated with damage to the retinal-pigment epithelium (RPE) during age-related macular degeneration [174–176]. The higher levels of optical aberrations and geometrical distortions at large field angles caused by both anatomy and instrumentation have been a major obstacle to quantitative assessment of these diseases in the retinal periphery and furthermore the impact of these aberrations on retinal OCT scans has been difficult to quantify and compare between devices.

A standardised method for inter-device comparison, measurement accuracy or measurement precision for OCT instruments has yet to be agreed upon [89, 177, 178]. Subjective comparison and assessment is hampered by the natural variations between eyes from characteristics such as eye length, retinal morphology, severity of pathologies and the ability of a patient to fixate. We describe here the design, manufacture and application of a phantom eye for both OCT and reflectance imaging that mimics a comprehensive range of optical characteristics of the human eye and has potential as a standard-reference phantom for verification and optimisation of instrument design, for calibration and for inter-instrument performance comparison. Although many phantom eyes have been developed that enable the assessment of single metrics across a narrow FOV [171], to our knowledge our WPE is the first optical analogue of the eye to allow assessment of both narrow and wide-field performance.

A modern ophthalmoscope is a complex system involving illumination and imaging optics and in many cases image enhancement, segmentation, montage and projection software, optical filtering and interface tools. Recent publications for narrow-field eyes have prioritised the importance of retinal-target design in the analysis of these capabilities. The optical design of a phantom provides an equally vital role of enabling both calibration and holistic characterisation of system performance. We attempt to achieve the following requirements for the WPE:

- High contrast features across a large field angle of the phantom retina to enable the measurement of imaging contrast and geometric distortion.

- Inclusion of physical features that are sufficiently small to enable determination of axial and transverse point-spread functions (PSF) [159, 179].

- Calibrated axial structures that allow the assessment of image-processing algorithms, such as those used for layer segmentation in OCT such as depicted in Fig. 5.2 [172, 173, 180].

- Mimicking of retinal tissue e.g. for the validation of image-enhancement algorithms. [116, 181].

## 6.2 Optical Design and Fabrication

We report a WPE that mimics the salient optical characteristics of a human eye across $\pm 70^\circ$ external FOV, equivalent to $\pm 90^\circ$ about the centre of the eye. The design of the WPE is based on the schematic-eye model by Navarro *et al.* [21], summarised in Table 2.1, since it closely replicates the optical aberrations and optical path-lengths (OPL) of the human eye [19]. More complete schematic-eye models have been reported, for example containing GRIN lenses (mimicking the graded index property of the human eye) and reflecting variations in eye parameters with demographics [22]; however, their complexity makes manufacture impractical. The optical design was modelled and optimised in *Zemax*. The biological material of the schematic eye was substituted by combinations of the standard glasses, BK7, FSi, CaF2 and PMMA; where the prescription of the glass and refractive surfaces were optimised to achieve a close similarity to the optical point-spread function (PSF), aberrations, OPL and image distortion to the schematic eye.

Sufficient wide-field performance was achieved with a two-lens system consisting of a fused-silica cornea and $CaF_2$ crystalline lens. The WPE is water-filled to provide a close match to the chromatic dispersion of the ocular media of the human eye. The low-refractive index of the lens materials provides a lower deviation of the OPL and distortion than other lens combinations. The use of $CaF_2$ also for cornea would offer potentially superior OPL matching to the schematic eye; however, the poorer surface quality that is machinable for $CaF_2$ could cause excessive scattering of light at the air/glass interface. The optical performance has been optimised for wavelengths 532 nm and 830 nm to match the majority of illumination sources used in reflectance and OCT imaging. Finally, the curvature of the first lens was fixed to that of the schematic eye to maintain both a realistic corneal reflex and assessment of the effectiveness of reflex blocking mechanisms in devices. The prescription for the wide-field phantom is summarised in Table 6.1.

The WPE was modelled for a 2 mm entrance pupil at field angles 0-70° relative to the optical axis. This pupil is sufficient for most wide-field ophthalmic cameras, since for larger pupils the aberrations of eye become excessive and severely degrade image quality [126]. This value can be compared with the beam width of only 0.32 mm for the *Optos* systems with the COE architecture, far below narrow-field fundus cameras. This design choice reduces both the potential performance and the sensitivity of the device to defocus.

Table 6.1 Optical prescription for wide-field phantom eye.

| Surface | Radius (mm) | Thickness (mm) | Ref. Index | Conic |
|---|---|---|---|---|
| Corneal Lens | 7.72 | 0.55 | 1.46 | -0.26 |
| Aqueous | 6.5 | 3.05 | 1.33 | 0 |
| Crystalline Lens | 11.22 | 3.93 | 1.44 | 0 |
| Vitreous | -5.9 | 16.32 | 1.33 | -0.55 |
| Retina | -12 | - | - | 0 |

The spot diagrams, showing the location and spread of rays along the image plane for the WPE model and Navarro schematic model are shown in Fig. 6.1, with the tangential and sagittal RMS spot sizes in Fig. 6.2 and the distortion of chief-ray intersection with the retina and deviation in OPL in Fig. 6.3. The spot size at $\lambda = 830$ nm is closer to the Navarro eye at 530 nm than 830 nm, indicating that the WPE has a lower longitudinal chromatic aberration than the Navarro eye. This deviation is a constraint of using these glasses in the lenses as they have a lower chromatic aberration than tissue.

The RMS spot size and spot shape at $\lambda = 532$ nm displays a sufficient similarity to that of the schematic eye for all field angles, as shown in both Fig. 6.2 (a) and (b). For field angles larger than 40° the tangential spot radius shown in Fig. 6.2 (b) increasingly exceeds that of the schematic eye. This reduction in performance is dominated by defocus, which can be compensated in an OCT device incorporating automated focal correction. The maximum deviation in distortion between the WPE and Navarro eye, represented here as the arc-length difference in the location of the chief-ray intersection with the retina, is 0.47 mm at 830 nm as shown in Fig. 6.2 (c). This deviation would result in a relatively minor 2.5% reduction in FOV at 70°. The maximum change in OPL, shown in Fig. 6.3 (d) for 830 nm is 64 μm. This shift in OPL in a 2 mm A-scan constitutes a 3.2% deviation in the location of the reference arm (axial position); less than an order-of-magnitude lower than the standard deviation in axial eye-length amongst people and hence will not significantly impact automated algorithms commonly used for segmentation, dispersion correction or retinal-flattening [182].

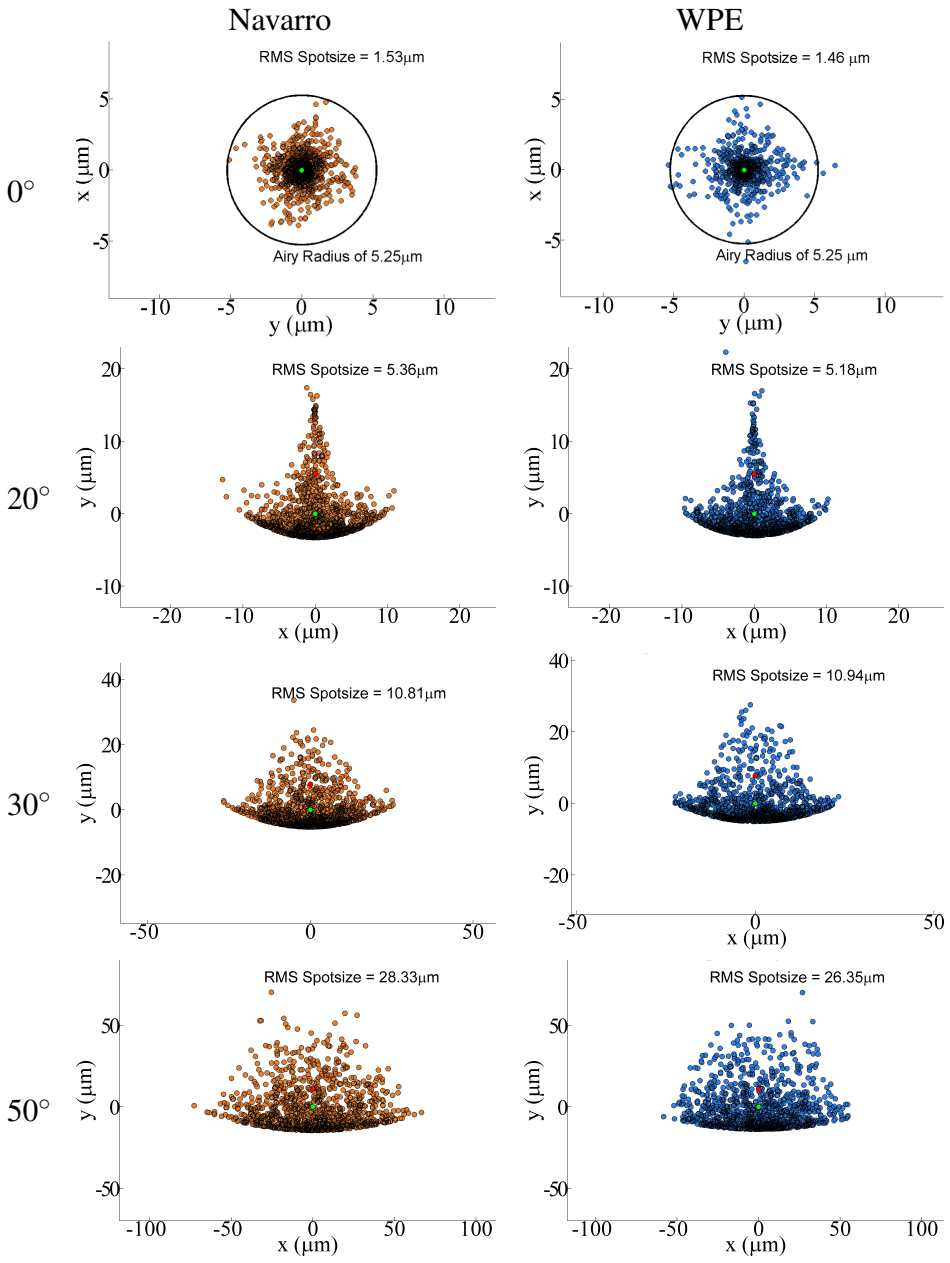


Fig. 6.1 The spot diagrams from the ray trace of both the Navarro Eye (Top) and WPE (Bottom), plotted on a plane perpendicular to the centroid for each field. Comparison of the figures shows that for off-axis spots, the shape and RMS width for the Navarro eye is replicated in the WPE. The dominant aberration at 50° is astigmatism although defocus begins to degrade the WPE spot size for larger field angles.

Fig. 6.2 The optical performance of the WPE (circle) and Navarro Eye (triangle). **(a)** The sagittal RMS-radius for eight entry fields for wavelengths 532 nm (green) and 830 nm (red). **(b)** The tangential RMS-radius.

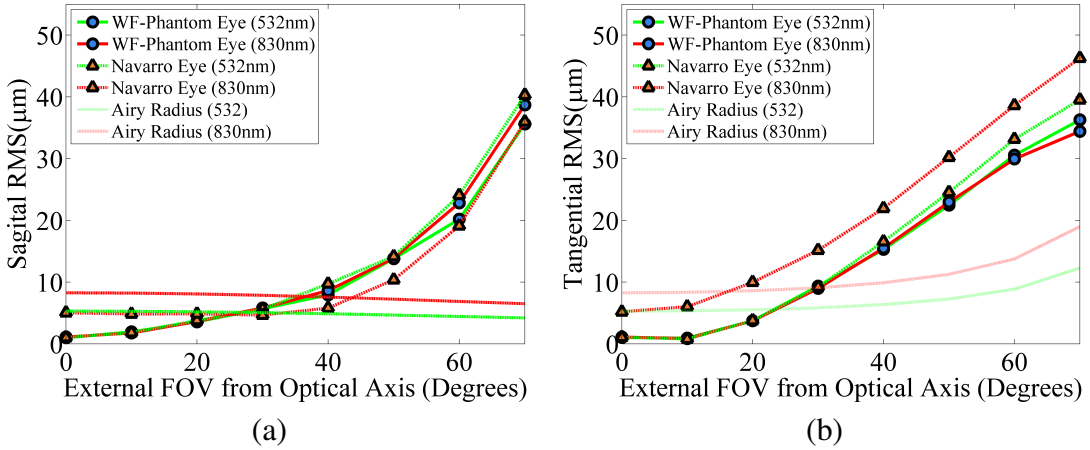


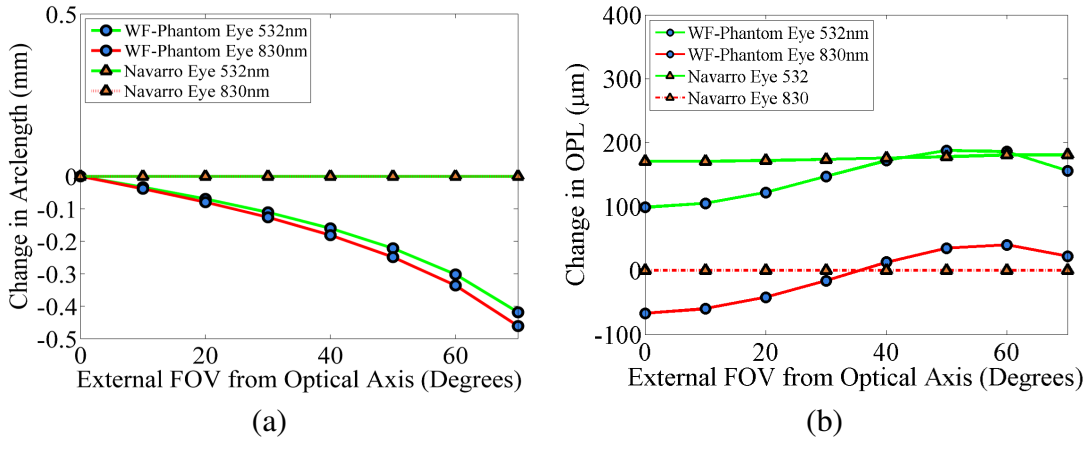


Fig. 6.3 The geometric performance of the WPE (circle) and Navarro Eye (triangle). **(a)** The 2D distortion of the WPE relative to the Navarro Eye. **(b)** The difference in the OPL a ray must traverse from the cornea to the retina.

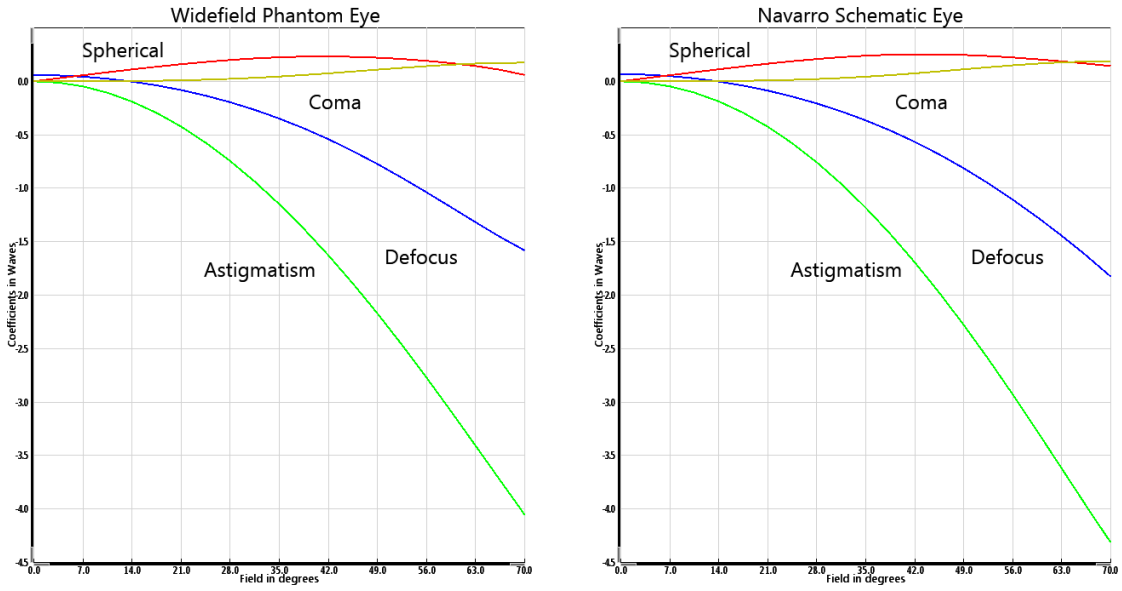


(a) (b)

Fig. 6.4 The primary zernike fringe coefficients for WPE and Navarro Eye.

### 6.2.1 Tolerance and Verification of the Lens Curvatures

The accuracy of the WPE is limited by the manufacturing precision of the components within the phantom. The lenses manufacture *Spanoptic* stated a tolerance of $\pm$ 0.01 mm for each radius of curvature, $\pm$ 0.2 mm for each lens thickness and $\pm$ 0.1 mm for the housing dimensions. The thickness tolerance allows a further angular freedom $\pm$ 0.56° on the corneal lens and $\pm$ 0.17° on the crystalline lens. The estimated performance range that resulted from this manufacturing precision was assessed in *Zemax* using Monte-Carlo Analysis. Modelling indicated that 98% of manufactured eyes would maintain diffraction-limited on-axis performance and 98% of the phantoms would have an RMS spot-radius at 30° off axis that is less than 12.1 µm - an increase from the nominal value of 8.6 µm. Assuming the lenses are manufactured to within their tolerance then this repeatability is sufficient.

Custom lens fabrication has become common within optical designs due to both the affordability of diamond turning fabrication and the precision in design afforded by ray-tracing software like *Zemax*. This flexibility requires the individual inspection of the lenses; not for concern over the precision of the fabrication but to mitigate concern over the possible human error. This quality assurance is typically performed by the manufacturer at a small extra expense to the customer. In the case of the WPE lenses this lens characterisation was ordered but not provided. The retrospective fulfilment of this service required damaging

of one of the lens pairs which at the time was not affordable. It was proposed that the lens characterisation would be fulfilled internally until a repeat order was required.

Exploratory measurements of the lens diameters and back focal-length for the lens pair ($f = 9.5$ mm) with a vernier scale showed that the manufacture conformed to the $\pm$ 0.1 mm tolerance specified in the design. This low level of investigation was not sufficient to characterise either the off-axis lens properties or provide the level of precision required to use an optical phantom to characterise a device. To increase the precision and FOV of the verification, multiple experiments were attempted including recording the transmitted wave-front through the lens pair using a Shack-Hartman wave-front sensor. A Shack-Hartman wave-front sensor measures an array of local wave-fronts tilts that are combined to provide the wave-front description of the beam in terms of its Zernike coefficient. Unfortunately, the large divergence of the lens pair required a precision in placement of the laser, lens and sensor that was impractical with the available equipment.

OCT can be used to measure the curvature of the cornea and crystalline lens of the eye much the same way an optical profiler characterises a reflective surface. This measurement was used to improve the verification of the phantom lens. This experiment first required that both the transverse and axial pixel scaling of the *Optos OCT/SLO* used were calibrated. The transverse pixel scaling was measured as 86 pixels for 1 mm $\pm$ 12µm by imaging a steel-rule in air. This measurement required that the lens surfaces were imaged both in air and at the same axial position as the calibration or else introduce a difference in field curvature. The axial pixel scale was measured as 59 pixels for 1 mm $\pm$ 17µm by imaging a flat on a high-precision translation stage and recording the number of pixels across a known translation. The errors given are the scaled digital resolution of the device. The true error of this experiment is likely to be higher as the lenses lack fiducial markers that can be used to check the positional accuracy of the lenses. The field curvature within the image was mitigated by calibration using a reference flat. A flowchart depicting the analysis protocol has been provided in Fig 6.5 with the *Matlab* script for the extracting the lens characterisation from the image provided in Appendix B.2. The lenses were positioned by both maximising the specular reflection of the lenses and by maintaining transverse symmetry within the image. After positioning the specular reflection on-axis which was minimised by obscuration of the central point.

The results of the OCT measurement of lens curvature has been provided in Table 6.2 with the plots from the analysis included in Appendix A.4. The lens verification showed positive results for the lens characterisation with the difference between the measured and specified value being within the measurement precision of the procedure. The systematic error was calculated as the standard deviation of the possible results given by the measurement precision

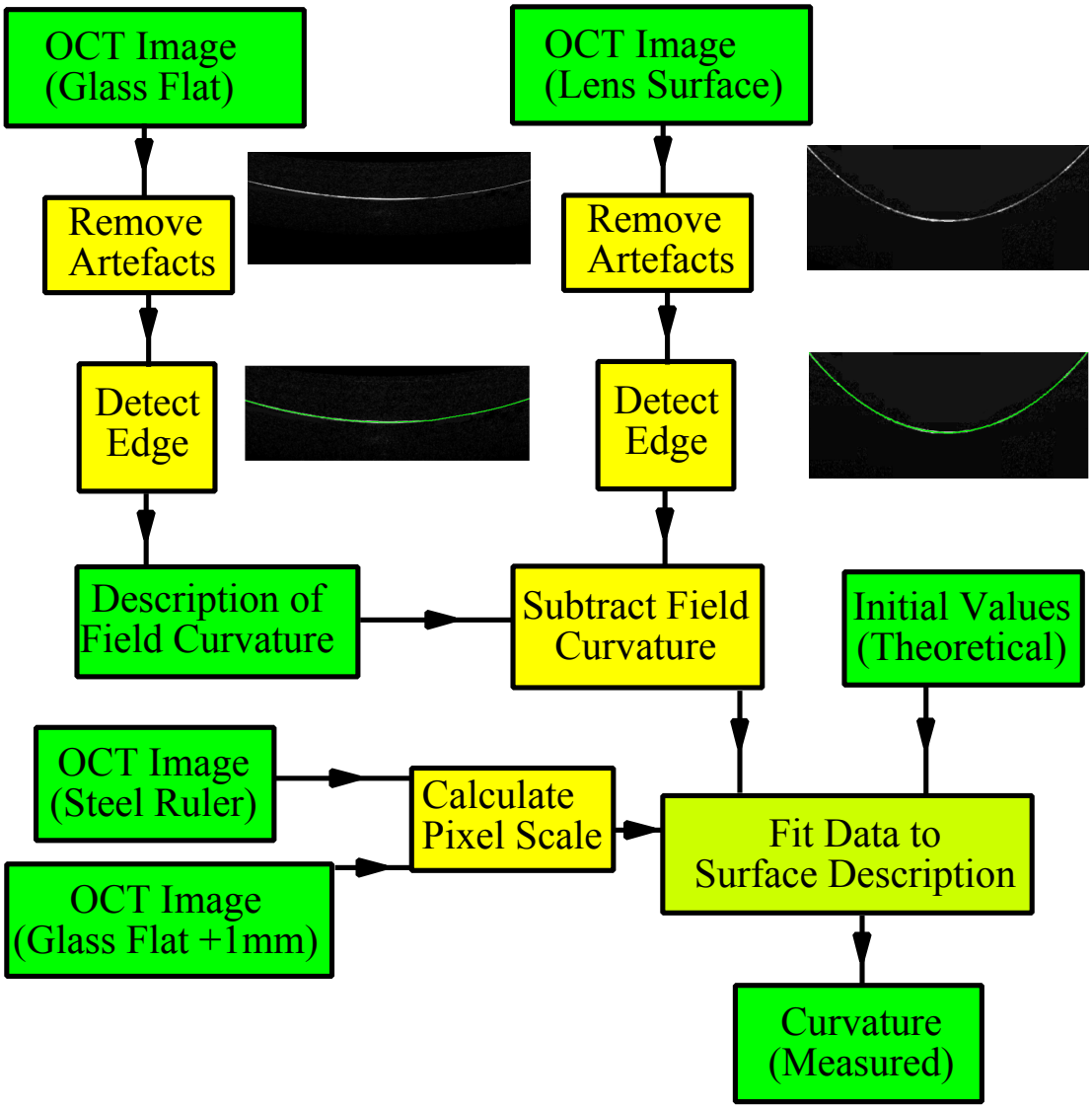


Fig. 6.5 Flowchart for the lens verification procedure. Post calibration of the the pixel scale, segmentation of the lens edge is used to fit the conic equation.

in axial and transverse pixel scaling. The segmented diameter was always substantially below the full diameter of the lens surface. This feature resulted from insufficient FOV of the device, obscuration by the iris (for lens front surface), signal roll-off and on-axis saturation. The reduced surface diameter measured meant the conic values were difficult to calculate for the automated procedure and therefore were fixed in to the calculation.

| Surface | Measured Radius (mm) | Δ (mm) | Segmented Diameter |
|---|---|---|---|
| Cornea Front | 7.71 | -0.01 | 67% |
| Cornea Back | 6.47 | -0.03 | 43% |
| Lens Front | 11.25 | 0.05 | 41% |
| Lens Back | -5.93 | -0.03 | 77% |

Table 6.2 The measured optical prescription for the wide-field phantom eye, the conic value have not been included. The statistical error is ± 0.09 (mm); with the systematic error is likely higher. The segmented diameter denotes the width of the lens observed in the image.

The measured curvature is sufficient to corroborate that the lenses have been manufactured to the specified fabrication tolerance. This verification method remains inferior to the profilometer characterisation normally provided by lens manufacturers; however, greater precision in the positioning of the lens and the development of a custom OCT device for lens verification would improve accuracy of this method. In addition to lens verification, this curvature measurement could also be used to measure the retinal eccentricity, which is an important parameter for the accuracy of peripheral measurement within the eye.

## 6.3 Mechanical Design and Fabrication

The critical dimensions for the phantom housing are shown in Fig. 6.6. The lenses are mounted in a water-filled, anodised-aluminium housing that has been machined to a 100 μm precision.

The WPE was designed to allow simple exchange of targets. Opening and re-assembly of the WPE is a source of optical variation within the phantom. The distances between the cornea, lens and retina were altered in *Zemax* by 0.1 mm to see how they impacted the magnification of the WPE. The chief-ray of the beam with a 70° external field angle intersects the retina at an arc-length of 37.1 mm from the optical axis or 37.5 mm for Navarro Eye. Moving each of the optical elements by 0.1 mm resulted in a maximum shift in the location of this intersection by 0.097 mm. For a 180° image this would be constitute as an added distortion of -0.05%. The most likely scenario is that the plate mounting the corneal

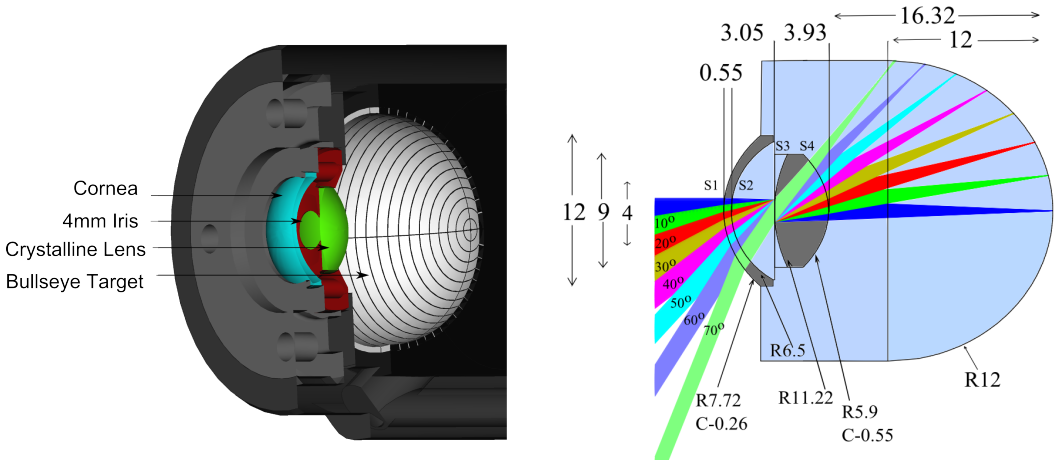


(a) (b)

Fig. 6.6 CAD drawings of all the components that comprise the phantom. **(a)** A cross section of WPE housing containing a Bullseye Target. **(b)** A 2D-ray trace of the WPE. Each beam corresponds to a 10° field angle. The surface apertures that must be maintained to ensure that there is no vignetting are (mm left to right) S1: 9.2 S2: 8 S3: 2 S4: 8

lens introduces a +0.1 mm if the mount is not screwed in all the way. It is unlikely that this variability will have a significant impact on the efficacy of the WPE.

## 6.4 Targets for OCT, Reflectance and Florescence Imaging

Recent advances in additive manufacturing, often referred to as 3D-printing, have made it possible to create arbitrary structures consisting of multiple materials with a tolerance of under 10 µm. Conventional techniques such as laser ablation, guided deposition are ideal for planar surfaces but their small depth-of-focus make their use cost prohibitive on large topographies. In addition, fabrication techniques developed for the semiconductor industry such as spin coating, used successfully across a narrow FOV by Baxi et al. [173], do not provide the dimensional control for small transverse features.

The targets tested in the WPE were fabricated using the state-of-the-art *Objet Eden 350V* 3D printer which has 30 µm transverse resolution, 16 µm axial resolution in 3D-printing and the ability to deposit multiple materials within a structure [183]. This 3D printing technique uses photo-polymerisation with sequential row deposition of multiple materials followed by UV curing to build each layer. The three target designs used to assess the suitability of 3D-printing as a method for manufacturing OCT and reflectance-imaging targets are shown in Figure 6.7.

Axial variation in the scattering coefficient in the retinal phantom was achieved using the materials *Verowhite* and *Fullcure720*. *Verowhite* contains approximately 0.8% titanium dioxide commonly used as a scatterer in tissue simulation [184], and *Fullcure720* is a transparent plastic with similar optical properties to PMMA. A transverse variation in reflectance was attained by interleaving *Verowhite* and *Veroblack*. The material *Veroblack* contains carbon black to increase the absorption of the material. Figure 6.7 shows two target designs used to assess the suitability of 3D-printing as a method for manufacturing OCT and reflectance imaging targets.

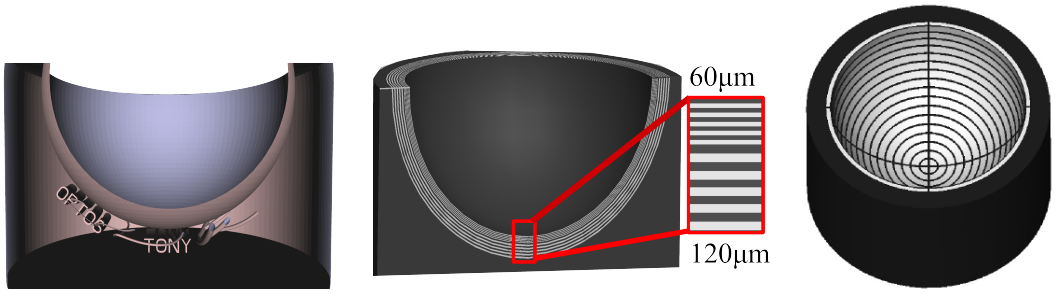


(a) EF-Target (b) AL-Target (c) BE-Target

Fig. 6.7 Left: Cross-sectional view of the target containing embedded features (EF-Target). Centre: Cross-sectional view the target containing axial layers (AL-Target). Right: External view of the target with a bullseye pattern at the surface (BE-Target).

### 6.4.1 Embedded-Feature Target

The Embedded-Feature Target (EF-Target) was designed to demonstrate if 3D-printing could be used to fabricate anatomically representative targets for both reflectance imaging and OCT. The target was fabricated using two materials which allowed for contrasting scattering properties within the target: the clear plastic *Fullcure720* and the highly scattering plastic *Verowhite*. The EF-Target includes structures such as imitation-vessels and alphabetic letters to aid subjective assessment of image quality and verify the precision and flexibility of the 3D-printing fabrication.

The images provided within Fig. 6.8 show no observable scattering in the *Fullcure720*, where as the *Verowhite* provides a strong non-saturating signal. The letters are formed with inhomogeneous axial and transverse precision which results in rough edges of the feature. The flat streaks run perpendicular to the ink-jet deposition direction. The streak thickness conforms to the axial resolution of 16 µm and the horizontal width approximately of 100 µm, which is three times larger than the precision specified by the manufacturer along the transverse axis.

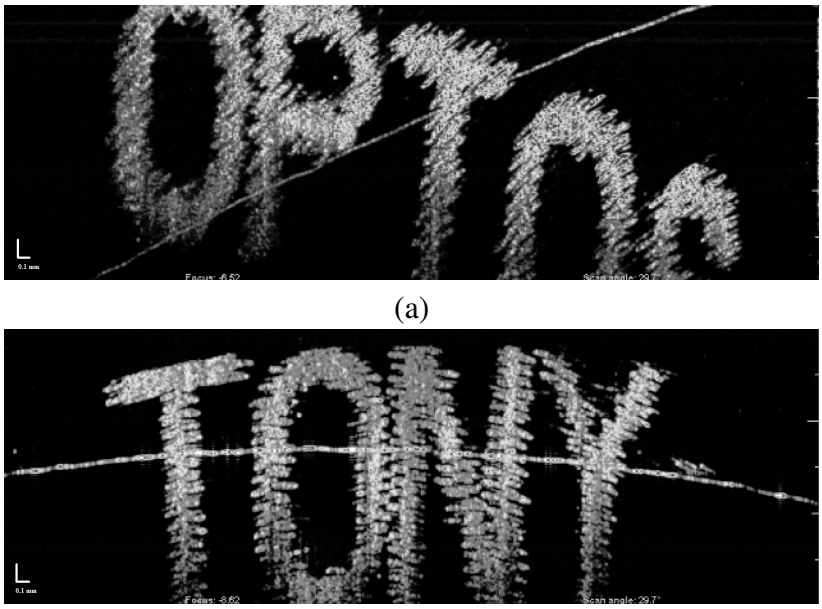

(a)

(b)

Fig. 6.8 OCT Images of the Embedded-Feature Target, the lettering thickness is 0.2 mm and 1.2 mm high. (a) Off-axis image showing the lettering Optos. The intersecting line is the mirror artefact from the vitreoretinal interface. (b) On-axis image showing the lettering Tony.

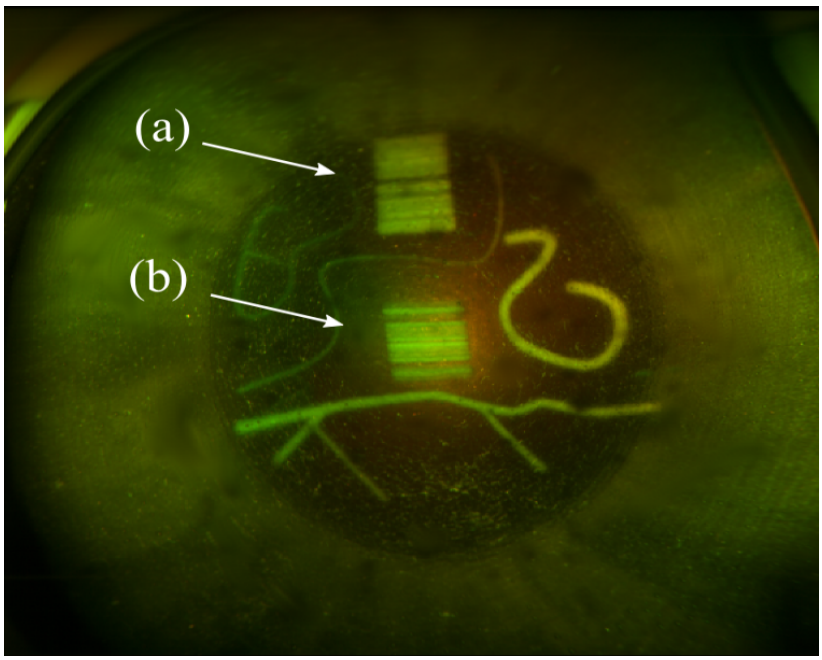


Fig. 6.9 SLO **opto**map showing the embedded features. (a) and (b) correspond to Fig. 6.8 (a) and (b)

### 6.4.2 Axial-Layer Target

The Axial-Layer Target (AL-Target) was designed to investigate if 3D-printing could be used to fabricate anatomical layers that allow the user to assess the accuracy and precision of OCT device thickness measurement. The multiple configurations of the AL-Target were tested with the 60/120 μm AL-Target investigated primarily. This target incorporates five alternating thin layers of the highly-scattering *Fullcure720* and *Verowhite* at 60 μm thickness and five deeper alternating layers of 120 μm thickness extending across the hemisphere of the target. These thicknesses were found to be the lowest multiple of the 3D-printing axial resolution for which physical merging of layers did not occur at the off-axis locations. The relatively large 120 μm thickness is nevertheless within the normal range of thicknesses for the RNFL [178] and so provides a pertinent scale-size for assessment of OCT measurement performance.

The OCT images of the AL-Target shown in Fig. 6.10 exhibit high-contrast layers. On axis, all layers from 30 μm and 120 μm are well defined and resolved; however, with increasing field angle, the images of the 30 μm and 60μm layers develop a more irregular surface and begin to merge as can be seen in Fig. 6.11 (b-e). Furthermore, there is substantial intensity streaking in the images. Both of these artefacts are attributed to the irregular surface of the target, which results from the limited transverse resolution of the 3D-printing process. These artefacts are demonstrated to be associated with the target rather than OCT device, since artefact-free images were acquired off-axis for a target composed of continuous, stacked layers of clear and matt *Scotch* tape (polypropylene and cellulose adhered with acrylic) that were attached to a cylindrical 3D-printed mount, shown in Fig. 6.11 (f).

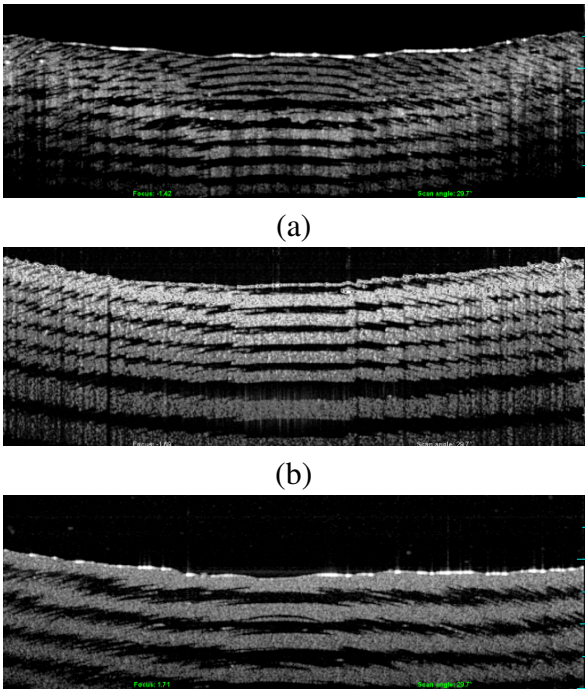

(a) (b) (c)

Fig. 6.10 On-axis images of the Axial-Layers Target. (a) 30/60 μm AL-Target (b) 60/120 μm AL-Target (c)100 μm AL-Target

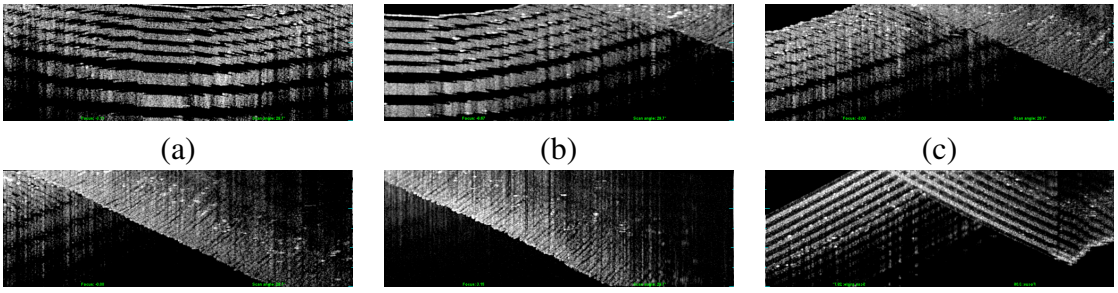

(a) (b) (c)

(d) (e) (f)

Fig. 6.11 B-scans of the AL-Target at five external field angles. The off-axis locations were produced by rotating the phantom on angular translation stage. As the angle of the WPE increases, a mirror artefact of the merged 60 μm layers as a result of the retinal curvature begins to dominate. **(a)** On-axis image; all layers are distinguishable. **(b)** 10° **(c)** 20° **(d)** 30° **(e)** 40° off-axis roughly 10 rings in Fig. 5 **(b)**, only the 120 μm layers are visible **(f)** 40° off-axis cylindrical *scotch*-tape target.

### 6.4.3 Bullseye Target

The Bullseye Target (BE-Target) was designed to provide characterisation of both the distortions and maximum FOV of wide-field ophthalmoscopes. The design incorporates concentric rings of the high-scattering and high-absorption materials *Verowhite* and *Veroblack* with an alternating width of 1 mm and 0.1 mm, respectively, intersected with a highly-scattering cross hair. An example of how the BE-target can be used for distortion analysis has been provided in Fig. 6.12. Analysis of the two images shows that Fig. 6.12 (a) has very little distortion along the horizontal and vertical axis. This property can be observed by the lack of change in the ring spacing with field angle; however, distortion is observed in the cross-section angles and spherical symmetry. The rings in Fig. 6.12 (b) appear to be the least distorted of the two images as it has been displayed a stereographic projection which maintains angle; however, this property is accommodated by increasing the number of pixels between rings with field angle - in effect, controlled distortion. Detailed qualification of the distortion in different ophthalmoscopes is provided in the next chapter, with *Optos* systems investigated in Section . The materials *fullcure720* and *verowhite* can be used to create an OCT configuration of the BE-Target. This configuration has been used in subsequent OCT images of the BE-Target.

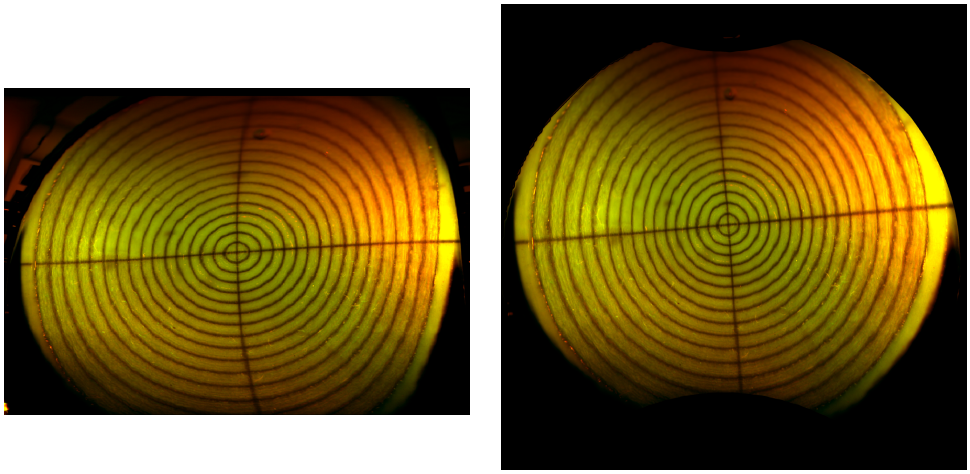

(a) (b)

Fig. 6.12 Initial validation images from the Optos projection software. (a) Unprojected **opto**map from an Optos 200Tx (b) Same **opto**map after stereographic projection. The inhomogeneous colouring is caused by chromatic aberrations altering the transmission through the *confocal* pinhole in the system resulting in a change in intensity across the FOV.

### 6.4.4 Target Assessment

#### Verification of the Target Scattering Intensity

The scattering profiles of *fullcure720* and *verowhite* were measured by imaging both the AL-Target and a human eye in the *Optos OCT SLO* device without image enhancements such as averaging or gamma correction. Plots displaying the raw intensity and the log-normal histogram are shown in Fig. 6.13. The brightest parts of the retina, the RPE and RNFL, reflect with approximately double the intensity of the scattering layers in WPE. This is a small subjective difference since OCT images are displayed on a logarithmic scale. The histogram in Fig. 6.13 (b) further shows the similarity of the intensities with a difference in mean pixel intensity of 1%. The slight increase in near-saturation pixels in the WPE result from the higher refractive index contrast between the target and the water.

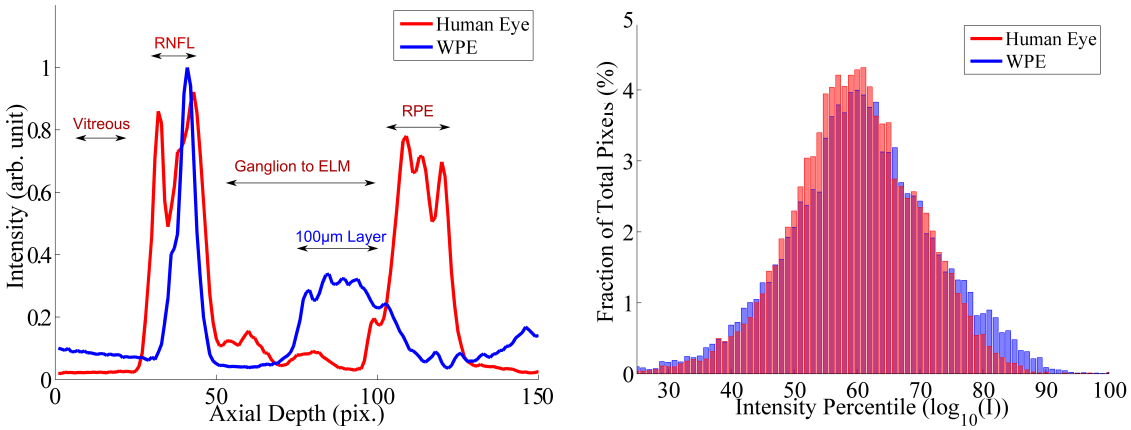


Fig. 6.13 **(a)** The mean intensity across a row of a 200 pixel B-Scan of both a human retina and a revision of target A containing all 100 µm layers. **(b)** Log-normal histogram of the intensity in (a). This plot shows that while the human eye and WPE appear very similar in overall intensity in a B-scan, the WPE has an increased number of near saturated pixels due to the increase in refractive index difference at the vitreoretinal interface; however, the strong overlap in the majority of pixels shows that WPE is a good representation of the retina across the B-scan.

#### Axial Precision of the 3D-Printed Targets

The verification of the layer thickness of the AL-Target was performed initially by imaging the cleaved target using a microscope. The low confocality of this method resulted in images with low contrast which prevented reliable automated segmentation of both the thick and thin

layers within the target as can be see in Fig. 6.14 for repeated measurements. This method found that the thickness of the thick layers was 121.0 ± 8.8 µm which concurs with the specified thickness, where the errors are given as the standard deviation of the measurements.

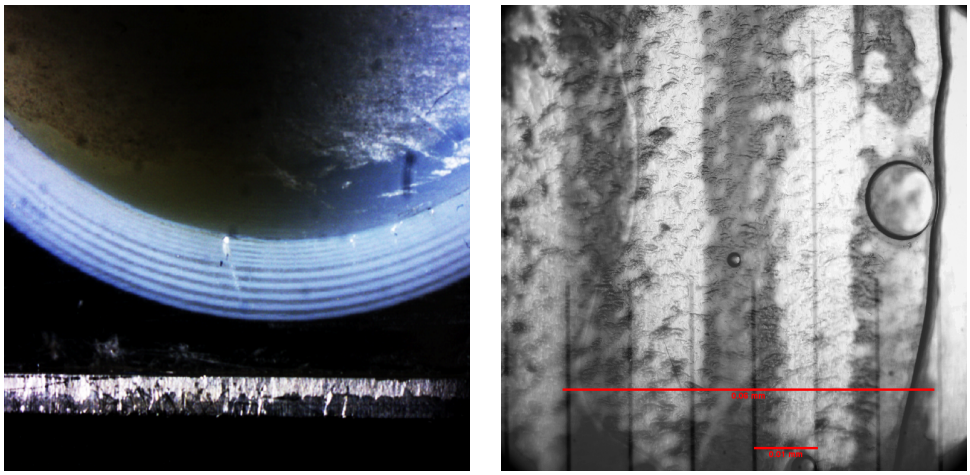

Fig. 6.14 Microscope images of the AL-Target cleaved through the centre. (a) Common bench-top microscope showing both the AL-Target and a 0.1 mm reference shim (b) Contrast enhanced image from the Nikon Eclipse Ti with digital resolution of 7.2µm. The low contrast of this image meant that locating the layers without post-processing was impractical for repeated measurement. The cleaved target was immersed in water to improve transmission to the clear plastic layers.

The layer thicknesses in AL-Target were verified using a research OCT system, which was calibrated with a sub-micron precision translation stage. From these images, the mean thickness of the layers was measured as 59.9 ± 2.8 µm for each of the five thin layers and 121.3 ± 3.2 µm for each of the five thick layers. An example measurement from the thin and thick layers has been given in Fig 6.15. These measurements were performed only across a narrow-field angle as a result of the off-axis layer merging.

### Transverse Precision of Fabrication

The outer diameter of the target was confirmed to match the design using a vernier scale that have a precision of ±10 µm. Both the arclength and spacing between the ring transitions in the BE-Target were verified using calibrated imaging, as shown in Fig. 6.16 and were found to be separated by 1.09 ±0.03 mm in the image. This separation is within 10 µm of the correct value of 1.1 mm with a standard deviation below the image-resolution of wide-field ophthalmic devices.

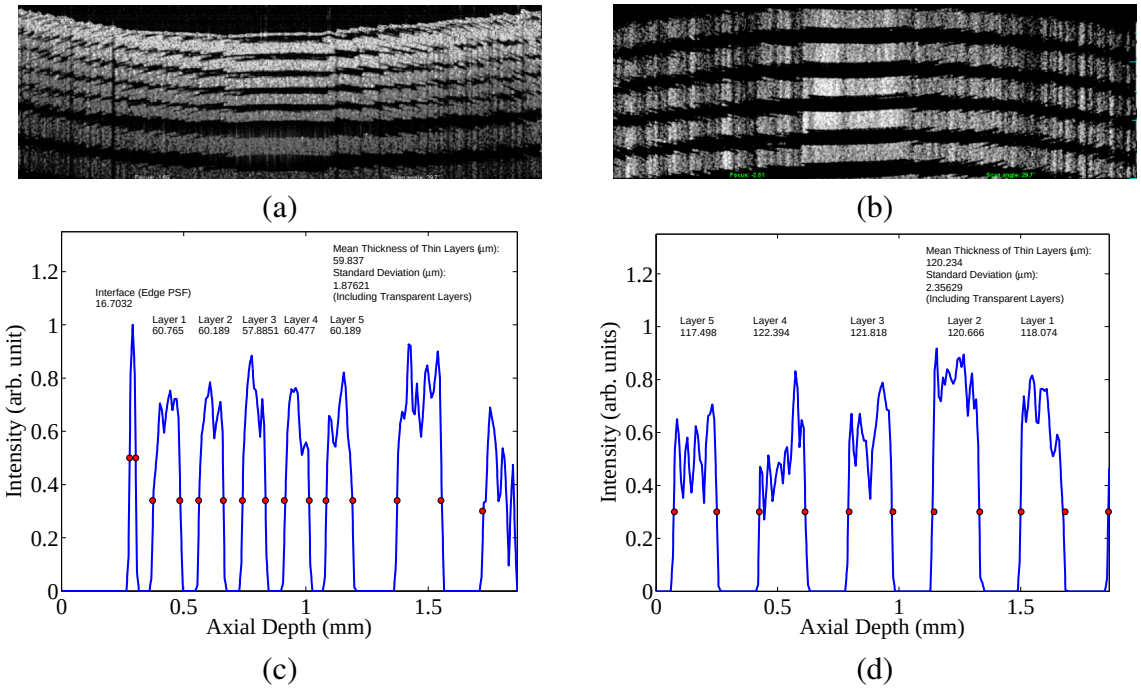


Fig. 6.15 (a) OCT B-scan used in the verification of the AL-Target thin layers. Although the scattering layers appear thicker than the transparent layers in the image, closer analysis of the intensities show that the FWHM intensity of both the scattering and non-scattering layers are of approximately-equal thickness. (b) Complex-conjugate image of thick layer used for simplicity of the analysis code. (c) Plot of a single measurement of the thin-layer thicknesses. (d) Plot of a single measurement of the thick-layer thicknesses. Images exported from commercial systems typically are subject to thresholding of noise, as in this case. The influence of this thresholding is not considered significant on the layer measurement

Analysis of an on-axis image was used to verify that there were no distortions in the ring ellipticity which could have occurred from flaws in the fabrication. The ratio of the horizontal and vertical pixel spacing was measured, which showed a modest gradient at the furtherest rings of <4%. However, as can be seen in Fig. 6.17 (c) and (d), the standard deviation of the measured thickness of the outer five rings is greater than 10% of the ring spacing due to the reduced number of pixels per ring and the reduction in ring contrast. Therefore this small error has been attributed to reduced measurement precision. The results of both these measurements verify that the rings of the BE-Target can be used to accurately measure distortion in a wide-field ophthalmoscope.

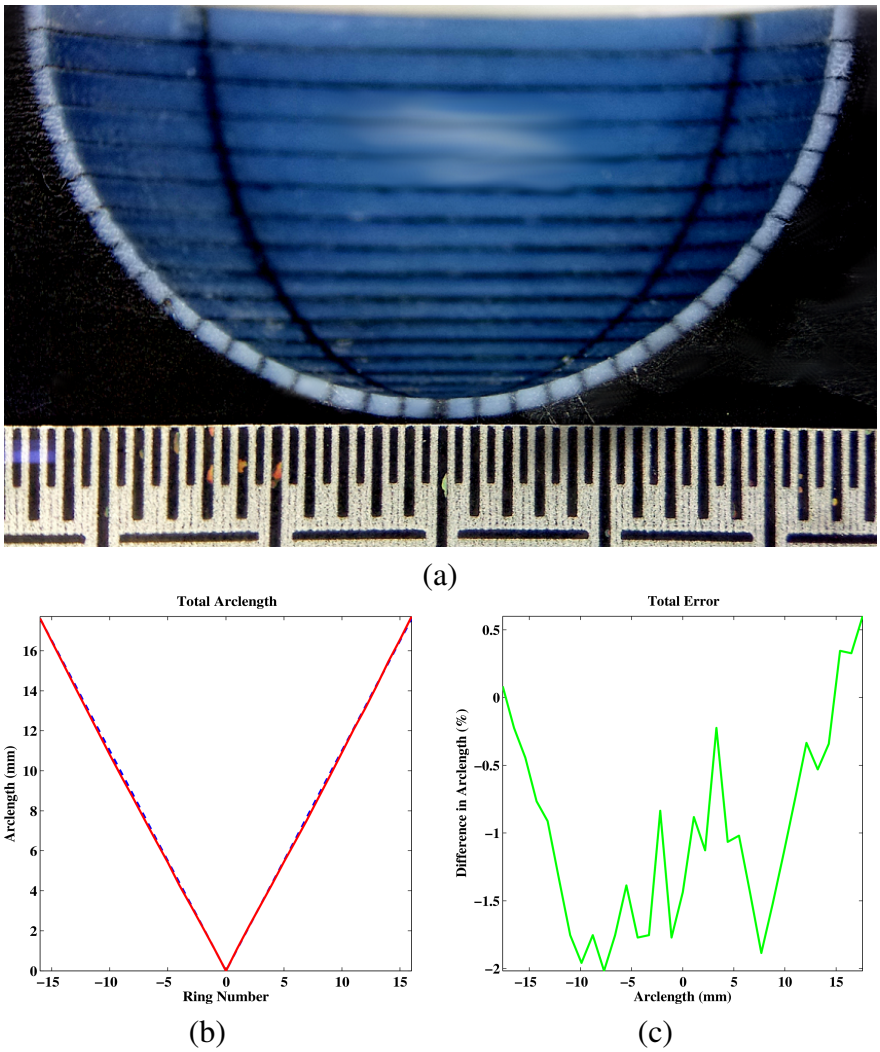


(a) (b) (c)

Fig. 6.16 (a) Cross-sectional view of BE-Target showing calibration rule. (b) Total distance from centre in red with expected distance provided by the blue dash. (c) Percentage difference in total arclength from the centre. The low error in arclength could be caused primarily by thes precision in manual ring selection.

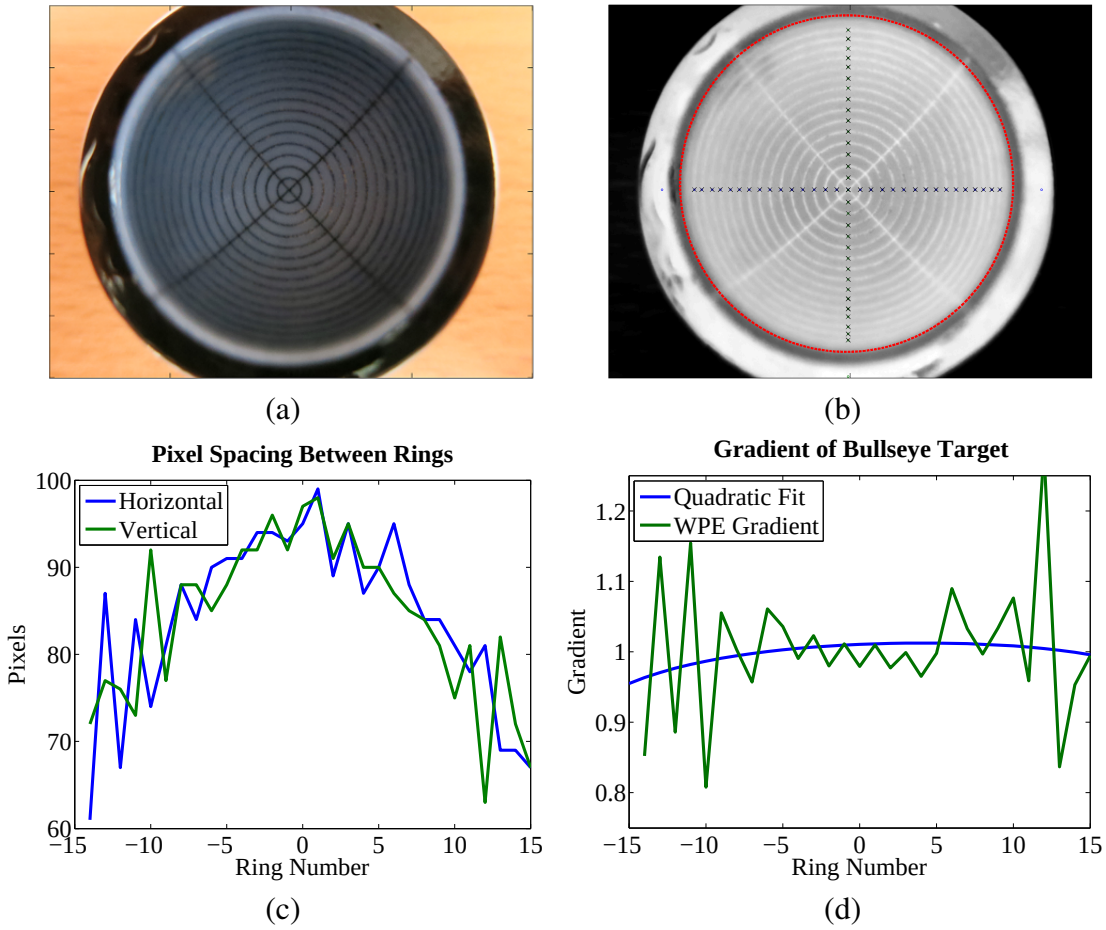


Fig. 6.17 (a) Input image for verification of the target ellipticity. (b) The image was processed to improve contrast a the rings were selected in *Matlab*. After calibration from camera distortion the horizontal and vertical pixel spacing is plotted in (c). The gradient of ring spacing has been plotted in (d).

## 6.5 Mounted-Retinal Target

The WPE was used for the validation of a novel biomarker with potential to highlight ophthalmic diseases such as AMD earlier than currently possible [185]. The work was performed for Dr Imre Lengyel and his team at the Institute of Ophthalmology at the University College London. A common mechanism within retinal diseases such as AMD is the accumulation of protein and lipid deposits below the RPE that prevent the effective exchange of nutrients to the neuron cells above. The formation of mineral calcifications are a precursor to this process as they act as a binding mechanism for the accumulated deposits [186]. Detection of these calcifications can be used to provide detection of AMD before the formation of drusen, which would allow both a better understanding of the causes and possible preventative treatment. In addition, the drusen profile on the peripheral retina can be used to predict an amyloidosis status of patients and potentially provide earlier diagnosis for Alzheimer's disease. [187].

Hydroxyapatite (HAP), a mineral within bone, is commonly synthesised for biologically representative phantoms that mimic calcified tissue. One quadrant of the OCT configuration of the BE-target was painted with a mixture of HAP micro-particles of $5 \pm 2.5$ µm diameter suspended in an semi-rigid agar solution. The second quadrant was painted with the same mixture after being treated with a IRDye 800CW BoneTag dye that has peak absoprtion of 780 nm and peak-fluorescence at 795 nm. The final two quadrants were left clear. A wide-field reflectance and an ICG fluorescence image were acquired of the target and are shown in Fig. 6.18. Both the quadrants painted with HAP are visible within SLO; however, only the quadrant treated with the bone tag is visible in the ICG image.

The HAP particles were used to demonstrate the inclusion of nano-scale particles inside the WPE. This form of phantom has been demonstrated by other groups for the measurement of the PSF within an optical system across a narrow-FOV [180, 188]. The combination of a high-resolution phantom inside a wide-field phantom has yet to be achieved and would allow a single target capable of fully characterising an OCT device. Further work would be required to optimise this technique for PSF measurement; in particular, the use of a centrifuge to ensure that particle density is homogeneous within the agar, a small increase in the radius of curvature of the target to ensure the micro-particles are placed at the focal plane of the device and a more rugged suspension medium.

The second step in the validation of a novel biomarker was to apply the bone tag to a biopsied retina from a donor suffering severe AMD. Retinal tissue was donated from both a diseased patient where AMD drusen was shown to be present and another shown to have no AMD, to provide a control. The RPE tissue was removed by Dr Lengyls group and treated with the fluorescing bone tag. The sample was provided to myself for integration into the

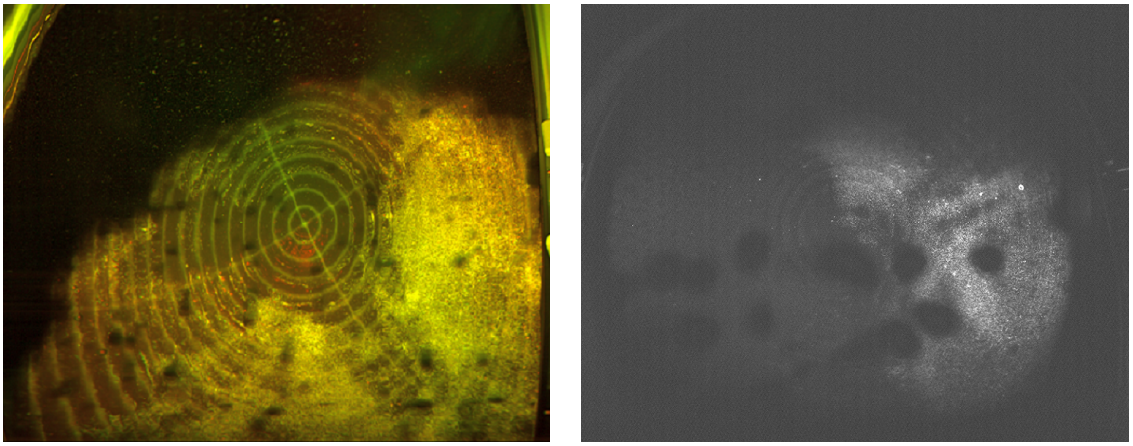

(a) (b)

Fig. 6.18 (a) SLO image of the HAP beads in an agar suspension. The dark portion of this image is caused by poor alignment of the WPE (b) ICG image showing the stained quadrant of the target fluorescing. The dark blotch artefacts in each of the images are caused by bubbles in the phantom. They were not easily removed from the phantom due to the delicate composition of the agar.

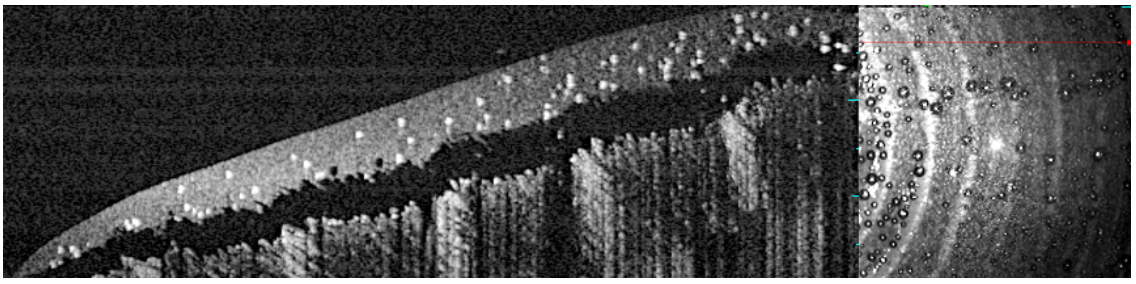

Fig. 6.19 Left: OCT image of the 5 μm HAP beads. Right: SLO Image showing the off-axis rings of the BE-Target. Small circles in right image are bubbles that result from filling the WPE in unfiltered water.

WPE and image acquisition. The wide-field reflectance image and ICG fluorescence image of these samples are shown in Fig. 6.20. As can be seen in Fig. 6.19 (b), the diseased RPE shows calcified deposit corresponding to drusen down the middle of the sample.

The low intensity appearance of the tissue samples in Fig. 6.20 (b) which should not be visible is thought to be due to either residual dye remaining within the tissue or increased autofluorescence of the exhumed RPE. Autofluorescence is not normally seen in the *Optos* ICG and therefore the first case is more likely. The different luminescence between both samples is due to the different optical properties from two different RPE samples. The increased auto-fluorescences on the right side of the AMD sample is caused in by a fold in the tissue. The detection of the both the auto-fluorescence of the tissue and that provided by the dye is extremely valuable as the dyes used in-vitro are harmful to patients making the verification of new flourescence devices challenging.

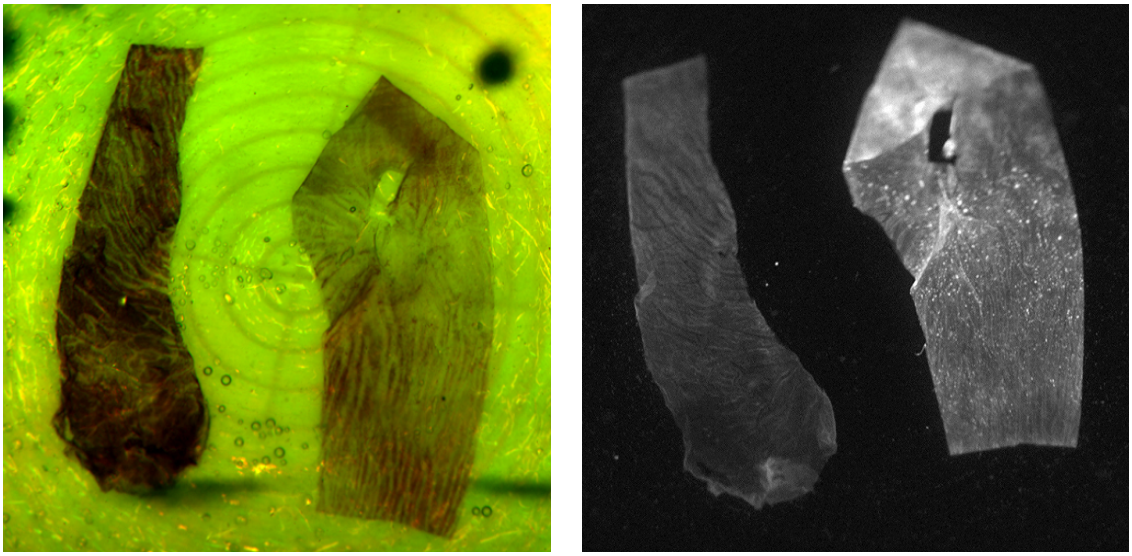

(a) (b)

Fig. 6.20 (a) SLO image of stained RPE. The left tissue is the control and the right tissue has been identified as containing AMD drusen across the centre. (b) ICG image showing the stained RPE with clear fluorescing specks associated with the drusen. Autofluorescence is present however it is not known if this is due to the tissue or the bone tag.

OCT images of the RPE tissue with drusen are provided in Fig. 6.21. The cross-section is through the region containing drusen; however, in the OCT images there are no clear features associable with the pathology. It is not clear how these drusen should appear *in-vitro* and it likely that the discontinuities caused by these drusen would have been more distinguishable *in-vivo* without the physical folding of the tissue.

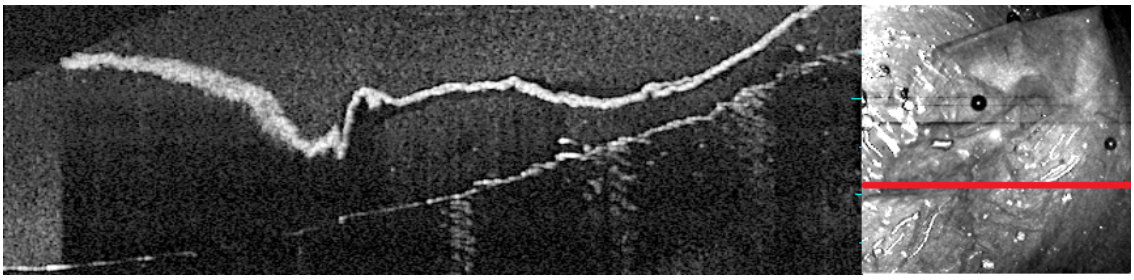

Fig. 6.21 Left: OCT image the RPE layer stuck to the BE-Target using agar. Right: associated SLO reflectance image of the tissue. The red line corresponds to the cross-section made by the b-scan through the tissue

## 6.6 Further Work

The optical performance of the WPE has been shown to be suitable for the characterisation the imaging performance of a wide-field ophthalmoscope; however, the water-filled vitreous of the phantom eye, which is critical for both the maintenance of a representative OPL and allow the exchange of different targets, requires the regular removal of bubbles. The frequency of the bubble removal can vary from a few weeks to a few months. The water-filled vitreous is therefore limited for longitudinal studies as they typically require a minimal variance in the sample. Such longer term usage may include the measurement of device performance across the life cycle of the device or the use of the phantom to recalibrate of the device in the field. A proposed redesign of the optics to accommodate a silicone-filled vitreous would alleviate this problem for special 'fixed' phantoms. Maintaining the optical properties of the human eye in this phantom will be achievable as the refractive power of each surface will be closer to the eye using silicon and water than currently using glass and water.

The targets used are not yet anatomically representative; such as including varying layer thicknesses or anatomy such as the optic disc, and therefore do not yet allow the use of the WPE in device validation. The inclusion of anatomy and pathology would require increased precision than is currently possible with 3D printing or the combination with high precision fabrication techniques, such as spin-coating, lithography and nano-particle deposits. Furthermore the hard substrate could include trenches that could house capillary tubes and fixed with silicone. These capillaries could be fed through one of the valve tubes in the eye to mimic blood flow or allow the calibration of contrast agents.

## 6.7 Conclusion

We have described a phantom eye that enables the assessment of OCT, SLO, ICG and fundus camera performance across a substantially wider $FOV_{ext}$ than the $\pm 10^{\circ}$ has previously been reported. The imaging performance of the WPE is very close to that of a schematic human eye for a $FOV_{ext}$ less than $\pm 40^{\circ}$. For larger field angles a small increase in field curvature causes a modest increase in defocus in the WPE. The wide-field images recorded with an OCT and SLO show that this defocus does not degrade the ability to characterize imaging performance in the retinal periphery.

Three 3D-printed phantoms have been fabricated with features across a $FOV_{int}$ of $180^{\circ}$, which show a sufficient similarity to the scattering properties of the retina to enable generation of an OCT image with features similar to those found in human eyes, as is pertinent for assessment of OCT-device imaging performance. The 3D-printing has been shown to accurately produce large-scale features; however, the spatial resolution is currently similar to that of OCT and therefore insufficient to produce the high-resolution transitions desirable for measuring the axial and transverse PSF across a hemisphere. The non-isometric precision of the fabrication is likely to yield better flat targets. The larger features, such as the bullseye rings and the hemispherical shape of the vitreoretinal interface, facilitate the measurement of variations with FOV of OCT-imaging parameters, such as distortion and axial-PSF. Use of the larger features in the BE-Target in conjunction with the use of contrast dyes have shown the potential of the WPE to calibrate flourescence imaging such as FA and ICG. This ability is extremely valuable as the dyes used in-vitro are harmful to patients making the verification of new flourescence devices challenging.

Further improvements in 3D-printing technology, along with hybridising the 3D-printing with high-resolution fabrication techniques will allow the accuracy of axial and transverse measurement tools to be assessed on low-cost, customizable retinal targets that combine geometric and sub-resolution features. The use of phantoms for both the verification of medical device performance and as a proxy to validation of functionality will still need to be performed in conjunction with clinical studies. Clinical studies are still needed as the measure the performance of the device to compensate for the variation between patients; however, the use of phantoms could greatly reduce the cost and duration of clinical studies by allowing more challenging costly 'repeatability of performance' to be undertaken with a phantom eye.

# Chapter 7

# Performance Comparison in Widefield Reflectance Systems

## Chapter Summary

The purpose of this chapter is to report how the wide-field phantom eye from Chapter 6 is used to measure the extent that the field of view, warping and image quality impact the measurement capability of the *Optos* devices, *200Tx* and *Daytona*, in comparison with competitor systems: *Heidelberg Spectralis* and *Zeiss* fundus camera. Although many devices offer both SLO and OCT and therefore share common optics, the two modalities have been investigated in separate chapters to allow for a sufficient analysis of the different metrics that characterise each modality.

An imaging protocol was developed for the assessment of ophthalmic systems which can be used by both clinical and instrument-assessment personnel to improve consistency of acquisition. The analysis of these images was performed in *Matlab* using a script developed by the author with a general user interface for non-technical users. An image dataset of 50 images was used to measure the variation between 50 *Optos* systems and to analyse the efficacy of a new phase-correction technique in *Optos* architecture. Images from competitor systems were acquired on a *Heidelberg Spectralis* configured for three external field angles (30°, 52°, 102°) and also from the *Carl Zeiss FF4* fundus camera. The *Heidelberg* software was used to acquire measurements on several of these images to assess the accuracy of the device against known feature sizes. Finally conclusions are given on the both the distortion, field of view and measurement capabilities of the devices.

## 7.1 Method for the Verification of Reflectance Ophthalmoscopes.

To compare devices, as part of either a longitudinal or inter-device study requires a consistent interface between all devices and targets, regardless of whether the target is a patient or phantom. To fulfil this requirement, three interface parameters must be actively fixed for comparative measurements.

1. Minimise the tip and tilt of the target relative to device. Failure to minimise the tilt between the device and target changes the location of the centre of the retina within the image.

2. Minimise the transverse displacement (decentre) of the target from the optical axis. Although, the transverse displacement does not alter the centre location within the image, as displacement does not alter the position of the chief ray it can introduce a change in the illumination properties of the image and can introduce a small non-symmetric distortion for large field angles.

3. Minimise the axial displacement between the pupil and the scanning vertex. Variation in the axial displacement results in a large change in image magnification and is the greatest source of transverse measurement error in a well calibrated system.

The first two requirements are more easily met when acquiring an image from a live patient than a phantom for two reasons. Firstly, the internal light for patient-fixation within the device ensures that the curvature of the retina is orientated towards a consistent location. Secondly, the sensitivity of non-mydriatic devices to vignetting by the iris ensures that the transverse positioning is accurate. Unfortunately, the introduction of distortion by axial displacement is more challenging to mitigate in patient imaging than phantom imaging as the impact of axial-positioning on image quality is challenging to isolate from the anatomical variation between patients. Most devices use the location of the pupil to control the objective to pupil distance; however, the anatomical variation between eyes means that the image-pupil and therefore optical magnification varies between patients.

### 7.1.1 WPE Interface for Optos Devices

To image the WPE without tilt and decentre the outlined positional requirements must be achieved manually. The *Optos 200Tx* and *Daytona* devices use a test frame for input and return path alignment, which is shown containing the WPE in Fig. 7.1. The test frame is used

to minimise the variation in tip and tilt between images and is used simultaneously with the patient alignment software which is used to ensure the target is positioned correctly in the x,y and z plane. This interface is the most stable and least labour-intensive method for target alignment for longitudinal studies of device stability. Unfortunately, the systematic device variance from both the tolerances in the device fabrication and the alignment of the internal optics, along with the variance in the test frames, requires some manual readjustment of the displacement for each device. This adjustment is not ideal as it introduces experimental variance to the device assessment as the patient alignment software has a large acceptance range.

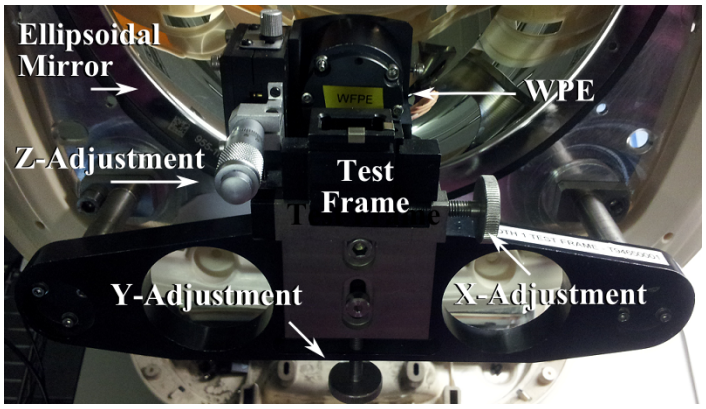


Fig. 7.1 The test frame for the 200Tx annotated to show the degrees of freedom. This attachment was designed to mitigate the variability in tip and tilt from the alignment protocols that occur during device assembly.

### 7.1.2 Reflectance Imaging Analysis Tool

A wide-field analysis tool with a GUI was written in *Matlab* to improve the consistency of the analysis over multiple devices and to allow the verification method to be available for future use by non-technical users. The tool was designed to segment the rings of the BE-Target on an image and use the enclosed pixel values to provide FOV and distortion metrics. This tool can be applied across multiple devices, by optimising the ring segmentation parameters; low-pass filter size, threshold intensity and number of rings, for the measurement of:

1. Image Decentre
2. Field of View ($FOV_{int}$ $FOV_{ext}$ $FOV_{arc}$)
3. Radial Distortion
4. Vertical Contrast

The $\mathrm{FOV}_{int}$ of an image can be easily determined in arclength, from the number or dark rings $i$ extending radially from the centre of an image.

$$\mathrm{FOV}_{\mathrm{arc}}(mm) = 1.1i + 0.5(mm), \qquad i = 1 \ldots 16$$

The conversion from arclength to internal angle in degrees can be calculated by

$$\mathrm{FOV}_{\mathrm{int}} = \pm \frac{180}{\pi r} \mathrm{FOV}_{\mathrm{arc}}. \tag{7.1}$$

Using the linear approximation for small angles provided in Section 5.1 and the radius of the Navarro eye of 12 mm then the $\mathrm{FOV}_{ext}$ can be approximated as $\frac{7}{2}\mathrm{FOV}_{\mathrm{arc}}$ across a narrow $\mathrm{FOV}_{ext}$. In the cases where the phantom is tilted the $\mathrm{FOV}_{ext}$ is calculated from half the total number of rings visible. A conversion between the different notation for FOV has been provided in Table 7.1, which accounts for the non-linearity of the WPE across a wider-FOV.

| Ring Centre | Image Height (mm) | $\mathrm{FOV}_{\mathrm{arc}}$ (mm) | $\mathrm{FOV}_{\mathrm{ext}}$ WPE (°) | $\mathrm{FOV}_{\mathrm{ext}}$ Nav (°) | $\mathrm{FOV}_{\mathrm{int}}$ (°) |
|---|---|---|---|---|---|
| 1 | 1.15 | 1.15 | 4.04 | 3.98 | 5.48 |
| 2 | 2.24 | 2.25 | 7.91 | 7.81 | 10.74 |
| 3 | 3.31 | 3.35 | 11.79 | 11.63 | 15.99 |
| 4 | 4.35 | 4.45 | 15.69 | 15.48 | 21.25 |
| 5 | 5.35 | 5.55 | 19.61 | 19.34 | 26.50 |
| 6 | 6.31 | 6.65 | 23.55 | 23.22 | 31.75 |
| 7 | 7.22 | 7.75 | 27.54 | 27.13 | 37.01 |
| 8 | 8.07 | 8.85 | 31.56 | 31.07 | 42.25 |
| 9 | 8.85 | 9.95 | 35.63 | 35.06 | 47.51 |
| 10 | 9.55 | 11.05 | 39.78 | 39.10 | 52.76 |
| 11 | 10.18 | 12.15 | 43.98 | 43.20 | 58.01 |
| 12 | 10.72 | 13.25 | 48.28 | 47.37 | 63.26 |
| 13 | 11.17 | 14.35 | 52.69 | 51.63 | 68.51 |
| 14 | 11.52 | 15.45 | 57.24 | 56.00 | 73.77 |
| 15 | 11.78 | 16.55 | 61.98 | 60.49 | 79.02 |
| 16 | 11.94 | 17.66 | 66.98 | 65.17 | 84.32 |
| Edge | 12.00 | 18.85 | 72.71 | 70.40 | 90.00 |

Table 7.1 Reference table for $\mathrm{FOV}_{\mathrm{ext}}$, $\mathrm{FOV}_{\mathrm{int}}$ and $\mathrm{FOV}_{\mathrm{arc}}$ conversion based on *Zemax* and CAD models of the WPE which is used within the Reflectance Imaging Analysis GUI. The different internal angle for the WPE and Nav represent the different input angles required to access the same point in the target. Arclength is measured from the centre of the eye; therefore, full-field angles should be halved before using the conversion.

The radial distortion is calculated as the radial change in the image magnification, as given by,

$$\Delta M = (N_m - N_e)/N_e, \tag{7.2}$$

where $N_m$ is the number of pixels measured across the diameter of the final ring imaged and $N_e$ is the expected arclength of the final ring, calibrated using the number of pixels across the first ring. This common description of distortion is only valid for radially symmetric systems and therefore is an incomplete description for the original **opto**map. To mitigate this error the distortion of an original **opto**map will be calculated along a diagonal cross section, $M(d)$ which includes both the horizontal, $M(x)$ and vertical distortion, $M(y)$ of the system.

The accuracy of this distortion measurement is limited by the confidence in the measurement of $N_e$. The primary error in this measurement originates from assessing the number pixels which span the 2.3 mm diameter of the first ring and which is selected by locating 0.1 mm thick transitions. A simple method to improve the distortion measurements would be to include a feature verified externally to a high precision which has sharp transitions at the central pole of the target. This distortion metric does not include any description of the angular warping within an image; however, this property can be measured by placing the phantom at different rotations and gaze angles (tilt) and comparing the angular location of known features within the phantom.

The vertical contrast metric $\mathrm{C_{ext}}$ is used to quantify the uniformity of the image illumination and resolution, both of which are factors in the image contrast. The contrast profile is given by the region around the centre of the image where the condition in Eq. 7.3 has been met.

$$C_{ext} = \mathrm{FOV_{ext}(i)} \ \forall \ \ (\mathrm{I}(x,i)_{max} - \mathrm{I}(x,i)_{min}) > 0.5 \qquad (i = y,\ x = -100:100) \tag{7.3}$$

The choice of cut-off intensity is arbitrary and has been chosen to coincide with the commonly used FWHM. The vertical coordinate, $i$ runs through the entire image height. The intensity of each row is chosen as $\pm 100$ pixels around the central axis where one of the dark columns of the BE-Target has been orientated along the vertical axis.

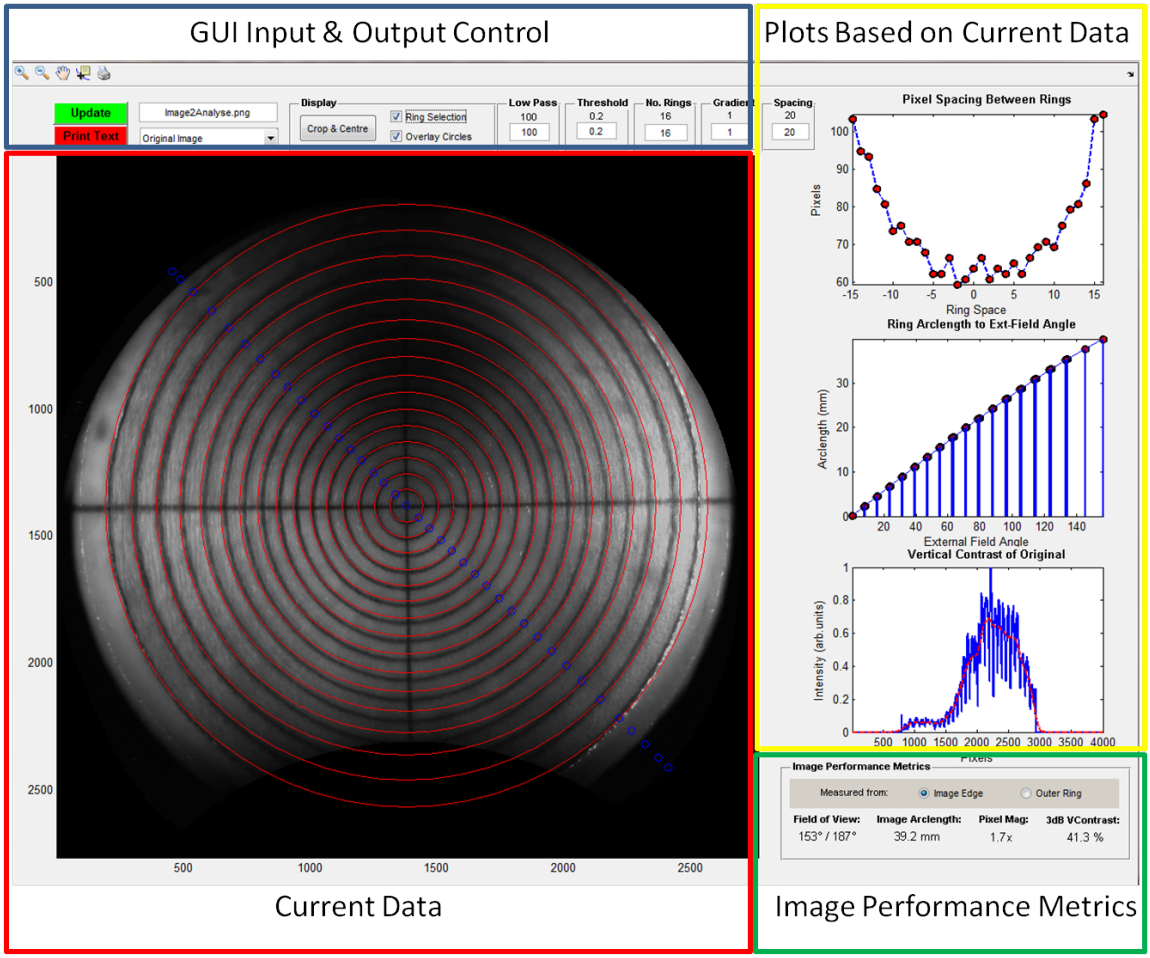


Fig. 7.2 Example image within the Widefield Analysis GUI. The main figure (left) is the image being analysed with the rings segmented (in this case) diagonally and the circles overlaid to match the measured radius for subjective angular distortion analysis. The sub-figures on the right of the GUI are from top to bottom: The number of pixels between rings, the FOV conversion table, and a plot of the vertical contrast.

## 7.2 Variation in the Distortion of Optos 200Tx & Daytona

The WPE containing the BE-Target (in reflectance configuration) has been used by the Research Department at *Optos* for the validation of the projection algorithm, shown previously in Fig. 6.12 and the verification of image measurement. A critical purpose of the WPE is for the assessment and control of the variability on a production line.

Images of the WPE were acquired for a study on the variance in distortion across 25 *Optos 200Tx* devices and 25 *Daytona* devices. A single image from each was captured at the final stage of quality-control procedures after the systems were considered operational by

*Optos* assembly technicians. The *200Tx* devices and *Daytona* devices were tested at different manufacturing sites. The images were then processed using a version of the Reflectance Imaging Analysis Tool for which the source code has been included in Appendix B.3. The images were used to measure four properties of the devices: Firstly, the horizontal and vertical decentre of the image; secondly the full $FOV_{int}$ along the horizontal and diagonal axis of the image; thirdly, the radial distortion along the horizontal and diagonal of the image and finally, the contrast between the dark and light pixels along the vertical axis. The results of this assessment are shown in Table 7.2 and plotted in Fig. 7.3.

Ideally a further 25 images from the same device would have been recorded to allow a meaningful separation of inter-device variability and device repeatability. However, the objective of the study was to quantify the total variability that would impact the new projection algorithm being developed by *Optos* and therefore this small distinction was not of high-enough value to *Optos* to justify the time it would have taken to acquire and share these images in the tight restrictions on the manufacturing duration. A smaller sample size of 3 systems were made available for a brief period to investigate intra-device variation. The average intra-device displacement across 9 images was 0.06 mm in horizontal and 0.02 mm in vertical. This small error in intra-device variation also accounts for the variation that results from the manual selection of the image centre.

| Device | Axis | Decentre (mm) | $FOV_{int}$ (°) | $\Delta M$ | $C_{ext}$ (°) |
|---|---|---|---|---|---|
| Daytona | (x) | 0.65 ± 0.31 | 187.8 ± 2.0 | -0.01 ± 0.03 | - |
| Daytona | (y) | -0.04 ± 0.36 | - | - | N/A |
| Daytona | (d) | 0.72 ± 0.33 | 179.4 ± 3.4 | -0.10 ± 0.03 | - |
| 200 Tx | (x) | -0.12 ± 0.39 | 190.2 ± 2.4 | -0.04 ± 0.01 | - |
| 200 Tx | (y) | -1.73 ± 0.53 | - | - | 53.8 ± 14.6 |
| 200 Tx | (d) | 1.72 ± 0.49 | 175.0 ± 2.7 | -0.16 ± 0.02 | - |

Table 7.2 Results from the variance analysis of the *Optos* SLO devices showing the mean value and standard deviation across measurements. The variables (x,y,d) correspond to the axis of the image for which the cross-section was analysed to extract the metric (horizontal, vertical, diagonal). The measurements provided show a substantial variation in all four metrics.

### 7.2.1 Discussion on the Variation in Optos Devices

**Variation in Decentre:** The image centre was identified manually in the analysis software by selecting the centre of the cross-hair on the BE-Target. This selection found that the radial

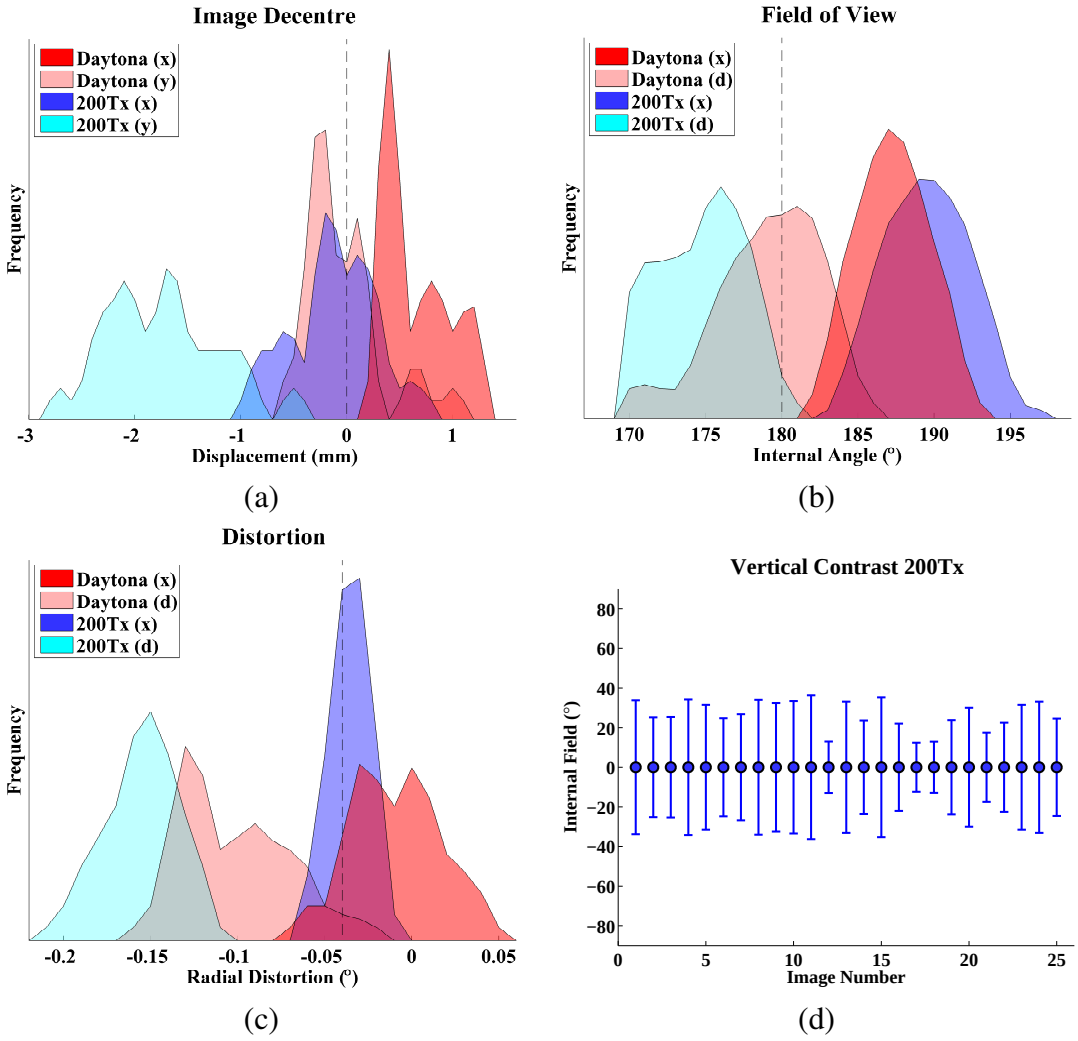


Fig. 7.3 Distribution of metrics across 25 *Daytona* and 25 *200Tx* devices. (a) Substantial variation across all axis with the worst case being for 200Tx vertical axis. (b) FOV distribution showing similar variance between devices. (c) Substantial variation can be seen in distortion the distortion along different axis, with the exception of *200Tx* horizontal axis. A Gaussian spread was generated by applying a ([1 3], 1) pixel Gaussian filter to histogram. The frequency of plots (a) to (c) ranged from zero to five. Variation in the FOV $_{\text{int}}$ that the image contrast exceed 0.5 along the vertical axis in the 200Tx.

arclength from the central pixel to the centre of the BE-Target ranged from -0.5 to 1.2 mm with a standard deviation of 0.33 in the *Daytona* and -2.7 to 0.6 mm with a standard deviation of 0.49 in the *Optos 200Tx*. The distribution of the image decentre is provided in Fig. 7.3 (a) and is substantially higher in both mean value and deviation than expected. There are three probable causes of decentre in the image; firstly, the misuse of the test frame could induce a vertical sag in the WPE and would lead to the centre of the cross-hair being located below the centre of the image. Secondly, variations in the timing of the electronic signals that control the image line start (vertical) or the frame start (horizontal) could induce a non-symmetric cropping of the image. Thirdly, the imprecision in the positioning of the scanning elements in the input-path could introduce misalignment in optical relay. This misalignment would also result in variation in the illumination between images and distortion in the ring spacing.

In the *Daytona* system, the mean value of approximately zero in the vertical axis indicates that the most probable source of variance between these devices was the misalignment of the frame start. This conclusion assumes a normal distribution of the decentre caused by this misalignment of the frame-start detector, which is reasonable considering the detector can both too high and too low. Also the set up procedure for this subsystem has a requirement of detecting the scan across a time window, which might be causing the wide range of image centres. To confirm this hypothesis would require tolerance analysis in Zemax to confirm the normal distribution and to investigate other probable sources.

In the 200Tx, systematic error along the vertical axis implies that either there was a repeated misuse of the test frame during this study or a fundamental flaw in the system alignment. The fact that this value is negative and far exceeds the variation in the horizontal axis makes it most likely that there was an issue with the use of the test frame. To confirm this hypothesis images were recorded with the test frame on a single device made available to the author, both correctly and again in the most extreme-probable way to misuse the test frame. The vertical translation induced by the misuse of the test frame was observed to be 0.3 mm, which is substantially below the range observed by the study. This outcome contradicts the original hypothesis; however, further experimentation will be required to form further conclusions.

textbftextitVariation in Field of View: The variation in the image decentre leads to a variation in the FOV as can be seen in Table 7.2 and Fig. 7.3 (b). Any variation in the FOV is significant as it alters the calibration parameters between systems and therefore results in a need for complex calibration for measurement and image registration algorithms. Although substantial, the variation in FOV appears to be fairly consistent across devices with a marginal increase in the diagonal axis. This property is unsurprising as the distortion in an original

**opto**map is greatest along the diagonal axis. From this investigation it is clear that competitor studies discussed in Section 5.2 comparing the properties of two products based on a single representative are ultimately limited by the intra-product variance [189]. Without knowledge of this parameter, measurement error must be presumed to be large. A limitation of the analysis reported here is that it provides no metric for the quality of the field of view which is important when assessing what parts of an image a clinician can use to detect pathology and anatomy.

textbftextitVariation in Distortion: The relative ring spacing in the images of the BE-Target were measured to investigate radial distortion. The horizontal axis of an original **opto**map should not display radial distortion as a result of the horizontal scanner is equidistant to a fixed curvature on the ellipsoidal mirror for all angles. Widefield images should show some distortion even if the scanning is linear as an emmetropic eye introduces a small amount of radially symmetric distortion, mentioned in both Section 4.5 and expanded upon in Section 5.3.2. At a $FOV_{ext}$ of 180° such as seen by both *Daytona* and the 200Tx $\Delta M_{eye}$ = -0.04, which would mean a transverse measurement calibrated on-axis would have an error of 4% off-axis.

As expected, both systems show little or no distortion over and above this value along the horizontal axis. The distortion from the eye in the diagonal axis was expected to be larger as a result of the varied power in the ellipsoidal mirrors. This change in magnification is now routinely corrected by a stereographic projection algorithm. The projection of **opto**maps means that the the range of distortion and not the absolute value is critical, as the projection does cannot yet be calibrated for each device. Based on these results the variance in the distortion across this axis would limit the effectiveness of the stereographic projection and produce an error in an arclength measurement of a system by up to ± 6.1% in the *Daytona* system and ± 3.6% in a *200Tx* system, the range of distortions measured. This error could lead to wrongful classification of whether pathology was growing or in remission.

**Variation in Contrast:** The illumination properties of an image acquired from the 200Tx depend on the ability to focus light through a narrow aperture in the return path. This means that both the light from a different axial plane (such as the anterior segment) and the light exiting the optical relay with a non-planer wave-front will be heavily attenuated. Transmission of the light that originates from the retina is difficult to maintain in the 200Tx because of the variable power in the ellipsoidal mirrors along the vertical axis. In theory, the optical roll-off should be consistent between devices as the curvature of the mirrors is constant at the same field for different devices; however, the imprecision in the fabrication of optical elements requires that the position of the pinhole has to be optimised to maximise

the contrast of on-axis imaging. The optimisation of the image illumination is provided by the transverse adjustment of the lens before the pinhole and axial adjustment of the pinhole is provided to select the axial plane of greatest transmission. Adjustment of the lens will compensate for transverse displacement of the beam by introducing a moderate deflection, this has further ramifications on the alignment of the detector. The varied transmission to the detector wastes the dynamic range of an image.

### 7.2.2 Verification of Phase-Correction Technique

The WPE and image analysis tool were used to verify the performance of the *Daytona* with phase mask verses both the 200Tx and the *Daytona* without. The phase mask is a recent development by the Research Team at *Optos* and is designed to correct the effects of the variable power of the ellipsoidal mirrors. This phase mask consists of a glass plate where the optical power (curvature) changes along the vertical axis ensure the beam is collimated in the return path for all field angles. Both the large PSF and variable attenuation by the pinhole that results from the focus with the vertical field angle results in an inefficient use of the dynamic range within an image, which reduces contrast. The improvement in vertical contrast between *200Tx* and the *Daytona* with and without the phase mask can be seen in Fig. 7.4 (a-c). This FOV equates to a high quality region with the phase mask of $\pm$ 48.2° external field opposed to $\pm$ 30.3° in the 200Tx and $\pm$ 39.2° in the *Daytona*. A net improvement of 59% between the 200Tx and *Daytona* with the phase mask.

The accuracy of these values is limited in a number of ways. Firstly the comparison is provided by a single device and as already established there is currently a significant variability in the sample stock of 200Tx. Although, the image provided from the 200Tx was chosen as it had a contrast approximately average for the variability-study sample. Secondly, the choice of the threshold at 50% contrast is some way above what would be required to image vasculature and therefore analysis between the phantom and retinal images would be required to select a more effective threshold. Finally, at the time of writing this thesis the phase mask is still under development with plans to extend the FOV further. This phase of development means that access to devices with the finished phase mask installed is unlikely. Furthermore, the stereographic projection has not been tuned for the phase mask and thus some unintentional distortion is still present in the image, which will be corrected before production commences.

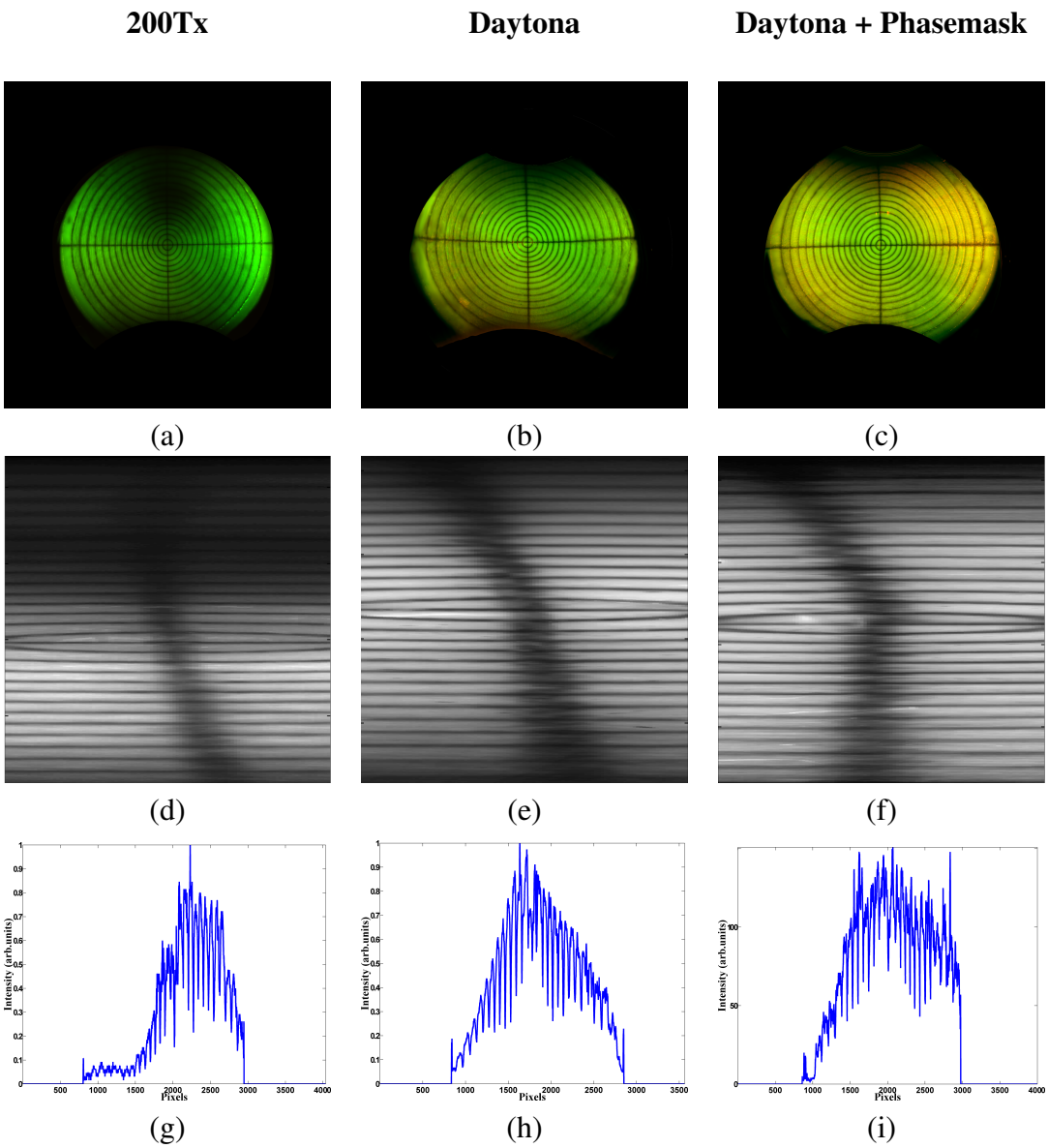


Fig. 7.4 (a-c) Comparison of vertical contrast of *200Tx* vs *Daytona* with and without the phase mask. Previously, Optos *believed* that the the *200Tx* has a slightly large-vertical FOV than the *Daytona*. However, this study has shown that the 'high-contrast' FOV is greatest in the *Daytona* than the *200Tx*. (d-f) 100 pixel wide segments where the contrast was examined. (g-i) Plots showing the contrast and roll-off of the devices.

## 7.3 Verification of Competitor Ophthalmoscopes

In Section 5.3 a discussion is provided on why it is not in manufacturers interests to provide reliable specifications for their devices. This lack of reliability makes competitor systems essentially black-box devices that can be used to validate the role of the WPE for the characterisation of prototype devices. The acquisition of images from different commercial devices requires a degree of flexibility in the phantom interface. Many devices are either not perpendicular to the ground or require a lens attachment as for the *Heidelberg Spectralis*. In these circumstances the verification method must be customised for each case; however, comparative studies require the assessment to be based on a common method.

The acquisition of images from commercial ophthalmic device requires access to clinical screening centres. Images from the *Heidelberg* (SLO/OCT), Optovue (OCT) and *Zeiss* (Fundus Camera) ophthalmoscopes were acquired at two screening centres in the United States. To maintain the consistency of the study, the photographer was provided with a detailed protocol and a WPE mount was fabricated as shown in Fig. 7.5. The mount was designed to provide steps of tilt to the WPE by 20°; centred on the iris of the phantom. This centre of rotation was chosen to mimic the optical scanning of the *Optos* system; although, conventional navigation through eye steering would rotate about the centre of the eye. Rotation of the entire mount by 90° allowed tilt to be investigated. The protocol required the user of the BE-Target to acquire images with both tip and tilt in the range of -60° to 60° in en-face images and again with the AL-Target for OCT images.

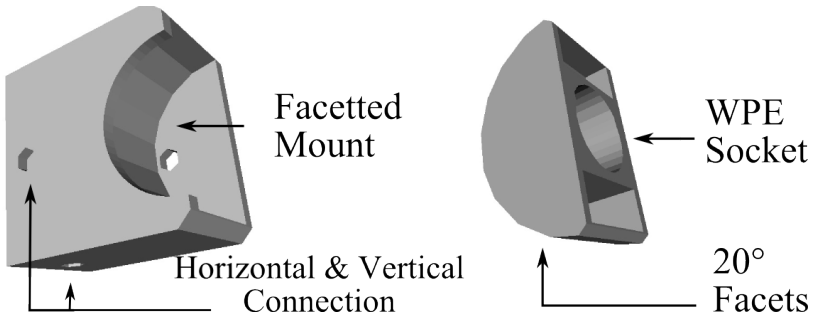


Fig. 7.5 CAD illustration of the Faceted Mount developed as a common interface that maintains fixed angles in the acquisition of images from competitor systems.

### 7.3.1 Heidelberg Spectralis

The *Heidelberg* are the principle competitor to *Optos* for providing ultra-widefield images. The term "ultra-widefield" is generally given to a reflectance ophthalmoscopes with a $FOV_{ext}$ greater than 60°, which can be used to image beyond the retinal arcades, as discussed in

greater detail in Section 2.5. The *Spectralis* uses a range of lens attachments to achieve large field angles that change the magnification and shift the scanning vertex of the optical system. A summary of the motivation for a large FOV was outlined in Section 2.5. *Heidelberg* have a strong reputation for high-precision measurement, which makes it an ideal benchmark to comparatively verify the capability of *Optos* system for measurement and to assess the value of the WPE.

### Spectralis 30 Degree Lens

The basic specification of the*Heidelberg Spectralis* is a narrow-field SLO with a $\text{FOV}_{ext}$ of 30°. In this configuration, the software provides the capability to both measure directly from images and to steer the device on a gimble, around the pupil, for automatic real time (ART) montaging. This tool must be purchased in addition to the device and is branded "Painting with ART$^{TM}$" because the photographer appears to be colouring in a blank canvas with a small FOV. The images of the phantom eye were acquired following the previously discussed protocol, with both the tip and tilt acquired at -60° to 60° and are shown overlaid in Fig. 7.6 (a). The ART tool was used to show the quality of the automated montaging within the *Spectralis* and is displayed in Fig. 7.6 (b).

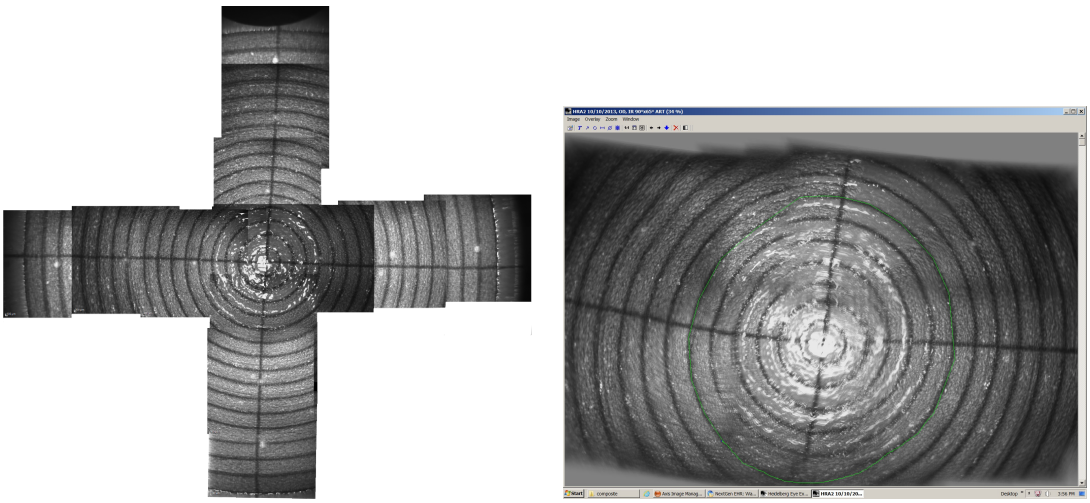

(a) (b)

Fig. 7.6 (a) Steered Images of the *Heidelberg Spectralis* with a 30 Degree lens montaged in *Matlab*. The field of view achievable via ± 60° external angle was approximately 180° horizontally and 172° vertically. (b) Example of the automated managing tool "ART" use on the BE-Target.

Table 7.3 shows the outcome of the analysis on the central image. The full-FOV was measured to be higher than the 30° reported by *Heidelberg* at 31.2°. In addition, the images displayed very little distortion below the accuracy of this analysis, for both axis and in steered images. The 30° lens appears capable of steering to a FOV approximately 180° within the eye. Although this is unlikely to be achievable in a real eye because of the limited comfortable gaze angles afforded by the eye of ±15° [11], this capability is important for the later validation of steered OCT images. In this configuration, the OCT and SLO optics are common and therefore using this form of steering the photographer is able to access the full FOV of the AL-Target using the *Spectralis*. To reproduce the FOV of an **opto**map in this manner in a patient is impractical as it would require 49 images and a range of motion that is not capable by the *Spectralis* gimble. Furthermore, the confidence in navigation would be low given the variability in path anatomy, patient position and navigation linearity.

Table 7.3 Metrics for non-steered *Heidelberg Spectralis* with the 30° Lens. The Arclength is defined as the total circumference within the image. The angles are ± around the optical axis, ΔM was calculated using Eq. 7.2 and the precision is given as half the ring thickness over the diameter of the central ring. Conformal refers to the property whether an image preserves angles.

| Axis | $FOV_{arc}$ (mm) | $FOV_{int}$ (°) | $FOV_{ext}$ (°) | Δ M | Conformal |
|---|---|---|---|---|---|
| Horizontal | 8.9±0.05 | 42.5±0.02 | 31.6±0.02 | 0.02±0.02 | Yes |
| Vertical | 8.8±0.05 | 42.0±0.02 | 31.0±0.02 | 0.04±0.02 | Yes |

Measurement based on this configuration recorded the image diameter to be 8.83 ± 0.05 mm, which is 0.7% below the true value of 8.9 mm which can be observed from the number of rings in the image. The full-$FOV_{ext}$ seen in the images acquired using the ART feature is approximately 88° x 56°, slightly below the full-$FOV_{ext}$ claimed for the image of 90° x 65°. This higher value is likely to correspond to the size of the window or "canvas" onto which the montaged images are collected, so the small description is not considered significant. The obvious discontinuities in the montaging may be due to the non-anatomical appearance of the target and specular reflections in the image; however, a similar image of a retina without the specular reflection maintained some ghosting and discontinuities shown in Fig 7.7. It is unlikely that this feature is designed to provide precise measurement as the software support for the measurements was disabled automatically while using ART.

### Spectralis 55° Lens

The *Spectralis* can be used with a lens attachment to increase the $FOV_{ext}$ from 30° to 55°; however, this also reduces the magnification and pixel density proportionally. Images were acquired using the same protocol as before with the exception of the ±60 tip and tilt

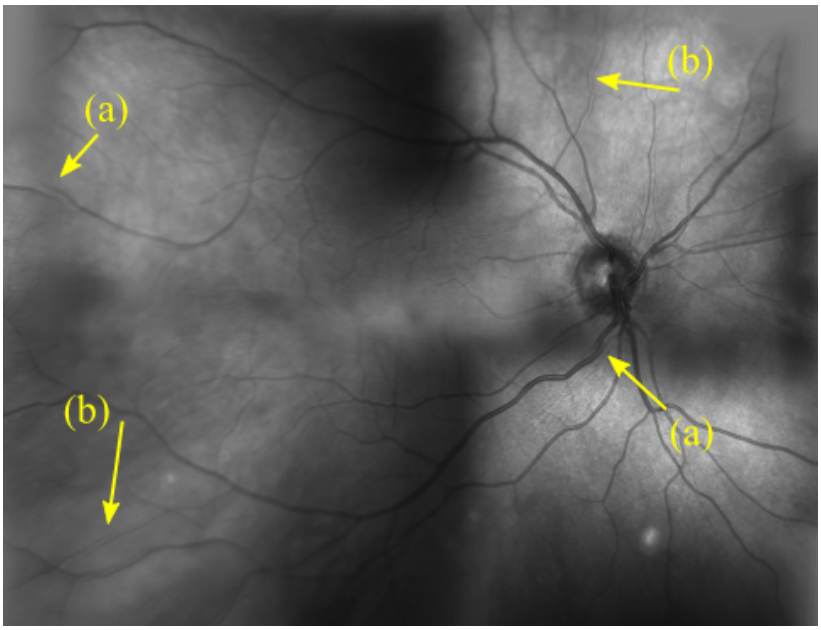


Fig. 7.7 An ART Montage of a retina showing artefacts in both the stitching and intensity. (a) Discontinuities (b) Ghosting.

orientations as they were obstructed by the lens attachment. The images from this acquisition are shown approximately overlaid in Fig. 7.8. Table 7.4 contains the analysis of the images from the 55° lens.

The full $FOV_{ext}$ was measured to be 54.6°, which matches the value outlined by *Heidelberg* as 55.1°; in addition, the ΔM was measured as 0.02 ± 0.02, which is negligible. The automated measurement from this device produced a diameter of the 6th ring as being 13.65 mm, which is 0.35 mm higher than the true value of 13.3 mm and corresponds to an error of 2.6%.

Table 7.4 Metrics for Heidelberg *Spectralis* with the 55 Degrees Lens.

| Axis | $FOV_{arc}$ (mm) | $FOV_{int}$ (°) | $FOV_{ext}$ (°) | Δ M | Conformal |
|---|---|---|---|---|---|
| Horizontal | 15.5±0.1 | 74.0±0.2 | 54.6±0.2 | 0.02±0.02 | On-axis |
| Vertical | 15.5±0.1 | 74.0±0.2 | 54.6±0.2 | 0.02±0.02 | On-axis |

The images on the left of Fig. 7.8 show that the small amounts of distortion can be observed for angles radially distant from centre. This moderate distortion is inevitable without a re-projection of the pixels for different gaze angles. To quantify this distortion the number of pixels between the intersection between the cross-hair and the fifth ring in both the on-axis image and the tilted image (D20) were measured as annotated in Fig. 7.8. This measurement showed only a 2.7% change in the number of pixels between the same

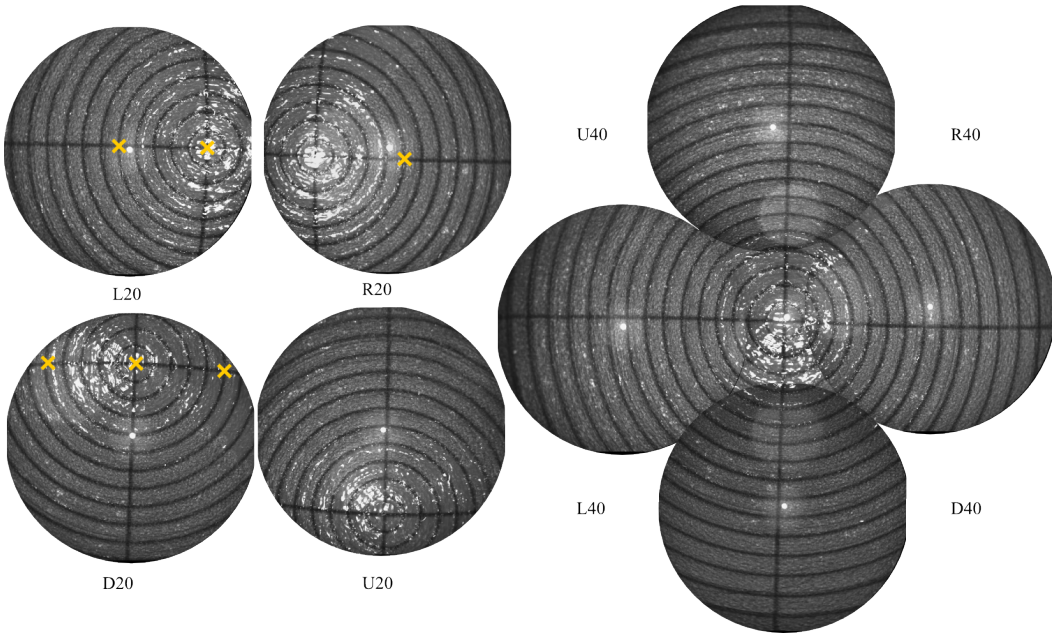


Fig. 7.8 Images from the *Heidelberg Spectralis* with the 50°s lens. The identification of the images (U,D,L,R) corresponds to (Up, Down, Left and Right) with the numeric referring to the tip/tilt of the phantom.

points and resulted in the horizontal line bending by 6°. At this magnitude it is unlikely that the distortion would reduce the efficacy of measurement from this lens configuration. The ART montaging software was again applied to the phantom eye and shown in Fig. 7.9 to assess whether the software was sufficient to allow measurement. As with the 30° lens, it is apparent from the image that the montaging is imperfect and therefore it is inadvisable to use this feature for measurement.

### Spectralis 102 Degree Lens

Two hand-held lenses are available to further extend the FOV of the *Spectralis*. Firstly, the Staurenghi contact lens has been available for nearly 10 years and offers a $FOV_{ext}$ of 150°. Secondly, the non-contact ultra-widefield lens offers a $FOV_{ext}$ of 102° [189]. Both lens attachments are only available for flourescence imaging because of the increased complexity required to maintain an acceptable focus across a wide-FOV. Each lens component will produce Fresnel reflections which are difficult to completely mitigate with confocality and coatings if they originate from a range of axial planes in the system. The flourescence light which is of a different wavelength can easily be gated using a chromatic filter.

The 102° lens shares the property as *Optos* of being non-contact and therefore as a closer competitor has been chosen for investigation over the Staurenghi lens. Images were acquired

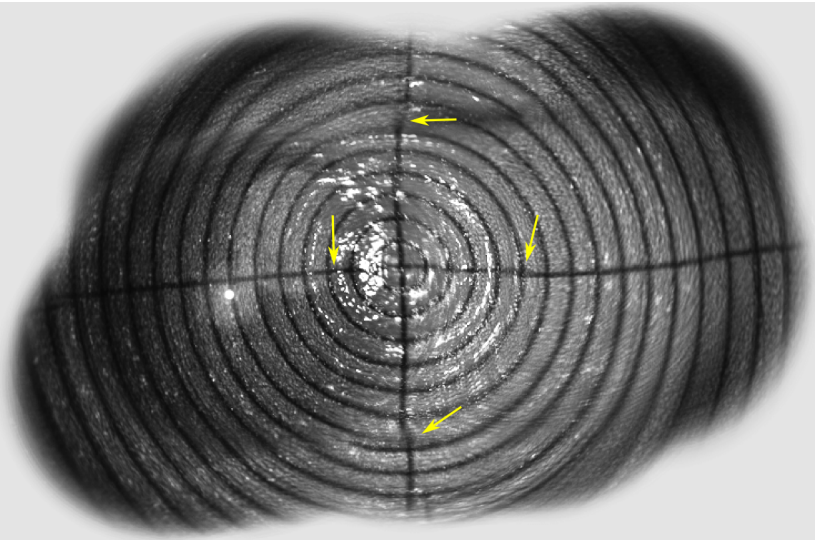

Fig. 7.9 An ART Montage of a WPE showing errors in both the stitching and illumination.

using the same protocol as used for -40°:20°:40° and both an on-axis and off-axis image have been provided in Fig 7.10. Overlaying the images as before was not possible as a result of the worsening radially distant distortion as seen by comparing the horizontal line in both the on axis and tip -40° in Fig 7.10 (a) and (b).

The full-FOV of the system was measured as 101.8° which matches the value provided by *Heidelberg*. There did appear to be some minor barrel distortion on the on-axis image which will be reviewed in more detail in Sec 7.4. The gaze-angle distortion was quantified by measuring the number of pixels between the intersection of the cross-hair and the ninth ring in both the on-axis image and the tilted image (D40). This measurement showed a 6.4% increase in the number of pixels between the same points and resulted in the horizontal line bending by 16°.

Table 7.5 Metrics for on-axis *Heidelberg Spectralis* with the 102° Lens

| Device | $FOV_{arc}$ (mm) | $FOV_{ext}$ (°) | $FOV_{int}$ (°) | Δ M (%) | Conformal |
|---|---|---|---|---|---|
| Horizontal | 27.6±0.1 | 131.8±0.2 | 101.5 ±0.2 | 0.04±0.02 | On-Axis |
| Vertical | 27.8±0.1 | 132.7±0.2 | 102.3 ±0.2 | 0.03±0.02 | On-Axis |

**Severity and origin of reflections for the Heidelberg Spectralis**

Five types of reflection artefacts were observed while using the *Heidelberg Spectralis* to image the BE-target that are generally not seen in the *Optos* reflectance images; these are shown in Fig. 7.11. *Reflection 1* has been observed in other narrow-field IR reflectance

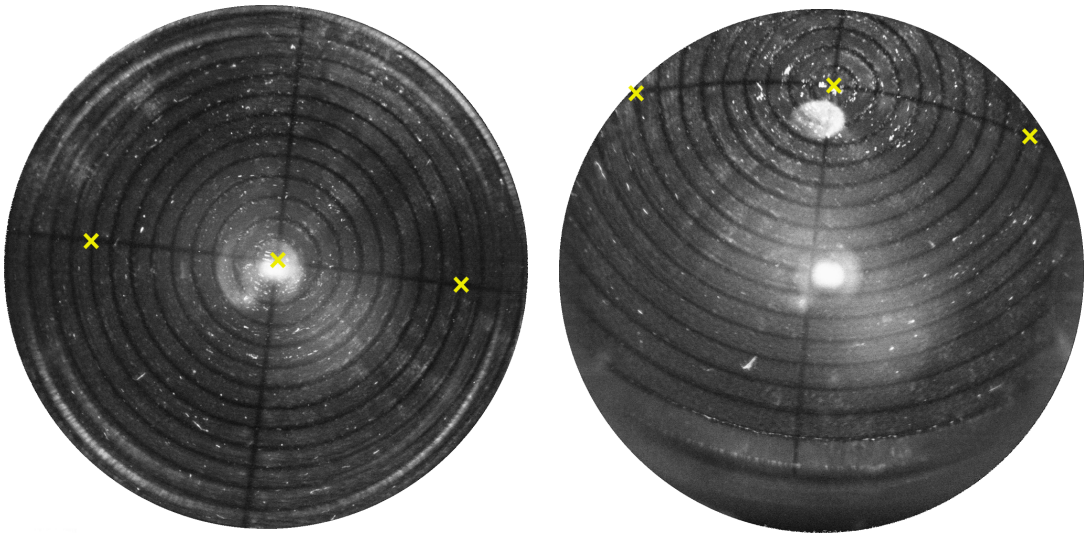

(a) (b)

Fig. 7.10 (a) On-Axis 102° Lens (b) Off-Axis NCWF Lens (D40) showing distortion relative to the gaze-angle

devices and is caused by the plastic target being more prone to specular reflection at longer wavelengths than the retina. This specular reflection has a higher intensity than scattered light and therefore can cause saturation in an image calibrated for retinal imaging. *Reflection 2* and *Reflection 3* are caused by the fixation target which is stationary per image therefore has a higher ener on the retina than the scanning beam. The *Spectralis* has a function to turn the fixation off which should be implemented in further studies. *Reflection 4* is the lens reflex from the 102° non-contact lens. This artefact is identifiable by the sharpness and its central location across images. *Reflection 5* is the reflex from the cornea of the WPE.

The final two artefacts are present in the images as they were acquired using reflectance imaging with a lens which enables only fluorescence imaging. These reflection artefacts would be present in a reflectance image of a human retina as well, and is most likely the reason why reflectance images are currently not available with the ultra-widefield non-contact lens. Understanding why the new NCWF lens from *Heidelberg* was a primary motivation for *Optos* in this study and it is now clear that both corneal and lens reflex dominates the images that can not be corrected with the appropriate lens coatings and special filters.

### 7.3.2 Zeiss FF4

The *Zeiss FF4* series is a tradition fundus camera ophthalmoscope included as a comparison to the wide-field scanning laser ophthalmoscopes. Like most systems within this market, the device claims to provide a $FOV_{ext}$ of 30° which is recorded on a CCD array opposed to a

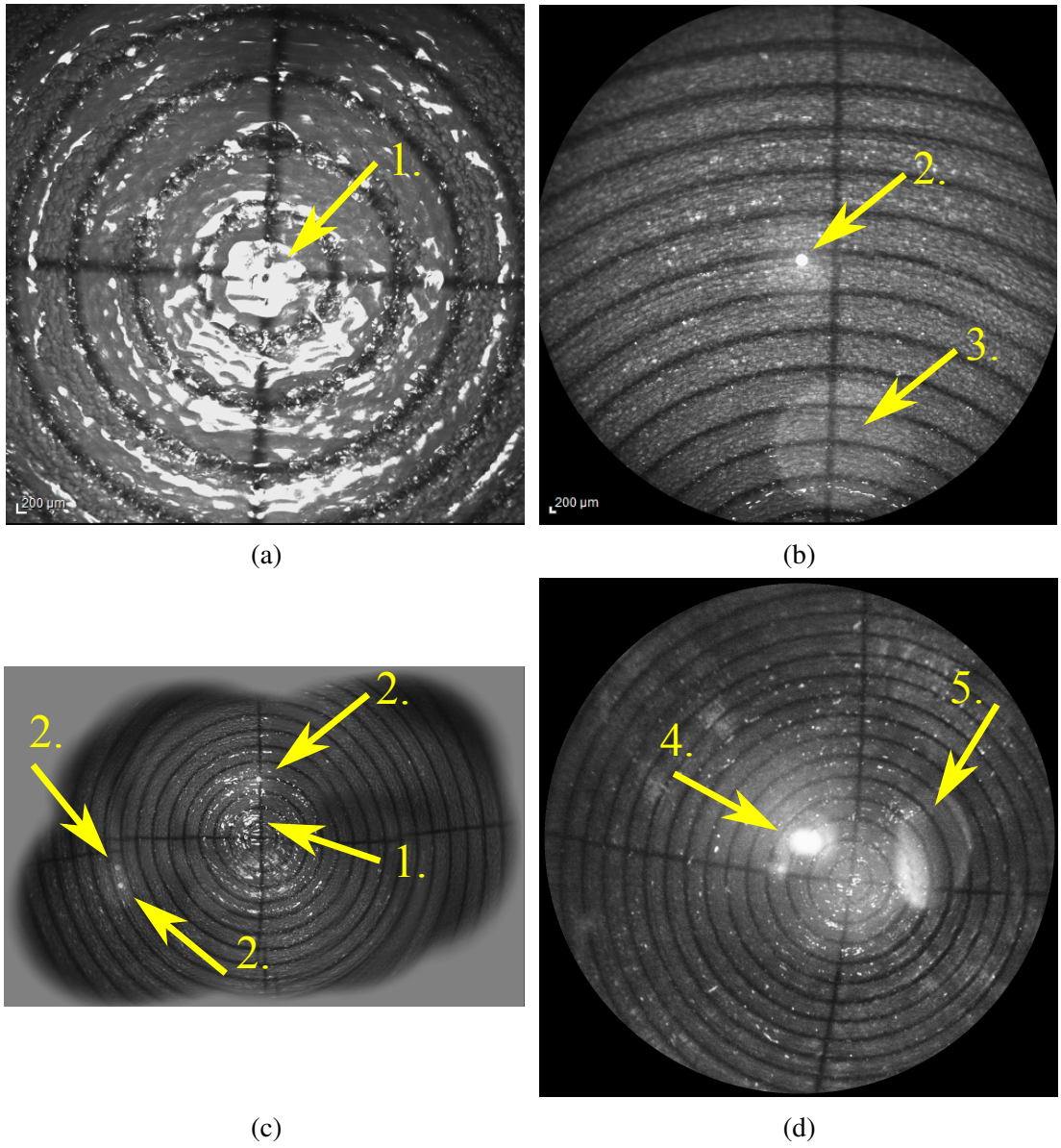


(a) (b)

(c) (d)

Fig. 7.11 Shows the four types of images acquired on the *Heidelberg Spectralis*. Image (a) has been annotated to highlight *Reflection 1* the on-axis specular reflection inherent in narrow-field IR SLO images. Image (b) shows two reflective artefacts *Reflection 2* which is cause by the fixation target of the device and *Reflection 3* which is a ghost image of the fixation target cause by light scattering and being vignetted by the pupil. Image (c) shows *Reflection 2* in three locations. Image (d) shows two reflection artefacts *Reflection 4* which is the reflex from the non-contact WF lens and *Reflection 5* which is corneal reflex.

single point detector. The images of the BE-Target were acquired with both the tip and tilt of -40°:20°:40° and are shown overlaid in Fig. 7.12.

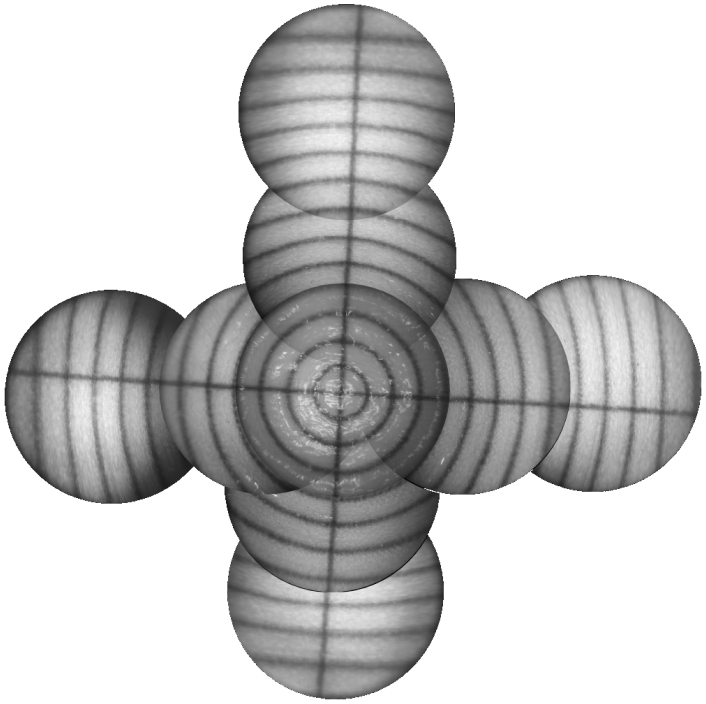

Fig. 7.12 (a) Montaged images from a steered *Zeiss FF4* fundus camera.

The analysis metrics provided in Table 7.6 show a full $FOV_{ext}$ was measured as 31.4° and the system presented images with a low distortion of 0.02. Subjective analysis of the imaging performance is very favourable although the shorter wavelength is less susceptible to specular reflection. The *Zeiss FF4* did not have any measurement tools which could be analysed.

Table 7.6 Metrics for Zeiss FFA Fundus Camera

| Device | $FOV_{arc}$ (mm) | $FOV_{int}$ (°) | $FOV_{ext}$ (°) | Δ M (%) | Conformal |
|---|---|---|---|---|---|
| Horizontal | 9.0±0.05 | 31.6±0.02 | 43.0±0.04 | -0.02±0.2 | Yes |
| Vertical | 8.9±0.05 | 31.2±0.02 | 42.6±0.04 | -0.02±0.2 | Yes |

## 7.4 Comparison of Distortion between the Heidelberg and Optos SLO

It is clear from the *Heidelberg* images in Section 7.3.1 that the optical system is rotationally symmetric, hence the distortion or warping present in the images has rotational symmetry about the optical axis, and that the image distortion is purely a function of distance to the fovea. By contrast, since the unprojected *Optos* system lacks rotational symmetry, the degree of distortion present in an **opto**map does not only depend on the distance of the retinal feature to the fovea but also on its angular position. To compare the geometric distortion of both systems, we can measure the apparent locations of retinal features along the horizontal and vertical directions that intersect the fovea. The apparent locations of the rings along the horizontal and vertical directions have been annotated in Fig. 7.13 and compared for both systems against the true locations the rings, which have been determined from a precise optical model of the phantom eye.

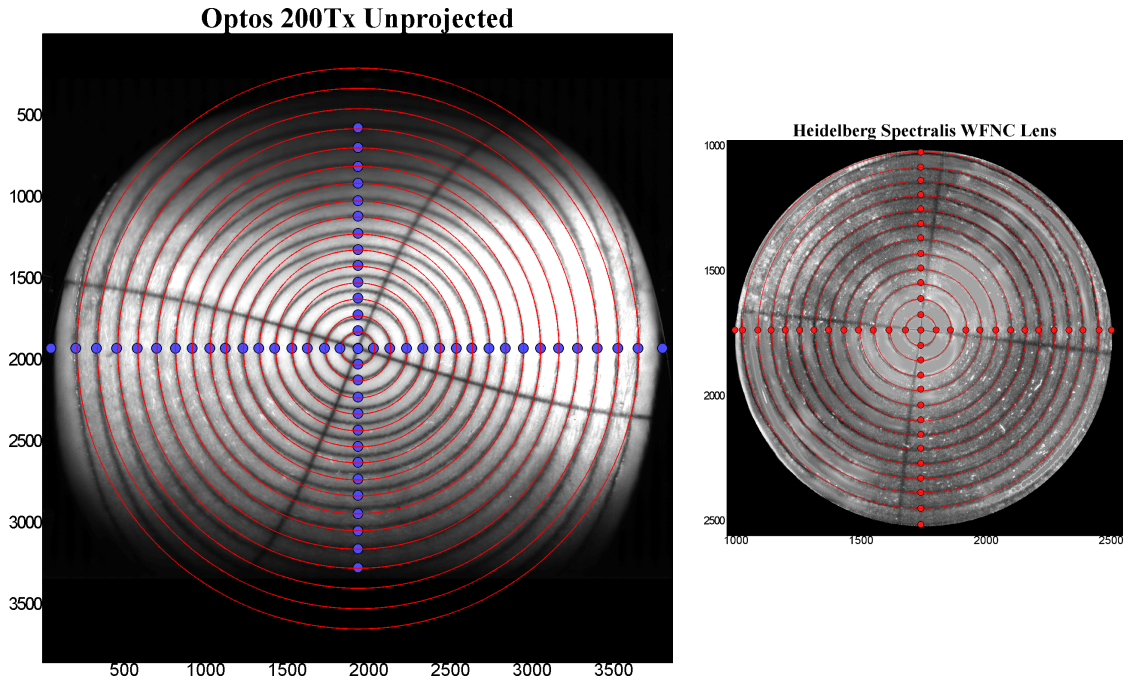


Fig. 7.13 Reflectance Images from the (Left) *Optos 200Tx*, red channel and (Right) *Heidelberg Spectralis* non contact near infra-red channel. The annotation shows the automatic selection of rings in the image. As the *Spectralis* suffered from high specular reflection on-axis processing of the image was required to mitigate saturated areas via extrapolation of the cross and first ring. Where the right image appears smooth, saturated pixels were replaced by the mean pixel intensity, this was found to produce stable segmentation of the rings.

The distortion for the horizontal and vertical directions for both systems are shown in Fig. 7.14 (a) and Fig. 7.14 (b) respectively. The following conclusions can be drawn from this analysis:

1. The *Heidelberg* system suffers from minor barrel distortion: The apparent spacing between the rings become smaller with field of view.

2. Along the horizontal direction, the *Optos* system suffers from pincushion distortion as the apparent spacing between the rings becomes larger with an increase in field angle. The *Optos* system should not in principle suffer from geometric distortion along the horizontal direction since it is a mirror-based system with circular symmetry along any horizontal axis. The majority of the distortion has been shown to match what is induced by the curvature of the retina in Fig. 7.14. The minor additional distortion may arise due to the acceleration and deceleration in the scanning mirror.

3. The distortion along the vertical direction of the **opto**map is non-linear with field angle and substantially greater than in the 102° *Heidelberg* system. Post-detection image processing is required to remove it. By applying a stereographic projection to the **opto**map we can remove this vertical field-varying distortion and obtain a mapping of the retina is rotationally symmetric and from which meaningful geometric measurements can be obtained.

4. The projection of the retina provided by the 102° *Heidelberg* is conformal (angles are preserved) but it is not stereographic as the ring spacing does not increase with field angle.

## 7.5 Field of View Comparison of Commercial Systems

The BE-Target was used to measure the maximum FOV and the distortion of the images produced by five ophthalmic devices and modalities, as shown in Fig. 7.15, following any internal distortion correction executed within the ophthalmoscopes. The results from analysis of these images are provided in Table 7.7.

The image shown in Fig. 7.15 (a) was acquired on the *Optos 200Tx* SLO [10] and is presented with a stereographic projection that preserves angles between features within the image. This notation is a deviation to previous sections which based the FOV on the maximum diameter; however, as is convention in *Optos* marketing-literature the FOV are provided as the maximum radius measured. This internal field angle was measured to be

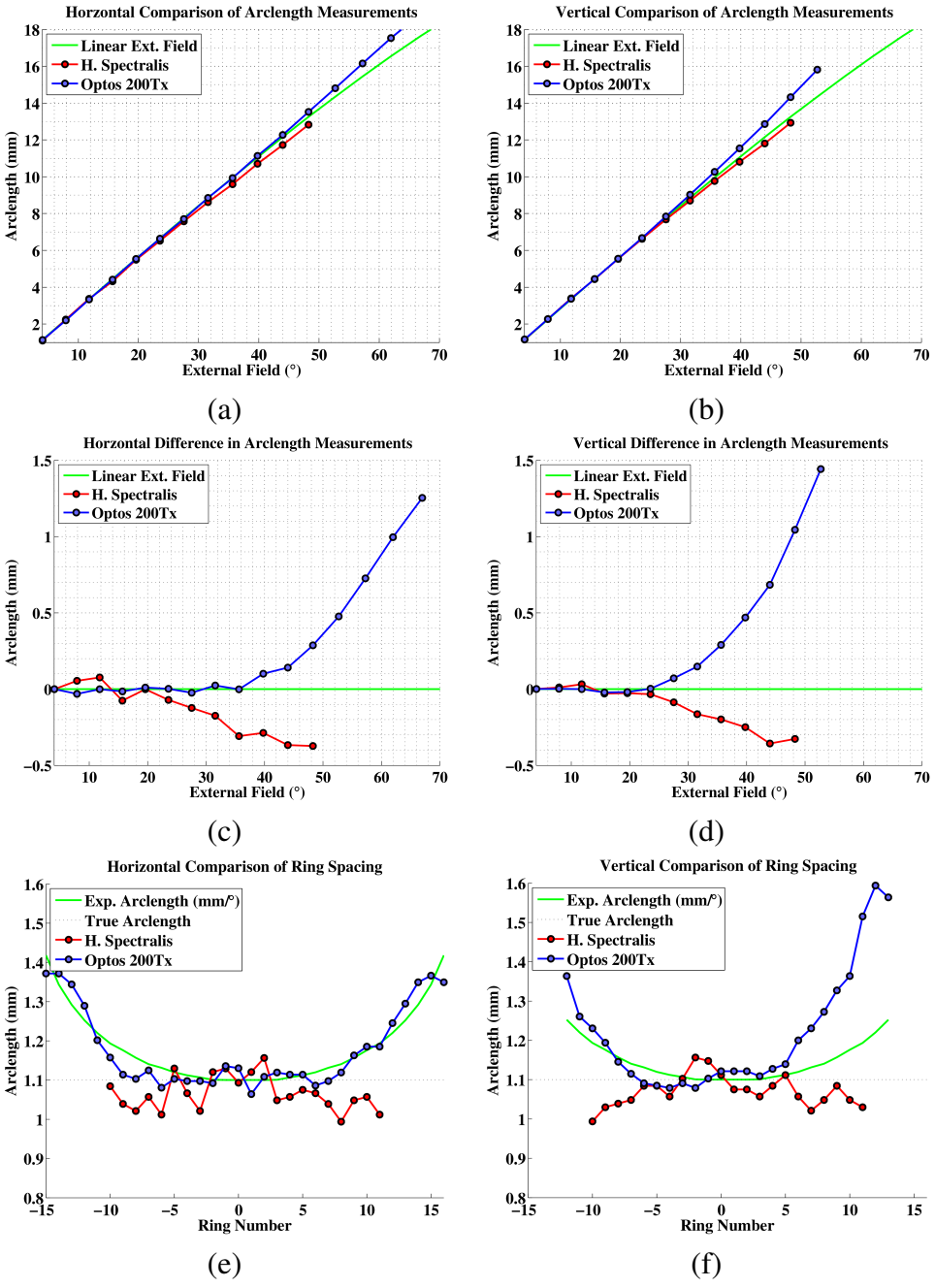


Fig. 7.14 Results of the wide-field distortion analysis of *Heidelberg Spectralis* and *Optos 200Tx* in the horizontal (Left) and vertical axis (Right). Fig. (a) shows the radius of each ring across horizontal axis calibrated to pixel scale of the first ring. Fig. (b) shows the same across the vertical axis. Fig.(c-d) are the difference in arclength from Fig. (a-b). Fig. (e) is a plot of the pixel spacing with the expected distortion for a linear scan in green. Fig. (f) shows the same in the vertical axis. These results show the asymmetric distortion in the original ***opto****maps*.

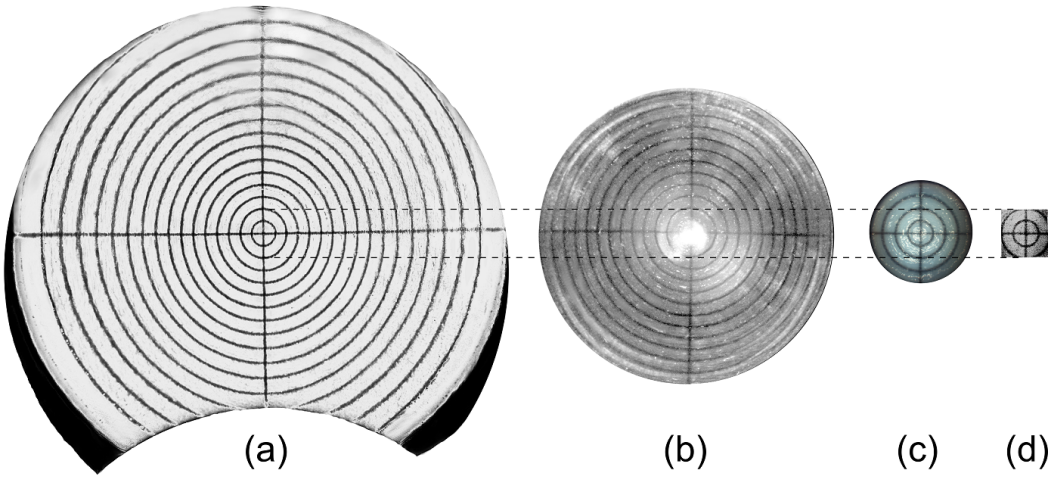


Fig. 7.15 **(a)** Ultra-widefield SLO reflectance image shown using the *Optos 200Tx* with a stereographic projection. **(b)** Reflectance image from *Heidelberg Spectralis* with a wide-field non-contact lens designed for fluorescence imaging. **(c)** *Zeiss FF4* Fundus Camera. **(d)** en-face view of a C-scan of the BE-Target acquired using the Optos *OCT SLO*.

Table 7.7 FOV and distortion comparison of the five device modalities from the images shown in Fig. 7.15. The change in magnification of the *Optos 200Tx* and *Spectralis* use the furthest ring visible in both devices (12). The uncertainty for the *Optos* products is given as the variance measured above, otherwise the measurement error is from the WPE feature size.

| **FOV** | **SLO** | | **Fundus Cam.** | **OCT** | |
|---|---|---|---|---|---|
| | Optos 200Tx | *Spectralis* | Zeiss FF4 | Optos (3D) | Optos (2D) |
| $FOV_{arc}$ (mm) | $39.8 \pm 0.5$ | $27.8 \pm 0.1$ | $9.0 \pm 0.05$ | $4.9 \pm 0.05$ | $6.8 \pm 0.05$ |
| $FOV_{int}$ (°) | $190.2 \pm 2.4$ | $132.7 \pm 0.5$ | $43.0 \pm 0.2$ | $23.4 \pm 0.2$ | $32.5 \pm 0.02$ |
| $FOV_{ext}$ (°) | $153.7 \pm 2.3$ | $102.3 \pm 0.4$ | $31.4 \pm 0.2$ | $17.4 \pm 0.2$ | $23.8 \pm 0.02$ |
| $\Delta M(\%)$ | $+7.5 \pm 0.4$ | $-3.5 \pm 0.4$ | $-1.6 \pm 0.7$ | $< 1.0$ | $< 1.0$ |

$\pm$ 99.9 $\pm$ 0.5°, which is in agreement with the field angle published by *Optos* of 200° for the 200Tx.

The image shown in Fig. 7.15 (b) was acquired on a *Heidelberg Spectralis* SLO with a non-contact wide-field lens. This lens is designed for fluorescence imaging and therefore Purkinje reflections and lens reflex are present at the centre of Fig. 7.15 (b). The maximum external field angle was measured to be $\pm$ 51.6 $\pm$ 0.4°, which is in agreement with the specified field angle by *Zeiss* of 102° when using the lens attachment. The Zeiss FF4 fundus camera and the Optos *OCT SLO* using a raster C-scan shown in Fig. 7.15 (c) and Fig. 7.15 (d) have substantially narrower field of view than the SLO devices from *Optos* and *Heidelberg* at $\pm 12.0 \pm 0.2°$ and $\pm 8.6 \pm 0.2°$ respectively. A more detailed analysis of the optical properties of OCT systems is provided in the next chapter.

## 7.6 Conclusion

In this chapter we have introduced a method for the acquisition, analysis and comparison of both narrow-field and wide-field ophthalmic systems. This method was used to measure the variation betweens *Optos* systems and showed substantial variability. This method was again used to validate a prototype defocus-correction technique and the result showed a substantial improvement in the vertical FOV. Finally an investigation was conducted to see how well the phantom eye could characterise competitor ophthalmic systems. These measurements were then used to comparatively assess the performance of the *Optos* system.

The investigation into the variation between *Optos* systems found that across the four metrics assessed; image decentre, FOV, distortion and contrast, there was a higher than expected variation. The *Daytona* showed a lower decentre than the *200Tx*, which was unexpected as the *200Tx* has more options for alignment during assembly. Further investigation showed that experimental error could not account for the scale of the decentre in the 200Tx. Further measurements will be required to isolate the cause of the high variance in the centre in both systems. The high standard deviation in both FOV and distortion of 2% and 6% respectively, indicates that to implement accurate measurements in an *Optos* system will require the calibration of each device both post assembly or device servicing. This solution is not yet considered practical as it would increase the measurement software complexity, the device build time and raises concerns over the regulatory approval for the measurement software. Another option is to reduce the acceptable module tolerances; however, this will increase the cost of manufacturing the device. As each system should be capable of the same vertical contrast roll-off the large variability measured indicates that the alignment pass-criteria for a device is current too low or not correctly implemented. A similar measurement was not possible on the *Daytona* sample; however, subjective analysis showed improvement in roll-off performance. The improved contrast in the *Daytona* compared with the *200Tx* indicates that the reduced degrees of freedom in alignment of the pin-hole in this modular system are favourable for consistent high performance.

The fields of view and distortion were measured using the WPE for *Heidelberg Spectralis* and *Carl Zeiss FF4*. The maximum FOV of the *Spectralis* and *Carl Zeiss FF4* in the 102° configuration was measured to be substantially smaller than for *Optos* systems. The extent of warping for the 102° field is comparable across the horizontal axis of the *Zeiss* and *Optos* systems. Across the vertical image axis, the displacement in the *Optos* system is substantially greater; however, this can be removed by re-mapping the image onto a conformal projection with rotational symmetry, e.g., stereographic projection, which is now standard in *Optos* systems.

Severity and origin of reflections in *Heidelberg* images comprise of reflection artefacts from lenses in the system during the infra-red reflectance imaging. The montaging quality for phantom eye and human eye suffers from many occurrences of ghosting and blending artefacts and reflections both with a phantom eye and human eye. Measurement capability in physical units are available only with 30° and 55° capture types; they are disabled in 102° and montaging capture types. The accuracy of measurements is relatively high (0.7% for 30° and 2.6% for 30°); however, worse than the potential capability of the *Optos* system for the same field which was measured to be below 0.2% (see Fig. 7.14 (c) and (d)).

The method of using the WPE to characterise systems was successful; however, throughout this chapter a number of improvements to the method are apparent. Firstly, the addition of a high-precision feature that has had dimensions verified to below 10 µm and includes sharp edges would greatly improve the accuracy of the distortion measurement. The current error from this measurement is too close to the true value to be confident about the results. Secondly, the distortion measurement by convention is only accurate for radially symmetric systems and therefore requires repeated measurement along different axes for comparison. The use of the WPE to measure FOV distortion is well suited to a metric based on area as well as radius for rotationally unsymmetrical devices like the *200Tx* and *Daytona*. This new area metric for distortion would require further consideration as to the most effective implementation. Finally, the plastic target suffers from substantial specular reflection. To remove this would require an investigation into either new materials, post-fabrication surface roughening or integration of filters into the eye may reduce specular reflection. Care must be taken not to distort the features of the ocular phantom when implementing these solutions.

# Chapter 8

# Performance Comparison in Commercial & Prototype OCT Systems

## Chapter Summary

This chapter reports both a comparison of the image quality of commercial OCT devices using the WPE and an investigation on how image quality impacts on the measurement performance of commercial OCT devices. Images were acquired of the AL-Target on the *Optos OCT/SLO*, *Heidelberg Spectralis*, *Carl Zeiss Cirrus* and *Optovue iVue*. The images were exported using the native software of each device and analysed in *Matlab* to see if there was any correlation between the variation in image performance and measurement accuracy. A summary table of the key performance metrics is compiled at the end of the first section for a comparison between devices.

Navigated images across an $\text{FOV}_{\text{ext}}$ of $\pm 40^{\circ}$ were acquired on each of the commercial devices to investigate if the predicted artefacts stated in Chap. 4.1; a loss in the optical efficiency, variation in birefringence, insufficient imaging range and image distortion, would manifest in images images acquired off-axis. In addition, these images were used to investigate what further requirements are needed to design and calibrate a wide-field OCT system that can provide consistent measurement between on and off-axis. Finally, images were acquired from the final *Optos* prototype device, referred to as *Lotte*. This acquisition shows that high-performance imaging is possible across a wide-field while using an ellipsoidal-scan system. Furthermore, the FOV and radial distortion is measured for this prototype using the WPE.

## 8.1 Performance Comparison On-Axis in Commercial OCT Systems

The WPE is designed to allow the optical performance of a device to be assessed based on the images acquired of the customisable targets in the WPE. As discussed in Chap. 7, images of commercial systems were captured both on-axis and then again with tilts of -40° to 40° of both the BE-Target for reflectance imaging and the AL-Target for OCT imaging. It would also have been advantageous to take repeated acquisitions for each field to allow the measurement of the intra-device variation; however, the clinician with access to the *Heidelberg Spectralis*, *Carl Zeiss Cirrus* and *Optovue iVue* had a limited time with each device. This dataset is still be effective for analysing the method used to measure the performance of OCT devices and to indicate aspects of the phantom design that should be improved.

### 8.1.1 Measurement Accuracy of the Optos OCT/SLO

The 60/120 μm AL-Target was used with the WPE to assess the accuracy of the *Optos OCT/SLO* [10] for measurement of the on-axis thickness of retinal layers, such as the RNFL. The *Optos OCT/SLO* provides both axial measurement of ring scans as well as topographic thickness maps. Segmentation of a human RNFL using this device was shown previously in Fig. 5.2. The layer-thickness measurement tool on the device was used to segment the anterior-side, 120 μm scattering layer in the AL-target as indicated by the green lines in Fig. 8.1.

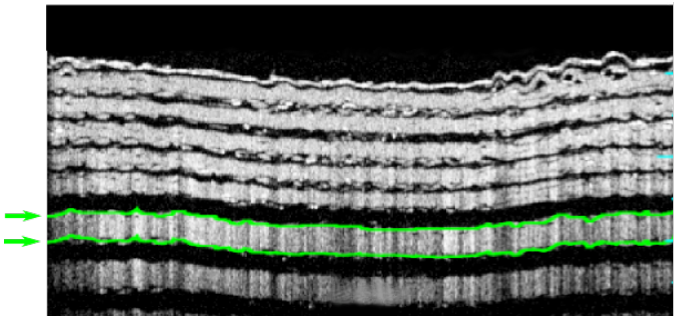

Fig. 8.1 Circular OCT B-scan of the Target B with a 10.7 mm circumference acquired using the method as Fig 5.2. The first 120 μm layer has been segmented; shown in green.

Automated segmentation was repeated to acquire 30 images of the AL-Target from the same system to provide a measurement of the variation in the segmentation. Minor discontinuities in the segmentation were caused by specular reflections and were corrected

manually in the device software. The mean in-air thickness for this layer was measured as 130.1 $\pm$ 5.6 µm, 7% greater than the calibrated measurement of 121.3 µm described in Section 6.4.4. The automated layer thickness was scaled to account for the ratio of the refractive index of *Fullcure720* (1.48) with that of the retina (1.36). Unfortunately, the discontinuities in the 60 µm layers prevented automated segmentation of this layer using the device software.

Manual segmentation of the 120 µm layer was also performed by myself across 30 images to compare against the previous automated segmentation and investigate if the rough surface of the target influenced the measurement of layer thickness. The mean in-air thickness for this layer was measured to be 127.5 $\pm$ 1.7 µm, 5% greater than the calibrated measurement. The difference in thickness measurement for both layers is less than the axial pixel spacing for the device of 6.3 µm and could be caused by a difference in perceived edge of the layer. However, the manual measurement of 127.5 $\pm$ 1.7 µm is still greater than the calibrated measurement of 121.3 µm, meaning that the *Optos OCT/SLO* has a small, sub-resolution error in agreement with the calibrated measurement.

The AL-target was reprinted using 100 µm layers to more-accurately resemble the RNFL for automated top-layer segmentation. This target is shown imaged in Fig. 8.2 (a) and segmented as indicated by the green lines in Fig. 8.2 (b). This phantom was used for the *Heidelberg Spectralis*, *Carl Zeiss Cirrus* and *Optovue iVue*. Limited access to this device prevented a full repartition of the above experiment with the new target. The performance comparison extracted using the image in Fig. 8.2 (a) is provided in Tab. 8.1 at the end of Section 8.1.

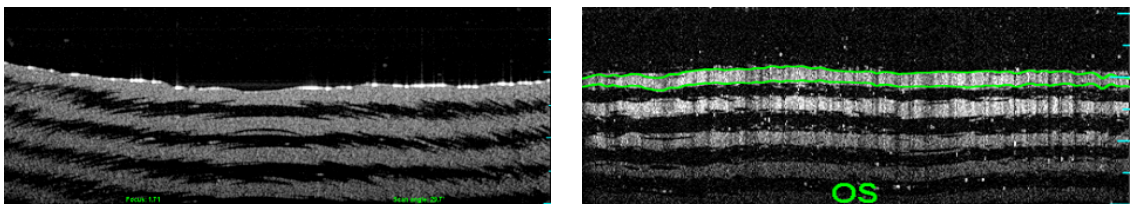


(a) (b)

Fig. 8.2 (a) B-scan of the 100 µm - Bullseye Target used in the device comparison. (b) Successful automated segmentation ring scan from the *Optos OCT/ SLO*

### 8.1.2 Measurement Accuracy of the Heidelberg Spectralis

The 100 µm AL-Target was used in the WPE to assess the accuracy of the *Heidelberg Spectralis* OCT system [4] for measurement of the on-axis thickness of retinal layers, such

as the RNFL. The *Spectralis* provides measurement in both, radial scans through the macular and ring scans of the RNFL. Automated segmentation was performed on a radial B-scan of the AL-Target as shown in Fig. 8.3 (a). The automated segmentation selected the water-target interface and the posterior side of the fourth scattering layer (highlighted in red). The mean thickness of the *Spectralis* measurement was 758 $\pm$ 29µm calibrated for the refractive difference of *Fullcure720* (1.48) with that of the retina (1.36), corresponding to a error in thickness of 8%.

Segmentation of the seven layers was repeated on the exported B-Scan in an algorithm, provided in Appendix B.4 that was developed for use in *Matlab* and is shown in Fig. 8.3 (b). The mean axial thickness of this segmentation was measured in Matlab to be 700 $\pm$ 23µm when calibrated for the refractive index of the plastic. The two measurement profiles are plotted together in Fig. 8.3 (c). The systematic error in the *Spectralis* is relatively modest and is likely to have been increased by the texture of the layers and the presence of saturated pixels increasing the apparent thickness of the edge. The limited time of the photographer did not permit the acquisition of repeated images which could have facilitated the evaluation of the reproducibility of *Spectralis* [151]. In addition, investigating the impact of changing variables such as focal position, FOV and the use of the BE-Target in the OCT images could have provided more conclusive analysis of measurement accuracy.

The software used to segment the image from the *Spectralis* provides both an axial and transverse measurement. This feature allows the transverse scale of the device to be compared with the value measured using the BE-Target in Chapter 7. The range of 9.0 mm provided by the plot in Fig. 8.3 (b) shows a strong agreement with the 8.9 mm arclength measured in the previous chapter. This feature is valuable as fabrication artefacts common across each of the images used in the dataset can be used with the measurement from the *Spectralis* image to measure the FOV in those devices. The full image performance metrics for the *Heidelberg Spectralis* can be found in Table. 8.1.

### 8.1.3 Measurement Accuracy of the Optovue iVue

The 100 µm AL-Target was used in the WPE to assess the accuracy of the *Optovue iVue* OCT system [190] for measurement of the on-axis thickness of retinal layers [191]. The *iVue* provides measurement in both rings scans as well as in topographic thickness maps. Automated segmentation was performed on an on-axis ring scan of the AL-Target as shown in Fig. 8.3 (a).

The segmentation of the highly-scatter layer had varied success, shown by the measurement profile in Fig. 8.3 (c). The segmentation at superior and inferior quadrants of the B-scan appears to accurate, where as in the nasal and temporal quadrants has substantially

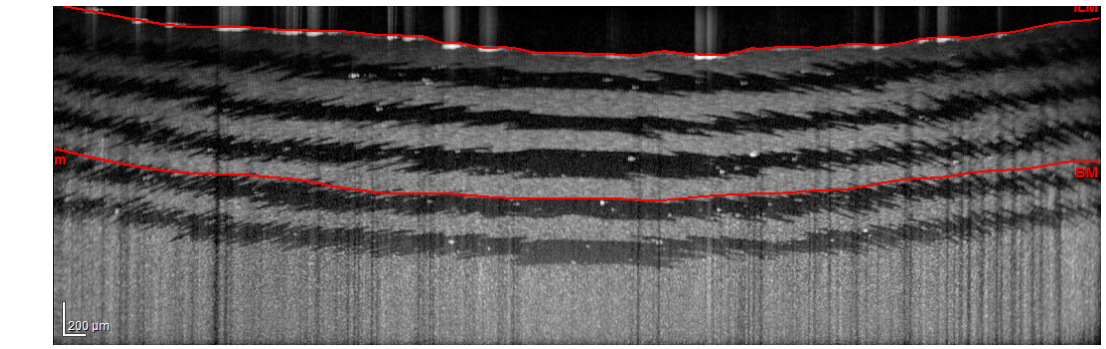


(a)

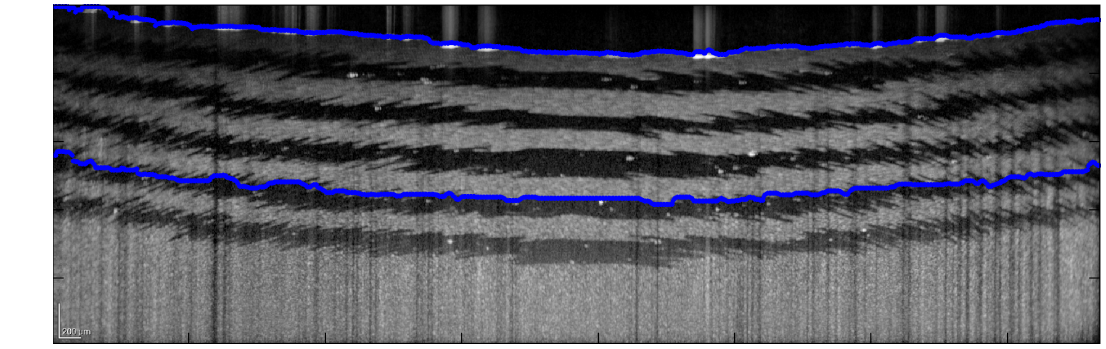

(b)

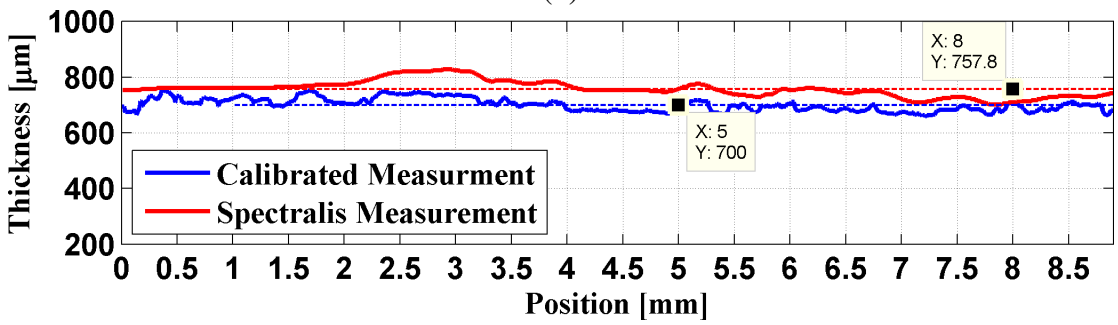


(c)

Fig. 8.3 (a) Image of AL-Target segmented using the software native to the *Heidelberg Spectralis*, shown in red. The total axial depth of this image was measured as 1.73 mm (in tissue). (b) Image exported without segmentation, segmented using an algorithm in Matlab, shown in blue (c) Plot of the thickness of the segmentation layers calibrated for the refractive index difference between plastic and tissue.

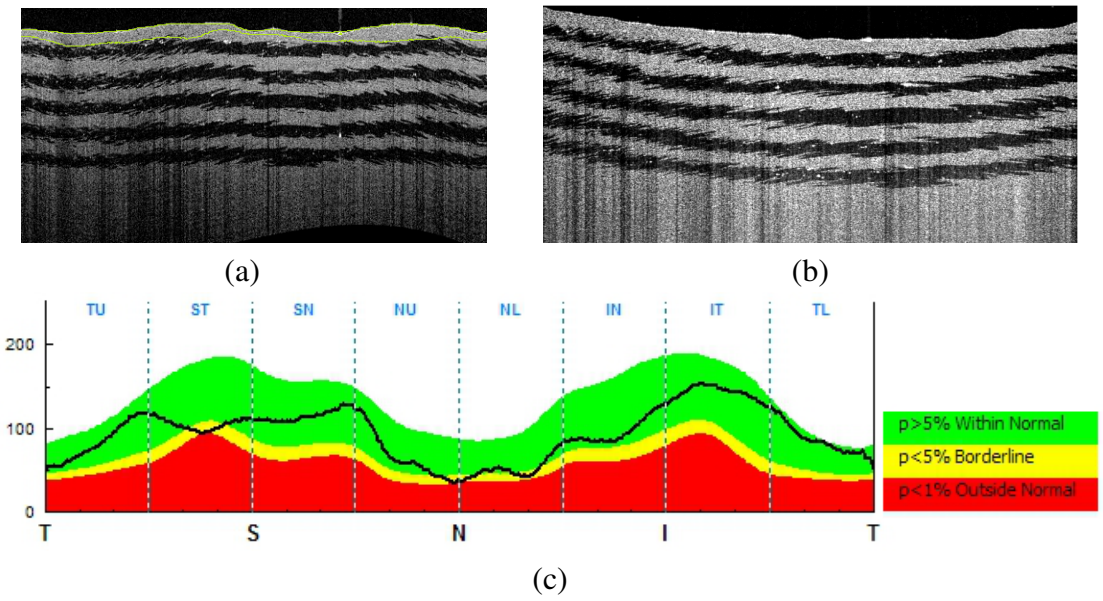


Fig. 8.4 (a) Ring scan segmented with the *iVue* software, shown in green. (b) Standard radial B-scan. (c) Thickness profile showing the normative database for the device, a healthy patient would have an RNFL thickness in the green region. The thickness profile shown in black appears to follow the normative thickness.

over estimated the measurement. The measured thickness appears to follow the normative thickness shown by the green bands on in Fig. 8.3 (c). The recorded thickness profile indicates that the measured thickness may have been altered by the software to provide a more normal looking profile. Segmentation algorithms are tuned to target a range of features to correctly identify the layer, such as intensity and location relative to other layers; however, any parameter that influences the measured thickness would reduce the accuracy of the device when segmenting pathology. To confirm if the *iVue* software attempts to fit a normative shape requires additional measurements to investigate if this profile is maintained. In addition, further images acquired after rotation of the WPE would ensure that the target texture is not causing the poor segmentation.

The mean thickness of the top layer was measured in the superior and inferior quadrants of the B-scan to be $104 \pm 16$ µm, when calibrated for the refractive difference. This value is 4% above the correct thickness is below the error of this measurement. A radial scan is acquired as shown in Fig. 8.3 (b) for the comparison of image performance metrics provided in Table. 8.1. The roughness of the layers in the B-scan indicate that the WPE was tilted with respect to the device by between 5° to 10°. This error occurred because the en-face imaging accompanying the device failed during this imaging session. The tilt is likely to

have minimal impact of the image assessment as the reduced contrast in layers provides only a minimal reduction in specular reflection.

### 8.1.4 Measurement Accuracy of the Carl Zeiss Cirrus

The 100 µm AL-Target was used in the WPE to assess the accuracy of the *Carl Zeiss Cirrus* OCT system for measurement of the on-axis thickness of retinal layers [192, 193]. The *Cirrus* provides measurement in both rings scans as well as topographic thickness maps. Automated segmentation was performed on an on-axis image of the AL-Target as shown in Fig. 8.3 (a). Unfortunately the image could not be exported on its own and the image shown was taken from measurement report and therefore is severely down-sampled. This reduced quality prevents quantitative analysis of the segmentation performance in *Matlab*. The mean thickness measured by the *Cirrus* device was 82 $\pm$ 12 µm when calibrated for the refractive difference, which is below the correct thickness of 100 µm. This discrepancy is most likely due to poor segmentation of the AL-Target based on the measurement profile displayed in Fig. 8.3 (a). The thickness profile provided by the segmentation report is provided in Fig. 8.6.

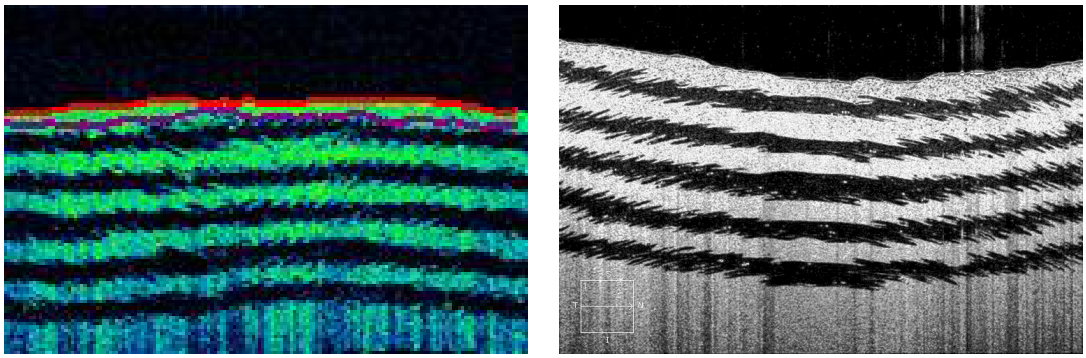

(a) (b)

Fig. 8.5 (a) Segmented ring scan of the 100 µm AL-Target, was severely down sampled when exported. (b) B-scan central to the field.

### 8.1.5 Comparison of On-Axis Performance

In Chapter 5 the key performance metrics for OCT are reviewed and a description on how they can be measured is listed in Table 5.1. These performance metrics were measured using the WPE and are shown in Table 8.1 for the *Optos OCT/SLO*, *Heidelberg Spectralis*, *Optovue iVue* and *Carl Zeiss Cirrus* from images shown in figures 8.2, 8.3, 8.4, 8.5. The measurement of the SNR is replaced by three different image-quality metrics which describe

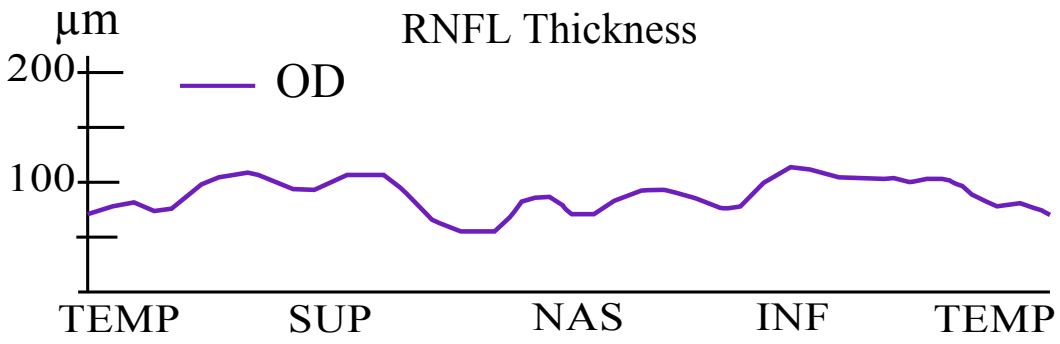


Fig. 8.6 RNFL profile from Fig. 8.5 with a mean thickness recorded as 82 ± 12 µm.

the information content within the images. This omission is because both the enhancement, averaging and compression of the final images mean that the SNR extracted is unlikely to be related to the measurement performance of the device. In addition, the measurement of distortion has also been omitted as image distortion is was shown in Chapter 5 to be not substantial for $FOV_{ext}$ of $\pm 40^{\circ}$ measured in this chapter. This comparison is provided to demonstrate the benchmark for OCT performance for developing a new system and make it easy to see if there is a correlation between imaging performance and measurement performance.

The **A-scan rate** in Table 8.1 was reproduced from the manufacturers specifications. These values show that the *Spectralis* has the fastest A-scan speed of the compared devices. Commercial devices were released in 2013 that have a higher A-Scan rate than the *Spectralis* [8, 194]; however, as *Heidelberg* was a market leader for A-scan speed between 2007 and 2013 the *Spectralis* can still be considered performance-leading in this comparison [62]. In addition, the use of retinal tracking and registration to extend the scanning duration without motion artefacts means that the *Spectralis* is likely to yield the best performance in this comparison.

The device with the greatest number of pixels per image including the most dense **pixel pitch** was found to be the *Spectralis*. This feature improves contrast in the image by reducing the spread of intensity across an image and also reduces the impact of speckle as coherent interference dominates a smaller pixel. Typically manufacturers have a pixel pitch of half the spot size to minimise any aliasing of high frequency features. It is possible that the images could have been interpolated to appear to have a higher pixel pitch; however, this is unlikely as intensity-induced intensity spikes across could not be observed across multiple pixels.

The device with greatest **imaging depth**, by a small margin, was the *Carl Zeiss Cirrus* at 1.8 mm. This is more than is necessary as the retina is only around a 0.5 mm thick, however, will be important when attempting to navigate off-axis because of the curvature of the retina.

| Metric | Optos OCT/SLO | Optovue iVue | CZ. Cirrus | H. Spectralis |
|---|---|---|---|---|
| Optical Performance Metrics | | | | |
| A-Scan Rate (Hz) | 27,000 | 26,000 | 27,000 | 40,000 |
| Transverse Samples | 656 | 870 | 750 | 1535 |
| Axial Samples | 220 | 385 | 500 | 496 |
| Trasnverse Pitch (μm) | 10.5 | 7.7 | 8.0 | 5.8 |
| Axial Pitch (μm) | 6.3 | 4.5 | 3.6 | 3.5 |
| Imaging Depth (mm) | 1.40 | 1.73 | 1.80 | 1.73 |
| Intensity Roll-Off | 54% | 84 % | 73 % | 44 % |
| FOV (mm) | 6.86 | 6.68 | 5.97 | 8.83 |
| Axial LSF (μm) | 18.2 | 12.0 | 8.3 | 14.5 |
| Transverse Resol. (μm) | 21.2 | - | - | - |
| Image Quality Metrics | | | | |
| Entropy | 0.59 | 0.19 | 0.05 | 0.12 |
| $\sigma\bar{I}_{pixels}$ | 49.5 | 56 | 82.3 | 44 |
| Hist. Ratio | 1.42 | 1.21 | 1.63 | 1.76 |
| Measurement Performance | | | | |
| Error in Thickness | +7% | +4% | N/A | +8% |

Table 8.1 Optical performance metrics that were extrapolated from the AL-Target imaged using the *Optos OCT/SLO*, the *Optovue iVue*, the *Carl Zeiss Cirrus* and the *Heidelberg Spectralis*. Measurements are calibrated for imaging performance in tissue. Intensity roll-off (measured as the fall in intensity across the line-spread functions with depth), appears to rise for the *Spectralis* as the focal position is not of the vitreo-target interface.

The *Optovue iVue* appears to have the intensity 'roff-off' with the ratio in intensity of the first and deepest observed layer being 84%. Although, the roll-off performance in the *Spectralis* appears to increase in intensity for deeper layers, as shown in the Appendix. A.5, this artefact has resulted because the plane of best focus of the device was positioned on the last layer by the operator. The device with the *widest-FOV* is the *Spectralis*. This feature is coupled with a dense pixel pitch meaning that there is no loss in spatial sampling as a result of this larger area imaged.

The **axial resolution** of the system was measured by analysing the line-spread function of a flat region of the vitreo-target interface, and calibrating to show the in-tissue value. This measurement will be limited by axial pitch of the system, for example, the measurement of the LSF for the *Cirrus* is approximately equal to double the pitch (the digital limit to which the system can image). The *Cirrus* performs best in this analysis although the accuracy of this method to measure optical performance requires not being limited by the digital sampling. The specified axial resolution for the *Optos OCT/SLO*, *iVue*, *Cirrus* and *Spectralis* are 6µm, 5µm, 5µm, 4µm respectively; however, only *Optos* and *Heidelberg* present this value as digital resolution (pitch). Resolution is defined as the minimum separation at which two reflectors are resolvable. Provided the image is linear in intensity then the LSF is a more accurate representation than the pitch [17].

The **transverse resolution** was measured on the *Optos OCT/SLO* in Sec. 5.3.1, and again using the USAF-target inserted into the WPE. Elements 5 (horizontal) and 6 (vertical) were the minimum feature size to exceed the noise of 4.1%, measured from the surrounding ceramic as the standard deviation of the normalised intensity. This corresponds to a resolution between 17.5 µm - 19.7 µm, approximately double the pixel pitch, measured as 10.5 µm.

The **measurement accuracy** was observed to be poorerst on the *Spectralis* at 8%; however, *iVue* would have been substantially worse had all four quadrants being included in the final metric and the performance of the *Cirrus* is unknown as a result of the failed segmentation. The accuracy of a measurement is only important if its deviation from the truth could cause a change to a disease diagnosis. From this analysis it is feasable that diagnosis, or more likely a measurement of disease progression, could change as a result of measurement across different devices. This problem can be mitigated in the industry by requiring that normative databases to be collected published each device with the use of the WPE or similar, but narrow-field phantoms, like the one from Baxi el al. [173] would allow measurement results to be transferred between devices. Images and measurements of the Baxi model eye were acquired on the *Optos OCT/SLO*, this is included in Appendix A.6.

Without repeated measurements and reliable segmentation across more systems, it is difficult to identify whether the of loss in accuracy is as a result of insufficient calibration or

as a consequence of any variations in imaging performance. The methodology reported in this chapter does show that images of the WPE can be used to characterise image performance and can be used to predict how prototype systems compare with established device benchmarks. However, a greater sample size will be required to assess the acceptable levels of variation in image performance of a device. The source code for this analysis which includes, B-Scan flattening, simple-segmentation and the measurement of quality metrics is included in Appendix. B.4.

## 8.2 Navigated OCT

### 8.2.1 Off-Axis Performance of the Optos OCT/SLO

The BE-Target was used to assess the distortions present in navigated OCT images of the human eye in which wide-field images are constructed from a montage of narrow-field images. The images were captured on an *Optos OCT/SLO* that has an imaging depth of 1.29 mm in water. The navigation of the WPE was achieved by rotation of the WPE by 10° about the centre of the iris and manual adjustment of the reference-arm OPL. A montage image of the BE-Target with an internal FOV of a 180° is shown in Fig. 8.7. The OPL required to image the entirety of the BE-Target was $5.4 \pm 0.1$ mm which is in reasonable agreement with the 5.2 mm for the optical model in Section 4.4. The full external-FOV required to image the WPE was measured to be $\pm 70 \pm 2°$, which is also in agreement with the modelling. The consensus with modelling is critical for the use of the WPE to calibrate optical and geometric aberrations in wide-field images during automated scanning protocols.

Several properties of OCT images produced from navigated imaging are evident from the B-scan image of the WPE in Fig. 8.7. Firstly, the FOV of each component varies with field angle; from $\pm 12.0°$ for an on-axis image to $\pm 4.7°$ for the furthest off-axis image. Secondly, the off-axis components have a reduced signal-to-noise ratio as a result of higher levels of optical aberration, principally astigmatism and defocus. Finally, this form of navigation results in a change in the radial magnification of $+6.3 \pm 0.4\%$ when considering only the transverse axis of the B-scan. However, this distortion is substantially higher when measuring along the arc-length of the anterior side surface ($+25.5 \pm 0.4\%$) or the posterior-side surface ($+20.9 \pm 0.4\%$). This variation between the anterior and posterior distortion across a modest 0.6 mm axial thickness indicates that the transverse measurement in the retinal periphery in OCT will require calibration for the axial eye-length.

Early wide-field images from the integration of OCT into the COE and Daytona, see Fig. 3.14 and 3.21, revealed what appeared to be thinning of the retina off-axis. It was not

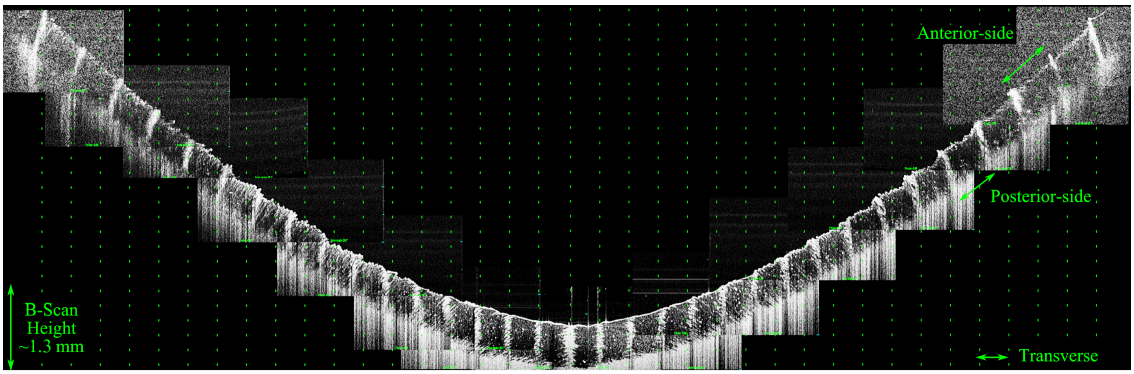


Fig. 8.7 A montaged image of the entire hemisphere of the BE-Target, in OCT configuration, displaying a 37.7 mm B-scan. The green dots have been provided to show the transverse distortion within the image. The number of pixels between each ring increases away off-axis.

apparent whether this feature was caused by anatomy or artefact. Modelling reported in Sec. 4.5 indicated that measured thickness would actually increase with FOV, by up to 17% due to oblique incidence. Plotting in Fig. 4.4 indicating that qualitative inspection of images would give the impression of layer thinning, however, this would not be present in images flattened to remove curvature. The flattening algorithm in the OCT analysis code was applied to the images used to create a montage image of the BE-Target in Fig. 8.7. The images were lined up together to investigate if there was an appreciable change in the thickness of the BE-Target with field angle, which is shown in Fig. 8.8.

As can be seen in Fig. 8.8 (b) there is a 13.4% rise in the thickness from 0.6 mm to 0.68 mm, which is slightly below the estimated value of 17%, and could be a result of either the fabrication precision or the apparent increase in LSF shown in Fig. 8.8 (a) for large field angles. This increase in thickness, although moderate should be considered when comparing pathology to measured off-axis to normative sizes for on-axis pathology.

To investigate the how the transverse resolution changes with field angle the line-spread function (LSF) was measured across a $\text{FOV}_{\text{ext}}$ of $\pm$ 30° . The LSF is equivalent to the resolution performance of an imaging system, provided that the image being analysed has not been subject to non-linear image enhancement - such as thresholding or gamma correction. A Ronchi grating was printed on transparent Mylar polyester film (1.64), shown in Fig. **??** (f), and was attached to the cylindrical target, previously shown imaged in Fig 6.11 (f). Flexible planar-targets can be attached to a cylindrical shape to match the geometry of the eye, provided the imaging remains central along the axis perpendicular to the target curvature. The LSF of the *Optos OCT/SLO* was measured from the navigated images that were linear in

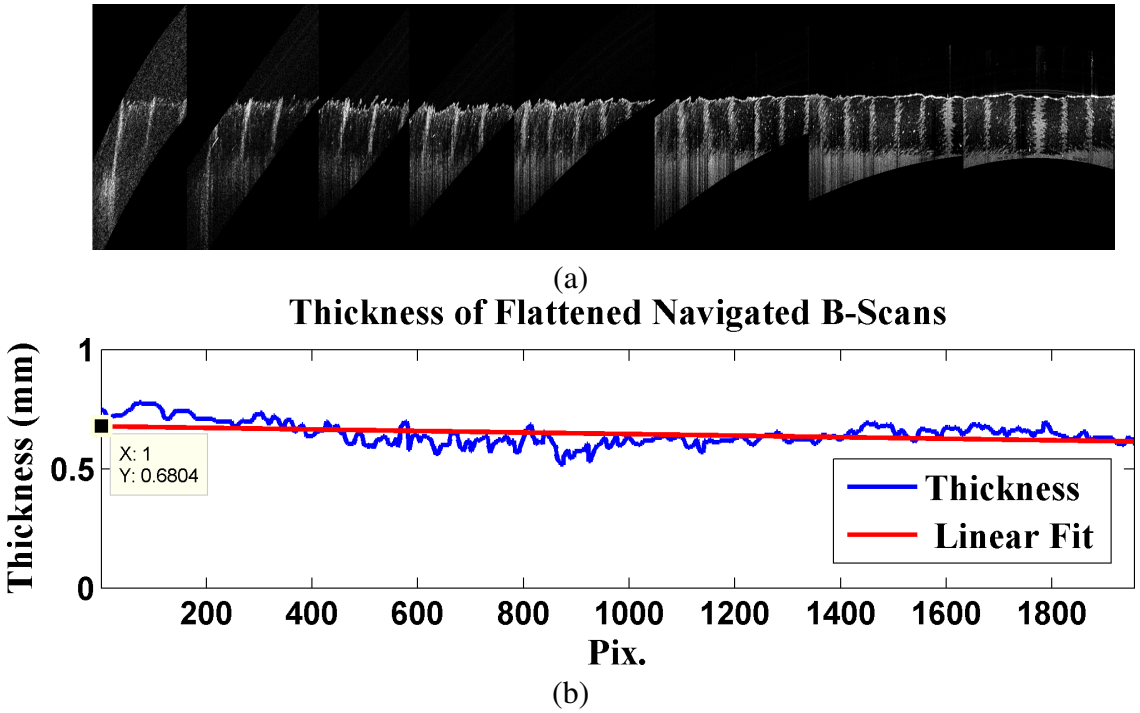


Fig. 8.8 Flattened and lined up B-Scans from Fig. 8.7. (a) The dark columns between samples have been removed and the transverse scale is not meaningful as the images where not registered. (b) Profile of the segmented 0.6 mm thick layer in the BE-Target.

intensity, by taking the derivative of the transverse profile for each of the features highlighted in Fig. 8.9.

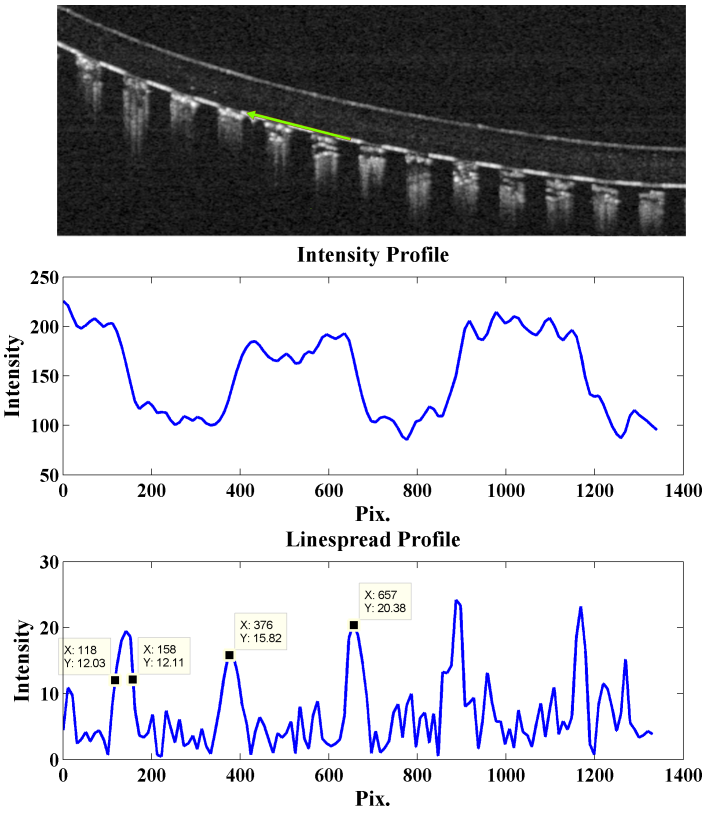


Fig. 8.9 OCT Image of the Ronchi Ruling on the Cylindrical Target. The edges of a diagonal profile were used for LSF measurement, highlighted in green. The feature width is 0.25 mm on a 0.25 mm thick film. The LSF is provided by the with of the peaks on the bottom image, with the scaling set by the number of pixels between.

The mean FWHM of the LSF was measured as 26.8 $\pm$ 1.8 µm, across an external FOV of $\pm$ 30° with no substantial variation recorded with respect to field angle. The difference between the LSF measured using the cylindrical target and the resolution limit measured using the USAF-Target is most likely caused by the increased contrast of the USAF-target features, (with the USAF target using chrome of white, rather than the cylindrical target using black ink on transparent plastic). The variation in resolution concurs with the modelling shown in Fig. 6.2 (b) that predicts that the WPE remains diffraction limited across this FOV. Measurement of the LSF for larger field angles was prevented by an increased noise obscuring the sampling of the feature transition. This limitation could be overcome by increasing the contrast of the bars or averaging pixels vertically along a substrate with similar scattering properties to tissue. The measurement of the LSF for device verification will be important

in the intra-device comparison and calibration of wide-field and navigated OCT devices; however, it has a limited capacity for commercial comparison where the user is unlikely to have full control over the parameters of image enhancement

### 8.2.2 Off-Axis Performance of the Heidelberg Spectralis

The *Heidelberg Spectralis* was used to image the AL-Target at different field angles by rotating the WPE around the pupil by integers of 20°. The images have been paired with navigated SLO images from Fig. 7.6 with Fig. 8.10. The maximum internal-FOV from navigating OCT in this device can be measured by counting the rings in this image to be ±52° (±39.8° external-FOV). The degeneration in the layers from the fabrication prevents valuable quantitative analysis; however, it is clear from the images that there is a substantial reduction in the coupled light in Fig. 8.10 (a) and (e). In addition, the device should present mirror artefact in both these images. As this artefact is not present, it can only be assumed that *Heidelberg* distinguish the positive and negative components of the Fourier transform and remove the unwanted artefact. This artefact is present in off-axis images from the *Optos OCT/SLO*, and *Cirrus* but it is not clear if present in off-axis images from the iVue, shown in Appendix. A.5.1.

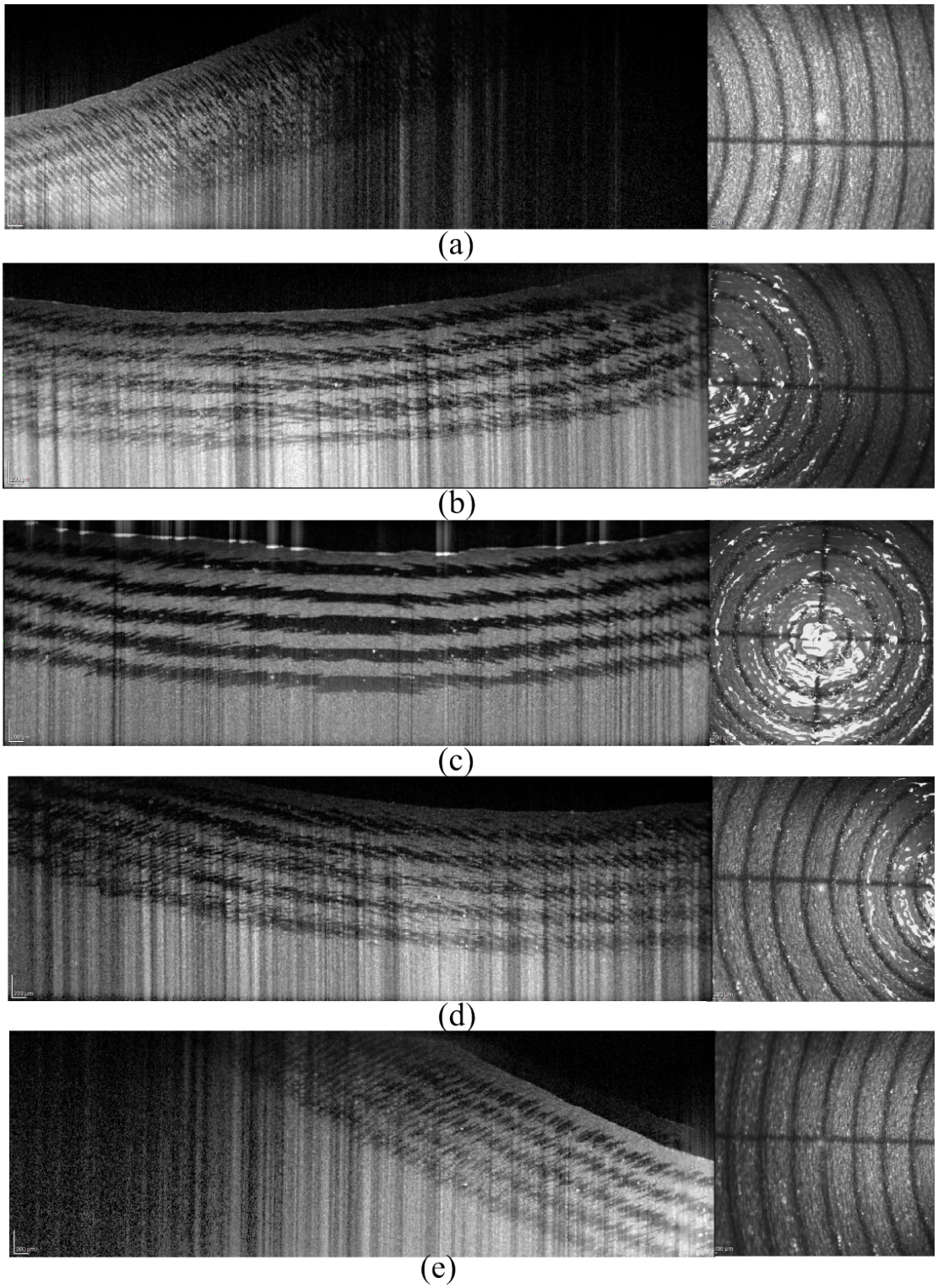


Fig. 8.10 Navigated *Spectralis* B-scans with the corresponding reflectance image from the 30° configuration discussed in Chapter 7.

## 8.3 Lotte - Optos OCT Prototype

In this section, the initial performance of the Optos OCT prototype is reviewed. The prototype system was named *Lotte*, as it was considered an early milestone in the project to develop ultra-widefield OCT, which was called Project Charlotte. The objective of this design was to create narrow-field OCT device that could be navigated within a $FOV_{ext}$ of $\pm 70^{\circ}$ (or a full-$FOV_{int}$ of $180^{\circ}$). The technology inside this final demonstrator was redeveloped entirely since the *Optos OCT/SLO*. The hardware control and supporting software for the *Optos Lotte* is still under development and therefore the images used for characterisation were exported as raw spectra and were converted to the spatial domain in *Matlab*. In addition, the galvanometers were driven using a sinusoidal signal to minimise the vibrations that are caused by the acceleration peaks of a more-typical saw tooth, used to drive the scanners at high speeds. This sinusoidal scan speed results in a non-linear pitch, particularly towards the edge of images. This distortion was not yet routinely removed from the images via cropping. This mid-development phase for the device resulted in limited access to the *Optos Lotte* for characterisation.

The *Optos Lotte* uses the same optical configuration as was described in Chapter 3 and with the vertical change in power of the ellipsoidal mirrors corrected using a liquid-lens. The scanning is provided by a configuration of three galvanometers that navigate a small-FOV across approximately the same FOV of the *Optos Daytona*. The first two galvanometers operate before the first ellipsoidal mirror that, as in the demonstrators, limits the external-FOV to around $\pm 20^{\circ}$ in the horizontal axis. A modified horizontal scanner from the *Daytona* SLO allows the redirection of the field to different horizontal positions, with the unconstrained vertical galvanometer allowing redirection along the vertical field of the first ellipsoidal mirror.

Three images were acquired with navigation along the horizontal axis and are provided in Fig. 8.11. The image quality has substantially improved since the First Demonstrator, with defined retinal and choroidal information into the far periphery. The sinusoidal driving of the scan appears to extend the appearance of the FOV with no new information, although these features are easily distinguishable by the loss of contrast in the choroid. There does appear to be some loss in axial resolution and intensity as the layer definition is increasingly limited by the transverse resolution. This reduction in quality indicates that to maintain image performance off-axis will most likely require optical correction more advanced than just focal control, to replicate the axial resolution in the transverse axis. Ideally, further investigation would be reported in this thesis but access to the device is currently limited as the software and hardware improvements result in regular downtime for the device.

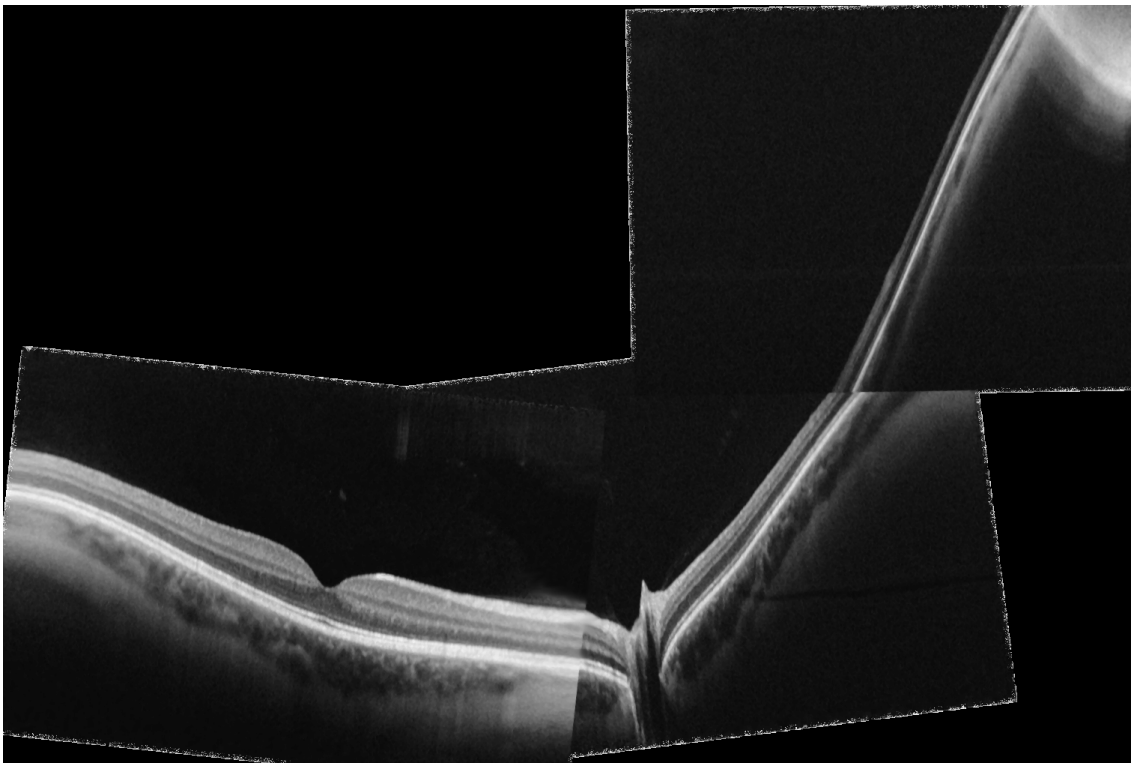

Fig. 8.11 Three navigated images from the *Optos Lotte* integrated within the *Daytona* architecture.

The BE-Target was used to measure to $FOV_{ext}$ of the *Optos Lotte*. The angular calibration of the galvanometer voltage was first estimated by measuring the angle subtended by the virtual point. This measurement indicated that in this configuration the maximum $FOV_{ext}$ for the device (without navigating) would be $\pm 15^{\circ}$ horizontal and $\pm 10.5^{\circ}$ vertical. The BE-Target was imaged on axis and then again vertically navigated, to what was thought to be $\pm 10.5^{\circ}$. As these images along are not sufficient to determine the FOV, a raster scan was acquired across the same FOV and registered to a volume using *ImageJ*. From this image it was easy to measure the FOV to be $\pm 15.8^{\circ}$ horizontal and $\pm 4.1^{\circ}$ in the vertical axis. This measurement was used to explain a difficult that was observed when correlating the optimal current for the liquid lens with the vertical field angle(based on a look up table) and allowed for the recalibration of the scan voltage and lens current to the correct field angle.

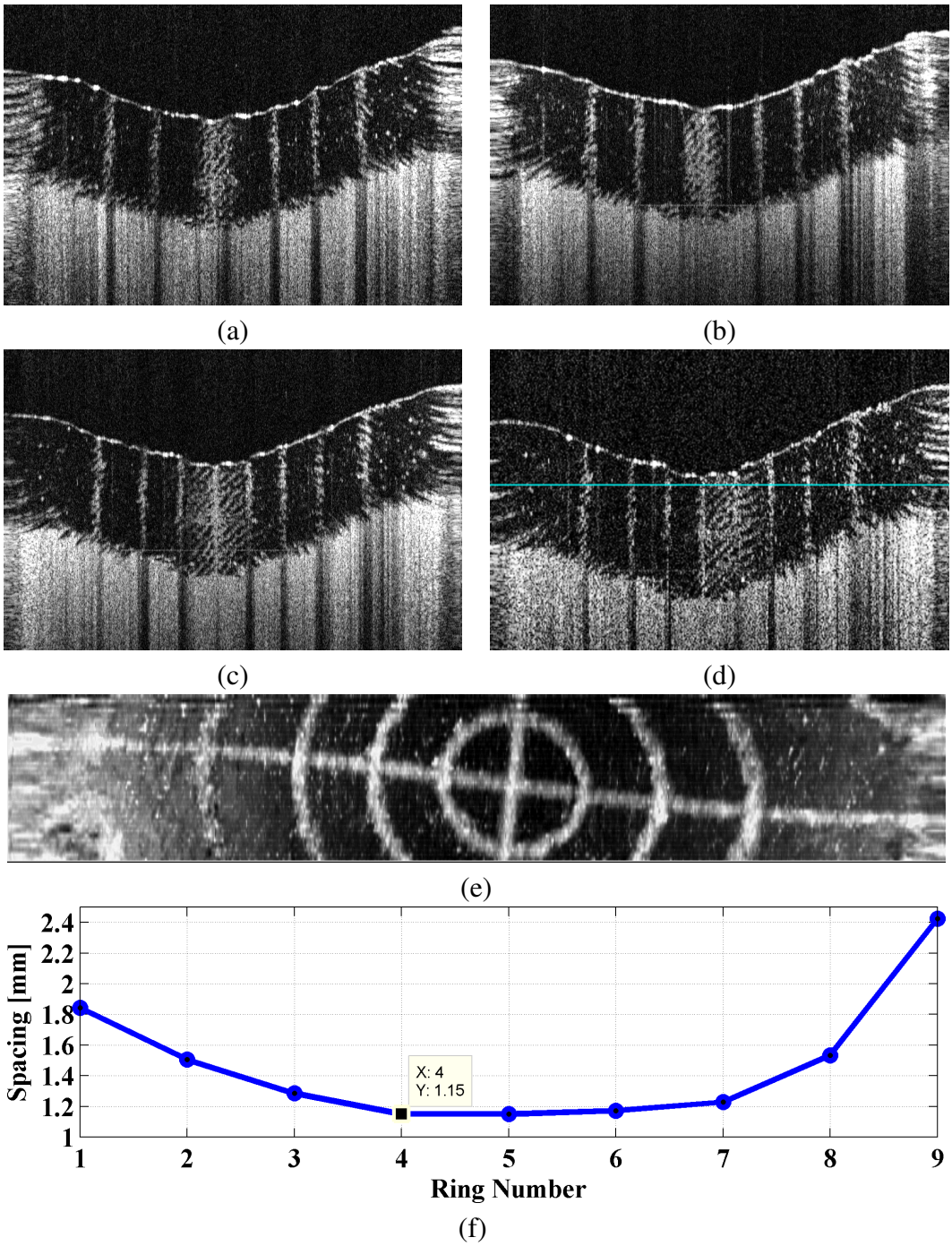


Fig. 8.12 (a) $\pm 15.8°$ wide B-Scan navigated vertically by $+4.1°$ (b) B-Scan navigated vertically by $-4.1°$ (c) B-Scan on-axis (d) Cross section of raster volume in *ImageJ* (e) en-face view of the BE-Target on the *Optos* Prototype (f) Horizontal spacing between rings in the 3D projection in (e).

## 8.4 Conclusion

Images were acquired of the AL-Target from the *Optos OCT/SLO*, *Heidelberg Spectralis*, *Zeiss Cirrus* and *Optovue iVue* for a comparison of the imaging performance and measurement accuracy. The *Spectralis* was shown to have superior performance in terms of FOV and pitch; however, the limited precision of the targets prevented the measurement of the axial and transverse resolution of each system. The low number of images recorded for the *Heidelberg Spectralis*, *Carl Zeiss Cirrus* and *Optovue iVue* devices made the assessment of accuracy and precision difficult and indicated that further images would be required to compare systems. Sufficient evidence was gathered to show that the WPE phantom eye has the capability to measure FOV, pitch, depth, roll-off and LSF, while providing a consistent B-scan to extract image quality metrics.

The study also highlighted key areas requiring improvement for the WPE targets such as precision in fabrication and specular reflection from the material. A target aiming to determine the accuracy of segmentation must also provide a closer replication of retinal anatomy than the AL-Target. This similarity would make acquisition simpler for photographers to allow the further investigation into measurement accuracy and allow the validation of segmentation performance. This investigation will be needed to ascertain how critical imaging performance is to segmentation consistency and accuracy.

The *Optos Lotte* is progressing well and has been demonstrated to have near market-competitive image quality on-axis. This OCT device from *Optos* will offer a significant advancement to the OCT market when the distortions introduced by wide-field imaging are well characterised and corrected. The narrow-field imaging without navigation is not likely to rival the *Optovue Avanti*, *Topcon Swept Source* or the new lens addition from the *Heidelberg Spectralis*, ideally suited to the ophthalmology market; however, the integration into the current successful *Daytona* and *California* devices offers significant advantages to the clinical outcomes of diabetic screening in the optometry market where it is likely to reach a greater number of patients, earlier in their disease progression.

The navigated imaging developing in the *Optos Lotte* which will be controlled using a previously acquired **opto**map offers the ophthalmology market a huge advancement in the investigation of disease development in the retinal periphery. Currently OCT devices such as *Spectralis* offer the ability to steer the device on a gimble or eye steer $\pm 15^{\circ}$ to search for off-axis pathology. The quantitative control of field angle provides an opportunity to overcome the variability that is inherent in the current navigation methods which limit quantitative analysis during longitudinal studies.

# Chapter 9

# Conclusions

## 9.1 Claims of the Thesis

The primary conclusion of this thesis is that the human retina can be imaged using optical coherence tomography across an external field of view of $\pm 70^{\circ}$ with an imaging performance similar that demonstrated on-axis. Claims supporting this conclusion are provided in this section along with further detail on the conclusion itself.

*Claim 1:* To image the human retina across a $\text{FOV}_{\text{ext}}$ of $\pm 70^{\circ}$ (full-$\text{FOV}_{\text{int}}$ of $180^{\circ}$) with optical coherence tomography (OCT) using commercial technology, currently requires the use of a navigated narrow field-angle scans of less than $\pm 20^{\circ}$ (full-$\text{FOV}_{\text{int}}$ of $60^{\circ}$). This limitation is present for threes reasons: Firstly, to image the same FOV and pitch of as **opto**map SLO image (12 mega pixels) on a state-of-the-art-spectrometer (70 kHz), would require both a 3 minute acquisition time and at least 74 GB of memory (for a 12-bit image). Although this not insurmountable, these images could not be provided live to a clinician as is current convention with OCT devices.

It may be possible to increase the FOV accessible to OCT using sparse acquisition with reconstruction following repeated images, similar to that used in super-resolution imaging [195]. Theoretically this could be achieved using the fast scanning polygon in the Optos system. This approach was never investigated in this Thesis due to concerns about the scan arc being too great during a pixel aquasition that fringe wash out would occur, as was discussed in Section 4.4.

Secondly, the changing orientation of the retina with field angle results in the layer definition in the B-scan being increasingly dominated by the transverse resolution (20 μm) - typically 2-5 times poorer than the axial resolution (5 μm). This challenge can be overcome

by increasing the beam width at the cornea above 2 mm; however, this change would require adaptive optics to compensate for the high-order aberrations of the eye.

Finally, the narrow-field navigation of OCT requires a optimisation of the defocus, pathlength, polarisation in the reference arm and the calibration of radial and axial of distortion that would not be common across the image, as is shown in both Section 3.5 and 8.3, image quality could be seen to degrade off-axis. This deterioration was shown to be caused by the geometry of the eye through modelling in *Zemax* in Section 4.

*Claim 2:* OCT imaging of the retina across a $FOV_{ext}$ of $\pm 70^{\circ}$ can be achieved through the use of an ellipsoidal scan relay only if the asymmetric power of the ellipsoidal mirror is corrected with field angle. This asymmetric defocus of the scan system dominates all other sources of signal reduction mentioned in *Claim 1* as the reduced coupling efficiency into the single mode fibre results in severe signal attenuation. This claim was shown through modelling in Section 3.1.5 and demonstrated as being overcome through qualitative analysis of images in Fig. 8.12. Although only a modest vertical field angle of $4.1^{\circ}$ was demonstrated in this thesis in Fig. 8.12 (a) and (b) even this small field required refocusing of the liquid lens.

*Claim 3:* Both the OCT research community and manufacturers require a consistent method to verify the optical performance and calibrate device measurement. The performance metrics that should be measured are: the transverse and longitudinal point-spread function, field of view, distortion, imaging range, sensitivity roll-off and measurement accuracy. These metrics are reviewed in Chapter 5 and the use of a phantom eye is presented as the most effective method for the assessment of OCT devices.

*Claim 4:* Ultra-widefield OCT has a greater need for a method that can provide both consistent verification and calibration than narrow-field imaging. This need is principally because the challenges of wide-field OCT discussed in Section 4 cannot be corrected for each narrow-field, as reported in Section 8.3, but also because the variation in the distortion and FOV of an ultra-widefield will make any calibration more challenging, demonstrated in Section 7.2.

*Claim 5:* A wide-field phantom eye is reported that enables the assessment of OCT, SLO and fundus-camera performance across a substantially wider FOV than has been previously reported. The optical properties of the WPE matches those of the Navarro schematic eye in terms of PSF, aberrations, OPL and distortion for field angles less than $\pm 70^{\circ}$, with a small decrease in chromatic aberration. The wide-field images recorded with OCT and SLO show that this variation does not degrade the characterisation of the imaging performance in the retinal periphery. The flexibility of the WPE allows customised retinal targets that can be used to characterise specific modalities and metrics. During the project, the FDA

published a prototype phantom eye that can be used to calibrate measurement in an OCT ophthalmoscope across a $FOV_{ext}$ of $\pm 10^{\circ}$ and potentially assess device precision [173]. Access to this phantom was granted late in the project; therefore, it is only reported on in Appendix A.6. This report showed that the phantom did not contain retinal layers that count be automatically segmented by the *Optos OCT/SLO*, indicating that the phantom requires further improvement.

*Claim 6:* Three 3D-printed targets have been fabricated for the WPE with features across $\pm 90^{\circ}$, with varying feature size and material configurations. The large-scale features, such as the bullseye rings and hemispherical shape of the vitreoretinal interface, have been used to measure the field of view, optical and variation in path length, distortion and axial-PSF with field angle. The materials used for 3D-printing have been shown to have scattering properties sufficiently similar to that of retinal tissue to generate OCT images for the assessment of OCT-device segmentation and SNR performance.

*Claim 7:* Creating targets using 3D-printing will require a further development the technology or hybridising the 3D-printed targets with higher-precision techniques to measure axial and transverse resolution. Attaching flexible resolution charts to 3D-printed cylindrical geometry has been demonstrated as a low cost method to measure off-axis transverse resolution across a $FOV_{ext}$ of $\pm\ 30^{\circ}$. Further development of the contrasting materials would increase the range of field angles available for assessment.

*Claim 8:* We have introduced a method for the acquisition, analysis and comparison of both narrow-field and wide-field ophthalmic systems. This method was applied to both *Optos* and competitor systems. Analysis of these images showed *Optos* to have a largely superior FOV in the *Daytona* and *200Tx*; however, the *Optos OCT/SLO* had inferior OCT performance than competitors. This method was used again to measure the variation betweens *Optos* systems. This investigation showed substantial variability, which means multiple units of the same device should be assessed to conduct an accurate analysis of device performance.

## 9.2 Analysis of Thesis

The research presented in this thesis is largely of an exploratory nature and is designed to highlight problems that should be investigated in greater detail in a further investigations. For example, the degradation in the OCT image quality off-axis is observed in images of the WPE targets, retinas and from modelling; however, the empirical data does not allow the user to distinguish the impact of the individual causes of the degradation. Additional access to each of the assessed devices will need to be provided to allow the prioritisation compensation mechanisms the degradation and variation, such as dynamic focus or birefringence, or even

adaptive optics. The fluid priorities of *Optos* meant that for the majority of this project there was no wide-field OCT prototype available to investigate. This problem is most readily seen by the analysis of a single image from each competitor device in Chapter 7, which prevented any analysis of the systematic variability within each device. As mentioned in this Chapter, this limitation was imposed by the limited time the clinician had with each of the competitor systems as access to these devices by rival companies like *Optos* is actively restricted. Furthermore, the reflectance images (particularly from *Heidelberg*) were considered of greater significance to *Optos* as this was their leading product. In future, further modelling should be conducted to predict the results of the exploratory investigation before using the limited access to the device. This would allow the full requirements of a study to be known during the experimental planning. In addition, access to addition systems could have been achieved with less constraints through connections within the University.

This thesis provides an introduction to someone with a limited experience as to the challenges of ultra-widefield ophthalmic imaging. This characteristic of the thesis is thanks to both the commentary on the development stages of ultra-widefield OCT along with the exploratory investigation into the challenges of wide-field imaging in both reflectance modalities and OCT. Unfortunately, we are not able to provide a full conclusion on the development of UWF-OCT with recommendations on how improve this device as the prototype was still in development at the time of thesis submission. However, we provide prediction for the key technology challenges in Section 9.3 and for the market trends in ultra-widefield OCT in Section 9.4. Within reason, this thesis has been written independently of confidentiality concerns; however, some technology detail about the UWF-prototype has been omitted. This omission does not substantially reduce the reproducibility of the reported work.

## 9.3 Implications of Thesis Claims

Significant challenges remain in the development of an ultra-widefield OCT system that must be determined before the device is suitable for release. The variability in image performance with field angle must be quantified. In addition, how this variability with field angle deteriorates the measurement precision. Also the analysis of off-axis distortion in this thesis has focused on optimal imaging conditions such as imaging of an emmetropic eye, positioned stationary on the optical axis. Deviation from these conditions will require recalibration of pixel scaling and projection algorithms to maintain the accuracy of measurements and cross-modality registration.

The performance comparison between commercial systems in Chapter 7 and 8 should have been acquired in tandem with measurements from healthy subjects to demonstrate conclusively whether the WPE is an effective analogue to the optical response of the human eye, although steering to the same field angle as the phantom would not be possible. This data would allow the change in image quality from the variation in patient anatomy and pathology to be assessed and could be factored into conclusions on the permissible variability in image performance. This joint assessment will be necessary for the prototype device to ensure the anatomy that has not been represented in the WPE, such as corneal birefringence (discussed in Sec. 4.3), does not deteriorate the imaging performance. The implications of retinal pathology and the varying prescription between patients should be modelled in ray-tracing software such as Zemax, with a follow up study involving the WPE if the aberrations are found to be severe.

There are limitations remaining for the WPE for both the optical design and the fabrication of the targets. For the optical design, an investigation must be conducted to see if changes in axial length between the lens and target accurately reproduces the same changes in image quality as refractive error. This experiment can be conducted by printing phantoms with varying object distance and ellipsoidal curvature. New lenses may be required to simulate forms of myopia or hyperopia that are caused by higher-order aberrations. A further limitation is the variability introduced by the interchangeability of the phantoms that leads to accumulation air in the vitreous and a possible variation element spacing in reassembly. For longitudinal studies it may be advantageous to use a silicone filled phantom that once sealed does not need reopening. This modification would require increasing the power of the lenses to compensate for the higher refractive index of the vitreous and a careful analysis of the chromatic dispersion of the new material.

The limitations in the target, which result from the insufficient fabrication precision of 3D-printing, have been discussed throughout Chapters 6, 7 and 8. The insertion of a high-precision feature near the optical axis, which has had dimensions verified to below 10 µm and includes sharp edges, would greatly improve the accuracy of the distortion measurement. In addition, the plastic target exhibits substantial specular reflection. To remove this will require an investigation into either new materials, post-fabrication surface roughening or the integration of polarising filters into the eye that would reduce specular reflection. Care must be taken not to distort the features of the ocular phantom when implementing these solutions. In addition, a target aiming to determine the accuracy of segmentation must also provide a closer replication of retinal anatomy than the AL-Target. This similarity would make acquisition simpler for photographers and would allow both investigation into measurement precision and allow the validation of segmentation performance. This investigation will be

needed to ascertain how critical imaging performance is to segmentation consistency and accuracy.

## 9.4 Market Predictions for OCT

*As of December 2014* Recent developments in the FOV of commercial OCT devices summarised in Section 1.2 with full-$FOV_{ext}$ of 40-60° are likely to become standard in the industry [7–9]. This improved on-axis FOV makes it easy to simultaneously image both the macula and optic disc. This improvement is desirable to health services and insurers who would benefit from a higher patient throughput. Developing a revenue stream to make this increased FOV a standard-of-care, will require changes in the accounting and billing of private health sectors such as the US to accommodate the ability to screen for multiple diseases with a single scan.

Ultra-widefield OCT, with full-$FOV_{ext}$ of 60-150° is unlikely to develop further outside an academic application of the technology, where the additional cost of the improvements to speed such as buffered delay lines, dual beam imaging and longer post processing of images are not as significant as in industry. Fundamentally, the value generated by ultra-widefield SLO is that it makes screening for diseases in the eye much easier and quicker for both the patient, photographer and grader. Since OCT was first demonstrated, there has been little evidence indicating that OCT is any more effective at initial screening of pathology than the established lower-cost technique of either white-light cameras and SLOs. Without this evidence there will be little incentive to overcome the sizeable technical challenges outlined in this thesis to provide the huge FOV of an **opto**map with OCT.

Navigation of OCT across an ultra-widefield FOV has a valuable role to play in the next few years, with the release of the first ultra-widefield, navigable OCT device announced by *Optos* before the end on 2015. I have first hand experience of pathology in the far retinal periphery that is easily screened by ultra-widefield SLO which would benefit significantly from referral to navigable OCT device for identification, measurement and tracking. The pathology shown in Fig. 9.1 was imaged in the author during a development of a normative database for the *Daytona* in 2012 and is thought to be lattice degeneration - a precursor to retinal detachment. The location of the pathology was measured using calibration from the BE-Target as being 19.5 mm from the macula, ($FOV_{ext}$) of 75°. The diagnosis for this pathology is to keep re-imaging annually and watch for any changes in the pathology size. This longitudinal measurement is well suited to the quantitative strength of OCT. Other pathology such peripheral retinal/choroidal haemangioblastoma have been diagnosed in this manner, after being easily screened by ultra-widefield SLO and then confirmed through a more challenging steered-OCT [196]. Integrating this patient care into a single well calibrated device will reduce the need for referral duration between screening session and repeated imaging by an ophthalmologist and therefore will significantly improve patient outcomes in rapidly progressing pathology.

Fig. 9.1 Possible lattice degeneration of author's retina acquired via steering an *Optos California*. The approximate distance of the pathology to the macula in this image is 19.5 mm or a $\text{FOV}_{\text{int}}$ of 110°.

# References


[1] A. T. Corcoran, G. Muyo, J. I. van Hemert, and A. R. Harvey, "Development of a widefield phantom eye for retinal optical coherence tomography," in *SPIE BiOS*, pp. 89450F–89450F, International Society for Optics and Photonics, 2014.

[2] A. Corcoran, G. Muyo, J. van Hemert, A. Gorman, and A. R. Harvey, "Application of a wide-field phantom eye for optical coherence tomography and reflectance imaging," *Journal of Modern Optics*, vol. 0, no. 0, pp. 1–11, 2015.

[3] M. Fitzpatrick, "Ophthalmologists eye new examination tool," *JAMA*, vol. 286, no. 13, pp. 1567–1568, 2001.

[4] H. Engineering, "Faq about spectralis oct," 2011.

[5] T. Klein, W. Wieser, C. M. Eigenwillig, B. R. Biedermann, and R. Huber, "Megahertz oct for ultrawide-field retinal imaging with a 1050nm fourier domain mode-locked laser," *Optics Express*, vol. 19, no. 4, pp. 3044–3044, 2011.

[6] L. Reznicek, T. Klein, W. Wieser, M. Kernt, A. Wolf, C. Haritoglou, A. Kampik, R. Huber, and A. S. Neubauer, "Megahertz ultra-wide-field swept-source retina optical coherence tomography compared to current existing imaging devices," *Graefe's Archive for Clinical and Experimental Ophthalmology*, pp. 1–8, 2014.

[7] Y. Matsuo, T. Sakamoto, T. Yamashita, M. Tomita, M. Shirasawa, and H. Terasaki, "Comparisons of choroidal thickness of normal eyes obtained by two different spectral-domain oct instruments and one swept-source oct instrument," *Investigative ophthalmology & visual science*, vol. 54, no. 12, pp. 7630–7636, 2013.

[8] Optovue, "Optovue launches next generation widefield enface oct," Nov 2013.

[9] H. Engineering, "Widefield oct with spectralis." Online, 2014.

[10] Optos, "Optos oct slo product brochure," March 2014.

[11] J. Schwiegerling, *Field Guide to Visual and Ophthalmic Optics*. Proc. SPIE, 2004.

[12] D. Atchison, *Optics of the Human Eye*. Oxford Boston: Butterworth-Heinemann, 2000.

[13] W. Merriam, "Encyclopedia brittanica," 2006.

[14] R. P. Hemenger, L. F. Garner, and C. S. Ooi, "Change with age of the refractive index gradient of the human ocular lens.," *Investigative ophthalmology & visual science*, vol. 36, no. 3, pp. 703–707, 1995.

[15] A. Glasser and M. C. Campbell, "Presbyopia and the optical changes in the human crystalline lens with age," *Vision research*, vol. 38, no. 2, pp. 209–229, 1998.

[16] A. Wilson and G. Woo, "A review of the prevalence and causes of myopia," *Singapore Med J*, vol. 30, no. 5, pp. 479–84, 1989.

[17] E. Hecht, *Optics*. Reading Mass.: Addison-Wesley, 2002.

[18] W. Hagins, "The visual process: excitatory mechanisms in the primary receptor cells," *Annual review of biophysics and bioengineering*, vol. 1, no. 1, pp. 131–158, 1972.

[19] R. C. Bakaraju, K. Ehrmann, E. Papas, and A. Ho, "Finite schematic eye models and their accuracy to in-vivo data," *Vision Research*, vol. 48, no. 16, pp. 1681 – 1694, 2008.

[20] A. Gullstrand, "Neue methoden der reflexlosen ophthalmoskopie," *Berichte Deutsche Ophthalmologische Gesellschaft*, vol. 36, 1910.

[21] R. Navarro, J. Santamaria, and J. Bescos, "Accommodation-dependent model of the human eye with aspherics," *J Opt Soc Am A*, vol. 2, no. 8, pp. 1273–81, 1985.

[22] A. V. Goncharov and C. Dainty, "Wide-field schematic eye models with gradient-index lens," *J. Opt. Soc. Am. A*, vol. 24, pp. 2157–2174, Aug 2007.

[23] H.-L. Liou and N. A. Brennan, "Anatomically accurate, finite model eye for optical modeling," *J. Opt. Soc. Am. A*, vol. 14, pp. 1684–1695, Aug 1997.

[24] T. T. Berendschot, P. J. DeLint, and D. van Norren, "Fundus reflectance–historical and present ideas," *Prog Retin Eye Res*, vol. 22, no. 2, pp. 171–200, 2003.

[25] J. van de Kraats, T. Berendschot, and D. van Norren, "The pathways of light measured in fundus reflectometry," *Vision Research*, vol. 36, no. 15, pp. 2229 – 2247, 1996.

[26] H. Feldmann, "From otoscope to ophthalmoscope and back.," *Laryngorhinootologie*, vol. 74, no. 11, pp. 707–17, 1995.

[27] J. Hecht, "A short history of laser development," *Appl Opt*, vol. 49, no. 25, pp. F99–122, 2010.

[28] W. Boyle and G. Smith, "Charge-coupled devices-a new approach to mis device structures," *Spectrum, IEEE*, vol. 8, no. 7, pp. 18–27, 1971.

[29] J. C. Blanks, Y. Torigoe, D. R. Hinton, and R. H. Blanks, "Retinal pathology in alzheimer's disease. i. ganglion cell loss in foveal/parafoveal retina," *Neurobiology of aging*, vol. 17, no. 3, pp. 377–384, 1996.

[30] D. R. Hinton, A. A. Sadun, J. C. Blanks, and C. A. Miller, "Optic-nerve degeneration in alzheimer's disease," *New England Journal of Medicine*, vol. 315, no. 8, pp. 485–487, 1986.

[31] J. B. Fisher, D. A. Jacobs, C. E. Markowitz, S. L. Galetta, N. J. Volpe, M. L. Nano-Schiavi, M. L. Baier, E. M. Frohman, H. Winslow, T. C. Frohman, *et al.*, "Relation of visual function to retinal nerve fiber layer thickness in multiple sclerosis," *Ophthalmology*, vol. 113, no. 2, pp. 324–332, 2006.

[32] R. Kromer, N. Serbecic, L. Hausner, L. Froelich, F. Aboul-Enein, and S. C. Beutelspacher, "Detection of retinal nerve fiber layer defects in alzheimers disease using sdoct," *Frontiers in psychiatry*, vol. 5, 2014.

[33] V. Polo, E. Garcia-Martin, M. Bambo, J. Pinilla, J. Larrosa, M. Satue, S. Otin, and L. Pablo, "Reliability and validity of cirrus and spectralis optical coherence tomography for detecting retinal atrophy in alzheimers disease," *Eye*, 2014.

[34] J. E. Shaw, R. A. Sicree, and P. Z. Zimmet, "Global estimates of the prevalence of diabetes for 2010 and 2030," *Diabetes research and clinical practice*, vol. 87, no. 1, pp. 4–14, 2010.

[35] E. S. Huang, A. Basu, M. O'Grady, and J. C. Capretta, "Projecting the future diabetes population size and related costs for the us," *Diabetes care*, vol. 32, no. 12, pp. 2225–2229, 2009.

[36] W. H. Organization, "visual imparement and blindness," 2009.

[37] I. Gorczynska, V. J. Srinivasan, L. N. Vuong, R. W. Chen, J. J. Liu, E. Reichel, M. Wojtkowski, J. S. Schuman, J. S. Duker, and J. G. Fujimoto, "Projection oct fundus imaging for visualising outer retinal pathology in non-exudative age-related macular degeneration," *Br J Ophthalmol*, vol. 93, no. 5, pp. 603–9, 2009.

[38] BBC, "Uk rise in age-related macular degeneration predicted," 16 March 2011.

[39] J. P. Ganley and J. Roberts, "Eye conditions and related need for medical care," *Vital Health Stat 11*, no. 228, pp. 1–69, 1983.

[40] A. Sommer, J. Tielsch, and J. Katz, "Relationship between intraocular pressure and primary open angle glaucoma among white and black americans: The baltimore eye survey," *Archives of Ophthalmology*, vol. 109, no. 8, pp. 1090–1095, 1991.

[41] L. D. Hubbard, R. J. Brothers, W. N. King, L. X. Clegg, R. Klein, L. S. Cooper, A. R. Sharrett, M. D. Davis, and J. Cai, "Methods for evaluation of retinal microvascular abnormalities associated with hypertension/sclerosis in the atherosclerosis risk in communities study," *Ophthalmology*, vol. 106, no. 12, pp. 2269–80, 1999.

[42] M. C. J. R. A. W. D. Wolfing, JI. Chung, "High-resolution retinal imaging of cone rod dystrophy," *Ophthalmology*, vol. 113, pp. 1014–1019, June 2006.

[43] J. Knudson, A. G., "Mutation and cancer: statistical study of retinoblastoma," *Proc Natl Acad Sci U S A*, vol. 68, no. 4, pp. 820–3, 1971.

[44] T. J. Wolfensberger and M. Gonvers, "Optical coherence tomography in the evaluation of incomplete visual acuity recovery after macula-off retinal detachments," *Graefes Arch Clin Exp Ophthalmol*, vol. 240, no. 2, pp. 85–9, 2002.

[45] H. Riley, "Peripheral retina lecture notes," 2007.

[46] A. Manivannan, J. Plskova, A. Farrow, S. McKay, P. F. Sharp, and J. V. Forrester, "Ultra-wide-field fluorescein angiography of the ocular fundus," *Am J Ophthalmol*, vol. 140, no. 3, pp. 525–7, 2005.

[47] M. Stehouwer, F. D. Verbraak, H. R. de Vries, and T. G. van Leeuwen, "Scanning beyond the limits of standard oct with a fourier domain optical coherence tomography integrated into a slit lamp: the sl scan-1," *Eye (Lond)*, vol. 25, no. 1, pp. 97–104, 2011.

[48] D. Mitry, D. G. Charteris, D. Yorston, B. W. Fleck, A. Wright, H. Campbell, and J. Singh, "Rhegmatogenous retinal detachment in scotland: research design and methodology," *BMC Ophthalmol*, vol. 9, p. 2, 2009.

[49] M. Takano and S. Kishi, "Foveal retinoschisis and retinal detachment in severely myopic eyes with posterior staphyloma," *Am J Ophthalmol*, vol. 128, no. 4, pp. 472–6, 1999.

[50] R. Y. Foos, "Vitreoretinal juncture; topographical variations," *Invest Ophthalmol*, vol. 11, no. 10, pp. 801–8, 1972.

[51] G. Staurenghi, F. Viola, M. A. Mainster, R. D. Graham, and P. G. Harrington, "Scanning laser ophthalmoscopy and angiography with a wide-field contact lens system," *Archives of ophthalmology*, vol. 123, no. 2, pp. 244–252, 2005.

[52] C. Wu, R. A. Petersen, and D. K. VanderVeen, "Retcam imaging for retinopathy of prematurity screening," *Journal of American Association for Pediatric Ophthalmology and Strabismus*, vol. 10, no. 2, pp. 107–111, 2006.

[53] A. Elsner and J. D. F. Burns, S.and Weiter, "Infrared imaging of sub-retinal structures in the human ocular fundus," *Vision Res*, vol. 36, pp. 191–205, Jan 1996.

[54] M. Wojtkowski, T. Bajraszewski, I. Gorczynska, P. Targowski, A. Kowalczyk, W. Wasilewski, and C. Radzewicz, "Ophthalmic imaging by spectral optical coherence tomography," *Am J Ophthalmol*, vol. 138, no. 3, pp. 412–9, 2004.

[55] Nidek, "Optical coherence tomography rs-3000 advance," July 2012.

[56] D. Huang, E. A. Swanson, C. P. Lin, J. S. Schuman, W. G. Stinson, W. Chang, M. R. Hee, T. Flotte, K. Gregory, C. A. Puliafito, and et al., "Optical coherence tomography," *Science*, vol. 254, no. 5035, pp. 1178–81, 1991.

[57] A. F. Fercher, K. Mengedoht, and W. Werner, "Eye-length measurement by interferometry with partially coherent light," *Opt Lett*, vol. 13, no. 3, pp. 186–8, 1988.

[58] H. Gilgen, R. Novak, and R. Saalathe, "Submillimeter optical reflectometry," *Light Wave Technology*, vol. 7, no. 8, pp. 1225 – 1233, 1989.

[59] D. F. Kiernan, W. F. Mieler, and S. M. Hariprasad, "Spectral-domain optical coherence tomography: a comparison of modern high-resolution retinal imaging systems.," *American Journal of Ophthalmology*, vol. 149, no. 1, pp. 18–31, 2010.

[60] W. Wieser, B. R. Biedermann, T. Klein, C. M. Eigenwillig, and R. Huber, "Multi-megahertz oct: High quality 3d imaging at 20 million a-scans and 4.5 gvoxels per second," *Opt Express*, vol. 18, no. 14, pp. 14685–704, 2010.

[61] B. Potsaid, I. Gorczynska, V. J. Srinivasan, Y. Chen, J. Jiang, A. Cable, and J. G. Fujimoto, "Ultrahigh speed spectral / fourierdomain oct ophthalmic imaging at70,000 to 312,500 axial scans per second," *Opt. Express*, vol. 16, pp. 15149–15169, Sep 2008.

[62] W. Drexler, R. Leitgeb, and C. K. Hitzenberger, "New developments in optical coherence tomography technology," in *Medical Retina* (F. G. Holz, R. Spaide, G. K. Krieglstein, and R. N. Weinreb, eds.), Essentials in Ophthalmology, pp. 201–216, Springer Berlin Heidelberg, 2010.

[63] R. Huber, M. Wojtkowski, and J. G. Fujimoto, "Fourier domain mode locking (fdml): A new laser operating regime and applications for optical coherence tomography," *Opt Express*, vol. 14, no. 8, pp. 3225–37, 2006.

[64] J. M. Schmitt, A. Knuttel, and R. F. Bonner, "Measurement of optical properties of biological tissues by low-coherence reflectometry," *Appl Opt*, vol. 32, no. 30, pp. 6032–42, 1993.

[65] M. J. Yadlowsky, J. M. Schmitt, and R. F. Bonner, "Multiple scattering in optical coherence microscopy," *Appl Opt*, vol. 34, no. 25, pp. 5699–707, 1995.

[66] J. M. Schmitt, M. J. Yadlowsky, and R. F. Bonner, "Subsurface imaging of living skin with optical coherence microscopy," *Dermatology*, vol. 191, no. 2, pp. 93–8, 1995.

[67] M. Choma, M. Sarunic, C. Yang, and J. Izatt, "Sensitivity advantage of swept source and fourier domain optical coherence tomography," *Opt Express*, vol. 11, no. 18, pp. 2183–9, 2003.

[68] A. F. Fercher, W. Drexler, C. K. Hitzenberger, and T. Lasser, "Optical coherence tomography - principles and applications," *Reports on Progress in Physics*, vol. 66, no. 2, pp. 239–303, 2003.

[69] J. Izatt and M. Choma, "Theory of optical coherence tomography," in *Optical Coherence Tomography* (W. Drexler and J. Fujimoto, eds.), Biological and Medical Physics, Biomedical Engineering, pp. 47–72, Springer Berlin Heidelberg, 2008.

[70] S. Yun, G. Tearney, J. de Boer, N. Iftimia, and B. Bouma, "High-speed optical frequency-domain imaging," *Opt Express*, vol. 11, no. 22, pp. 2953–63, 2003.

[71] A. F. Fercher, C. K. Hitzenberger, G. Kamp, and S. Y. Elzaiat, "Measurement of intraocular distances by backscattering spectral interferometry," *Opt. Commun.*, vol. 177, no. 43-48, 1995.

[72] M. Wojtkowski, R. Leitgeb, A. Kowalczyk, T. Bajraszewski, and A. F. Fercher, "In vivo human retinal imaging by fourier domain optical coherence tomography," *J Biomed Opt*, vol. 7, no. 3, pp. 457–63, 2002.

[73] A. Zuluaga and R. Richards-Kortum, "Spatially resolved spectral interferometry for determination of subsurface structure.," *Optics Letters*, vol. 24, no. 8, pp. 519–521, 1999.

[74] R. Leitgeb, C. Hitzenberger, and A. Fercher, "Performance of fourier domain vs. time domain optical coherence tomography," *Opt Express*, vol. 11, no. 8, pp. 889–94, 2003.

[75] J. F. de Boer, B. Cense, B. H. Park, M. C. Pierce, G. J. Tearney, and B. E. Bouma, "Improved signal-to-noise ratio in spectral-domain compared with time-domain optical coherence tomography," *Opt Lett*, vol. 28, no. 21, pp. 2067–9, 2003.

[76] W. Y. Oh, S. H. Yun, B. J. Vakoc, M. Shishkov, A. E. Desjardins, B. H. Park, J. F. de Boer, G. J. Tearney, and B. E. Bouma, "High-speed polarization sensitive optical frequency domain imaging with frequency multiplexing," *Opt Express*, vol. 16, no. 2, pp. 1096–103, 2008.

[77] T. Klein, W. Wieser, R. Andra, T. Pfeiffer, C. M. Eigenwillig, and R. Huber, "Multi-mhz fdml oct: snapshot retinal imaging at 6.7 million axial-scans per second," *Proc. SPIE*, vol. 8213, no. 82131E, 2012.

[78] C. Blatter, T. Klein, B. Grajciar, T. Schmoll, W. Wieser, R. Andre, R. Huber, and R. A. Leitgeb, "Ultrahigh-speed non-invasive widefield angiography," *Journal of biomedical optics*, vol. 17, no. 7, pp. 0705051–0705053, 2012.

[79] Y. Zhao, Z. Chen, C. Saxer, Q. Shen, S. Xiang, J. F. de Boer, and J. S. Nelson, "Doppler standard deviation imaging for clinical monitoring of in vivo human skin blood flow," *Opt Lett*, vol. 25, no. 18, pp. 1358–60, 2000.

[80] C. E. Saxer, J. F. de Boer, B. H. Park, Y. Zhao, Z. Chen, and J. S. Nelson, "High-speed fiber based polarization-sensitive optical coherence tomography of in vivo human skin," *Opt Lett*, vol. 25, no. 18, pp. 1355–7, 2000.

[81] R. Leitgeb, M. Wojtkowski, A. Kowalczyk, C. K. Hitzenberger, M. Sticker, and A. F. Fercher, "Spectral measurement of absorption by spectroscopic frequency-domain optical coherence tomography," *Opt Lett*, vol. 25, no. 11, pp. 820–2, 2000.

[82] B. H. Park, C. Saxer, S. M. Srinivas, J. S. Nelson, and J. F. de Boer, "In vivo burn depth determination by high-speed fiber-based polarization sensitive optical coherence tomography," *J Biomed Opt*, vol. 6, no. 4, pp. 474–9, 2001.

[83] A. Szkulmowska, M. Szkulmowski, D. Szlag, A. Kowalczyk, and M. Wojtkowski, "Three-dimensional quantitative imaging of retinal and choroidal blood flow velocity using joint spectral and time domain optical coherence tomography," *Opt Express*, vol. 17, no. 13, pp. 10584–98, 2009.

[84] M. E. Brezinski, "Optical coherence tomography for identifying unstable coronary plaque," *Int J Cardiol*, vol. 107, no. 2, pp. 154–65, 2006.

[85] J. A. Izatt, M. D. Kulkarni, S. Yazdanfar, J. K. Barton, and A. J. Welch, "In vivo bidirectional color doppler flow imaging of picoliter blood volumes using optical coherence tomography," *Opt Lett*, vol. 22, no. 18, pp. 1439–41, 1997.

[86] R. Leitgeb, L. Schmetterer, W. Drexler, A. Fercher, R. Zawadzki, and T. Bajraszewski, "Real-time assessment of retinal blood flow with ultrafast acquisition by color doppler fourier domain optical coherence tomography," *Opt Express*, vol. 11, no. 23, pp. 3116–21, 2003.

[87] S. Yazdanfar, M. Kulkarni, and J. Izatt, "High resolution imaging of in vivo cardiac dynamics using color doppler optical coherence tomography," *Opt Express*, vol. 1, no. 13, pp. 424–31, 1997.

[88] M. Wojtkowski, T. Bajraszewski, P. Targowski, and A. Kowalczyk, "Real-time in vivo imaging by high-speed spectral optical coherence tomography," *Opt Lett*, vol. 28, no. 19, pp. 1745–7, 2003.

[89] U. E. Wolf-Schnurrbusch, L. Ceklic, C. K. Brinkmann, M. E. Iliev, M. Frey, S. P. Rothenbuehler, V. Enzmann, and S. Wolf, "Macular thickness measurements in healthy eyes using six different optical coherence tomography instruments," *Invest Ophthalmol Vis Sci*, vol. 50, no. 7, pp. 3432–7, 2009.

[90] M. Wojtkowski, "High-speed optical coherence tomography: basics and applications," *Appl Opt*, vol. 49, no. 16, pp. D30–61, 2010.

[91] O. News, "Lightlab imaging announces strategic supply agreement with axsun technologies inc. for high performance swept source lasers," 2008.

[92] B. Potsaid, B. Baumann, D. Huang, S. Barry, A. E. Cable, J. S. Schuman, J. S. Duker, and J. G. Fujimoto, "Ultrahigh speed 1050nm swept source / fourier domain oct retinal and anterior segment imaging at 100,000 to 400,000 axial scans per second," *Opt. Express*, vol. 18, pp. 20029–20048, Sep 2010.

[93] J. G. Fujimoto, S. De Silvestri, E. P. Ippen, C. A. Puliafito, R. Margolis, and A. Oseroff, "Femtosecond optical ranging in biological systems," *Opt Lett*, vol. 11, no. 3, p. 150, 1986.

[94] A. Downes, R. Mouras, and A. Elfick, "A versatile cars microscope for biological imaging," *Journal of Raman Spectroscopy*, vol. 40, no. 7, pp. 757–762, 2009.

[95] B. Cense, N. Nassif, T. Chen, M. Pierce, S. H. Yun, B. Park, B. Bouma, G. Tearney, and J. de Boer, "Ultrahigh-resolution high-speed retinal imaging using spectral-domain optical coherence tomography," *Opt Express*, vol. 12, no. 11, pp. 2435–47, 2004.

[96] V. Christopoulos, L. Kagemann, G. Wollstein, H. Ishikawa, M. L. Gabriele, M. Wojtkowski, V. Srinivasan, J. G. Fujimoto, J. S. Duker, D. K. Dhaliwal, and J. S. Schuman, "In vivo corneal high-speed, ultra high-resolution optical coherence tomography," *Arch Ophthalmol*, vol. 125, no. 8, pp. 1027–35, 2007.

[97] J. A. Rodriguez-Padilla, r. Hedges, T. R., B. Monson, V. Srinivasan, M. Wojtkowski, E. Reichel, J. S. Duker, J. S. Schuman, and J. G. Fujimoto, "High-speed ultra-high-resolution optical coherence tomography findings in hydroxychloroquine retinopathy," *Arch Ophthalmol*, vol. 125, no. 6, pp. 775–80, 2007.

[98] C. Torti, B. Povazay, B. Hofer, A. Unterhuber, J. Carroll, P. K. Ahnelt, and W. Drexler, "Adaptive optics optical coherence tomography at 120,000 depth scans/s for non-invasive cellular phenotyping of the living human retina," *Opt Express*, vol. 17, no. 22, pp. 19382–400, 2009.

[99] B. J. Kaluzny, M. Gora, K. Karnowski, I. Grulkowski, A. Kowalczyk, and M. Wojtkowski, "Imaging of the lens capsule with an ultrahigh-resolution spectral optical coherence tomography prototype based on a femtosecond laser," *Br J Ophthalmol*, vol. 94, no. 3, pp. 275–7, 2010.

[100] A. Unterhuber, B. Povazay, K. Bizheva, B. Hermann, H. Sattmann, A. Stingl, T. Le, M. Seefeld, R. Menzel, M. Preusser, H. Budka, C. Schubert, H. Reitsamer, P. K. Ahnelt, J. E. Morgan, A. Cowey, and W. Drexler, "Advances in broad bandwidth light sources for ultrahigh resolution optical coherence tomography," *Phys Med Biol*, vol. 49, no. 7, pp. 1235–46, 2004.

[101] M. Wojtkowski, V. Srinivasan, T. Ko, J. Fujimoto, A. Kowalczyk, and J. Duker, "Ultrahigh-resolution, high-speed, fourier domain optical coherence tomography and methods for dispersion compensation," *Opt Express*, vol. 12, no. 11, pp. 2404–22, 2004.

[102] A. Fercher, C. Hitzenberger, M. Sticker, R. Zawadzki, B. Karamata, and T. Lasser, "Numerical dispersion compensation for partial coherence interferometry and optical coherence tomography," *Opt Express*, vol. 9, no. 12, pp. 610–5, 2001.

[103] W. Drexler and J. Fujimoto, *Optical coherence tomography: technology and applications*. Biological and medical physics, biomedical engineering, Springer, 2008.

[104] J. De Boer, "Spectral/fourier domain optical coherence tomography," in *Optical Coherence Tomography*, pp. 147–175, Springer, 2008.

[105] A. G. Podoleanu and D. A. Jackson, "Noise analysis of a combined optical coherence tomograph and a confocal scanning ophthalmoscope," *Applied Optics*, vol. 38, no. 10, pp. 2116–2127, 1999.

[106] D. J. Faber, E. G. Mik, M. C. Aalders, and T. G. van Leeuwen, "Light absorption of (oxy-)hemoglobin assessed by spectroscopic optical coherence tomography," *Opt Lett*, vol. 28, no. 16, pp. 1436–8, 2003.

[107] E. A. Boettner and J. R. Wolter, "Transmission of the ocular media," *Investigative Ophthalmology & Visual Science*, vol. 1, no. 6, pp. 776–783, 1962.

[108] F. A. B. Gross, H. Blechinger, *Handbook of Optical Systems, Volume 4, Survey of Optical Instruments*, vol. 4. Wiley-VCH, 2008.

[109] M. Wojtkowski, A. Kowalczyk, R. Leitgeb, and A. F. Fercher, "Full range complex spectral optical coherence tomography technique in eye imaging," *Opt Lett*, vol. 27, no. 16, pp. 1415–7, 2002.

[110] M. Szkulmowski and M. Wojtkowski, "Averaging techniques for oct imaging," *Optics express*, vol. 21, no. 8, pp. 9757–9773, 2013.

[111] C. Dorrer, N. Belabas, J.-P. Likforman, and M. Joffre, "Spectral resolution and sampling issues in fourier-transform spectral interferometry," *JOSA B*, vol. 17, no. 10, pp. 1795–1802, 2000.

[112] X. S. Y. K. Schmitt, J.M., "Speckle in optical coherene tomography," *Journal of biomedical optics*, vol. 4, pp. 95–105, 1999.

[113] P. H. Tomlins and R. K. Wang, "Digital phase stabilization to improve detection sensitivity for optical coherence tomography," *Measurement Science and Technology*, vol. 18, no. 11, p. 3365, 2007.

[114] D. Alonso-Caneiro, S. A. Read, and M. J. Collins, "Speckle reduction in optical coherence tomography imaging by affine-motion image registration," *Journal of biomedical optics*, vol. 16, no. 11, pp. 116027–1160275, 2011.

[115] M. Pircher, E. Gotzinger, R. Leitgeb, A. F. Fercher, and C. K. Hitzenberger, "Speckle reduction in optical coherence tomography by frequency compounding," *J Biomed Opt*, vol. 8, no. 3, pp. 565–9, 2003.

[116] D. P. Popescu, M. D. Hewko, and M. G. Sowa, "Speckle noise attenuation in optical coherence tomography by compounding images acquired at different positions of the sample," *Optics Communications*, vol. 269, no. 1, pp. 247 – 251, 2007.

[117] J. Holmes, S. Hattersley, N. Stone, F. Bazant-Hegemark, and H. Barr, "Multi-channel fourier domain oct system with superior lateral resolution for biomedical applications," in *Biomedical Optics (BiOS) 2008*, pp. 68470O–68470O, International Society for Optics and Photonics, 2008.

[118] J. M. Schmitt, S. H. Xiang, and K. M. Yung, "Differential absorption imaging with optical coherence tomography," *Journal of the Optical Society of America A*, vol. 15, no. 9, pp. 2288–2288, 1998.

[119] A. Fercher, *Inverse Scattering, Dispersion, and Speckle in Optical Coherence Tomography*. Biological and Medical Physics, Biomedical Engineering, Springer Berlin Heidelberg, 2008.

[120] J. F. de Boer, C. E. Saxer, and J. S. Nelson, "Stable carrier generation and phase-resolved digital data processing in optical coherence tomography," *Appl Opt*, vol. 40, no. 31, pp. 5787–90, 2001.

[121] R. Leitgeb, W. Drexler, A. Unterhuber, B. Hermann, T. Bajraszewski, T. Le, A. Stingl, and A. Fercher, "Ultrahigh resolution fourier domain optical coherence tomography," *Opt Express*, vol. 12, no. 10, pp. 2156–65, 2004.

[122] D. L. Marks, A. L. Oldenburg, J. J. Reynolds, and S. A. Boppart, "Digital algorithm for dispersion correction in optical coherence tomography for homogeneous and stratified media," *Appl. Opt.*, vol. 42, pp. 204–217, Jan 2003.

[123] M. E. Brezinski, *Optical coherence tomography: principles and applications*. Academic press, 2006.

[124] M. Bass and O. S. of America, *Handbook of Optics*. Handbook of Optics, McGraw-Hill Professional Publishing, 1994.

[125] C. D. Lu, M. F. Kraus, B. Potsaid, J. J. Liu, W. Choi, V. Jayaraman, A. E. Cable, J. Hornegger, J. S. Duker, and J. G. Fujimoto, "Handheld ultrahigh speed swept source optical coherence tomography instrument using a mems scanning mirror," *Biomedical optics express*, vol. 5, no. 1, pp. 293–311, 2014.

[126] B. J. Wilson, K. E. Decker, and A. Roorda, "Monochromatic aberrations provide an odd-error cue to focus direction," *J. Opt. Soc. Am. A*, vol. 19, pp. 833–839, May 2002.

[127] A. G. Podoleanu, "Combining slo and oct technology," *Bull Soc Belge Ophtalmol*, no. 302, pp. 133–51, 2006.

[128] D. Koyama, R. Isago, and K. Nakamura, "High-speed focus scanning at 1 kHz by a variable-focus liquid lens using acoustic radiation force," vol. 1433, pp. 709–712, May 2012.

[129] A. Wilson, "Tunable optics," tech. rep., Vision Systems, 2010.

[130] A. S. Redner and B. Hoffman, "Residual stress testing for transparent polymers,"

[131] H. B. klein Brink, "Birefringence of the human crystalline lens in vivo," *J. Opt. Soc. Am. A*, vol. 8, pp. 1788–1793, Nov 1991.

[132] G. Van Harten, F. Snik, and C. Keller, "Polarization properties of real aluminum mirrors, i. influence of the aluminum oxide layer," *Polarization*, vol. 121, no. 878, pp. 377–383, 2009.

[133] L. Bour, *Polarized light and the eye*, vol. 1. CRC Press, 1991.

[134] Q. Zhou, "Retinal scanning laser polarimetry and methods to compensate for corneal birefringence," *Bull Soc Belge Ophtalmol*, vol. 302, p. 89, 2006.

[135] C. Hitzenberger, E. Gotzinger, and M. Pircher, "Birefringence properties of the human cornea measured with polarization sensitive optical coherence tomography," *Bull Soc Belge Ophtalmol*, vol. 302, p. 153, 2006.

[136] R. W. Knighton and X.-R. Huang, "Linear birefringence of the central human cornea," *Investigative ophthalmology & visual science*, vol. 43, no. 1, pp. 82–86, 2002.

[137] L. J. Bour and N. J. Lopes Cardozo, "On the birefringence of the living human eye," *Vision research*, vol. 21, no. 9, pp. 1413–1421, 1981.

[138] J. W. Jaronski and H. T. Kasprzak, "Linear birefringence measurements of the in vitro human cornea," *Ophthalmic and Physiological Optics*, vol. 23, no. 4, pp. 361–369, 2003.

[139] R. J. Nordstrom, "The need for validation standards in medical imaging," in *Proc. SPIE* (R. J. Nordstrom, ed.), vol. Proc. of SPIE, pp. 756702–756702–7, 2010.

[140] A. M. Zysk, F. T. Nguyen, A. L. Oldenburg, D. L. Marks, and S. A. Boppart, "Optical coherence tomography: a review of clinical development from bench to bedside," *Journal of Biomedical Optics*, vol. 12, no. 5, p. 051403, 2007.

[141] 3D-OCT, "Buyers guide to fourier domain optical coherence tomography," 11 2006.

[142] Optos, "Product description," 2011.

[143] T. Fujiwara, Y. Imamura, R. Margolis, J. S. Slakter, and R. F. Spaide, "Enhanced depth imaging optical coherence tomography of the choroid in highly myopic eyes," *American journal of ophthalmology*, vol. 148, no. 3, pp. 445–450, 2009.

[144] M. Garvin, M. Abràmoff, K. Lee, M. Niemeijer, M. Sonka, and Y. Kwon, "2-d pattern of nerve fiber bundles in glaucoma emerging from spectral-domain optical coherence tomography.," *Invest Ophthalmol Vis Sci*, 2012.

[145] H. Van Dijk, F. Verbraak, P. Kok, M. Stehouwer, M. Garvin, M. Sonka, J. Devries, R. Schlingemann, and M. Abramoff, "Early neurodegeneration in the retina of type 2 diabetic patients.," *Invest Ophthalmol Vis Sci*, 2012.

[146] P. Albrecht, M. Ringelstein, A. Mueller, N. Keser, T. Dietlein, A. Lappas, A. Foerster, H. Hartung, O. Aktas, and A. Methner, "Degeneration of retinal layers in multiple sclerosis subtypes quantified by optical coherence tomography.," *Mult Scler*, 2012.

[147] A. O., P. Ieri, B. Ozkan, and Y. Calar, "Correlation between retinal morphological and functional findings and clinical severity in parkinson's disease.," *Doc Ophthalmol*, 2007.

[148] S. B. Park, K. R. Sung, S. Y. Kang, K. R. Kim, and M. S. Kook, "Comparison of glaucoma diagnostic capabilities of cirrus hd and stratus optical coherence tomography," *Arch Ophthalmol*, vol. 127, no. 12, pp. 1603–1609, 2009.

[149] S. R. Sadda, Z. Wu, A. C. Walsh, L. Richine, J. Dougall, R. Cortez, and L. D. LaBree, "Errors in retinal thickness measurements obtained by optical coherence tomography," *Ophthalmology*, vol. 113, no. 2, pp. 285 – 293, 2006.

[150] K. R. Sung, J. S. Kim, G. Wollstein, L. Folio, M. S. Kook, and J. S. Schuman, "Imaging of the retinal nerve fibre layer with spectral domain optical coherence tomography for glaucoma diagnosis," *Br J Ophthalmol*, 2010.

[151] M. N. Menke, S. Dabov, P. Knecht, and V. Sturm, "Reproducibility of retinal thickness measurements in healthy subjects using spectralis optical coherence tomography," *American Journal of Ophthalmology*, vol. 147, no. 3, pp. 467 – 472, 2009.

[152] D. E. Johnson, S. R. El-Defrawy, D. R. Almeida, and R. J. Campbell, "Comparison of retinal nerve fibre layer measurements from time domain and spectral domain optical coherence tomography systems," *Canadian Journal of Ophthalmology / Journal Canadien d'Ophtalmologie*, vol. 44, no. 5, pp. 562 – 566, 2009.

[153] M. Balasubramanian, C. Bowd, G. Vizzeri, R. N. Weinreb, and L. M. Zangwill, "Effect of image quality on tissue thickness measurements obtained with spectral domain-optical coherence tomography," *Opt. Express*, vol. 17, pp. 4019–4036, Mar 2009.

[154] S. Hong, Y. Kim, J. Shim, C. Y. Kim, and G. J. Seong, "Inter-device agreement of retinal nerve fiber layer thickness measurements using spectral domain cirrus hd oct," *Korean J Ophthalmol*, vol. 25, pp. 105–109, 2011.

[155] D. S. Chauhan and J. Marshall, "The interpretation of optical coherence tomography images of the retina," *Investigative Ophthalmology & Visual Science*, vol. 40, no. 10, pp. 2332–2342, 1999.

[156] G. J. Jaffe and J. Caprioli, "Optical coherence tomography to detect and manage retinal disease and glaucoma," *American Journal of Ophthalmology*, vol. 137, no. 1, pp. 156 – 169, 2004.

[157] D. L. Budenz, A. Michael, R. T. Chang, J. McSoley, and J. Katz, "Sensitivity and specificity of the stratusoct for perimetric glaucoma," *Ophthalmology*, vol. 112, no. 1, pp. 3–9, 2005.

[158] P. H. Tomlins, *Point-spread function phantoms for optical coherence tomography*. National Physical Laboratory, 2009.

[159] A. Agrawal, M. Connors, A. Beylin, C.-P. Liang, D. Barton, Y. Chen, R. A. Drezek, and T. J. Pfefer, "Characterizing the point spread function of retinal oct devices with a model eye-based phantom," *Biomed. Opt. Express*, vol. 3, pp. 1116–1126, May 2012.

[160] P. D. Woolliams, R. A. Ferguson, C. Hart, A. Grimwood, and P. H. Tomlins, "Spatially deconvolved optical coherence tomography," *Appl. Opt.*, vol. 49, pp. 2014–2021, Apr 2010.

[161] C. Akcay, P. Parrein, and J. P. Rolland, "Estimation of longitudinal resolution in optical coherence imaging," *Applied optics*, vol. 41, no. 25, pp. 5256–5262, 2002.

[162] P. D. Woolliams and P. H. Tomlins, "Estimating the resolution of a commercial optical coherence tomography system with limited spatial sampling," *Measurement Science and Technology*, vol. 22, no. 6, p. 065502, 2011.

[163] A. Agrawal, C.-W. Chen, J. Baxi, Y. Chen, and T. J. Pfefer, "Multilayer thin-film phantoms for axial contrast transfer function measurement in optical coherence tomography," *Biomedical optics express*, vol. 4, no. 7, pp. 1166–1175, 2013.

[164] P. H. Tomlins, G. N. Smith, P. D. Woolliams, J. Rasakanthan, and K. Sugden, "Femtosecond laser micro-inscription of optical coherence tomography resolution test artifacts," *Biomedical optics express*, vol. 2, no. 5, pp. 1319–1327, 2011.

[165] P. Woolliams and P. Tomlins, "The modulation transfer function of an optical coherence tomography imaging system in turbid media," *Physics in medicine and biology*, vol. 56, no. 9, p. 2855, 2011.

[166] D. M. Stein, H. Ishikawa, R. Hariprasad, G. Wollstein, R. J. Noecker, J. G. Fujimoto, and J. S. Schuman, "A new quality assessment parameter for optical coherence tomography," *British Journal of Ophthalmology*, vol. 90, no. 2, pp. 186–190, 2006.

[167] M. E. van Velthoven, M. H. van der Linden, M. D. de Smet, D. J. Faber, and F. D. Verbraak, "Influence of cataract on optical coherence tomography image quality and retinal thickness," *Br J Ophthalmol*, vol. 90, no. 10, pp. 1259–62, 2006.

[168] Y. Huang, S. Gangaputra, K. E. Lee, A. R. Narkar, R. Klein, B. E. K. Klein, S. M. Meuer, and R. P. Danis, "Signal quality assessment of retinal optical coherence tomography images," *Investigative Ophthalmology & Visual Science*, vol. 53, no. 4, pp. 2133–2141, 2012.

[169] E. J. Fernández and P. Artal, "Dynamic eye model for adaptive optics testing," *Appl. Opt.*, vol. 46, pp. 6971–6977, Oct 2007.

[170] D. Mordant, I. Al-Abboud, G. Muyo, A. Gorman, A. Sallam, P. Rodmell, J. Crowe, S. Morgan, P. Ritchie, A. Harvey, and A. McNaught, "Validation of human whole blood oximetry, using a hyperspectral fundus camera with a model eye," *Invest Ophthalmol Vis Sci.*, vol. 52, no. 5, pp. 2851–9, 2011.

[171] R. J. Nordstrom, "Phantoms as standards in optical measurements," *Proc. SPIE*, vol. 7906, pp. 79060–5, 2011.

[172] S. T. Rowe and R. J. Zawadzki, "New developments in eye models with retina tissue phantoms for ophthalmic optical coherence tomography," *Proc. SPIE*, vol. 8229, pp. 822913–8, 2012.

[173] J. Baxi, W. Calhoun, Y. J. Sepah, D. X. Hammer, I. Ilev, T. Joshua Pfefer, Q. D. Nguyen, and A. Agrawal, "Retina-simulating phantom for optical coherence tomography," *Journal of Biomedical Optics*, vol. 19, no. 2, pp. 021106–021106, 2013.

[174] A. Z. Soliman, P. S. Silva, L. P. Aiello, and J. K. Sun, "Ultra-wide field retinal imaging in detection, classification, and management of diabetic retinopathy," *Seminars in Ophthalmology*, vol. 27, no. 5-6, pp. 221–227, 2012. PMID: 23163280.

[175] P. S. Silva, J. D. Cavallerano, D. Tolls, A. Omar, K. Thakore, B. Patel, M. Sehizadeh, A. M. Tolson, J. K. Sun, L. M. Aiello, *et al.*, "Potential efficiency benefits of non-mydriatic ultrawide field retinal imaging in an ocular telehealth diabetic retinopathy program," *Diabetes care*, vol. 37, no. 1, pp. 50–55, 2014.

[176] F. Seidensticker, A. S. Neubauer, T. Wasfy, C. Stumpf, S. R. Thurau, A. Kampik, and M. Kernt, "Wide-field fundus autofluorescence corresponds to visual fields in chorioretinitis patients," *Clinical ophthalmology (Auckland, NZ)*, vol. 5, p. 1667, 2011.

[177] R. G. Sayegh, C. Simader, U. Scheschy, A. Montuoro, C. Kiss, S. Sacu, D. P. Kreil, C. Prünte, and U. Schmidt-Erfurth, "A systematic comparison of spectral-domain optical coherence tomography and fundus autofluorescence in patients with geographic atrophy," *Ophthalmology*, vol. 118, no. 9, pp. 1844 – 1851, 2011.

[178] L. K. Seibold, N. Mandava, and M. Y. Kahook, "Comparison of retinal nerve fiber layer thickness in normal eyes using time-domain and spectral-domain optical coherence tomography," *Am. J. Ophthalmol.*, vol. 150, pp. 807–817, December 2010.

[179] M. G. Sandrian, P. Tomlins, P. Woolliams, J. Rasakanthan, G. C. Lee, and A. Y. *et al.*, "Three-dimensional calibration targets for optical coherence tomography," *Proc. SPIE*, vol. 8229, p. 822914, 2012.

[180] D. M. de Bruin, R. H. Bremmer, V. M. Kodach, R. de Kinkelder, J. van Marle, T. G. van Leeuwen, and D. J. Faber, "Optical phantoms of varying geometry based on thin building blocks with controlled optical properties," *J Biomed Opt*, vol. 15, no. 2, p. 025001, 2010.

[181] A. Curatolo, B. F. Kennedy, and D. D. Sampson, "Structured three-dimensional optical phantom for optical coherence tomography," *Opt. Express*, vol. 19, pp. 19480–19485, Sep 2011.

[182] L. Llorente, S. Barbero, D. Cano, C. Dorronsoro, and S. Marcos, "Myopic versus hyperopic eyes: axial length, corneal shape and optical aberrations," *Journal of Vision*, vol. 4, no. 4, 2004.

[183] Objet, "The 16 micron layer 3d printing system," 2012.

[184] B. W. Pogue and M. S. Patterson, "Review of tissue simulating phantoms for optical spectroscopy, imaging and dosimetry," *Journal of Biomedical Optics*, vol. 11, no. 4, pp. 041102+, 2006.

[185] R. Thompson and I. Lengyel, "Methods and compositions for detecting drusen and predicting age-related macular degeneration," Mar. 6 2014. WO Patent App. PCT/US2013/057,661.

[186] J. M. Flinn, P. Kakalec, R. Tappero, B. Jones, and I. Lengyel, "Correlations in distribution and concentration of calcium, copper and iron with zinc in isolated extracellular deposits associated with age-related macular degeneration," *Metallomics*, 2014.

[187] I. Lengyel and T. Peto, "Method and system for predicting an amyloidosis status," Aug. 22 2013. US Patent App. 13/772,600.

[188] A. Agrawal, T. J. Pfefer, N. Gilani, and R. Drezek, "Three-dimensional characterization of optical coherence tomography point spread functions with a nanoparticle-embedded phantom," *Opt. Lett.*, vol. 35, pp. 2269–2271, Jul 2010.

[189] M. T. Witmer, G. Parlitsis, S. Patel, and S. Kiss, "Comparison of ultra-widefield fluorescein angiography with the heidelberg spectralis® noncontact ultra-widefield module versus the optos® optomap®," *Clinical ophthalmology (Auckland, NZ)*, vol. 7, p. 389, 2013.

[190] Optovue, "ivue specifications." Website, Nov 2014.

[191] Y. Deng, K. Soules, D. Leung, W. Li, B. Jang, Q. Zhou, *et al.*, "Repeatability and reproducibility of ivue fd-oct system," *Investigative Ophtalmology and Visual Science*, vol. 54, no. 6, p. 1447, 2013.

[192] C. Zeiss, "Specification for the ciruss 500 and 5000." Website, 2014.

[193] V. Manjunath, M. Taha, J. G. Fujimoto, and J. S. Duker, "Choroidal thickness in normal eyes measured using cirrus hd optical coherence tomography," *American journal of ophthalmology*, vol. 150, no. 3, pp. 325–329, 2010.

[194] Topcon, "3d oct-1 maestro - revolutionary new oct," May 2013.

[195] S. Borman and R. L. Stevenson, "Super-resolution from image sequences-a review," in *mwscas*, p. 374, IEEE, 1998.

[196] H. Heimann, F. Jmor, and B. Damato, "Imaging of retinal and choroidal vascular tumours," *Eye*, vol. 27, no. 2, pp. 208–216, 2012.

# Appendix A

## A.1 Electronic Control of the COE

The electronic control of the COE begins when the operator chooses the imaging mode. The system is primed, which includes starting the polygon, powering lasers that require warming and the execution of safety protocols. An external line scan system monitors the revolution rate of the polygon by measuring optical feedback from a tapped off portion of the scan. Patient position is achieved using a semi-automated parallax measurement of the pupil eccentricity. The operator triggers the capture that starts the slow scan mirror and frame start recording. Detectors capture the photons on avalanche photodiode that use a transimpedence amplifier to convert the current to voltage. The voltage-signal receives a gain based on the imaging mode from a secondary amplifier. The analogue voltage is sampled on a differential high-speed DAC which produces a combined sample rate of 132 MHz. The amplitude of the voltage is converted to a pixel value during the down sampling of the image from 12-bit to 8-bit for display which is performed via a histogram correction operation.

## A.2 COE PSF Analysis

Figure A.1 displays the physical optics propagation, or Gaussian traced spots for six locations in the eye. These plots show that horizontal scanning introduces astigmatism as the numerical aperture of the eye increases for the shorter focal lengths as the retina curves towards the pupil off-axis. Vertical scanning introduces significant defocus from the variable curvature of the ellipsoid and the field curvature of the eye.

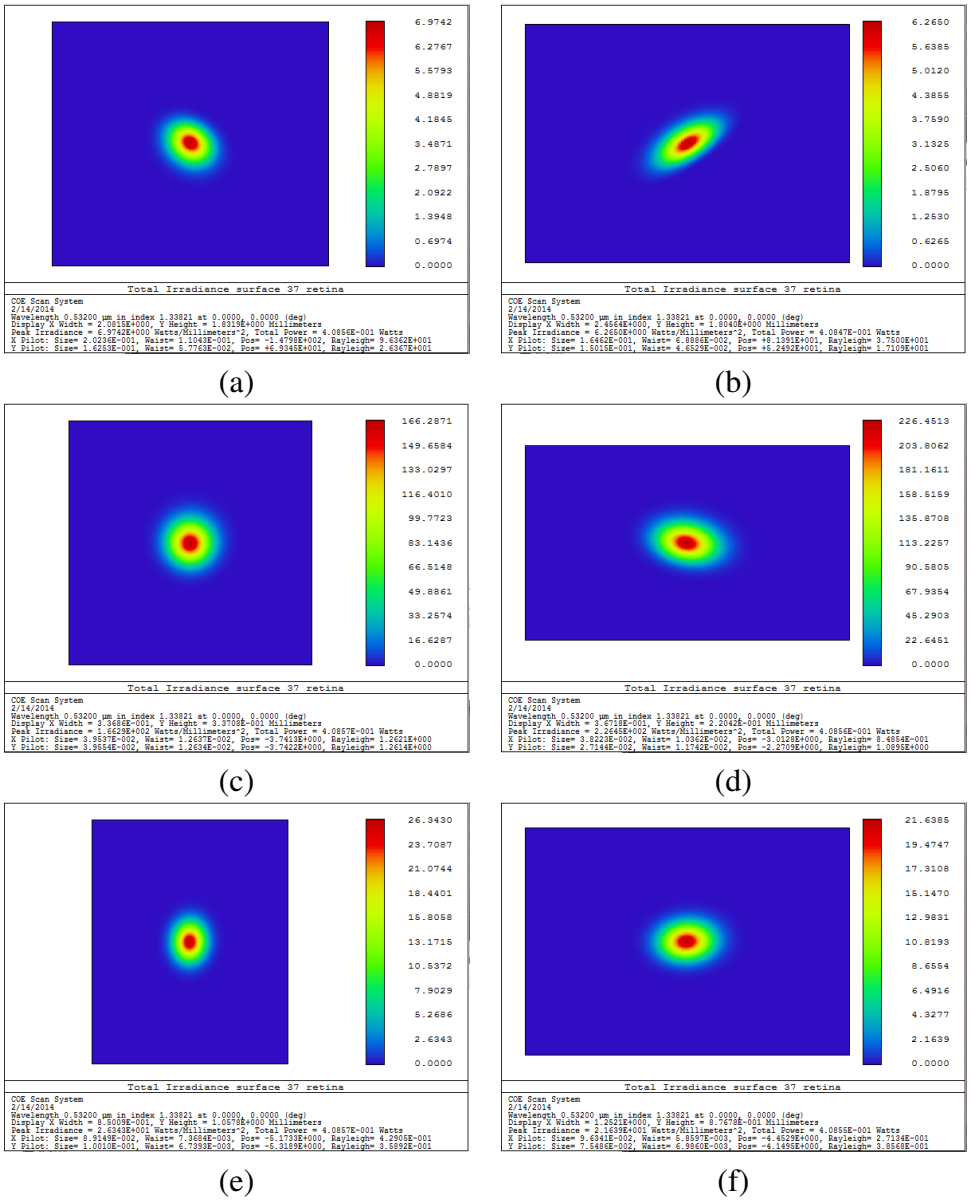


Fig. A.1 Physical optics propagation plots from Zemax from six separate locations in the eye. The left column shows the central position in the horizontal axis and the rows are descending locations in the retina; superior, on-axis, inferior.

## A.3 Liquid Lens Plots

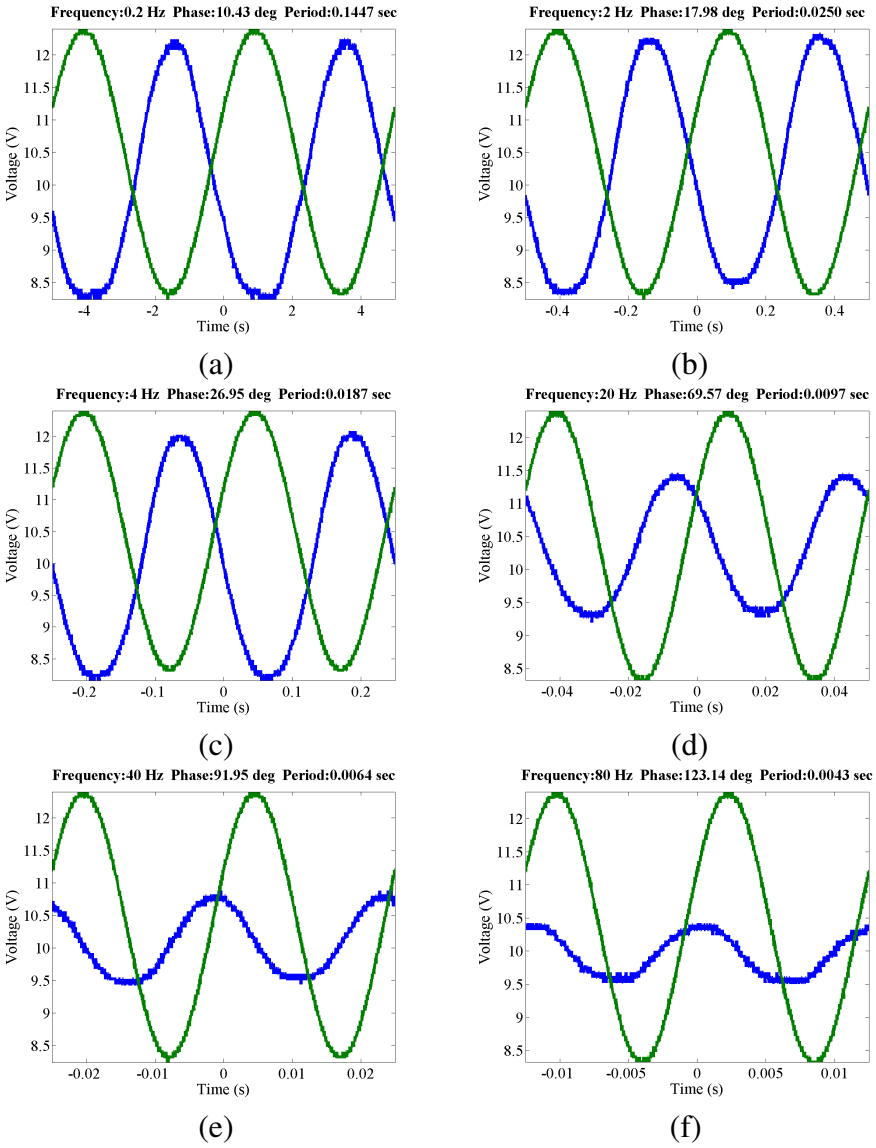


Fig. A.2 Six plots showing the detected voltage and drive voltage from a vignetted photoreceptor captured on an oscilloscope. By 8 Hz there is a significant phase delay of 41° and the focal shift achieved by the liquid lens has decreased to 86%.

## A.4 Verification of the WPE

The surface analysis plots are shown in Fig. A.3. These provide the basis for the verified WPE. The surface curvature was measured by imaging in OCT and fit to a conic equation in Matlab to extract the prescription of the lenses. This technique was also used for flattening the retina. The curvature segmented in Surface 2 was so narrow because of mirror artefacts obscuring the interface.

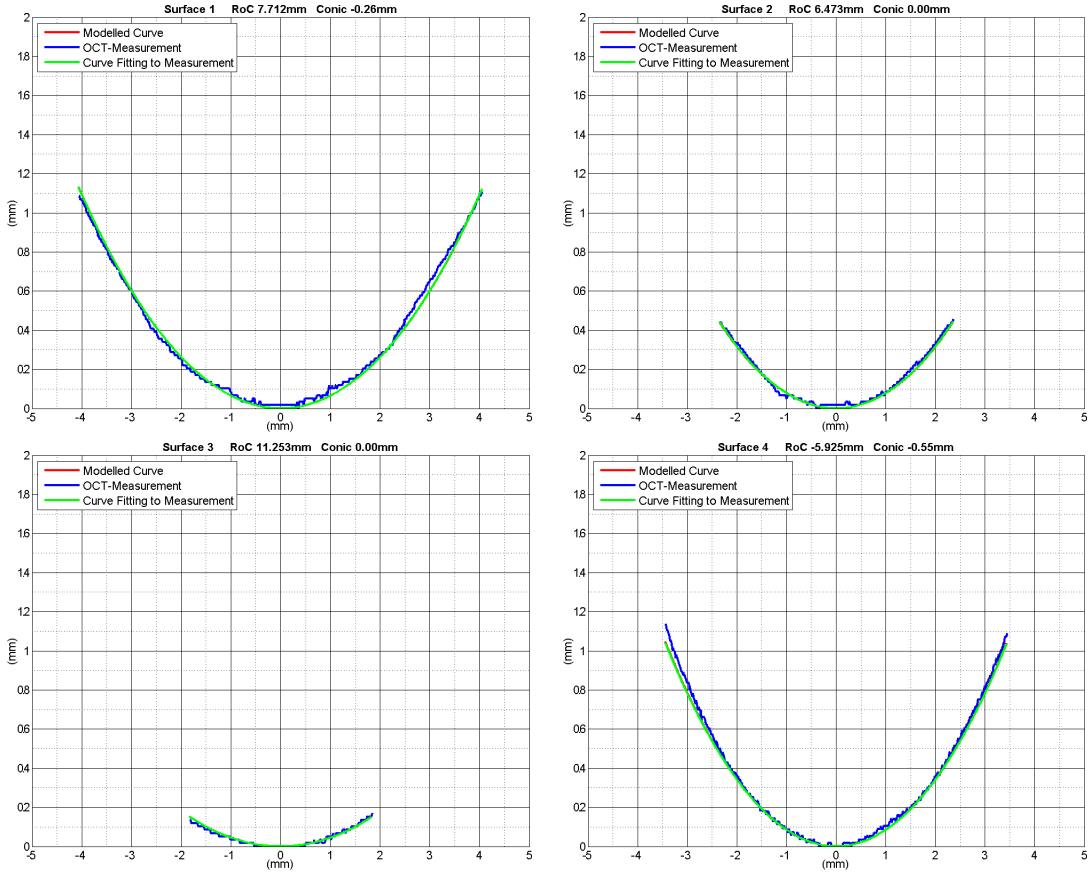


Fig. A.3 Plots of the verification of the corneal lens and the crystalline lens from the widefield phantom eye.

The distortion in camera used to verify the BE-Target had to be measured before it could be used to verify the BE-Target. The analysis plots from the verification of the BE-Target are shown in Fig. A.4

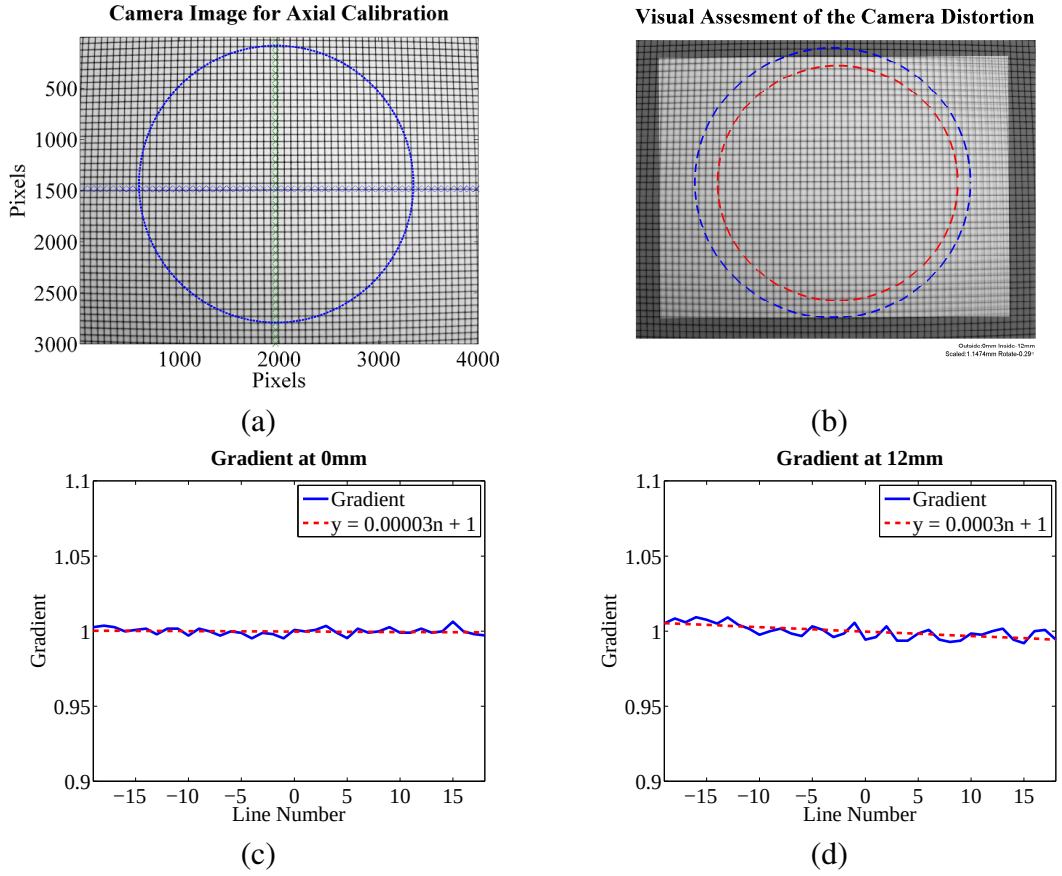


Fig. A.4 (a) The pixels of a 1 mm grid paper were selected for verification of traverse distortion. The blue ring shows the extent of bullseye diameter, denoted with red circle in Fig 6.17. (b) The two working distances for the camera required to image the near and furthest plane of the hemisphere (seperated by 12 mm) were registered to visualise compensate for longitudinal distortion. (c) and (d) show that there is no significant transverse distortion or an significant increase in transverse distortion due to a change in magnification.

## A.5 OCT Performance Comparison

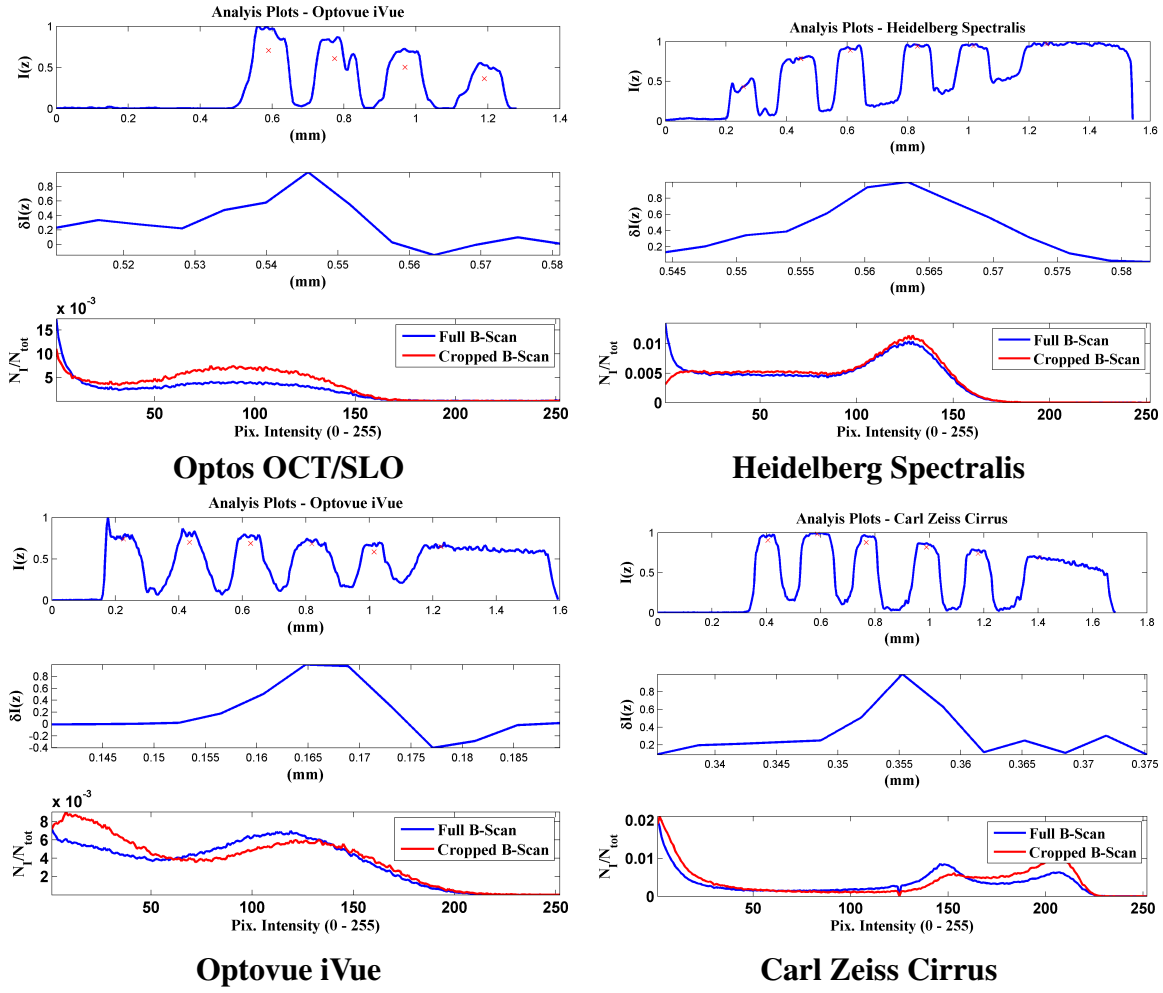


Fig. A.5 Analysis profile for the Optos OCT/SLO, Heidelberg Spectralis, Optovue iVue and Carl Zeiss Cirrus. Top: Horizontally averaged (100 pix.) A-Scan profile through the AL-Target. Middle: Line-spread function of the vitreo-target interface. Bottom: Histogram of the full image (Blue) Histogram of the AL-Target layers (Red)

### A.5.1 Optovue iVue & Carl Zeiss Cirrus - Off Axis

Images were aquired of the Optovue iVue an Carl Zeiss Cirrus off axis. The is little interesting in these images hence why they have been confined to the Appendix. It is clear in Fig. A.7 (b) that the Cirrus suffers from mirror artefact; however, its unclear whether the Optovue does. The

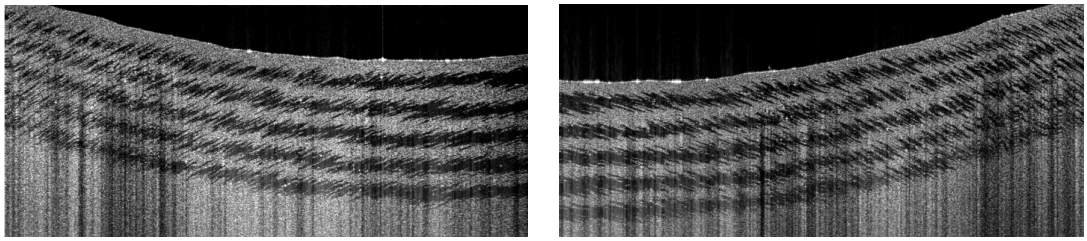

(a) (b)

Fig. A.6 (a) +20° Horizontally steered B-Scan of the AL-Target (b) -20° Horizontally steered B-Scan of the AL-Target

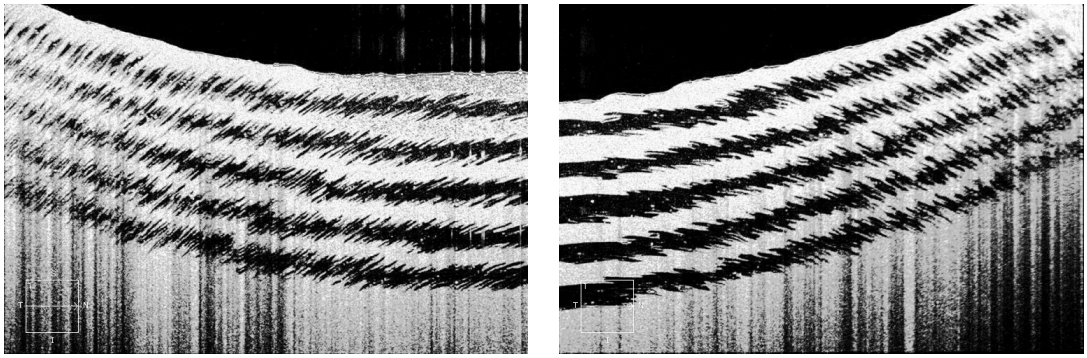

(a) (b)

Fig. A.7 (a) +20° Horizontally steered B-Scan of the AL-Target (b) -20° Horizontally steered B-Scan of the AL-Target

## A.6 Preliminary Assessment of the Baxi Model Eye

**Aim:** To assess if the Baxi model eye (BME) is sufficient to facilitate the validation of Lotte or act as a high resolution phantom for the comparison of Optos OCT/SLO and Lotte.

**Observations:**

1. The BME leaked in transit, contained an air bubble and required opening.
2. Eye model has no valves just uses hole to relieve pressure. Likely caused the leak.
3. Eye model a two lens system that is composed of moulded plastic.
4. Modelling shows BME and WPE are equivalent on-axis as both are diffraction onaxis limited.
5. Modelling shows BME is optically inferior to WPE off-axis.
6. Retina possibly hemispherical, curvature unknown.
7. Iris Diameter 8 mm - can only validate mydriatic imaging
8. B-Scans show excellent layer definition and realistic intensity jumps
9. RNFL appears to saturate the Optos OCT SLO
10. Macula feature found off centre, no optical disk obvious
11. RNFL layer thickness too thin for accurate segmentation by Optos OCT/SLO
12. Focus settings implied eye was highly myopic. This property contradicts modelling but is unsurprising as the eye housing lacked support for the correct reassembly of the lenses.

**Recommendation:** A longer study is required using either Optos OCT/SLO, currently not operation or a modified Optos OCT/SLO (available at lower image quality presently). Currently BME does not appear to have an optic disk, or sufficiently thick RNFL for segmentation. This is contrary to the publication and therefore may in fact appear elsewhere on the eye. Without an optic disk the phantom is only sufficient for resolution comparison.

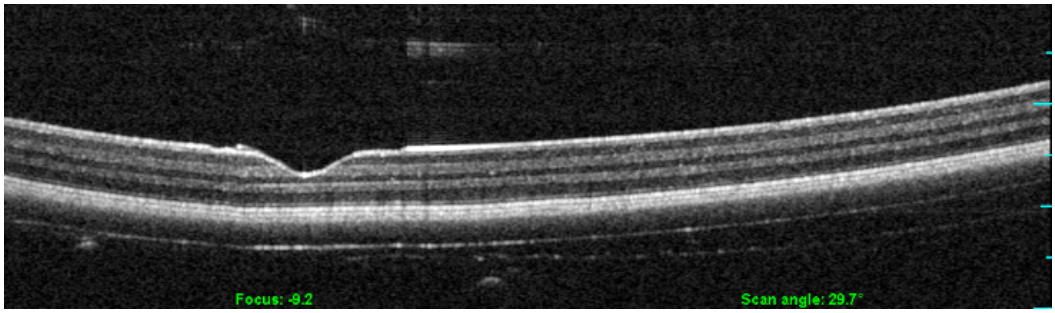


Fig. A.8 B-Scan showing macula. All layers are visible, importantly the thinnest the ELM.

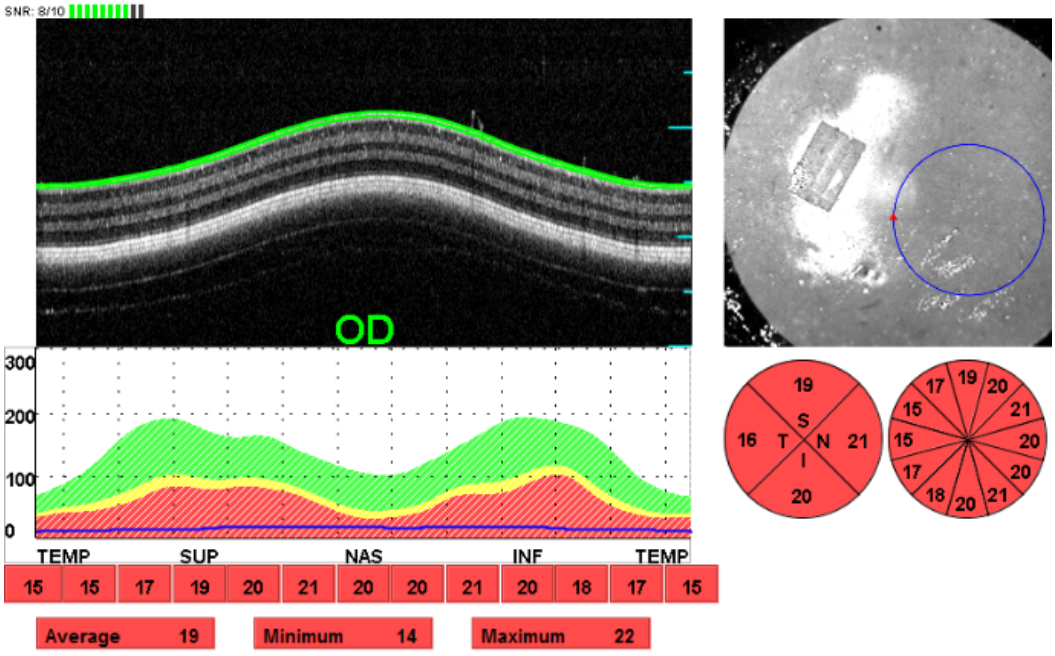


Fig. A.9 RNFL ring scan segmentation around what appears to be the centre of the retina. Segmentation locks onto bright thin layer. Unknown if this is the deliberate intensity or retinal-vitreous reflection SLO image on the top right shows a region of spin coated tissue with a rectangle where the foveal pit can be found. It is possible that the foveal pit rectangle from a different fabrication process.

# Appendix B

The provided code is for Matlab, any supporting m.files not listed are available by contacting the author on acorcoran03@gmail.com. Provided is the processing of spectral domain OCT signal, surface analysis code used to extract the curvature of an imaged surface, the reflectance imaging analysis code and the OCT imaging analysis code.

## B.1 OCT Processing and Dispersion Compensation

```
%%%
```

```
maxLambda=9.1000e-007; minLambda=7.7000e-007; c=2.998E8;

%% Generate Further Constants %%
meanLambda=(maxLambda+minLambda)/2;
nlambda=linspace(minLambda,maxLambda,nPixels);
wn1=1/minLambda; wn2=1/maxLambda;
nWavenumber=linspace(wn1,wn2, nPixels);
% wavenumber sampling, decending for increasing wavelength
meanWavenumber=mean(nWavenumber);
n0= 1.31830197; A = 1.07489208E-2; B = 1.47831952E-004;
n_lambda=n0+A/(meanLambda*1E6)+B/(meanLambda*1E6)^(7/2);%%
dz=meanLambda^2/(2*(maxLambda-minLambda));
% Pixel Resolution
z=(dz*(1:nPixels)-dz*nPixels/2)*1000/n_lambda;
% Thickness scale

%% Shape Frame %%
rawDataClip=rawData(1:nPixels*nAscans); %removes hneaders
frame=reshape(rawDataClip, nPixels, nAscans); %creates frame
clear rawDataClip
% convert from Zemax unicode output format
figure(1), plot(nlambda,frame(:,nXscans/2),'linewidth',2)
title('Spectrometer Output'); ylabel('Intensity'); xlabel('
    Wavelength (m)'); axis tight

%% Process: Smooth Spectrum %%
meanSpec=mean(frame,2)./max(mean(frame,2));
% averages + normalises across NAscabs only
H = fspecial('average',[30 1]);
smoothSpec = imfilter(meanSpec,H,'replicate');
% Filters high frequency signal (removes, cross correlation)
figure(2), plot(nlambda,smoothSpec,'linewidth',3)
title('Smooth A-Scan'); ylabel('Intensity'); xlabel('Wavelength (m
    )'); axis tight

%% Process: Clip Spectrum %%
leftClip=find(smoothSpec(1:nPixels/2)<0.05, 1, 'last');
% Find Left Threshold Point
rightClip=nPixels/2+find(smoothSpec(nPixels/2:nPixels)<0.05, 1, '
    first')-1;
% Find Right Threshold Point
smoothSpec(1:leftClip)=0;
smoothSpec(rightClip:nPixels)=0;

%% Process: Generate Inverse %%
invSpec=ones(2048,1);
```

```
% make piecewise vector
invSpec(leftClip:rightClip)=invSpec(leftClip:rightClip)./
    smoothSpec(leftClip:rightClip);
invSpec(1:leftClip)=0;
invSpec(rightClip:nPixels)=0;
figure(3), plot(nlambda,smoothSpec,'r',nlambda,invSpec,'g','
    linewidth',3)
title('Clipped and Inverted'); ylabel('Intensity'); xlabel('
    Wavelength (m)'); axis tight

%% Process: Normalise Each A-Scan %%
normSpec=frame./repmat(max(frame,[],1),[nPixels 1]);
figure(4), plot(nlambda,normSpec(:,nXscans/2),'linewidth',2)
title('Normalised Spectrum'); ylabel('Intensity'); xlabel('
    Wavelength (m)'); axis tight

%% Process: Flatten Spectrum %%
flatSpec=normSpec.*repmat(invSpec,[1 nAscans]);
figure(5), plot(nlambda,flatSpec(:,nXscans/2),'linewidth',2)
title('Flattened Spectrum'); ylabel('Intensity'); xlabel('
    Wavelength (m)'); axis tight

%% Remove Residue %%
residue0=(mean(flatSpec((leftClip+1:rightClip-1),:)));
clipLength=length(leftClip+1:rightClip-1);
flatSpec(leftClip+1:rightClip-1,:)=flatSpec(leftClip+1:rightClip
    -1,:)-repmat(residue0,[clipLength 1]);
hfSpec=flatSpec;
figure(6), plot(nlambda,hfSpec(:,nXscans/2),'linewidth',2)
title('High Frequency Component of Spectrum'); ylabel('Intensity')
    ; xlabel('Wavelength (m)'); axis tight

%% Process: Restore Spectral Shape to Cross Correlation Signal %%
lfSpec=hfSpec.*repmat(smoothSpec,[1 nAscans]);
figure(7), plot(nlambda,lfSpec(:,nXscans/2),'linewidth',2)
title('DC Cancelled Spectrum'); ylabel('Intensity'); xlabel('
    Wavelength (m)'); axis tight

%% Process: Interpolate Spectrum
tic
% Initialise
OCTDataBuffer.NSpectra=nAscans;
OCTDataBuffer.NPix = nPixels;
OCTDataBuffer.Pix0 = 1;
OCTDataBuffer.IMAQFreq = 20000;
AscanLength = 2048;
```

```
OCTDataBuffer.Ascans =frame(:);
NumberOfFFTBinsDesiredToBscanDepth=512;
BScanDepthInAirMillimeters=2.5; % Scan depth in millimeters
OCTDataBuffer.CamID = 3;
OCTDataBuffer.pCoefficients(1) = 4.330835e-04;
OCTDataBuffer.pCoefficients(2) = 2.401259e-08;
OCTDataBuffer.pCoefficients(3) = 1.499325e-12;
OCTDataBuffer.FFT1mmPosition = 2.150228e+02;
OCTDataBuffer.DownSampling=1;
j1=leftClip;
j2=rightClip;
%
CentrePosition=1024+1;
[~ , CentrePosition]=max(smoothSpec);
% Check PolyValueAt!!!
[InterpolationPts] = CalcSpectralRange(CentrePosition,
    OCTDataBuffer.pCoefficients, BScanDepthInAirMillimeters,...
      NumberOfFFTBinsDesiredToBscanDepth, OCTDataBuffer.
          FFT1mmPosition, AscanLength);
[ DataResampled ] = specProcGM(nAscans, OCTDataBuffer,invSpec,
    1.0/(2^12-1), j1, j2,smoothSpec, InterpolationPts, AscanLength)
    ;
% iterpolated Spectrum, specProcGM.m from G Muyo.
clear DataSmoothed DataResidual
display('Data interpolated');

%% for non well calibrated spectral output use below:
%DataResampled=fliplr(interp1(nlambda,lfSpec,1./nWavenumber,'
    spline'));
toc
figure(8), plot(nWavenumber,DataResampled(:,nXscans/2),'linewidth'
    ,2)
title('Interpolated Spectrum'); ylabel('Intensity'); xlabel('
    Wavenumber'); axis tight

%% Dispersion Compensation %%
% After removing the DC, calibrating the spectrometer and
    interpolation the first step is to find the analytical image of
     the real data: anImage=hilbert(DataResampled);
% The hilbert function in Matlab does more just the hibert
    transform, it creates the full analytical signal: hilbert(Re{S(
    v)}) = Re{S(v)} + i*im{S(v)} from this we can apply values for
    IGV and GVD below:
order=1E-9;
x=[0.8198, -0.553E-5];
% starting values for the GVD and IVG constants
```

```
%% feedback loop for x(1) %%
tic
if exist('x','var')
    % Checks if x exists as a variable
    x=x(1);
    sprintf('starting point of loop at x = %d', x)
else
    x=0;
    % begins the loop at zero if not
end
xo=x;
% creates starting point
initmfuncval=optomiseDisp1(xo, meanWavenumber,nWavenumber,anImage,
    nAscans);

% % % % % % % % % % % % % %
%% optomiseDisp1.m file: %%
% % % % % % % % % % % % % %

function [Metric] = optomiseDisp1(x,meanWavenumber,nwavenumber,
    anImage,nAscans)
order=1E-9;
IGV=repmat(exp(-1i*x*order*(meanWavenumber-nwavenumber)'.^2),[1
    nAscans]);
GVD=ones(2048,nAscans);%repmat(exp(-1i*x(2)*(meanWavenumber-
    nwavenumber)'.^3),[1 3000]);

dispCorImage=conj(fft(anImage.*IGV.*GVD)).*(fft(anImage.*IGV.*GVD)
    );
display('Bscan calculated');
c0=871; % manually selected start of the image
c1=1870; % manually selected end of the image
cz0=100; % manually selected top of the image
cz1=2048/4; % manually selected top of the image
croppedBscan=dispCorImage(cz0:cz1,c0:c1);
imshow(croppedBscan)
Metric=1-max(sum(gradient(croppedBscan),1));
display(x)
display(Metric)
end
% % % % % % % % % % % % % %

%runs feedback for initial conditions
[x,fval]=fminsearch(@(x) optomiseDisp1(x, meanWavenumber,
    nWavenumber,anImage,nAscans), xo);
```

```
sprintf('starting metric = %f',initmfuncval)
sprintf('ending metric = %f',fval)
sprintf('end point of loop at x = %d', x)
toc

%% feedback loop for x(2) %%
tic
if exist('x2','var')
    % Checks if x exists as a variable
     sprintf('starting point of loop at x = %d', x2)
else
     x2=0;
    % begins the loop at zero if not
end
x1=x;
xo=x2;
% creates starting point
initmfuncval=fval;
%runs feedback for initial conditions
[x2,fval]=fminsearch(@(x2) optomiseDisp2(x2,x1, meanWavenumber,
    nWavenumber,anImage,nAscans), xo);

% % % % % % % % % % % % % %
%% optomiseDisp2.m file: %%
% % % % % % % % % % % % % %

function [Metric] = optomiseDisp2(x2,x1,meanWavenumber,nwavenumber
    ,anImage,nAscans)
order=1E-9;
IGV=repmat(exp(-1i*x1*order*(meanWavenumber-nwavenumber).^2),[1
    nAscans]);
GVD=repmat(exp(-1i*x2*order*(meanWavenumber-nwavenumber).^3),[1
    nAscans]);

dispCorImage=conj(fft(anImage.*IGV.*GVD)).*(fft(anImage.*IGV.*GVD)
    );
c0=871; % manually selected start of the image
c1=1870; % manually selected end of the image
cz0=100; % manually selected top of the image
cz1=2048/4; % manually selected top of the image
croppedBscan=dispCorImage(cz0:cz1,c0:c1);

Metric=1-max(sum(gradient(croppedBscan),1));
display(x2)
display(Metric)
end
```

```
% % % % % % % % % % % % % %


sprintf('starting metric = %f',initmfuncval)
sprintf('ending metric = %f',fval)
sprintf('end point of loop at x = %d', x2)
x=[x1 x2];
sprintf('a1 = %d, a2 = %d', x(1),x(2))
toc

%% Run Dispersion Compensation with Optomised Values %%
x1o=x1*order;
x2o=x2*order;
IGV=repmat(exp(-1i*x1o*(meanWavenumber-nWavenumber).^2),[1
    nAscans]);
% Creates Compelex Image of Inverse Group Velocity
GVD=repmat(exp(-1i*x2o*(meanWavenumber-nWavenumber).^3),[1
    nAscans]);
% Creates Complex Image of Group Velocity Dispersion
dispCorImage=conj(fft(anImage.*IGV.*GVD)).*(fft(anImage.*IGV.*GVD)
    );
% applies FFT for Imaging

%% Display Image %%
DataFFTLOG=LogImage(dispCorImage, 0.1, 0.3);
display('Bscan calculated');
c0=871; % manually selected start of the image
c1=1870; % manually selected end of the image
cz0=100; % manually selected top of the image
cz1=nPixels/4; % manually selected top of the image
croppedBscan=DataFFTLOG(cz0:cz1,c0:c1);
figure(9);
imagesc(1:1000,fliplr(linspace(z(end/2+cz0),z(end),cz1)),
    croppedBscan);
set(gca,'YDir','normal'); colormap('gray'); title('Dispersion
    Corrected Bscan'); xlabel('X (No. of Ascans)'); ylabel('Z (mm)'
    )

%% Measure FWHM of Strongest Interface (Measure PSF) %%
disCorImageNorm=dispCorImage(:,:)/max(dispCorImage(:,nAscans/2));
disp('With Dispersion Compensation')
peakDC=find(disCorImageNorm(:,nAscans/2)==1);
psfSamp=1000;
win=50;
```

```
psfSpec=interp1(peakDC-win/2:peakDC+win/2,disCorImageNorm(peakDC-
    win/2:peakDC+win/2,nAscans/2),linspace(peakDC-win/2,peakDC+win
    /2,psfSamp))';
dc_Ind=find(psfSpec>0.5);
resampleFactor=psfSamp/length(peakDC-win/2:peakDC+win/2);
% increase in sampling due to interpolation
fwhmDC=(dc_Ind(end)+1-dc_Ind(1))*dz/resampleFactor;
disp(fwhmDC)
figure(10), plot(fliplr(z(1:end/2)),disCorImageNorm(1:end/2,
    nAscans/2))
title('A-Scan'); ylabel('Intensity'); xlabel('z(mm)'); axis tight

%% No Dispersion (for Comparison) %%
ndc_Image=(conj(fft(DataResampled)).*(fft(DataResampled)));
ndcDataFFTLOG=LogImage(ndc_Image, 0.3, 0.3);
display('Bscan calculated');
c0=871; % manually selected start of the image
c1=1870; % manually selected end of the image
cz0=100; % manually selected top of the image
cz1=nPixels/4; % manually selected top of the image
ndccroppedBscan=ndcDataFFTLOG(cz0:cz1,c0:c1);
figure(11);
imagesc(1:1000,fliplr(linspace(z(end/2+cz0),z(end),cz1)),
    ndccroppedBscan);
set(gca,'YDir','normal'); colormap('gray'); title('no Correction
    Bscan'); xlabel('X (No. of Ascans)'); ylabel('Z (mm)')

%% Measure PSF for no dispersion Compensation %%
ndcImageNorm=ndc_Image(:,:)/max(ndc_Image(:,nAscans/2));
disp('No Dispersion Compensation')
peaknDC=find(ndcImageNorm(1:nPixels/2,nAscans/2)==1);
psfSamp=1000;
win=50;
psfSpec=interp1(peaknDC-win/2:peaknDC+win/2,ndcImageNorm(peaknDC-
    win/2:peaknDC+win/2,nAscans/2),linspace(peaknDC-win/2,peaknDC+
    win/2,psfSamp))';
ndc_Ind=find(psfSpec>0.5);
resampleFactor=psfSamp/length(peakDC-win/2:peakDC+win/2);
%increase in sampling due to interpolation
fwhmnoDC=(ndc_Ind(end)+1-ndc_Ind(1))*dz/resampleFactor;
disp(fwhmnoDC)
disp('Without Dispersion Compensation')
figure(12), plot(fliplr(z(1:end/2)),ndcImageNorm(1:nPixels/2,
    nAscans/2))
title('A-Scan'); ylabel('Intensity'); xlabel('z(mm)'); axis tight
```

```
%% Compare the central A-scan of all two Methods %%
figure (13), clf, hold on
plot((-z(1:end/2))+3.7E-3,disCorImageNorm(1:end/2,nAscans/2),'g')
plot(z(end/2+10:end),ndcImageNorm((end/2+10:end),nAscans/2),'r')
h = legend('Dispersion Correction','No Dispersion Correction','DC
    Not Removed',1);
set(h,'Interpreter','none')
axis tight; xlabel('Position(mm)'); ylabel('Norm. Intensity')
```

## B.2 Surface Analysis Code

This code as able to take a anterior segment B-scan from a Optos OCT SLO and calculate the radius of curvature and conic value of a lens. The files requires a calibration flat image and an image of a lens, plus calibration of the axial and transverse pixel scaling of that device. As signal intensity is variable on the b-scan the peakseak function may need tuning to ensure that there is a peak to be found.

```
%%%
```

```
    L_flat(i)=l1;                          % scans rows
end

%% Detect Surface of Lens %%
for i = 1:Nx-1
    cs=surface(:,i);                       % scans columns
     [l1,p1]=peakseekDC(cs,16,42,5);       % manually optomised
    L_surface(i)=l1(1);                    % scans rows
end

%% use L_surface to straighten flat %%
y_straighten = (L_flat-max(L_flat));
L_flat_st=(L_flat-y_straighten);          % Flattening shift

%% use L_surface to straighten lens %%
% before applying the flattening algorythm the lens needs to be
    centred this is achieved by shaving enough pixels off the high
    sight of the lens until the lens minimum is placed at zero
crop=[1 Nx-1] %find(L_surface==L_surface(1));
   %
% used to find the first height where there are two equal heights
    at each side of the lens
L_surface_crop=L_surface(min(crop):max(crop)); % add plus one if
    stuck
y_straighten_crop=y_straighten
L_surface_st=L_surface_crop-y_straighten_crop;
nx_cal=((nx(round((Nx-(max(crop)))/2):(Nx-round((Nx-(max(crop)))
    /2))))-(max(nx)/2)).*tps;
L_SURF=-(L_surface_st-min(L_surface_st))*aps2;
% axial scale and shift axis to zero

%% Plot Ideal Values %%
R=5.9;              % Radius of Curvature
C=1/R;              % Curvature
K=-0.55;            % Conic Value
y=-max(nx_cal):aps:max(nx_cal);
z=(C.*y.^2)./(1+sqrt(1-(1+K)*C^2.*y.^2))
% equation of conic (from Zemax) also
%y=sqrt(2*R.*x+(K+1).*(x.^2));
 %% Fit Curve to Conic Equation to Data
xdata=nx_cal;
ydata =L_SURF;                         % sqrt(2*R.*xdata+(K+1).*(xdata
    .^2));
x0 = [0,C,K,0];                        % starting values (correct values)
% [y0,C,K,x0] variable calculated
[x,resnorm] = lsqcurvefit(@conic_equation,x0,xdata,ydata);
```

```
% % % % % % % % % % % % % %
%% conic_equation.m file: %%
% % % % % % % % % % % % % %

function F = myfun(x,xdata)
F=x(1)+(x(2)*(xdata-x(3)).^2)./(1+sqrt(1-((1+x(4))*x(1)^2.*(xdata-
    x(3)).^2)))
% % % % % % % % % % % % % % %

% Displace Values
Vertical_Displacement=x(1)
Horizontal_Displacement=x(4)
Radius_of_Curvautre=1/x(2)
Conic_Constant=K
```

## B.3 Reflectance Imaging Analysis Tool

This code was written to provide consistent analysis of images acquired on reflectance ophthalmoscopes. The following scripts have been omitted: crop200Tx.m, proc200Tx.m, circles200Tx.m, peakseakDC.m, scanAnglesWPE.m, vertSegment.m, xlsappend.m, scanAngles.mat Please contact the author if access is required.

```
%%%%%%%%%%%%%%%%%%%%%%%%%%%%%%%%%%%%%%%%%%%%%%%%%%%%%%%%%%%%%%%%%%%%%%%%
% Centring, FOV, Distortion and Contrast Measurement %
%    Optomised for uprojected 200TX and Daytona      %
%            Written: 14/04/2014                     %
%             Updated: 21-08-14                      %
%                 A Corcoran                         %
%%%%%%%%%%%%%%%%%%%%%%%%%%%%%%%%%%%%%%%%%%%%%%%%%%%%%%%%%%%%%%%%%%%%%%%%

%% Load Image for Analysis
prompt={'What Image Would You Like to Analyse? (1-25):'};
% The main title of your input dialog interface.
imaTitle='Image Selection';
answer=inputdlg(prompt,imaTitle);
imaNum=str2double(answer);
imageTitle = ['\imageStock\npDaytona' num2str(imaNum) '.tif'];
Ima1_rgb=imread(imageTitle);
if length(Ima1_rgb(1,1,:))==3
Ima1_gray=double(rgb2gray(Ima1_rgb));
else
    Ima1_gray=double(Ima1_rgb(:,:,1));
end
```

```
date_str=date;              % For later naming of printed file
width=numel(Ima1_gray(1,:)); height=numel(Ima1_gray(:,1));
imaSize=4000;
Ima1_gray_pad=padarray(Ima1_gray,[(imaSize-height)/2 (imaSize-
    width)/2]);
width=numel(Ima1_gray_pad(1,:)); disp('width of Tx'), disp(width),
height=numel(Ima1_gray_pad(:,1)); disp('height of Tx'), disp(
    height),
figure(1), imagesc(Ima1_gray_pad(:,:)), colormap('gray'), axis
    image

%% Crop to Area of Interest if centring is poor
[Ima1_gray_crop,width,height,noPixels,crop_x,crop_y]=...
     crop200TX(Ima1_gray_pad,width,height,noPixels);
centreDisp=[crop_x(1)-imaSize/2 crop_y(1)-imaSize/2];
figure(1), imagesc(Ima1_gray_crop)
title('Pre-Processed Image to Analisis Post Cropping')

%% Process Image
BgRow=1;                    % Remove periodic ambient intensity
low_pass=100;               % Flattens intensity in image
cThresh=220/255;            % Threshold does not alter to peak seaking
[procIma1] = proc200TX(Ima1_gray_crop,BgRow,low_pass,cThresh,
    height,width);
figure (2)
imagesc(imadjust(procIma1)),colormap(gray)
title('Processed Image to Analisis')
axis square

%% Generate  + Draw Circles
% This section of code generates rings that fit the radius of the
    WPE.
% For Diagonal:
nr = 15;                    % number of rings counted from the centre
pix_grad=1;                 % gradient of analysis
spacing = 55;               % number of rings counted from the centre
    Diag
% For Horizontal:
% pix_grad=0;               % gradient of analysis
% spacing = 65;             % number of rings counted from the centre
    Horiz

[cr,cx_pixel,cy_pixel,cr2,radius,l_ima1,pix_grad]= ...
     circles200TX(procIma1,nr,height,width,pix_grad,spacing);

% plots ring spacing:
```

```
figure (6)
plot((-nr+1):nr,abs(diff(cr)),'--bo','LineWidth',2,...
    'MarkerFaceColor',[1 0 0],'MarkerEdgeColor','k')
axis('tight'), xlabel('Ring Space'), ylabel('Pixels'), hold('off')

% Plots rings on Image:
figure(1)
title_str1=['UnProcessed 200TX with Rings: ' date_str];
title(title_str1)
for i=1:nr;
        rectangle('Position',[cx_pixel-cr2(i), cy_pixel-cr2(i),
           ...
         2*cr2(i), 2*cr2(i)],'curvature',[1 1],'EdgeColor','r')
end
axis image

%% Calculate FOV and Distortion
% Choose the first and last ring selections to consider
% Count from outside to in
prompt={'Selection corresponding to the left edge of the FOV:',...
    'Selection corresponding to the Right edge of the FOV:'};
title1='Manual FOV Selection';
answer = inputdlg(prompt,title1);
leftCrop = str2num(answer{1})-1;
rightCrop = str2num(answer{2})-1;

% Calculates the number of pixels between the selection
x0=cx_pixel;
x1=l_ima1(1+leftCrop);
x2=l_ima1(end-rightCrop);
y0=cy_pixel;
y1=pix_grad*(x1-x0)+cy_pixel;  %(y1-y0)=m(x1-x0)+c, c=0
y2=pix_grad*(x2-x0)+cy_pixel;  %(y1-y0)=m(x1-x0)+c, c=0
pixDiameter=sqrt((x1-x0)^2+(y1-y0)^2)+sqrt((x2-x0)^2+(y2-y0)^2);

% Known radius to final ring
knwnAL=1.05+1.1*(nr-1);
% Calculates Pixel Scale at Image Edge (Account for Disotrtion)
finalRingspacing=cr2(1)-cr2(2);
pixScale_finalRing=1.1/finalRingspacing;
% Calculates FOV which exceeds ring selection
extraFOVd=(pixDiameter-(2*cr2(1)))*pixScale_finalRing;
arclengthD=2*knwnAL+extraFOVd;
fieldAngleD=360*(arclengthD/(pi*24));

% Change Magnification + Distortion
```

```
dcr2=diff(cr2);  % Change in the number of pixels between rings
imaMag=dcr2(1)/dcr2(end);
imaDis=(dcr2(end)*-nr+sum(dcr2))/(dcr2(end)*-nr);

%% Arclength to External Field
% Load Zemax Scan Angles for CAD estimation of Ring Location
% Allows the conversion of External to Internal Scan Angles.
load('scanAngles.mat')
[internalAngle, arclength, external_scan, arclengths_intrp,...
    external_field]=scanAngleWPE(scanAngles,arclengthD) ;

%% Analyse Contrast through Vertical Segment
[vertContrast,fitContrast,fwhmContrast_precent,imageHieght]=...
    vertSegment( Ima1_gray_crop, 100, cx_pixel,height);

figure(9)
plot(vertContrast,'-b','LineWidth',2,'MarkerFaceColor', ...
[1 0 0],'MarkerEdgeColor','k') hold on, plot(fitContrast), hold
   off

FOV = [external_field*2, fieldAngleD, arclengthD];
vFOV=((2*1.1*14)-0.1)*fwhmContrast_precent/100;
ctrDisp=centreDisp/abs(dcr2(end)); % mm
rSpacing=abs(diff(cr));

%% Record Results
display ('Script Paused to allow figures to be reviewed')
figure(1),
choice = questdlg('Would you like save your data?', ...
            'Yes', ...
            'No');
% Handle response
switch choice
case 'Yes'
    if pix_grad == 0
        f = '\plotHorizontalMetricsDaytona\';
    elseif pix_grad == 1
        f = '\plotDiagonalMetricsDaytona\';
    end
[] = xlsappend([f 'radiusDaytonas.xlsx'],[imaNum radius],1);
[] = xlsappend([f 'vertContrast.xlsx'],[imaNum vFOV],1);
[] = xlsappend([f 'fieldofView.xlsx'],[imaNum FOV],1);
[] = xlsappend([f 'deCentering.xlsx'],[imaNum ctrDisp],1);
[] = xlsappend([f 'ringSpacing.xlsx'],[imaNum rSpacing],1);
[] = xlsappend([f 'distortion.xlsx'],[imaNum imaDis],1);
```

```
        disp(['Data from Image ' num2str(imaNum) ' has been saved'
            ])
    case 'no'
        disp('No data has been saved')
end
```

## B.4 OCT Imaging Analysis Code

Developed to provide consistent analysis of image quality metrics from an OCT device. This code should run without the need of further scripts.

```
%%%%%%%%%%%%%%%%%%%%%%%%%%%%%%%%%%%%%%%%%%%%%%%%%%%%%%%%%%%%%%%%%%%%%%%%
% PSF, Pitch, Quality Measurement & Image Flattening                    %
% Optomised for Onaxis and Widefield Images of AL-Target                %
%                  Written: 21/06/2014                                  %
%                   Updated: 05/10/2014                                 %
%                       A Corcoran                                      %
%%%%%%%%%%%%%%%%%%%%%%%%%%%%%%%%%%%%%%%%%%%%%%%%%%%%%%%%%%%%%%%%%%%%%%%%

%% Load Image and Calculate Paramters
BScan=imread('ModelE.tif');
BScan=rgb2gray(BScan); BScan=double(BScan(:,:,1));
width=numel(BScan(1,:)); height=numel(BScan(:,1));
refIndexPMMA=1.4853; refIndexWater=1.33;

%% Crop to Area of Interest
figure(1), imagesc(BScan),colormap('gray'), axis image
title('Please Choose Crop, Click and Drag Square')
[BScan,width,height]=...
    cropBscan(BScan,width,height);
figure(1), imagesc(BScan)
title('Pre-Processed Image to Analyse Post Cropping')

%% Threshold Image & Select an Image
BScan=BScan/max(BScan(:));          % Normalise
level = graythresh(BScan);          % Chose Threshhold Level
bw = im2bw(BScan,level);            % Thresholds Image
bw = bwareaopen(bw, 1);              % for0-7, (I,selectivity)
se90 = strel('line', 1, 90); se0 = strel('line', 1, 0);
BWsdil = imdilate(bw, [se90 se0]);
Select Edge in situations where B-scan intersects top or bottom
retheight=[]; width=size(BScan,2); height=size(BScan,1);
for i=1:width-1
    if sum(BWsdil(:,i))>1
        retH=find(flipud(BWsdil(:,i)),1,'last');
        retheight(i)=retH;
```

```
    else
        retheight(i)=0;
    end
end

%% Fit Curve to Conic Equation to Data
% pixel scaling (measured from image)
aps=(6.9E-3); tps=(10.5E-3); nx=1:width-1;
nx_cal=(nx-(length(nx)/2)).*tps;
x = [0,0,0]; xdata=nx_cal; ydata=(retheight)*aps;
[x,resnorm] = lsqcurvefit(@polynomEq,x,xdata,ydata);
z = x(1).*xdata.^2+x(2).*xdata+x(3);
% Convert Curve to Curvature
dx  = gradient(xdata); ddx = gradient(dx);
dy  = gradient(z); ddy = gradient(dy);
num   = dx .*ddy - ddx .*dy; denom = dx.*dx + dy.*dy;
denom = sqrt(denom); denom = denom .* denom .* denom;
curvatur = num ./ denom; curvature(denom < 0) = NaN;
RoC=1/mean(curvatur);

%% Flatten Image
Ipad=padarray(BScan, [200,0]); % Prep Image for Flattening
height=length(Ipad(:,1)); nx2=xdata;
z = (x(1).*nx2.^2+x(2).*nx2+x(3))./aps;
for i=(1):(width-1) % Flatten Image
    A = Ipad(:,i);
    circsize = round(z(i)-8-200);
    b = circshift(A,circsize);
    flatBscan(:,i)=b;
end
Ima=(flatBscan./max(flatBscan(:)))*255;
%% Calculate Information Metrics
[xy]=ginput(2); % Select region of interest
xyCd=round(xy);
Ima_crop=Ima(xyCd(1,2):xyCd(2,2),:);
E_crop=entropy(Ima_crop); STD_Crop=std(Ima_crop(:));

%% A-scan Profile
xmid=xyCd(1,1);
Ascanm=sum(Ima(:,xmid-50:xmid+50),2);
Ascanmn=Ascanm/max(Ascanm);
crop=find(Ascanm > 0.0001);
profile=Ascanmn(crop(1):crop(end));
N_prof=length(Ascanm(crop(1):crop(end)));
Ni_prof=N_prof*10;
m=linspace(0,N_prof,N_prof);
```

```
i_m=linspace(0,N_prof,Ni_prof);
Prof_int=interp1(m,profile,i_m);
figure(4),clf, subplot(3,1,1)
plot(1:Ni_prof,Prof_int,'linewidth',2)
h=fspecial('gaussian',[1 300], 100);
Prof_smooth=imfilter(Prof_int, h,'symmetric');
[l,p]=peakseekDC(Prof_smooth, 50,0.1,0.1);
hold on, scatter(l,p,'xr')
z_pixSpacing=mean(diff(l))/2;

%% Plot profile with scaled axis
figure(4),clf, subplot(3,1,1)
z_m=linspace(0,N_prof*(1/z_pixSpacing),N_prof);
zi_m=linspace(0,N_prof*(1/z_pixSpacing),Ni_prof);
Prof_int=interp1(z_m,profile,zi_m);
plot(zi_m,Prof_int,'linewidth',2)
hold on,, scatter(l*((zi_m(end)/Ni_prof)),p,'xr')
title('Analyis Plots - Optovue iVue')
SigDepth=l(end)*((zi_m(end)/Ni_prof))-l(1)*((zi_m(end)/Ni_prof));
rolloff=Idepth(end)/Idepth(1);

%% PSF Calculation
subplot(3,1,2), Dprof=diff(profile);
n=find(Dprof==max(Dprof));
N=n-6:n+6;, Ni=n-6:0.1:n+6;
zNi=linspace(z_m(n-6),z_m(n+6),1000);
NFFT=length(N); PSF=Dprof(N)/max(Dprof(N));
PSFi=interp1(z_m(N),PSF',zNi);
axis tight, subplot(3,1,3)

%% DFT of Edge-Spread for MTF
u=1/(2*170); I_f=fftshift(fft(Dprof(N)));
MTF=abs(I_f); MTFn=MTF/max(MTF);
f=u*(linspace(-1,1,NFFT)-1/NFFT);
%% Find FWHM of Profile
w=find(PSFi>0.5); WHM=(zNi(w(end))-zNi(w(1)))*1000;

%% Find Histogram Metric; image_hist=imhist(BScan);
image_hist_crop=imhist(Ima_crop./255);
image_hist=image_hist./sum(image_hist);
image_hist_crop=image_hist_crop./sum(image_hist_crop);
noise=sum(image_hist_crop(1:70)); % Threshold set manually
signal=sum(image_hist_crop(71:end));
QI=signal/noise;
```